



University of Kentucky
UKnowledge

Theses and Dissertations--Pharmacy

College of Pharmacy


2017

Development of Diverse Size and Shape RNA Nanoparticles and Investigation of their Physicochemical Properties for Optimized Drug Delivery

Daniel L. Jasinski

University of Kentucky, d.jasinski@uky.edu

Author ORCID Identifier:

 <http://orcid.org/0000-0001-9897-8506>

Digital Object Identifier: <https://doi.org/10.13023/ETD.2017.169>

[Right click to open a feedback form in a new tab to let us know how this document benefits you.](#)

Recommended Citation

Jasinski, Daniel L., "Development of Diverse Size and Shape RNA Nanoparticles and Investigation of their Physicochemical Properties for Optimized Drug Delivery" (2017). *Theses and Dissertations--Pharmacy*. 72.

https://uknowledge.uky.edu/pharmacy_etds/72

This Doctoral Dissertation is brought to you for free and open access by the College of Pharmacy at UKnowledge. It has been accepted for inclusion in Theses and Dissertations--Pharmacy by an authorized administrator of UKnowledge. For more information, please contact UKnowledge@lsv.uky.edu.

STUDENT AGREEMENT:

I represent that my thesis or dissertation and abstract are my original work. Proper attribution has been given to all outside sources. I understand that I am solely responsible for obtaining any needed copyright permissions. I have obtained needed written permission statement(s) from the owner(s) of each third-party copyrighted matter to be included in my work, allowing electronic distribution (if such use is not permitted by the fair use doctrine) which will be submitted to UKnowledge as Additional File.

I hereby grant to The University of Kentucky and its agents the irrevocable, non-exclusive, and royalty-free license to archive and make accessible my work in whole or in part in all forms of media, now or hereafter known. I agree that the document mentioned above may be made available immediately for worldwide access unless an embargo applies.

I retain all other ownership rights to the copyright of my work. I also retain the right to use in future works (such as articles or books) all or part of my work. I understand that I am free to register the copyright to my work.

REVIEW, APPROVAL AND ACCEPTANCE

The document mentioned above has been reviewed and accepted by the student's advisor, on behalf of the advisory committee, and by the Director of Graduate Studies (DGS), on behalf of the program; we verify that this is the final, approved version of the student's thesis including all changes required by the advisory committee. The undersigned agree to abide by the statements above.

Daniel L. Jasinski, Student

Dr. Peixuan Guo, Major Professor

Dr. David Feola, Director of Graduate Studies

DEVELOPMENT OF DIVERSE SIZE AND SHAPE RNA
NANOPARTICLES AND INVESTIGATION OF THEIR
PHYSICOCHEMICAL PROPERTIES FOR OPTIMIZED DRUG
DELIVERY

DISSERTATION

A dissertation submitted in partial fulfillment of the requirements for the degree of
Doctor of Philosophy in the College of Pharmacy at the University of Kentucky

By

Daniel L. Jasinski

Lexington, Kentucky

Co-Directors: Dr. Peixuan Guo, Professor of Pharmaceutical Sciences

and Dr. Joseph Chappell, Professor of Pharmaceutical Sciences

Lexington, Kentucky

2017

Copyright © Daniel L. Jasinski 2017

ABSTRACT OF DISSERTATION

DEVELOPMENT OF DIVERSE SIZE AND SHAPE RNA NANOPARTICLES AND INVESTIGATION OF THEIR PHYSICOCHEMICAL PROPERTIES FOR OPTIMIZED DRUG DELIVERY

RNA nanotechnology is an emerging field that holds great promise for advancing drug delivery and materials science. Recently, RNA nanoparticles have seen increased use as an *in vivo* delivery system. RNA was once thought to have little potential for *in vivo* use due to biological and thermodynamic stability issues. However, these issues have been solved by: (1) Finding of a thermodynamically stable three-way junction (3WJ) motif; (2) Chemical modifications to RNA confer enzymatic stability *in vivo*; and (3) the finding that RNA nanoparticles exhibit low immunogenicity *in vivo*.

In vivo biodistribution and pharmacokinetics are affected by the physicochemical properties, such as size, shape, stability, and surface chemistry/properties, of the nanoparticles being delivered. RNA has an inherent advantage for nanoparticle construction as each of these properties can be finely tuned. The focus of this study is as follows: (1) Construction of diverse size and shape RNA nanoparticles with tunable physicochemical properties; (2) Investigation of the effect that size, shape, and nanoparticle properties have on *in vivo* biodistribution; (3) Development of drug encapsulation and release mechanism utilizing RNA nanotechnology; and (4) Establishment of large-scale synthesis and purification methods of RNA nanoparticles.

In (1), RNA triangle, square, and pentagon shaped nanoparticles were constructed using the phi29 pRNA-3WJ as a core motif. Square nanoparticles were constructed with sizes of 5, 10, and 20 nanometers. The RNA polygons were characterized by AFM to demonstrate formation of their predicted geometry per molecular models. Furthermore, the properties of RNA polygons were tuned both thermodynamically and chemically by substitution of nucleic acid type used during nanoparticle assembly.

In (2), the biodistribution of RNA nanosquares of diverse sizes and RNA polygons of diverse shapes were investigated using tumor models in nude mice. It was found that increasing the size of the nanosquares led to prolonged circulation time *in vivo* and higher apparent accumulation in the tumor. However, it was observed that changing of shape had little effect on biodistribution. Furthermore, the effect of the hydrophobicity on RNA

nanoparticles biodistribution was examined in mouse models. It was found that incorporation of hydrophobic ligands into RNA nanoparticles causes non-specific accumulation in healthy organs, while incorporation of hydrophilic ligands does not. Lower accumulation in vital organs of hydrophobic chemicals was observed after conjugation to RNA nanoparticles, suggesting RNA has the property to solubilize hydrophobic chemicals and reduce accumulation and toxicity in vital organs.

In (3), a 3D RNA nanoprism was constructed to encapsulate a small molecule fluorophore acting as a model drug. The fluorophore was held inside the nanoprism by binding to an RNA aptamer. The ability of the stable frame of the nanoprism to protect the fragile aptamer inside was evidenced by a doubling of the fluorescent half-life in a degrading environment.

In (4), a method for large-scale *in vitro* synthesis and purification of RNA nanoparticles was devised using rolling circle transcription (RCT). A novel method for preparing circular double stranded DNA was developed, overcoming current challenges in the RCT procedure. RCT produced more than 5 times more RNA nanoparticles than traditional run-off transcription, as monitored by gel electrophoresis and fluorescence monitoring. Finally, large-scale purification methods using rate-zonal and equilibrium density gradient ultracentrifugation, as well as gel electrophoresis column, were developed.

KEYWORDS: RNA Nanotechnology, Bionanotechnology, Nanoparticle Properties, Drug Encapsulation, Rolling Circle Transcription

Daniel L. Jasinski

Student's Signature

May 3, 2017

Date

DEVELOPMENT OF DIVERSE SIZE AND SHAPE RNA NANOPARTICLES AND
INVESTIGATION OF THEIR PHYSICOCHEMICAL PROPERTIES FOR
OPTIMIZED DRUG DELIVERY

By

Daniel L. Jasinski

Dr. Peixuan Guo
Director of Dissertation

Dr. Joseph Chappell
Co-Director of Dissertation

Dr. David Feola
Director of Graduate Studies

May 3, 2017
Date

To my fiancé, my parents, and my family.
Thank you for your continual support and encouragement.

ACKNOWLEDGMENTS

First, I would like to thank my research advisor Dr. Peixuan Guo for his continual guidance and support throughout my Ph. D. studies. Thank you for giving me the opportunity to carry out my research in such a collaborative and supportive environment. With Dr. Guo's direction, I was allowed to cultivate and pursue my own research ideas, and expand my strengths while also developing new skills and ideas.

I would like to thank the members of my graduate committee: Dr. Joe Chappell, Dr. Mark Leggas, and Dr. Chris Richards. Their advice and continual interest in my research pushed me to excel as a scientist.

Additionally, I would like to thank lab members, past and present, of Dr. Guo's laboratory. I would like to give special thanks to Dr. Daniel Binzel, Dr. Emil Khisamutdinov, and Dr. Mario Vieweger, with whom I worked closely throughout my graduate career, for their insight and advice, both scientific and personal.

Additionally, I would like to thank all past and present members of the Guo laboratory; Dr. Dan Shu, Dr. Hui Zhang, Dr. Farzin Haque, Dr. Chard Schwartz, Dr. Ashwani Sharma, Dr. Taek Lee, Dr. Mehdi Rajabi, Dr. Shaoying Wang, Dr. Fengmei Pi, Dr. Hui Li, Dr. Zhengyi Zhao, Erfu Yan, Yanxi Xie, Zhouxiang Ji, Concong Xu, Hongran Yin, Sijin Guo, Zhefeng Li, Le Zhang, and Hongzhi Wang. My success in the Guo lab would not have been possible without our strong team work.

I would like to thank all the faculty and staff at the University of Kentucky College of Pharmacy and the Department of Pharmaceutical Sciences. Especially Catina Rossoll, graduate student coordinator, and Dr. Jim Pauly and Dr. David Feola, who both served as director of graduate studies during my graduate studies. Their help with my transition to

The Ohio State University is much appreciated, and without them I know the move would not have gone as smoothly as it did.

I would like to thank all the friends I have made throughout my graduate school career. Especially Daniel Binzel, Mario Vieweger, Emil Khisamutdinov, Steve Rheiner, and Ryan Hughes. They helped me to get through the everyday struggles encountered during graduate school.

Importantly, I would like to thank my parents, Dave & Suzanne Jasinski, and my brother, Chas Jasinski, for their unparalleled support, love, and encouragement throughout my graduate studies. Both my parents have demonstrated to me, throughout my life, what hard work and dedication truly look like. They have led by example to show me how to not only become a dedicated researcher, but also a good person. I will be forever indebted to them for their unselfish and gracious help throughout the last five years.

Finally, I would like to thank my now fiancé, Erica Schepp. The last five years have been a challenge being apart. Erica has been behind me the entire time, never wavering in her support for me pursuing my research dreams and my doctorate degree. I will be forever grateful to her for encouraging me to follow my interests, despite it keeping us apart for such a long time. I am thankful that I will get to spend the rest of my life with such a supportive, smart, and beautiful woman.

The work in this thesis dissertation was supported by the National Institute of Health under grants R01EB003730, R01EB019036, U01CA151648, and U01CA207946 to Peixuan Guo.

TABLE OF CONTENTS

Acknowledgments.....	iii
Table of Contents.....	v
List of Tables	viii
List of Figures.....	ix
List of Abbreviations	xii
Chapter 1: Introduction and Literature Review	1
Summary.....	1
Hypothesis.....	3
Literature Review	4
Chapter 2: Design, Construction, and Characterization of RNA Nanoparticles with Tunable Size, Shape, and Physicochemical Properties Based on phi29 pRNA-3WJ Core Motif	19
2.1: Design and Construction of RNA Nanoparticles with Tunable Shape.....	19
Introduction	19
Materials and Methods	21
Results	23
Discussion and Conclusions.....	27
Acknowledgements	28
2.2: Design and Construction of Physicochemically Tunable RNA Nanoparticles with Controllable Size	29
Introduction	29
Materials and Methods	32
Results and Discussion.....	35
Conclusions	44
Acknowledgements	45
Chapter 3: Effect of Nanoparticle Size, Shape, and Physicochemical Properties on Biodistribution in Mouse Tumor Models.....	58
3.1: The Effect of RNA Nanoparticle Size and Shape on Biodistribution	58
Introduction	58
Materials and Methods	61
Results	62
Discussion	65
Conclusions	68
Acknowledgements	69
3.2: The Effect of RNA Nanoparticle Hydrophobicity on Biodistribution	69
Introduction	69

Materials and Methods	72
Results and Discussion	74
Conclusions	80
Acknowledgements	80
 Chapter 4: Development of Three-Dimensional RNA Nanocages with Novel Small Molecule Encapsulation and Release Mechanism	93
Introduction	93
Materials and Methods	95
Results and Discussion	99
Conclusions	109
Acknowledgements	110
 Chapter 5: Large-scale <i>In Vitro</i> Synthesis and Purification of RNA Nanoparticles Using Rolling Circle Transcription.....	122
5.1: Co-Transcriptional Assembly of RNA Nanoparticles <i>via</i> Rolling Circle Transcription of Fully Double Stranded Circular DNA	122
Introduction	122
Materials and Methods	125
Results	128
Discussion	136
Conclusions	141
Acknowledgements	142
5.2: Large-scale Purification of RNA Nanoparticles using Preparative Ultracentrifugation.....	142
Introduction	142
Materials	145
Methods	148
Expected Results	155
Notes.....	156
Acknowledgements	160
 Chapter 6: Summary of Thesis Achievements and Outlook	171
Summary of Thesis Achievements.....	171
RNA Nanotechnology Outlook.....	172
Conclusions	175
Future Studies.....	175
 Appendices.....	181
Appendix 1. Supplemental Figures for Chapter 2	181
Appendix 2. Supplemental Figures for Chapter 3	192
Appendix 3. Supplemental Figures for Chapter 4	196
Appendix 4. Supplemental Figures for Chapter 5	204
 References.....	214

Vita.....246

LIST OF TABLES

Table 3.1. Elution time and %ACN elution of fluorophore species	81
Table 3.2. Amino acid hydrophobicity comparison to fluorophore species	82
Table 4.1. Fluorescence half-lives of prism constructs and control sequences	111
Table A.3.1. Nanoprism and control construct sequences	197
Table A.3.2. Nanoprism and control construct sequences	198
Table A.3.3. Nanoprism and control construct sequences	199
Table A.4.1. Sequences of RNA and DNA constructs	205
Table A.4.2. Summary of ribozyme cleavage efficiencies	206
Table A.4.3. Summary of sequences used in previously published papers using RCT and their ΔG values	207

LIST OF FIGURES

Figure 2.1. Design scheme for RNA triangle	46
Figure 2.2. Structural features of the pRNA 3WJ motif	47
Figure 2.3. Modular design technique used to construct RNA nanoparticles	48
Figure 2.4. Design of RNA polygons and their assembly properties	49
Figure 2.5. Structural verification and characteristics of RNA polygons	50
Figure 2.6. Comparison of polygon stabilities using TGGE and urea boiling assay	51
Figure 2.7. Design and assembly of RNA nanosquares	52
Figure 2.8. Structure verification and physical characteristics of RNA nanosquares	53
Figure 2.9. Comparison of hybrid nanosquares displaying tunable serum and thermodynamic stability	54
Figure 2.10. Assembly of multi-functional nanosquare harboring fluorogenic RNA aptamers	55
Figure 2.11. Fluorescence assays of multi-functional square	56
Figure 2.12. Ribozyme and siRNA activity of multifunctional RNA nanosquare	57
Figure 3.1. Design of diverse size and RNA polygons	83
Figure 3.2. <i>In vivo</i> biodistribution of diverse size RNA nanosquares in tumor bearing mice over 24 h	84
Figure 3.3. Organ images after 12 and 24 h of mice injected with 5, 10, and 20 nm RNA nanosquares	85
Figure 3.4. Serum degradation testing of RNA nanosquares	86
Figure 3.5. Organ images after 12 and 24 h of mice injected with diverse shape RNA nanoparticles	87
Figure 3.6. 3WJ introduction and characterization, and fluorophore conjugation scheme	88
Figure 3.7. Assembly of fluorophore labeled 3WJs and IPRP-HPLC characterization of 3WJ particles	89
Figure 3.8. Biodistribution in mice of 3WJ particles with different fluorophore labels	90
Figure 3.9. Comparison of predicted ClogP values of fluorophores and their nucleotide derivatives with predicted ClogP values of amino acids and their relationship to previously determined hydrophobicity scales	91
Figure 3.10. IPRP-HPLC analysis of fluorophore species and demonstration of RNA's ability to solubilize hydrophobic ligands	92
Figure 4.1. Design and 3D model of RNA nanoprism	112
Figure 4.2. Assembly and physical characterization of 3D RNA nanoprism	113
Figure 4.3. Encapsulation of malachite green fluorogenic RNA aptamer and fluorescence assay	115
Figure 4.4. Size alignment of RNase T1 with molecular model of the RNA nanoprism	116
Figure 4.5. Encapsulation and protection scheme of fragile RNA malachite green aptamer inside stable nanoprism frame	117
Figure 4.6. Schematic of small molecule and protein encapsulation inside the nanoprism	119

Figure 4.7. Serum degradation testing of nanoprisms constructed from RNA transcribed with different percentages of 2'F modified nucleotides, demonstrating tunable degradation profiles	120
Figure 4.8. Confocal images of folate functionalized and Cy5 labeled nanoprisms targeting KB cells	121
Figure 5.1. Assembly scheme of circular dsDNA encoding for self-cleaving ribozymes and target RNA sequence.....	161
Figure 5.2. Assembly confirmation of circular dsDNA and transcription analysis. Co-transcriptional assembly of the 3WJ nanoparticles is also confirmed.	162
Figure 5.3. Transcription and cleavage scheme for one-strand nanoparticle assembly...	163
Figure 5.4. Comparison of linear versus circular dsDNA transcription kinetics by ethidium bromide staining and fluorogenic aptamer analysis	164
Figure 5.5. Large-scale purification of RNA nanoparticles synthesized by RCT using gel column electrophoresis	165
Figure 5.6. Introduction to and mechanism of CsCl equilibrium density ultracentrifugation.....	166
Figure 5.7. Introduction to and mechanism of sucrose gradient rate-zonal ultracentrifugation.....	167
Figure 5.8. Gradient preparation and sample analysis of rate-zonal ultracentrifugation.	168
Figure 5.9. Gel analysis of results from RNA purification using CsCl equilibrium density ultracentrifugation and RNA nanoparticle purification using sucrose gradient rate-zonal ultracentrifugation	169
Figure A.1.1. Sequences and secondary structure of RNA polygons	182
Figure A.1.2. RNA polygons dissociation constant determination	183
Figure A.1.3. Population size distribution of RNA polygons from AFM images	184
Figure A.1.4. Sequences and secondary structures for 5, 10, and 20 nm RNA nanosquares	185
Figure A.1.5. Total strand participation assay of RNA nanosquares.....	186
Figure A.1.6. Melting temperature profiles of 5, 10, and 20 nm RNA nanosquares.....	187
Figure A.1.7. FBS degradation testing of nanosquare hybrids	188
Figure A.1.8. TGGE analysis of nanosquare hybrids	189
Figure A.1.9. Sequence and secondary structure of multi-functional RNA nanosquare.	190
Figure A.1.10. Fluorescence signal testing of multi-functional RNA nanosquare by PAGE	191
Figure A.2.1. Hydrophobicity comparisons of fluorophores and RNA/3WJ species using IPRP-HPLC.....	193
Figure A.2.2. Amino acid hydrophobicity comparison plots.....	194
Figure A.2.3. Chemical structures of fluorophores and their nucleic acid derivatives....	195
Figure A.3.1. Detailed sequence and assembly process of RNA nanoprism.....	200
Figure A.3.2. Magnesium ion effect on assembly of RNA nanoprism.....	201
Figure A.3.3. Control PAGE experiments excluding prism dimer and open prism constructs from gel shift assembly experiments	202
Figure A.3.4. Folate and Cy5 functionalized nanoprism assembly	203
Figure A.4.1. RNA size controls, example calculation of ribozyme efficiency, and sequence design and secondary structure of RCT 1.0 and RCT 1.1 ribozyme constructs	208

Figure A.4.2. PAGE assembly analysis of all circular dsDNA constructs	210
Figure A.4.3. Comparison of RCT cleaved 3WJ oligomer size to chemically synthesized oligomers of identical sequence.....	211
Figure A.4.4. Plots of DNA template concentration versus RNA output.....	212
Figure A.4.5. 2'F ribozyme cleavage attempt.....	213

LIST OF ABBREVIATIONS

2D	Two dimensional
2'F	2'-Fluorine RNA Modification
3D	Three Dimensional
3WJ	Three Way Junction
3WJ-a	A strand of the pRNA-3WJ
3WJ-b	B Strand of the pRNA-3WJ
3WJ-c	C Strand of the pRNA-3WJ
AGE	Agarose gel electrophoresis
AFM	Atomic Force Microscopy
bp	Base pairs
BSA	Bovine serum albumin
CsCl	Cesium chloride
DNA	Deoxyribonucleic Nucleic Acid
D _h	Hydrodynamic diameter
DLS	Dynamic light scattering
ds	Double Stranded
EB	Ethidium bromide
EPR	Enhanced permeability and retention
FBS	Fetal Bovine Serum
ΔG	Gibbs free energy value
IPRP	Ion-paired reverse-phased
HPLC	High-performance liquid chromatography
K _D	Dissociation Constant
h	Hours
MG	Malachite Green
miRNA	Micro Ribonucleic Acid
MPS	Mononuclear phagocytic system
mRNA	Messenger Ribonucleic Acid
nm	Nanometers
nt	Nucleotide
PAGE	Polyacrylamide Gel Electrophoresis
PBS	137 mM NaCl, 2.7 mM KCl, 100 mM Na ₂ HPO ₄ , 2 mM KH ₂ PO ₄ , pH 7.4
PCR	Polymerase Chain Reaction
pRNA	Packaging Ribonucleic Acid
RCT	Rolling Circle Transcription
RNA	Ribonucleic Acid
RNAi	Ribonucleic Acid Interference
RNase	Ribonuclease
RISC	RNA induced silencing complex
s	Seconds
siRNA	Small Interfering Ribonucleic Acid

SPIN	Spinach aptamer
ss	Single Stranded
STM	Scanning Tunnel Microscopy
SELEX	Systematic Evolution of Ligands by Exponential Enrichment
TBE	89 mM Tris-borate, 2 mM EDTA
TBM	89 mM Tris, 200 mM Boric Acid, 5 mM MgCl ₂
TEM	Transmission Electron Microscopy
TGGE	Temperature Gradient Gel Electrophoresis
T _m	Melting Temperature
TMS	50 mM Tris pH 8.0, 100 mM NaCl, 10 mM MgCl ₂
ΔG°	Change in Gibbs Free Energy
ΔH°	Change in Enthalpy
ΔS°	Change in Entropy
ΔT	Change in Temperature
τ	Time Constant

Chapter 1: Introduction and Literature Review

Chapter 1 was reproduced (with some modification) with permission from Jasinski, D; Haque, F; Binzel, DW; and Guo, P. “Advancement of the Emerging Field of RNA Nanotechnology.” *ACS Nano*, 2017. DOI: 10.1021/acsnano.6b05737. Copyright 2017 American Chemical Society.

SUMMARY:

Chapter 1 begins this thesis with an overview on nanotechnology and its application to advancing the field of drug delivery. The creation of RNA nanotechnology is then discussed, and previous and current RNA nanoparticle construction methods are introduced. Next, ways in which RNA nanotechnology overcomes current challenges in nanotechnology drug delivery are outlined. Finally, the importance of nanoparticle physical properties, such as size, shape, stability, and surface chemistry/properties, for *in vivo* drug delivery are discussed.

Chapter 2 introduces a method for the construction of RNA nanoparticles with diverse size, shape, and thermodynamic and chemical stability. RNA triangles, squares, and pentagons were constructed using the three-way junction (3WJ) motif from the packaging RNA (pRNA) of bacteriophage phi29. It was found that the inner angle of the 3WJ could be tuned from its native angle of 60°, ideal for triangle geometry, to 90° and 108°, ideal for square and pentagon geometry, respectively. The resulting nanoparticles display high thermodynamic stability despite stretching of the 3WJ from its ideal geometry.

RNA nanosquares with sizes of 5, 10, and 20 nm were constructed. Sizes were tuned by simply increasing or decreasing the number of RNA duplex turns between each corner of the square. Furthermore, nanosquare stability was tuned by chemically modifying one RNA strand used during construction. Nanosquare thermodynamic and serum stability was decreased and increased by modifying the structure with DNA and 2'-fluorine modified (2'F) RNA, respectively, thus demonstrating the tunable nature of RNA nanoparticles.

Chapter 3 considers how physical properties of RNA nanoparticles affect *in vivo* biodistribution. 2'F modified and fluorescently labeled nanosquares of different sizes were injected into tumor bearing nude mice and analyzed for tumor accumulation and nanoparticle clearance. A strong correlation between nanoparticle size, circulation time, and tumor accumulation was found. An increase in both tumor accumulation and circulation time is seen from the larger nanoparticles. However, the RNA nanosquares still show little fluorescence in healthy organs such as the liver and kidneys, compared to tumors, after 24 hours (h). Finally, the hydrophobic effects of externally conjugated chemicals on biodistribution was examined. It was found that increased hydrophobicity of conjugates caused accumulation of RNA nanoparticles in healthy tissue and organs, while more hydrophilic ligands showed weaker accumulation signal in vital organs.

Chapter 4 demonstrates a novel method for the encapsulation and controlled release of a model small molecule drug using RNA nanotechnology. Using previously designed RNA triangles, a three-dimensional (3D) nanoprism was constructed and characterized. A fluorogenic RNA aptamer was then encapsulated inside the nanoprism, allowing capture of a small molecule fluorophore, acting as a model drug, by binding to the aptamer. It was shown that the stable nanoprism frame protected the fragile RNA aptamer, which holds the

model drug, from degradation due to steric hindrance of degrading enzymes. Tuning the amount of 2'F modified nucleotides in the frame led to a controlled degradation profile of the nanoprism frame, allowing controlled release of the model fluorophore encapsulated within the nanoprism.

Chapter 5 details the development of large-scale synthesis and purification of RNA nanoparticles. A large-scale *in vitro* method for RNA nanoparticle synthesis was developed using rolling circle transcription (RCT) of a fully double stranded (ds) DNA template. This method overcomes current challenges associated with RCT to synthesize RNA nanoparticles from a single stranded (ss) DNA template displaying stable secondary structure, which hinders the progress of bacterial RNA polymerases. RNA nanoparticles were then purified by two large-scale methods: 1) rate-zonal and equilibrium density ultracentrifugation and 2) column gel electrophoresis. Both methods resulted in the purification of large amounts of pure RNA nanoparticles, paving the way towards pre-clinical development.

Chapter 6 summarizes the major findings and advancements of the research discussed in this thesis dissertation. Furthermore, the future direction of this work is described providing a prospective on research that is still needed to fully prove the benefits of RNA nanotechnology. Finally, the current state of RNA nanotechnology is discussed looking at the major hurdles that have been overcome, and the challenges that still need to be faced.

HYPOTHESIS:

The 3WJ motif from bacteriophage phi29 pRNA provides a stable RNA motif from which to build diverse size and shape, yet physicochemically tunable, RNA nanoparticles.

Different physical properties of RNA nanoparticles will affect biodistribution and pharmacokinetic profiles.

INTRODUCTION:

Nanotechnology and drug delivery

Nanotechnology can be defined as the science of engineering materials and systems; the ultimate goal being control over specific functions and properties of nanoparticles on a molecular scale. While the field of nanotechnology was conceived in 1959 by Richard Feynman's lecture "There's Plenty of Room at the Bottom" (1) it took more than two decades before one of Feynman's challenges, proposed during his lecture, was completed. Tom Newman, then a graduate student at Stanford, successfully printed the first paragraph of *A Tale of Two Cities* at 1/25000th scale (2). Nanotechnology was later defined by the National Nanotechnology Initiative to be the manipulation of materials with the size range of 1 – 100 nm in size. As imaging technology progressed, so did nanotechnology, as the development of techniques such as atomic force microscopy (AFM), transmission electron microscopy (TEM), and scanning tunneling microscopy (STEM) allowed researches more detailed imaging and analysis of nanoparticles. Nanoparticles have since been created from a wide variety of materials such as lipids (3); polymers (4); proteins and peptides (5); viruses and viral components (6); carbons (7); heavy metals, such as gold (8) and silver (9); iron oxide (10); deoxyribonucleic acid (DNA) (11); and ribonucleic acid (RNA) (12).

One major focus for the implementation of nanotechnology has been the advancement of drug delivery, and while nanoparticles are used in many applications, nanoparticle drug delivery is among the most promising (13,14). In traditional drug

delivery, therapeutic agents, such as small molecule drugs, are cleared from the body rather quickly. This results in low accumulation of the therapeutic agent at the target site, requiring increased dosage, which increases toxicity. A key feature of nanoparticles is their extended half-life *in vivo* compared to therapeutic agents, which increases the circulation time and bioavailability of therapeutic agents conjugated to or encapsulated within the nanoparticles (15,16). Many drugs currently under development are not soluble and cause off-target toxicity issues, limiting their practical application for the treatment of disease (17). Nanoparticles have previously shown the ability to conjugate or encapsulate hydrophobic and toxic drugs, with hopes to increase therapeutic dose to the disease site (18-23). Nanoparticles have shown to increase the solubility of highly hydrophobic drugs; deliver a high dosage of therapeutic to the disease site using release mechanisms such as pH sensitive linkages (24-28); and provide targeting to cells by use of cell specific peptides (29-31) and aptamers, specific RNA sequences selected to bind chemical or protein ligands, such as cell-surface receptors (32,33). As a result, the amount of therapeutic getting to the diseased site is increased, allowing lower dosage and decreased toxicity.

Many different materials are used to construct nanoparticles, each offering their own advantages and disadvantages, and nanotechnologists are continually searching for an ideal candidate to improve the current state of drug delivery. Lipid based nanoparticles allow for high therapeutic loading and delivery of payloads through membrane fusion with cells while remaining nontoxic and non-immunogenic (34,35). However, lipids have shown issues with thermodynamic stability, releasing their payload before reaching the target site (36). Also, reproducibility during nanoparticle construction results in inconsistent products (37). Similarly, polymer based nanoparticles allow for high levels of

therapeutic encapsulation (38). Moreover, polymers display a significant increase in thermodynamic stability and can easily be functionalized on the surface for targeting capabilities (39). Yet, polymers have shown issues with batch reproducibility, water solubility, and overall bioavailability. Biologically derived nanoparticles such as viruses, viral components, and proteins or peptides, illicit immune responses and generate toxicity. But, targeted delivery of these nanoparticles allows for a lower overall dose while having a high accumulation in targeted tissues (40-43). Inorganic nanoparticles such as carbon structures and metal ions can be created with high reproducibility at a lower cost than most nanoparticles. Additionally, these particles can be functionalized through chemical modifications. However, their accumulation in healthy organs such as kidneys, lungs, and liver result in toxicity and limit their overall potential for therapeutic delivery. DNA nanostructures are constructed with defined shape, size, and stoichiometry (44-46) and can achieve targeted delivery with the functionalization of DNA aptamers (47,48). However, relatively low thermodynamic stability limits DNA's ability for *in vivo* applications. Cationic nanoparticles, such as metal ions, some polymers, and proteins, display an overall positive charge allowing for endosomal escape through the proton sponge effect (49). However, positive charge also causes passive attraction with negatively charged cell membranes, thus leading to non-specific binding and cell entry.

Conception of RNA nanotechnology

The idea of RNA nanotechnology was first conceived in 1998(12) when the pRNA from bacteriophage phi29 was engineered to form a hexameric RNA nanoparticle from six copies of pRNA. Each of the pRNA monomers interacts using loop-loop complementary base-pairing, referred to as hand-in-hand interactions (50). The intermolecular connections

between adjacent pRNA units was the first demonstration of specific arrangement of RNA into an engineered nanoparticle. pRNA is a 120 nucleotide (nt) RNA that adopts a stable secondary structure. Its function is to act as a connector between the portal proteins and ATPase in the bacteriophage phi29 DNA packaging motor (51-54).

Within the pRNA is a unique three-way junction (3WJ) motif, which drives the assembly of the pRNA structure (55). The 3WJ has been extracted from the pRNA and used as a nanoparticle for drug delivery (56-61). It is thermodynamically stable (62,63), enzymatically stable with chemical modification (64), assembles without metal ions from its three component RNA oligomers (3WJ-a, 3WJ-b, 3WJ-c), and can accommodate the addition of multiple functional groups while still retaining folding and stability (55).

RNA's versatility in structure and function, propensity for bottom-up self-assembly, defined size and structure, favorable *in vivo* attributes, and large potential as a therapeutic modality make it an attractive candidate as a biomaterial for nanoparticle drug delivery. RNA's ability to adopt complex quaternary structures (12,65-69), to base stack (70,71), to form canonical Watson-Crick (A-U; G-C) and non-canonical (ex. G-U wobble) base pairing (72,73), leads to a variety of natural structural motifs (74,75). RNA nanotechnology uses such properties to construct nanoparticles for use in nanomedicine and bionanotechnology applications.

Beneficial properties of RNA for nanoparticle construction

Nanotechnology that revolves around the manipulation of biological materials is referred to as bionanotechnology, which includes the field of nucleic acid nanotechnology. First envisioned over 30 years ago (76), DNA self-assembly was exploited to form nanoparticles using base-pairing mechanism (A-T, G-C)(77,78). DNA nanostructures

including nano-capsules and other nano-carriers for drug delivery applications have since been constructed (79-81). DNA origami was developed as a powerful tool to build large 2D (82) and 3D architectures including tetrahedrons (83), nano-robots (84), helix bundles (85), and tensegrity-based shapes (86). Although DNA nanostructures have exemplified the power of the base-pairing mechanism for structure design, DNA cannot match the thermostability and structural and functional diversity of its nucleic acid counterpart, RNA.

Like DNA, RNA is a chain-like biopolymer composed of nucleotide subunits joined by phosphodiester bonds. Each nucleotide is composed of a ribose sugar, phosphate group, and nitrogenous base. The most common bases are cytosine (C), guanine (G), adenine (A), and uracil (U). The basis of RNA secondary structure is hydrogen bonding occurring between complementary nucleotides, G–C and A–U, analogous to that of canonical base pairing found in DNA. Furthermore, the presence of the 2'–OH in RNA has dramatic effects on its properties. The C3'–endo sugar conformation in RNA leads to A-type helical formation (11 bp/turn), offering improved thermostability over DNA B-type helix.

RNA was first characterized as the link between genomic DNA and protein, transferring the genomic code for proteins to the cell's translation machinery. Investigation of RNA structure revealed the catalytic nature of RNA with the discovery of ribozymes (87). The revolutionary finding of catalytic RNA, an attribute thought only to belong to proteins, led to a shift in the thought of the functions of RNA. In addition to functions generated by elaborately structured RNA molecules, specific base-pairing interactions mediated by single stranded regions of unstructured RNA have further expanded RNA's

functional repertoire (88). Years of research found that RNA performs diverse functions in biology, juggling tasks from catalysis to protein synthesis to gene regulation.

An emerging class of targeted therapeutic molecules has been developed based on RNA aptamers (89); single-stranded RNA sequences that fold into specific 3D configurations and bind with high selectivity and affinity to extracellular domains of cell surface receptors. A combination of electrostatic interactions, hydrogen bonding, and van der Waals forces mediates binding. Aptamers possess many advantages as targeting reagents including low cost, fast selection and optimization, convenient synthesis and modification with high batch fidelity, low immunogenicity, and long term stability (90,91). The development of the systematic evolution of ligands by exponential enrichment (SELEX) (92,93) process has made aptamer development possible for many proteins and peptides. Currently, tens of RNA aptamers are available for targeting specific cell surface receptors followed by subsequent internalization of RNA nanoparticles. RNA aptamers offer unique advantages to RNA nanotechnology, as the aptamer can easily be incorporated into RNA nanoparticles by sequence fusion.

Ribozyme-based therapeutic strategies have emerged as powerful tools for the treatment of cancer and viral infections. Ribozymes are RNA motifs that possess catalytic properties much like those of proteins. Ribozymes targeting mRNA show promise for gene therapy of breast cancer and hepatocellular carcinoma in animal models as they display similar effectiveness as RNAi, while exhibiting less off-target effects (94).

Riboswitches offer therapeutic avenues for addressing a wide range of diseases by regulating gene expression. Riboswitches are composed of two domains, a sensor portion (a natural aptamer) for ligand recognition, and an expression platform that can adopt two

mutually exclusive conformations based on ligand binding for controlling gene expression (without the need for protein cofactors) (95). Based on simplistic design principles, RNA nanotechnology can be applied not only to deliver the RNA switches *in vivo* but also to rationally engineer synthetic riboswitches to repress or activate gene expression in a ligand-dependent fashion.

The discovery of the RNA interference (RNAi) pathway in 1998 (96) created an avenue of treatments for many diseases, including cancer. RNAi is the process by which the expression of a gene is modulated by short double stranded RNA sequences, typically 21-23 nucleotides in length. There are two central molecules to RNAi, miRNA and siRNA (97). While miRNAs are endogenous to cells, and target multiple genes, siRNAs are mostly artificial sequences (some endogenous siRNAs do exist in cells (98)) that are designed to target a specific mRNA. Theoretically, any known mRNA sequence can be targeted using siRNAs and miRNAs, making diseases previously thought to be undruggable susceptible to RNAi therapy. RNA nanoparticles are designed such that endonuclease Dicer can access the dsRNA sequences encoding for the siRNAs and miRNAs and cleave them to generate functional miRNA and siRNA, which are then loaded into the RNA induced silencing complex (RISC) and thereby regulate gene expression by selectively targeting mRNAs.

RNA's negatively charged phosphate backbone renders RNA nanoparticles highly anionic, disallowing non-specific targeting to all cells. Furthermore, the high thermostability of RNA allows for the construction of stable RNA nanoparticles. While RNA is quickly digested *in vivo* by numerous of RNA specific nucleases, modifications to the 2' of the ribose sugar render RNA more thermodynamically and enzymatically stable.

One modification is substitution of fluorine for the hydroxyl at the 2' sugar positions of the pyrimidines, cytosine and uracil.

RNA's anionic charge, versatile structure, myriad of functional RNA motifs available for nanoparticle construction, and the availability of chemical modifications, which endow stability, contribute towards the fact that RNA is a unique biomaterial that can be utilized in nanotechnology and bionanotechnology.

RNA nanoparticles

While RNA nanoparticles were initially constructed to study RNA structure (99-101), advancements in the technology, such as improvements in stability, have allowed RNA nanotechnology to be developed with more biomedical applications in mind. There are three major challenges associated with using RNA as a nanoparticle: (1) Thermodynamic stability; (2) Enzymatic stability; and (3) immune response elicited by dsRNA. However, these issues have been overcome by the finding of an unusually stable 3WJ motif suitable for nanoparticle construction (55), chemical modifications to RNA allowing prolonged stability in serum (64,102), and studies showing the immunogenicity of RNA nanoparticles are very low *in vivo* (103).

Because of the versatility of RNA structure, many different methods have been developed over the years for RNA nanoparticle construction. Some of the most popular methods for RNA nanoparticle construction are through intermolecular interactions, computer aided design, RNA tectonics, rolling circle transcription (RCT), and modular design approach, the last method of which this thesis will focus.

The use of intermolecular interactions to construct RNA nanoparticles was pioneered by the Guo lab using pRNA as a monomer unit. The pRNA was engineered to

contain complementary kissing loops, which interact to form dimers, trimers, tetramers, pentamers, hexamers, and heptamers using “hand-in-hand” interactions (12,50,104,105). Furthermore, pRNA monomers were functionalized with palindrome sticky ends sequences to interact “foot-to-foot” to form nanoparticles (50,104,105).

RNA tectonics is a field pioneered by Neocles Leontis, Eric Westhof, and Luc Jaeger. Tectonics is a RNA nanoparticle construction method by which different RNA motifs, or tecto units, are arranged to interact and form nanoparticles. RNA nanoparticles can be constructed using motifs such as kissing loops, dovetails, pseudoknots, kink turns, and multi-way junctions (74,75,99,101,106). Increasing knowledge of RNA folding and the availability of databases such as the Nucleic Acid Database (NAD) (107) and the RNAjunction database (68) have increased the power of tectonics, as the number of motifs that can be used as potential tectoRNAs is quite large. Examples include the tecto RNA squares and cubes designed from tRNA and nanoprisms designed from pRNA (100,101,104,108-117).

Computer based nanoparticle design has become extremely powerful due to the predictive abilities of the software programs written specifically for RNA nanoparticle design. Several software programs have been developed over the years such as Nanotiler (118), Assemble2 (119), RNA2D3D (120), INFO-RNA (121), and NUPACK (122), which are useful to design *de novo* RNA nanoparticles. Examples are a six-membered RNA nanoring (123) and an RNA nanocube generated using Nanotiler (124). Long sequences as well as individual monomer units that contain internal structures can be computationally designed and experimentally assembled in a one-pot manner including co-transcriptional

assembly. Computer aided design is especially useful as RNA folding is complicated and engineering sequences for correct folding enhances stability for biomedical applications.

RCT produces large amounts of concatemeric RNA sequences from a circular DNA template using *in vitro* transcription (125). A ssDNA oligomer anti-sense to the target sequence is circularized through ligation, while a short splint ssDNA containing the RNA polymerase promoter sequence is annealed to the circular DNA allowing RNA polymerase initiation. After ligation, *in vitro* transcription occurs in a continuous fashion. RCT has been used to synthesize RNA microsponges containing thousands of copies of siRNA, which were then delivered to tumor bearing mice showing efficient tumor regression (38).

The focus of this thesis is a modular design approach using a natural 3WJ RNA motif, derived from the pRNA of bacteriophage phi29, as the core for nanoparticle construction (126). While similar to RNA tectonics, the modular design approach avoids the use of sticky end, loop-loop, or other intramolecular interactions resulting in more stable nanoparticles. Despite increased knowledge of RNA structure and folding, *de novo* design of RNA remains difficult. Using a RNA motif, of which the crystal structure is known, molecular modeling software can be used to design RNA nanoparticles. This technique was first used to construct RNA triangles (126). To do this, three 3WJ motifs were aligned in a planar configuration, and adjacent helices were attached using dsRNA. To construct the nanoparticle, four strands were used: three external short strands and one internal long core strand to tether all strands together. This method results in a fully double stranded RNA nanoparticle, held together by hundreds of hydrogen bonds.

Importance of nanoparticle physical properties

Nanoparticle properties such as size, shape, charge, surface chemistry/properties, and construction material, govern how the nanoparticles interact with their *in vivo* environment, mainly the mononuclear phagocytic system (MPS) (127), and largely control uptake and elimination pathways. In turn, the behavior of the nanoparticles, such as circulation time and biodistribution, are determined. The properties of nanoparticles are of paramount importance, as *in vivo* behavior is a determining factor of success for a particular nanoparticle.

One of the most important properties that determines how nanoparticles interact once in circulation is their size. Importantly, the size of nanoparticles determines the pathways in which they are taken into cells, such as pino- and phagocytosis (128), and which parts of the MPS they interact with, such as the liver or the kidneys. Smaller nanoparticles, less than 15 nm, are excreted quickly through the kidneys (129) while larger particles, 15-100 nm, have more interaction with macrophages, and are excreted more slowly through the liver (130). Interactions with the MPS dictate the circulation time of nanoparticles, as well as how long they stay in organs once they have reached their destination. For example, gold nanoparticles 50 nm in size accumulated in the liver and spleens of beagles, and remained in said organs for more than six months (131). Circulation time is extremely important for nanoparticles relying on the enhanced permeability and retention (EPR) effect, as longer circulation times gives the nanoparticles a higher chance to accumulate at the tumor site. In addition to circulation time, the size of nanoparticles also affects their entry into the tumor. It has been shown that smaller nanoparticles, less than 10 nm, have the highest penetration into the tumor tissue (132). Additionally, smaller

nanoparticles are taken into the cells of tumors, not just the tumor site, more rapidly and in higher amounts (133). Size also affects the composition and extent to which the protein corona forms. The protein corona has drastic effects on the “stealthiness” of a nanoparticle, and higher amounts of protein corona formation on a nanoparticle will result in faster removal by the MPS (128).

Along with size, shape is also an important factor for nanoparticle behavior *in vivo* (134). The geometry of a particle has a large effect on its interaction with macrophages. Studies have shown that less angular nanoparticles, side angles less than 45°, are completely enveloped by macrophages, whereas particles with sharper angles, side angles more than 45°, are unable to be completely phagocytized (135,136). Shape also affects where the particles accumulate as short rod particles have been shown to accumulate in the liver while longer rods go to the spleen (137). Furthermore, particles that display a higher aspect ratio, such as rods, are more efficient at accumulating in the tumor than spherical particles and plate shaped particles (128,132). Yet, higher aspect ratio nanoparticles also result in higher inflammation and stimulation of pro-inflammatory cytokines (128). As with size, shape also affects the formation of a protein corona, affecting the stealth nature of nanoparticles (138).

The surface charge of a nanoparticle can also affect its circulation, biodistribution, and cellular uptake. Neutral particles circulate the longest, while anionic and cationic particles see reduced circulation times (139). Particles that carry a charge have increased protein corona and protein opsonization, causing higher macrophage recognition and faster clearance (128). Cationic particles enter cells more rapidly and to a higher degree than neutral and anionic particles due to fusion with the negatively charged cell membrane.

However, cationic particles show high toxicity and significant immune reactions, thus, negatively charged and neutral particles are generally preferred. The charge of particles also affects the mechanism of uptake into cells, which has a large effect on their intracellular fate and drug delivery efficacy (132).

Surface functionalization and surface properties also play a role in interaction with the immune system. Generally, hydrophilic particles are preferred over hydrophobic, as hydrophilic particles see an increase in circulation time over their hydrophobic counterparts (140). Hydrophobicity of nanoparticles increases protein adsorption significantly, leading to faster clearance (141). Protein adsorption can also increase non-specific accumulation in vital organs. Increased hydrophobicity has also been linked to increased activation of immune system cytokines, both *in vitro* and *in vivo* (142). Surface functionalization, such as PEGylation, can drastically alter the way nanoparticles interact with their environment. Increased PEG density leads to higher uptake by liver kupffer cells, while lower PEG density increases uptake by kidney phagocytes (143,144). Also, albumin (BSA) coating can lead to aggregation of nanoparticles, and accumulation in the liver and spleen resulting in toxicity (145). Polymer coatings decrease protein binding and phagocytosis compared to their non-coated counterparts, and show resistance to accumulation in the spleen and liver (146,147).

Finally, the material chosen for nanoparticle construction has a large effect on interaction with the immune system and accumulation *in vivo*. Analysis of the accumulation of many different types of nanoparticles in tumors showed that inorganic materials have the highest percent accumulation (132). Even inside the realm of inorganic nanoparticles, gold nanoparticles seem to be better than QDs or iron oxide nanoparticles.

However, as inorganic materials degrade slowly over time, there are potential hazards with repeated administration and buildup of inorganic material. However, universal throughout all these studies is that cancer type and tumor model are the two most important factors when determining nanoparticle accumulation in tumors (132). This suggests that for each type of cancer, the ideal nanoparticle is not identical.

The tunable nature of RNA nanoparticles advances drug delivery

The fact that tumors arising from different cancer types are so diverse is a big challenge in cancer nanotechnology drug delivery. It is difficult to decide which nanoparticle system to use for each situation, due to the heterogeneity of different tumor types as well as heterogeneity within a single tumor. One major finding of this thesis is that the properties of RNA nanoparticles can be controlled during design and construction. As discussed above, the properties of nanoparticles have a huge effect on *in vivo* behavior. RNA nanoparticles are defined in size, shape, and properties, and are highly consistent in their assembly. Their properties are near identical from particle to particle, as the base pairing mechanism allows controlled self-assembly, not a random and aggregative assembly like in some other nanoparticles. It is possible that the *in vivo* behavior of RNA nanoparticles can be optimized based on the controllable size, shape, and properties that the nanoparticle engineer has on the system.

The nanoparticle designer can easily scan through varieties of RNA secondary and tertiary structural motifs from which to design and construct an RNA nanoparticle (ex. bulges, stems, hairpin, loops, and junctions). Such motifs are used as building blocks to design nanoparticles with diverse size and shape by engineering parameters such as motif angle and sequence length (103,126,148-150). Other parameters such as nucleotide type

can alter nanoparticle properties, including enhancing chemical stability using base or backbone modifications, or incorporating fluorescent dyes for nanoparticle tracking. The physiochemical properties of RNA nanoparticles can easily be fine-tuned to tailor-make the nanoparticle for desired applications *in vitro* and *in vivo*.

Chapter 2: Design, Construction, and Characterization of RNA Nanoparticles with Tunable Size, Shape, and Physicochemical Properties Based on phi29 pRNA-3WJ Core Motif

Chapter 2 was reproduced (with some modification) with permission from: Khisamutdinov, EF*; Li, H*; Jasinski, DL*; Chen, J; Fu, J; and Guo, P. “Enhancing immunomodulation on innate immunity by shape transition among RNA triangle, square, and pentagon nanovehicles.” *Nucleic Acids Research*, 2014. 42(15), 9996-10004. DOI: 10.1093/nar/gku516. Copyright 2014 Oxford Publishing; Jasinski, DL; Khisamutdinov, EF; Lyubchenko, YL; and Guo P. “Physicochemically tunable polyfunctionalized RNA square architecture with fluorogenic and ribozymatic properties.” *ACS Nano*. 2014. 8(8), 7620-7629. DOI: 10.1021/nn502160s. Copyright 2014 American Chemical Society.

Special thanks to Dr. Emil F. Khisamutdinov for help in preparation of data for figures 2.1, 2.5, 2.6, and 2.12, and to Dr. Luda S. Shlyakhtenko and Dr. Yuri Lyubchencko for AFM images in figures 2.5, 2.8, and 2.10.

Chapter 2.1: Design and Construction of RNA Nanoparticles with Tunable Shape

INTRODUCTION:

One area of biomimetic nanotechnology involves the construction of nano-scale, supramolecular architectures utilizing modular units of functional nucleic acids. The aim is to design nanostructures that undergo self-assembly in controllable and recyclable fashion. RNA was discovered as an attractive material to build nanoparticles *via* nanotechnology (12), offering a variety of structural modules and motifs that can be

manipulated into 1D, 2D, and 3D architectures (for review see reference (90)). In the past decade, a variety of geometric RNA nanoparticles and nano-scaffolds have been obtained *via* the approaches of hand-in-hand (12,105,151), foot-to-foot (50,104), branch extension (55,116,152,153), loop-receptor contact (113,154), loop-loop (108,114), “sticky” or “dangling” ends (104,124), and synthetic RNA-protein complex interactions (155). These motifs are available in data bases and can be used to build artificial nanostructures by manipulating their interchangeable units (156,157). Recently, RNA rolling circle transcription has been utilized to generate RNA sponges (38,158). In RNA tectonics, structural motifs like double helices, loops, and junctions can be isolated from large and complex RNA molecules appearing in structural data bases and used to build artificial nanostructures by manipulating their interchangeable units (99,159). As such, previously reported designs of RNA nanoparticles, e.g. tecto-square (109), square-shaped nano-scaffolds (110,111), RNA nano-rings (108), pRNA dimmers, tetramers, and hexamers (12,160-162), as well as RNA nano-cubes (124), RNA polyhedron (116), RNA bundles (163), RNA filaments (113,154), utilize fundamental principles of RNA structure and folding (75,164-167). Overall stability of conventional constructs though, mainly relies on the stability of canonical and non-canonical base pair (bp) forming by loop-loop, receptor-loop, or “sticky-ends” with only a few pairing nucleotides usually not exceeding six. A new approach is needed to increase overall stability of RNA nanoparticles, one that uses naturally-selected stable RNA building blocks for structure building, one example being the 3WJ motif from pRNA of bacteriophage phi29 DNA packaging motor. In addition to discovering that the pRNA-3WJ shows exceptional stability under physiological

conditions and in the presence of strong denaturing agents (55,152), recent studies also suggest that the thermodynamic stability of the 3WJ is entropy driven (63).

Previous studies constructed RNA triangles from the pRNA-3WJ module (**Fig 2.1**). In this report, we introduce a conceptual approach to the rational design of stable RNA architectures by stretching the 60° AOB angle (\angle) (**Fig 2.2**) of the thermodynamically stable pRNA 3WJ motif utilizing a modular design technique (**Fig 2.3**). We demonstrate that it can be stretched to wide conformations resulting in different 2D polygons: triangle ($\angle AOB = 60^\circ$), square ($\angle AOB = 90^\circ$), and pentagon ($\angle AOB = 108^\circ$). Intermolecular interactions such as kissing loops, receptor loop, or “sticky-ends” were avoided by introducing linkages through base pairing between corners of the polygons using RNA double helices. Therefore, this system is advantageous with an increased thermo-stability in the overall construct.

MATERIALS AND METHODS:

RNA nanoparticles design, synthesis, and self-assembly

The 3WJ crystal structure of the pRNA molecule (PDB ID: 4KZ2) was primarily used for designing polygon models using Swiss PDB viewer, as previously described (168). RNA strands for corresponding triangle, square, and pentagon, were synthesized by *in vitro* T7 transcription using polymerase chain reaction (PCR) generated DNA templates. RNAs were purified by denaturing polyacrylamide gel electrophoresis (PAGE) and were either Cy5 whole chain RNA labeled (Mirus Bio LLC) or 5'-end [γ - 32 P] ATP (PerkinElmer) labeled, as previously described (151).

RNA polygons were assembled in one pot by mixing equimolar concentrations (final concentration of 1 μ M) of four RNA strands for the triangle, five RNA strands for

the square, and six RNA strands for the pentagon in 1 X TMS buffer (50 mM Tris pH = 8.0, 100 mM NaCl, and 10 mM MgCl₂). Samples were annealed for 1 h in a thermocycler with controlled, slow cooling (1 °C/ min) from 80 - 4 °C.

Native PAGE, TGGE, and boiling resistance assays

RNA assemblies were evaluated on 7% (29:1) native polyacrylamide gels in the presence of 1 X TBM (89 mM Tris, 200 mM boric acid, 5 mM MgCl₂) buffer. Gels were run at constant 90 V, +4°C. Gels were imaged with Typhoon FLA 7000 (GE Healthcare) to visualize RNA strands. Temperature gradient gel electrophoresis (TGGE) analysis was performed on 7% native PAGE in a buffer containing 50 mM TRIS pH = 8.0, 100 mM NaCl, and 0.2 mM MgCl₂, as previously described (109,110,116). A gradient temperature of 30-70°C was applied perpendicular to electrical current, and the experiment was run for 1 h at 20 W. A total RNA concentration of 100 nM was used in TGGE analysis. Apparent T_M values corresponded to the temperature at which half of the polygons fractions were dissociated, and apparent K_D values for multiple RNA strands were calculated, as described previously (50).

Boiling resistance assay was performed in 10 µL containing 1 µM preassembled polygons in TMS buffer or in the presence of 8 M urea. Samples were incubated at 100°C for five minutes, then snap cooled on dry ice to prevent refolding following evaluation on 7% native PAGE at 4 °C. Boiling experiments were repeated 3 times and standard deviation measurements are indicated by error bars.

Quantification analysis was performed using ImageJ (169). Equal-sized boxes were drawn around the lanes corresponding to the triangle, square, or pentagon complexes and

corresponding quantified values for each type of polygon were divided by the sum of the values presented in the corresponding lane.

RESULTS:

RNA polygons: triangle, square, and pentagon fabrication and self-assembly

The structural features of the recently discovered ultrastable pRNA 3WJ module from the bacteriophage Phi29 DNA packaging motor were utilized for *in silico* design of the RNA triangle, square, and pentagon 2D polygons. During computer modeling we used the angle of the 3WJ formed by H1 and H2 as an inner angle of the polygons as we hypothesized that the angle could be stretched to a more open conformation. Throughout this report the intra-helical angle between H1 and H2 is denoted as $\angle AOB$, as shown in figure 2.2A. Each RNA model contained a pRNA 3WJ motif at each vertex, and the inner angles correspond to $\angle AOB$. The resulting 3D models exhibited flat conformations, as expect from the plane geometry of the 3WJ motif (168) (**Fig 2.4A**).

Each polygon was composed of a different number of RNA strands classified as short strands (external) and long strands (internal) (**Fig 2.4B**). By increasing the number of external strands and the propagation of the central strand, the tension on the inter-helical $\angle AOB$ increased to 60° , 90° , and 108° , allowing for 2D formation of corresponding triangle, square, and pentagon shapes. The measured widths, from one corner to another, were 10.2 nm, while the heights differed as follows: triangle = 9.1 nm, square = 10.2 nm, and pentagon = 12.7 nm. Following the transcription of individual RNA strands, self-assembly properties of the triangle, square, and pentagon designs were evaluated on 7% native polyacrylamide gel electrophoresis (PAGE) (**Fig 2.4C**). All polygon formations were obtained by one-step self-assembly (50,55,124,152). Each component strand of each

nanoparticle was whole chain labeled with Cy5 to evaluate participation of all RNA strands in their corresponding assemblies. Yield of correctly assembled polygons was estimated to be >90% based on native PAGE gel evaluations (**Fig A.1.1**). Equilibrium constants of dissociation were obtained from apparent K_D gels, and K_D values were determined to be 18.8 nM, 20.3 nM, and, 22.5 nM for triangles, squares, and pentagons, respectively (**Fig A.1.2**).

These results demonstrate that each RNA nanoparticle assembles into the desired nanostructure, and indicates stretching of the $60^\circ \angle AOB$ to wider conformations. The assembly of RNA strands into specific-shaped nanoparticles based on the $60^\circ \angle AOB$ of the pRNA 3WJ motif was controlled by modulating the number of short external stands and the length of the long internal strand.

Structural characterization of polygons by AFM and DLS

To further evaluate the size and shape of the resulting RNA assemblies, structural characterization of each polygon was conducted using atomic force microscopy (AFM). AFM images of the pRNA 3WJ based polygons revealed that the shapes of resulting polygons were similar to their predicted, theoretical 3D models (**Fig 2.5A**). The estimated average dimensions were found to be 13 ± 1.1 nm, 14 ± 1.8 nm, and 17 ± 1.6 nm for triangles, squares, and pentagons, respectively. These values do not reflect the true sizes of the RNA polygons due to the AFM tip convolution, but rather demonstrate that the average size of the nanoparticles increases from triangle to pentagon. In addition, the central cavity of each RNA shape is visible, and the size of the cavity gradually increased with the number of polygon vertices. The measured heights for all nanoparticles was found to be ~2 nm, in agreement with previously reported heights of nucleic acid double helices (109,170).

Quantification analysis was performed to compare apparent yields between polygons observed on AFM mica surface. Equal concentrations (1 nM) of the polygons were deposited on a mica surface and correctly folded polygons were manually counted in a 0.5 μm^2 area, resulting in 48 triangular particles, 33 square particles, and 17 pentagon nanoparticles (**Fig A.1.3**). The estimated number of triangular nanoparticles adsorbed on the mica was ~ 1.5 times more than that of the square, and three times more than that of the pentagon. However, native PAGE revealed that the yields among the three polygons were almost equal. The difference in adsorption amounts between polygons on the mica surface was presumably due to variation in their sizes and 3D conformations, resulting in different dynamic and physical properties.

DLS was performed to determine the apparent hydrodynamic diameters for each of the polygons. The diameters were found to be 9.1, 11.2, and, 13.5 nm for triangles, squares, and pentagons, respectively (**Fig 2.5B**). The increase in number of 3WJ cores corresponds with the larger observed diameter. The measured diameters agreed with their corresponding 3D models. However, there was a discrepancy between polygon sizes determined by AFM and DLS. This could be attributed to the fundamentally different techniques, as DLS determines the average size distribution profile of nanoparticles in solution assuming that the polygons have globular shapes [refer to manual at <http://www.malvern.com>], while AFM imaging can produce images larger than the real diameter due to tip size used (171) and the resolution of imaging equipment. Nevertheless, the two techniques demonstrated that the relative size of the nanoparticles increased from triangle to square to pentagon.

Accordingly, native PAGE, AFM, and DLS showed the formation of compact molecular 2D assemblies of triangle, square, and pentagon based on the pRNA 3WJ \angle AOB. Consequently, the naturally preserved 60° \angle AOB could be stretched to reach the formation of square and pentagon. The stretching, or tension, that the angle underwent could have had a significant impact on the overall stability of the nanoparticles. Therefore, it was of great interest to evaluate and compare the polygon's stabilities.

Stability comparison between triangle, square, and pentagon

The stabilities of polygons were studied using a perpendicular temperature gradient gel electrophoresis (TGGE) (Biometra GmbH). This convenient technique has garnered widespread use for measuring melting temperatures of RNA nanoparticles with multiple strands (50,108-110,116,172). The preassembled polygons were subjected to 7% native TGGE with a gradient temperature of 30-70 °C perpendicular to electrical current. The following apparent T_M values were obtained for the polygons at 100 nM total concentration (Ct) in presence of 0.2 mM $MgCl_2$: triangle $T_M = 56$ °C, square $T_M = 53$ °C, and pentagon $T_M = 50$ °C (**Fig 2.6A**). The triangular nanoscaffolds were more stable than squares and pentagons, although the number of RNA bp was much higher in the pentagon construct, as compared to the square and triangle. Usually, the stability of nucleic acids with the same base-pair content is directly dependent on metal ion and total nucleic acid concentrations. Since these two criteria were the same, it was assumed that the higher the number of bp in each RNA structure the higher the stability. Therefore, the most stable shape produced should be the pentagon. However, based on TGGE data the opposite was found. This was likely due to the tension caused by the stretching of the native pRNA 3WJ 60° \angle AOB. The triangular construct angle was preserved (60°), the square and pentagon angles were

stretched to the wider conformations of 90° and 108° , respectively. Previously it has been shown that any nucleotide mutations or deletions within the native core structure of the pRNA 3WJ motif would also result in the loss of its thermodynamic stability (55). Interestingly, the measured triangle and square T_M values differed by $+3^\circ\text{C}$, as did the square and pentagon. Boiling resistance assay in the presence and absence of 8 M urea further confirmed that the triangle was the most stable nanoparticle (**Fig 2.6B**). The quantification of nanoparticle bands after heating to 100°C resulted in $75 \pm 4\%$ recovery of the triangular assembly, suggesting a $T_M > 100^\circ\text{C}$. By definition, T_M is the measured temperature when half the RNA concentration has melted, i.e. 50% recovery. The percentage of recovery for square was $28 \pm 2\%$ and for pentagon was $16 \pm 5\%$, much lower than the value estimated for triangle recovery. The experiment with the presence of 8 M urea in boiling solution showed that the overall trend of stability remained the same, but the percentage of recovery was $55 \pm 4\%$ for triangle, $8 \pm 3\%$ for square, and no pentagon fraction was detected. Overall, the nanoparticle with fewer 3WJ motifs (triangle) resulted in a higher thermostability and resistance in chemical degradation, and the change in stability was in large part due to the stretching of the $\angle\text{AOB}$.

DISCUSSION AND CONCLUSIONS:

Artificial construction of RNA nanoparticles requires knowledge of the structural properties of RNA motifs, such as interhelical or intrahelical distances, X-Y and X-Y-Z angles, number and orientations of RNA branches in multi-way junctions, canonical and non-canonical interactions, binding sites for proteins, metal ions, and small molecules (75,90,154,159,160,173). Progression in RNA structural biology allowed for the analysis of RNA 3D motifs from existing RNA structures at atomic resolution and various data

bases, including www.pdb.com, RNA multi-way junction (68), and find RNA motif (174,175). This study, based on the previously reported versatile pRNA 3WJ 3D motifs (PDB accession ID: 4KZ2), shows that the 3WJ structure can be folded into desired conformations based on the dynamics of the $60^\circ \angle AOC$, demonstrating the ability to tune the physical and structural properties of RNA polygons for a variety of technological, biological, and medicinal needs. This approach, based on the propagation of the central RNA strand used to direct the folding of corresponding short or external strands into planar triangle, square, and pentagon conformations, resulted in the 60° , 90° and 108° bending of interhelical $\angle AOB$ of the pRNA 3WJ. This is especially important for medical applications where one needs to construct different RNA nano-scaffolds based on a non-toxic and thermodynamically stable building block. The following advantages result from this technique: i) the number and combination of therapeutic molecules can be tuned to an RNA-based nano-carrier; ii) the nano-scaffold has a controllable size and shape; and iii) variable thermodynamic and RNase resistance properties can be applied depending on the application of the nano-scaffold.

ACKNOWLEDGEMENTS:

We thank Luda Shlyakhtenko for AFM imaging at the Nanoimaging Core Facility supported by the NIH SIG program and the UNMC Program of ENRI to Yuri Lyubchenko. This work was supported by the National Institutes of Health EB003730 and CA151648 to P.G. The content is solely the responsibility of the authors and does not necessarily represent the official views of NIH. Funding to Peixuan Guo's Endowed Chair in Nanobiotechnology position was by the William Fairish Endowment Fund.

Chapter 2.2: Design and Construction of Physicochemically Tunable RNA Nanoparticles with Controllable Size

INTRODUCTION:

DNA, RNA, and proteins from living systems produce a variety of highly ordered nano-scale structures to perform diverse functions (55,90,176-178). The intricacies of these natural biomaterials have inspired their applications as building blocks to fabricate sophisticated nanodevices (99,115,156,179-187). In nanotechnology, RNA can be manipulated to assemble nanostructures with simple approaches as in DNA nanotechnology, while displaying versatility in structure and function similar to proteins. Thus, RNA has the advantage of two worlds, which garners tremendous interest in the directed design of a variety of RNA nanoarchitectures. Natural RNA molecules form a wide variety of complex structures by hierarchical folding that generates different motifs or modular units (75,106). These modular units can be “manually” extracted and used to fabricate artificial self-assembling RNA complexes of diverse 1D, 2D, and 3D nanoarchitectures with novel and unique functional features (50,55,99,152). Many RNA motifs exhibit phenomenal flexibility (68,168,188) and the angles needed to form many nanoassemblies are encoded in the primary sequence of the structural motifs. The structure of a complex RNA architecture can be engineered by programming the information of a 3D structural motif into the nanoparticle's primary sequences. However, the flexibility of RNA motifs has seldom been used to construct diverse shaped nanoparticles utilizing the same core structure.

Previous work in this lab has detailed the construction of RNA nanoparticles utilizing the pRNA from bacteriophage phi29 DNA packaging motor. Dimers, trimers,

tetramers, and hexamers have been constructed utilizing hand-in-hand and foot-to-foot interactions as well as arm extension technologies which implement kissing-loop, sticky-end, and complementary interactions(12,50,55,90,91,104,105,152,168,189,190). Additionally, the 3WJ and X-way motifs from the phi29 motor pRNA, themselves, have proven successful as therapeutic delivery systems (50,55,63,105,152). Other RNA nanoparticle-based delivery systems have shown potential as therapeutic carriers (108,110,113,116,124,187,191-193).

Size and shape play an important role in the delivery efficacy, biodistribution and circulation time of nanoparticles (194). Control over these properties can be of paramount importance for *in vivo* applications. However, in many cases fine tuning of size, shape, and physicochemical properties of nanoparticles is difficult to achieve. Having a library of diverse size nanoparticles with tunable properties is advantageous as pharmacokinetic mechanisms of drug delivery, distribution, and clearance are hard to predict (194-197). These facts are the motivation behind the development of a simple method to tune the size and thermodynamic and chemical properties of RNA nanoparticles.

The complexity of RNA's tertiary structure complicates *de novo* design of such nanostructures; however, by utilizing a pre-defined 3D motif as the design template many complications can be avoided. This approach utilizes a modular design technique, sometimes referred to as RNA biomimetics. It involves the use of pre-defined structural motifs taken from biology as building blocks to construct RNA nanostructures of defined shape and size for a variety of applications including nanomedicine (156,198). The use of pre-defined RNA motifs has shown to be a successful method towards the rational design of RNA nanoarchitectures (50,90,99,108). Naturally, the first step in applying the pRNA

3WJ in modular design was to construct triangles based on the native 60° angle of the pRNA 3WJ motif (**Fig 2.7A**) (168), ideal for the construction of an equilateral triangle. Utilizing this native angle triangular nanoparticles were constructed using the modular design technique (126). To create more diversity in size and shape, square shaped geometry was the next goal. By stretching the 3WJ, triangle, square, and pentagon can be formed (103). The next question to be addressed is whether we can tune the size of one polygon by using the same 3WJ while altering the length of each side.

In this report, we show the construction of multiple variants of square-shaped RNA architectures based on a modular design technique using the same core structure, the pRNA 3WJ. By simply increasing or decreasing the length of the RNA duplex between each corner of the square, nanoparticles of 5, 10, and 20 nanometers (nm) were constructed with diverse thermal stabilities. The thermodynamic stability of certain RNA tertiary motifs and the strong Watson-Crick base pairing in RNA folding ensure predictability in structure that make it possible to increase or decrease size by simply adding or removing nucleotides, directly affecting size. Further control over nanoparticle stability was demonstrated by modulating the oligonucleotide used as the “core” strand during construction of the square nanoparticle. Exploiting the different stabilities of RNA, DNA, and 2'-fluorine modified (2'F) RNA it is possible to add another dimension of regulation over the physicochemical properties of RNA nanoparticles. Moreover, due to the unique construction technique used, we show that it is possible to completely avoid intermolecular interactions such as kissing loop and sticky-end interactions during construction of the nanoparticles. The potential of using the resulting RNA square assembly for biomedical and imaging applications is evidenced by the incorporation of therapeutic RNA, ribozyme, and fluorogenic aptamers.

As shown here, the assembly properties and tunability of RNA nanoparticles can be easily exploited to determine a suitable combination of size and stability for a wide array of applications.

MATERIALS AND METHODS:

RNA synthesis, purification and labeling.

RNA oligomers were prepared by *in vitro* T7 transcription from dsDNA containing the T7 promoter prepared by polymerase chain reaction (PCR). Single-stranded (ss) DNA oligomers were purchased from Integrated DNA Technologies (IDT). Cy5 whole chain labeling was carried out on the RNA oligomers following the Mirus Cy5 Label IT Nucleic Acid whole chain labeling procedure. For TGGE analysis of core strand hybrid squares, Perkin Elmer [γ - ^{32}P]-ATP was used to label one of the short external strands at the 5' end.

Assembly of RNA Nanoparticles

Equimolar amounts of RNA oligomers were mixed to a final concentration of 1 μM in 1 X TMS buffer. The mixture was heated to 80°C for 5 minutes and then slowly cooled to 4°C over one hour using an Eppendorf Mastercycler Thermocycler. Confirmation of the assembly products were then run on native PAGE.

Native PAGE and TGGE analysis

All assembly experiments were performed on 7% (29:1) native PAGE and run at 100 V in a 4°C cold room for 120 minutes. Cy5 labeled RNAs were then scanned on the Typhoon FLA 7000 and total RNAs were stained with ethidium bromide (EB).

TGGE analysis was performed on 7% native PAGE in a buffer containing 50 mM TRIS pH = 8.0, 100 mM NaCl, and 0.2 mM MgCl₂. A gradient temperature of 40-75°C was applied perpendicular to electrical current, and experiment was run for 1 h at 20 W. A

total RNA concentration of 80 nM was used in TGGE analysis of the core strand hybrid constructs and 100 nM RNA concentration was used for TGGE comparison of the different sized squares. Apparent T_M values corresponded to the temperature at which half of the square fractions were dissociated, and apparent T_M values for multiple RNA strands were calculated, as described previously (50).

Quantification analysis was performed using *ImageJ* software (169). Equal-sized boxes were drawn around the lanes corresponding to the square complexes and corresponding quantified values for each hybrid square were divided by the sum of the values presented in the corresponding lane. All plots were generated using *OriginPro 8* software.

AFM Imaging

AFM images were taken using a MultiMode AFM NanoScope IV system (Veeco), as per previously reported methods (199). Briefly, the RNA samples were diluted with 1 X TMS buffer to a final concentration of 3-5 nM. Then, the droplet of samples (5-10 μ L) was immediately deposited on the specifically modified APS mica surface (170,171), excess samples were washed with DEPC treated water and dried under a flow of Argon gas. AFM images in air were acquired using MultiMode AFM NanoScope IV system (Veeco/Digital Instruments, Santa Barbara, CA) operating in tapping mode.

FBS resistance assay

The square nanoparticles with RNA, 2'F RNA, and DNA core strands were incubated in 2% FBS solution at 37°C for 14 hours. After removal from 37°C incubation at their respective time points, samples were frozen on dry ice to prevent any further degradation. The samples were then analyzed on 7% Native PAGE. *ImageJ* software was

used to integrate the intensities of the assembled square nanoparticles in the gel. Integration areas for each time point were compared to the integration area for the 0 minute time point to construct an RNase degradation comparison between the RNA, DNA, and 2'F-RNA hybrids. All plots were generated using *OriginPro 8* Software.

Spinach and Malachite Green Aptamer Fluorescence Measurements

Native 7% PAGE was used to detect the fluorescence emission of fluorogenic nanoparticles. The gel was stained simultaneously in a mixture of 5 μM MG and 5 μM DFHBI and scanned for the MG-apt fluorescence λ_{exc} centered at 635 nm, and for SPINACH-APT fluorescence λ_{exc} centered at 473 nm. After recording images at different excitation wavelengths, total RNA staining in EB solution was performed to detect all RNAs in the gel.

Fluorescence emission in solution was measured, as previously reported (153). Briefly, assembled square nanoparticles (0.1 μM) harboring MG and SPINACH aptamers in TMS buffer were mixed with MG (2 μM) and DFHBI (2 μM) (Lucerna, Inc, <http://www.lucernatechnologies.com>) and incubated at room temperature for 30 min. Fluorescence was measured using a fluorospectrometer (Horiba Jobin Yvon), excited at 450 nm (565–750 nm scanning for emission) for SPINACH and 615 nm (625–750 nm scanning for emission) for MG dyes.

Dual Luciferase Assay

Experiments were carried out as previously described (200). For square experiments carried out here, controls of cell only, plasmid only, and Lipofectamine 2000(Lipo) only were used. Cell only contains luminescence data of cells only, with no transfection reagent or plasmid DNA. Lipo only samples contained just Lipofectamine

2000 transfection reagent. The plasmid only samples contained DNA plasmid only, which were transfected into the cell utilizing the transfection reagent Lipofectamine 2000. For RNA controls, the 3WJ with luciferase siRNA was used, which has previously been shown to cause knockdown (201). Square scaffold and a square utilizing scrambled siRNA sequence were utilized as negative controls.

HBV Ribozyme Activity Assay

HBV ribozyme activity assay was carried out as previously detailed (66). Briefly, HBV RNA substrate was 5'-Cy5 labeled using the Mirus Cy5 labeling kit. The labeled substrate was incubated with square nanoparticle conjugated with HBV ribozyme for 60 minutes at 37°C in buffer containing 20 mM MgCl₂, 20 mM NaCl, and 50 mM Tris-HCl (pH 7.5). pRNA conjugated to HBV ribozyme served as a positive control and pRNA with a disabled HBV ribozyme was used as a negative control. The cleaved fragments were analyzed on the Typhoon Fluorescent Imaging system.

RESULTS AND DISCUSSION:

RNA Square Design

Square-shaped RNA nanoarchitectures were designed *in silico* utilizing planar geometry of the 3WJ structural motif. Swiss PDB Viewer (www.spdbv.vital-it.ch) was used to align four 3WJ building blocks (PDB ID: 4KZ2) (168) in a planar configuration utilizing the internal ~60° angle, created by helix one (H1) and helix two (H2), at each corner of the square (**Fig 2.7A**). A-type duplex RNA was then inserted to connect helix one H1 and H2 (**Fig 2.7A**). The resulting design featured a square with four "arms" extruding outwards from each of vertex of the square, facilitating the incorporation of additional RNA sequences, motifs, or functionalities. The final square contains five RNA

strands, whereby four short strands (A, B, C, D) are complimentary to one long “core” strand E (**Fig 2.7B**, **Fig A.1.4**). This results in a nanoparticle containing a 3WJ at each vertex and A-type duplex RNA along each edge. Extension of both the core and external strands by increasing the number of complementary nucleotides was exploited to obtain RNA squares with variable but predictable sizes (**Fig 2.8A**). By such means, small, medium, and large square architecture were designed using Swiss PDB Viewer and the sequences for all five strands were optimized to avoid non-specific interactions using the *Mfold* program (202).

Structural Characterization

Based on models, the sizes of the resulting square structures should be 5.1 nm, 10.2 nm and 20.1 nm along each edge. The size increase results from extension of the duplex RNA connecting the 3WJs at each corner. Based on nearest-neighbor thermodynamic parameters, larger size squares are expected to exhibit increased thermodynamic stability. As none of the 3WJ angles have a right angle according to its crystal structure (**Fig 2.7A**) the 3WJ motif must be stretched from $\sim 60^\circ$ to $\sim 90^\circ$ to accommodate square geometry. As a result, efficiency of self-assembly might be decreased. Consequently, our first experiments were aimed at characterizing the physical properties of the square constructs.

Native PAGE was first used to test the assembly and analyze assembly efficiency. Nanoparticle assembly was performed *via* “one-pot” self-assembly procedure by thermal denaturation of all RNA strands in TMS buffer and gradual cooling over one hour. ImageJ software was used to analyze the intensity of gel bands and the yield of correctly folded 10 and 20 nm squares was estimated to be more than 90% with a slight decrease in folding efficiency observed for the 5 nm square (**Fig 2.7C**). Additionally, the hypothesis that each

strand was involved in the assembly, and that strand substitution was not occurring, was tested. For this assay, each strand A through E was fluorescently labeled. Five different squares, each with one of five strands labeled, were then assembled and analyzed by native PAGE. The results demonstrate that each strand contributes to the assembly and therefore the overall stability of the square (**Fig A.1.5**).

While native PAGE experiments suggest the formation of compact, homogeneous, and distinct RNA nanoparticles, atomic force microscopy (AFM) was performed to demonstrate the formation of the square shaped RNA nanoarchitecture (**Fig. 2.8B**). Resulting AFM images strongly support the formation of the medium and large square shaped RNA architecture. Image resolution of RNA nanostructures is in many cases limited by tip size. Due to the resolution limits of the AFM images shown in this report, the small square only appears as dots with no square geometry obviously visible. The results are expected as the size of the small square model is 5.2 nm, a size too small to be clearly resolved. A small percentage of squares appear as diamond shape straying from square geometry. This can be attributed to the fact that AFM images were taken in air and not in solution, distorting shape when the nanoparticles are dried onto the mica surface. Alternatively, diamond shapes could be due to the flexibility of the 3WJ (168). Using the large square AFM images, particles were manually counted to determine efficiency of assembly by AFM. It was revealed that the large square formed with 70% efficiency.

When considering a nanoparticle for use as an *in vivo* therapeutic the size of the particle greatly affects the delivery efficacy. Too small a size and the particle will simply be excreted; too large a size and entry into the cell will be greatly hindered. Previous studies showed that the optimal size for the cellular uptake of nanoparticles is 10-50 nm (90,203-

206). Using dynamic light scattering (DLS), the average hydrodynamic diameters (D_h) of RNA square nanoparticles were determined to be 4.0 ± 0.9 nm, 11.2 ± 1.3 nm, and 24.9 ± 0.5 nm for the small, medium, and large size squares, respectively (**Fig 2.8C**). These values are in close agreement with the predicted size of the model structures. At sizes of 4.0 nm, 11.2 nm, and 24.9 nm we have constructed variable size nanoparticles with potentially diverse physicochemical properties.

We have presented a simple method to adjust the size of RNA nanoparticles, however we aim to show that adjustment of size leads to diverse thermodynamic properties among square variants. To compare the thermodynamic stability of the squares, temperature gradient gel electrophoresis (TGGE) was used to determine the melting temperatures (T_M) of each square ($T_M = 50\%$ square formation). A temperature gradient perpendicular to electrical current was applied and increasing T_M corresponding to an increase in size was observed (**Fig A.1.6**). Since each of the square constructs contains four 3WJ motifs, the increase in melting temperature can be attributed directly to an increase in the amount of base-pairing in the structures. This trend follows the nearest-neighbor predictions for increasing of thermodynamic stability.

Taken together, structural analysis by computer modeling, DLS, and AFM suggest the formation of compact, flat, square RNA nanoparticles. The native geometry, determined by crystallization, has H1 and H2 of the 3WJ in planar configuration (168). The computer model also results in planar geometry based on duplex alignment of connecting helices H1 and H2, strongly supporting the formation of planar square nanoparticles. Furthermore, the presence of square structures on AFM, and not triangular shapes, which would result from a 3D tetrahedron like structure (207), also supports flat,

square geometry. As expected, AFM imaging demonstrates the size differences among the small, medium, and large squares.

Previously, RNA triangles have been constructed using the same pRNA-3WJ (126). After analysis of the square nanoparticle, it was determined that the square and triangle display diverse properties in thermodynamic stability, size, shape, and stoichiometry: functions possible per nanoparticle. Although not explored in depth in this study, it is possible that utilizing these particles in different applications, where size and shape play an important role, could be beneficial.

Physicochemical Properties are Tunable

Native RNA structures are inherently sensitive to degradation by cellular nucleases, potentially limiting the application of RNA nanoparticles in clinical applications. Modifications to RNAs, such as 2'F on the ribose sugar of the RNA backbone, have been shown to reduce their sensitivity to cellular nucleases (55,64). These same 2'F modifications have also been shown to increase the thermodynamic stability of RNA nanoparticles (63). DNA has also proven to be more resistant to the degradation caused by cellular nucleases (55,90). To be useful as an *in vivo* therapeutic, modifications must be made to the native square nanoparticles to gain resistance to RNase while retaining the same structure. Previous studies demonstrating different chemical and thermodynamic stabilities of the pRNA 3WJ constructed of RNA, DNA, and 2'F-RNA were the driving force behind the replacement of the core strand of the square nanoparticle (63,64). Due to these diverse stabilities, it was predicted that replacement of the core strand with different oligonucleotides would result in a nanoparticle with diverse physicochemical properties.

To impart tunable chemical and thermodynamic stabilities onto the 10 nm square nanoparticle the internal core strand E was replaced with both 2'F-C/U modified RNA and with single stranded DNA. Analysis by native PAGE demonstrated that all the nanosquares co-migrated indicating formation of the same geometry (**Fig 2.9A**). Moreover, all nanoparticles assembled with comparable yields of ~90% as determined by integration of the intensity of gel bands (**Fig 2.9A**).

A degradation assay in fetal bovine serum (FBS) was performed on each 10 nm hybrid square assembly. It was observed that substitution of 2'F modified core strand for unmodified RNA greatly enhances the stability of the nanoparticles in FBS (**Fig 2.9B**). After 14 hours, ~92% of square nanoparticles with 2'F modified core strand remained, as compared to ~20% for square nanoparticles with RNA and DNA core strands (**Fig 2.9B, Fig A.1.7**). While different hybrid duplexes exhibit different stabilities or susceptibilities to different RNases (208,209), serum comparison mimics more closely an *in vivo* environment and allows the direct comparison of each hybrid square. Overall, resistance to nuclease degradation was enhanced by replacing the core strand with 2'F modified RNA.

To further examine the effect the core strand has on nanoparticle stability, TGGE analysis was performed to determine the T_M of each hybrid. A temperature gradient, perpendicular to electrical current, was applied from 40°C-80°C. The T_M 's for the 2'F-RNA, RNA, and DNA hybrid square nanoparticles were calculated to be 68.4 ± 0.1 °C, 57.7 ± 0.2 °C, and 51.8 ± 0.1 °C, respectively (**Fig 2.9C, Fig A.1.8**). Melting temperatures were determined at 0.2 mM MgCl₂, simulating physiological conditions in which the cytoplasmic magnesium ion concentration is generally lower than 1 mM. At 10 mM magnesium concentrations, no melting below 80 °C was observed (**Fig A.1.8D-F**). Tertiary

structure greatly affects the melting temperature, and therefore thermodynamic stability, of an RNA structure. The duplex cannot be solely responsible for the trend in melting temperature from 2'F-RNA hybrid to DNA-RNA hybrid as a large portion of each structure is 3WJ. It has been shown that complicated tertiary structures are more stable in RNA than DNA resulting in a less stable a DNA-RNA hybrid 3WJ (63). Interestingly, the melting temperatures correlate with the FBS resistance assay indicating that the 2'F-RNA hybrid square was the most stable, followed by the native RNA square, and the DNA hybrid architecture was the least stable.

In clinical applications, considering pharmacokinetics, biodistribution, and toxicity, the most stable nanoparticles will not always be the most effective treatment (195-197). Our results show that it is possible to tune the stability characteristics of the RNA square nanoparticles by substituting the core strand and varying the ratio of 2'F nucleotides. This simple modification produces physicochemically diverse structures that can be easily tuned based on application.

Functionalizing the Square Scaffold

For the square architecture to be useful as a potential therapeutic in nanomedical applications, functional molecules (RNAi, aptamers, ribozymes) must be successfully fused into the core structure while it retains native folding and properties. Thus, the question of whether the RNA scaffold can harbor different RNA functional moieties such as siRNA, ribozymes, and RNA fluorogenic aptamers was addressed. More importantly, if the functional molecules retain their activity when incorporated into the square scaffold.

As such, four functional RNA groups, RNA spinach (SPIN) aptamer (210), RNA malachite green (MG) aptamer (211,212), hepatitis B virus (HBV) ribozyme (213), and

siRNA targeting luciferase gene (160) were incorporated at each corner of the 10 nm square nanoparticle (**Fig 2.10A, Fig A.1.9**). The multi-functional square assembly showed more than 90% efficiency as analyzed by integration of gel bands (**Fig 2.10B**). Additional AFM imaging was performed to demonstrate the retention of square geometry with the fused functionalities (**Fig 2.10C**).

The MG and SPIN aptamers are synthetic RNA aptamer sequences, previously obtained through SELEX (Systematic Evolution of Ligands by Exponential Enrichment) (92) that bind the malachite green and DFHBI dyes respectively (210,212). Free fluorophores in solution do not exhibit fluorescence and emit light only upon binding to their correctly folded RNA aptamer structures (210,214). To assay if folding was retained when incorporated into the multi-functional square, fluorometer measurements were taken for the malachite green and DFHBI chemicals alone and in the presence of the functional RNA square (**Fig 2.11**). The multi-functional square was simultaneously incubated with both fluorophores and fluorescence measurements were then taken. Both aptamers retained their folding and bound their respective fluorophore as evidenced by an increase in malachite green and DFHBI emission upon binding. As a positive control, a 3WJ with the MG aptamer and the SPINACH aptamer were used, both of which have been previously shown to exhibit increased fluorescence signal when incubated with their respective fluorophores (55,153). Furthermore, we aimed to show the simultaneous dual-mode fluorescent properties of the functional square architecture. The PAGE gel was stained for both MG and spinach aptamer dyes. Individual fluorescence of each aptamer was detected when incorporated into the same nanoparticle (**Fig A.1.10**).

The HBV ribozyme is a hammerhead ribozyme that cleaves hepatitis B genomic RNA. Ribozymes show potential as therapeutic agents; however, they traditionally have shown low efficiency when tested *in vivo*. This can be attributed to the misfolding of ribozymes in an intracellular environment and their susceptibility to exonucleases (215). One method to protect ribozymes and prevent their misfolding is to harbor them in larger, more complex structures. However, ribozymes must maintain their native folding, to retain functionality, when fused to RNA or incorporated into nanoparticles (101). Upon incubation of the multi-functional square with HBV genomic RNA, cleavage of the RNA genome occurs. Figure 2.12A demonstrates that the HBV ribozyme retains its catalytic activity when fused with the RNA square, as the cleaved products are clearly seen on the gel and the bands are comparable with a positive pRNA-HBV control construct (66).

To test the ability of the RNA square to carry siRNA for gene silencing effects, an *in vitro* assay was performed with a dual-luciferase reporter system (201). An siRNA anti-sense strand, which targets the firefly luciferase gene, was hybridized with its complementary sense strand used as a sticky end fused onto the multi-functional square (**Fig 2.10A**). A decrease in target gene, firefly, luminescence compared to reference gene, renilla, indicates a decrease in target gene protein production, designating a positive result. In comparison to the positive control, a 3WJ nanoparticle with fused luciferase siRNA (201), the multi-functional square harboring luciferase siRNA caused a similar decrease in luminescence indicating similar gene knockdown activity (**Fig 2.12B**). Overall, the results indicated that the RNA square nanoparticles carrying luciferase siRNA displayed ~40% gene knockdown activity.

For DICER to recognize and process double stranded (ds) RNA, the 3'-overhang must be accessible and not trapped inside the inner cavity of the square nanoparticle. This possible obstruction proves to be no problem. This newly constructed square makes it simple to incorporate other diverse functional moieties into one of the four "arms" of the square. This can be done by simply fusing siRNA into one of the four external scaffold strands.

The results demonstrate that diverse functionalities retain their activity when incorporated into the square scaffold, making the RNA square an addressable and programmable poly-functional nanoscaffold for potential delivery of RNA therapeutics for application in medicine. Due to the unique five-strand construction of the square architecture functionalities such as RNA aptamers and siRNA for gene therapy can be added by simply encoding for functionalities in the primary sequence of one strand in the square.

CONCLUSIONS:

Here we report the design and construction of poly-functional RNA square architectures utilizing the 3WJ motif of bacteriophage phi29. The conserved 60° angle from the 3WJ was expanded to 90°, and formation of square geometry was achieved. The length of the connecting helix was increased or decreased to generate three distinct sizes of nanoparticles. These three sizes of nanoparticles demonstrate diverse thermodynamic stabilities. By modulating the oligonucleotide used as the core strand we tuned the physicochemical properties of the square scaffold. The four arms extending from the four corners of the square were used to incorporate RNA functionalities, each of which was demonstrated to fold independently and correctly while retaining their authentic

functionalities. The square nanoscaffold shows great promise for biomedical and imaging applications due to its tunable thermodynamic and biochemical stabilities. The technique shown here for simple design to finely tune physicochemical properties adds a new angle to exploit RNA nanoparticles in a clinical setting.

ACKNOWLEDGEMENTS:

We thank Drs. Luda Shlyakhtenko and Yuri Lyubchenko for preparing the AFM images. The work was supported by NIH grants CA151648 and EB003730, and funding to Peixuan Guo's Endowed Chair in Nanobiotechnology position from the William Fairish Endowment Fund. The content is solely the responsibility of the authors and does not necessarily represent the official views of NIH. We would like to acknowledge the core facilities of the Markey Cancer Center at the University of Kentucky.

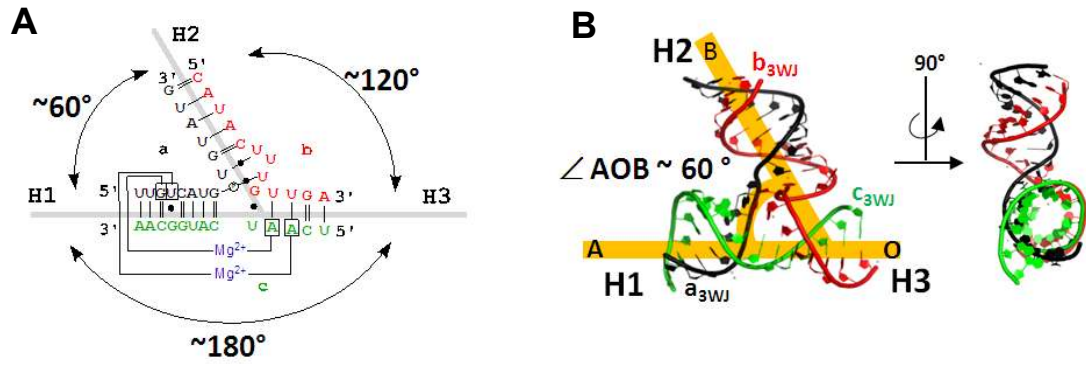


Figure 2.2. Structural features of the pRNA 3WJ motif. (A) Secondary structure of 3WJ motif with base pairs annotated with Leontis-Westhof nomenclature⁵⁶. (B) Tertiary structure of 3WJ motif with indication of $\angle AOB \sim 60^\circ$ angle formed between H1 and H2. Angle corresponds to inner angles of polygons.

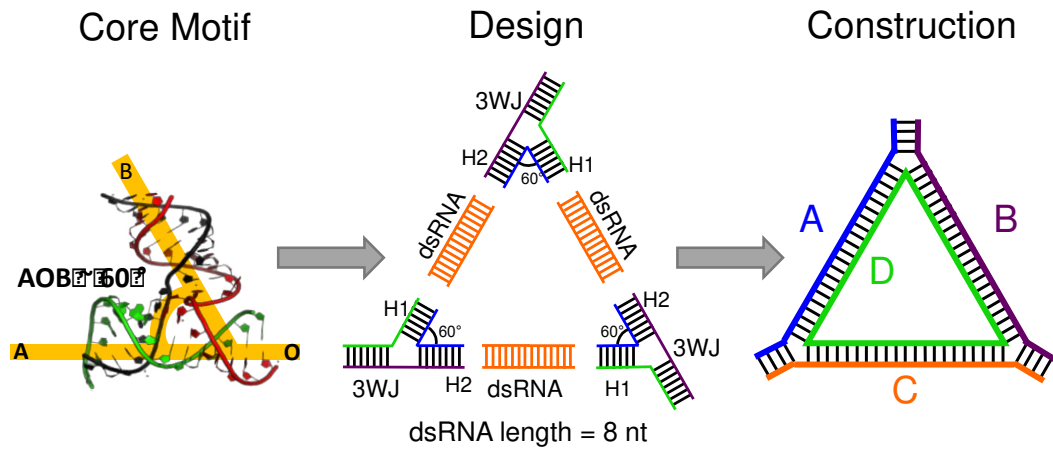


Figure 2.3. Modular design technique. Using the pRNA-3WJ as the vertex, diverse polygons were constructed. This figure represents the design scheme used for the initial design of RNA triangles from the 3WJ.

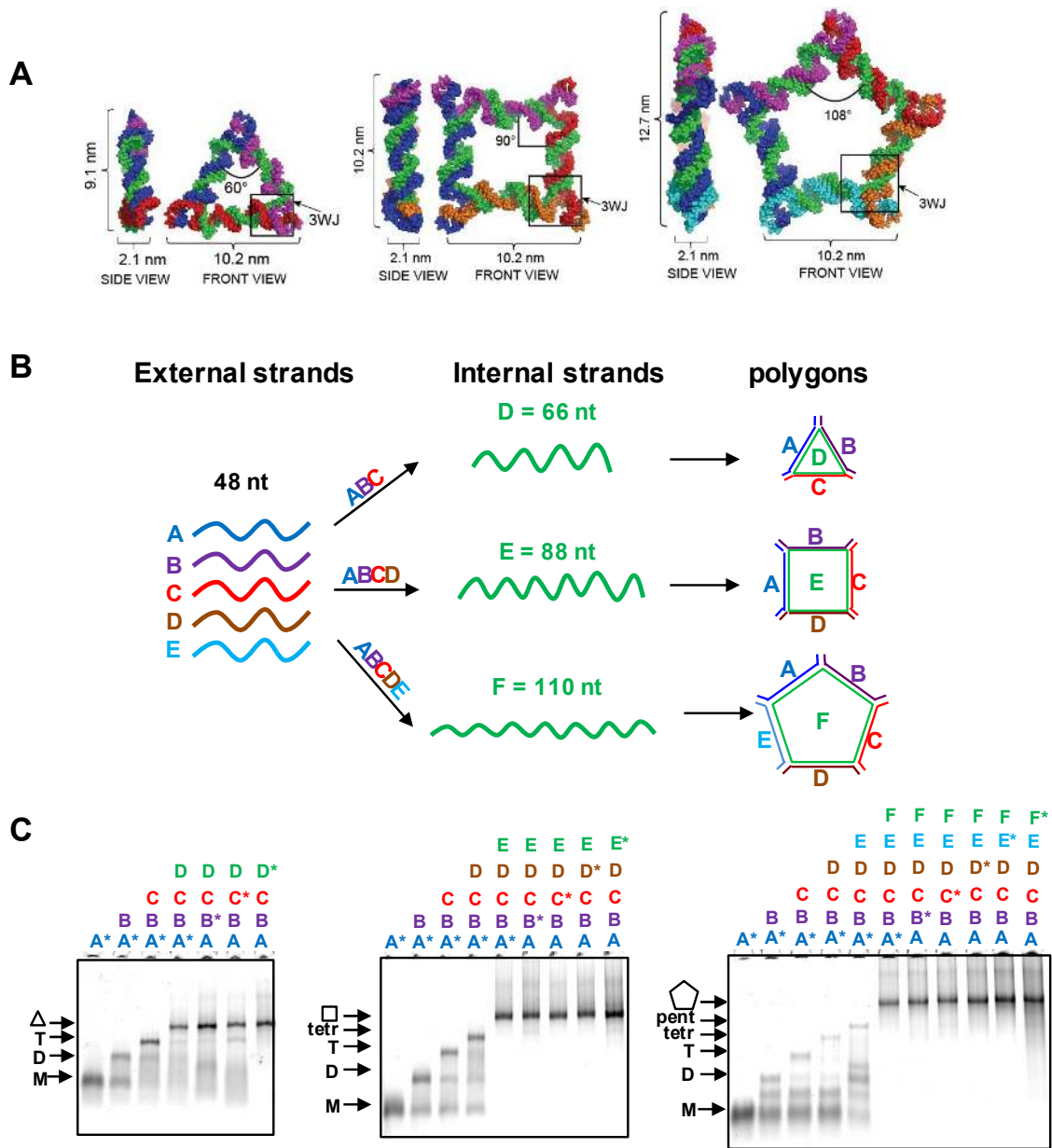


Figure 2.4. Design of Polygons and assembly properties. (A) 3D modeled structures of polygons with 3WJ motif located at vertices, inner angle corresponds to $\angle AOB \sim 60^\circ$. (B) The increasing length of the internal strand (green) stretches the 3WJ $\angle AOB$ at which the nanoparticles assemble, along with increasing number of external “short” strands. (C) Assembly properties of polygons evaluated on 7% native PAGEs. Asterisks “*” indicate the Cy5 labeled strands utilized on each type of polygon assembly.

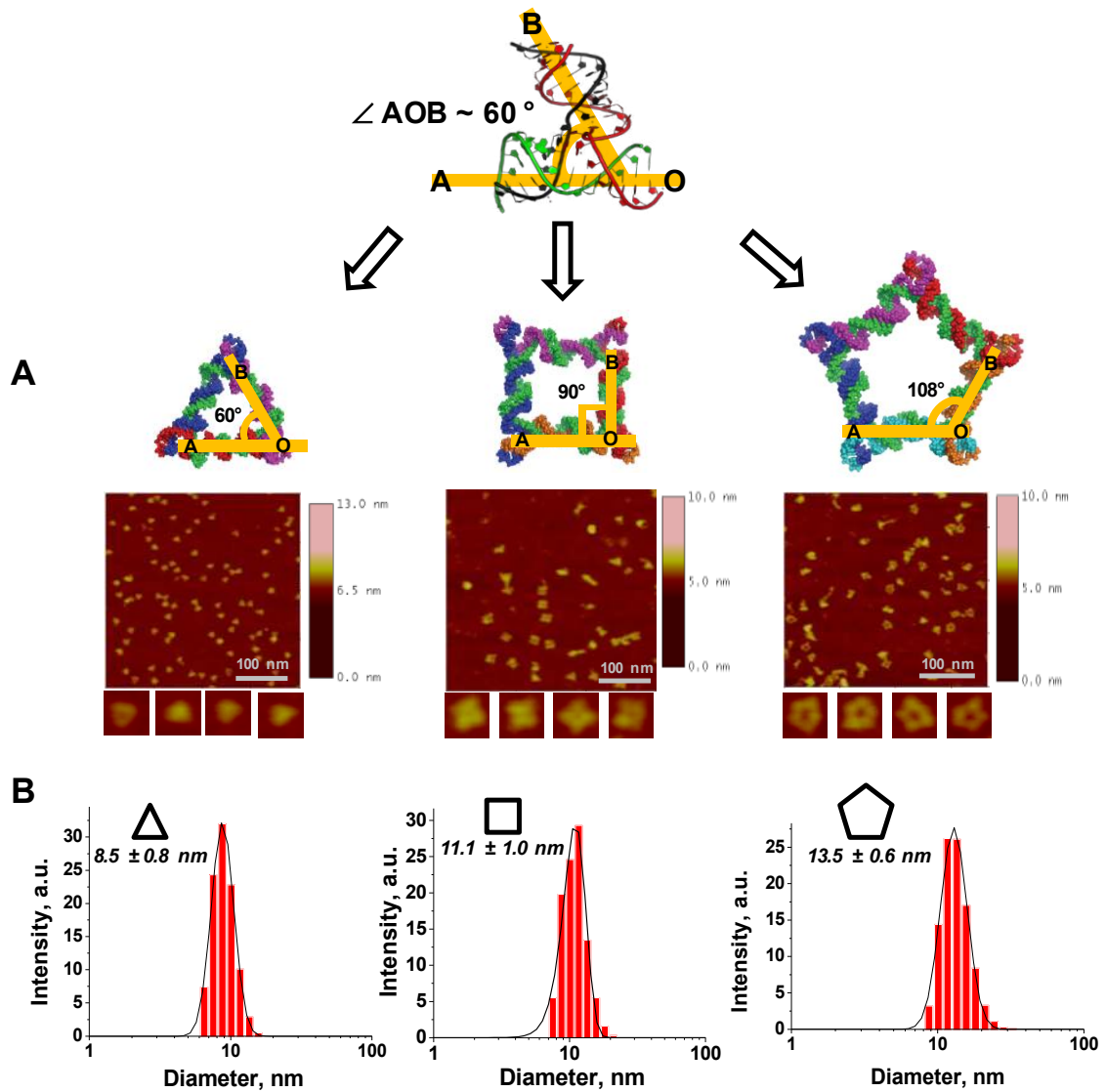


Figure 2.5. Structural characterization of polygons. (A) AFM images of triangular, square, and pentagonal nanoparticles derived from the pRNA 3WJ motif. (B) Polygons size distribution histogram obtained *via* dynamic light scattering.

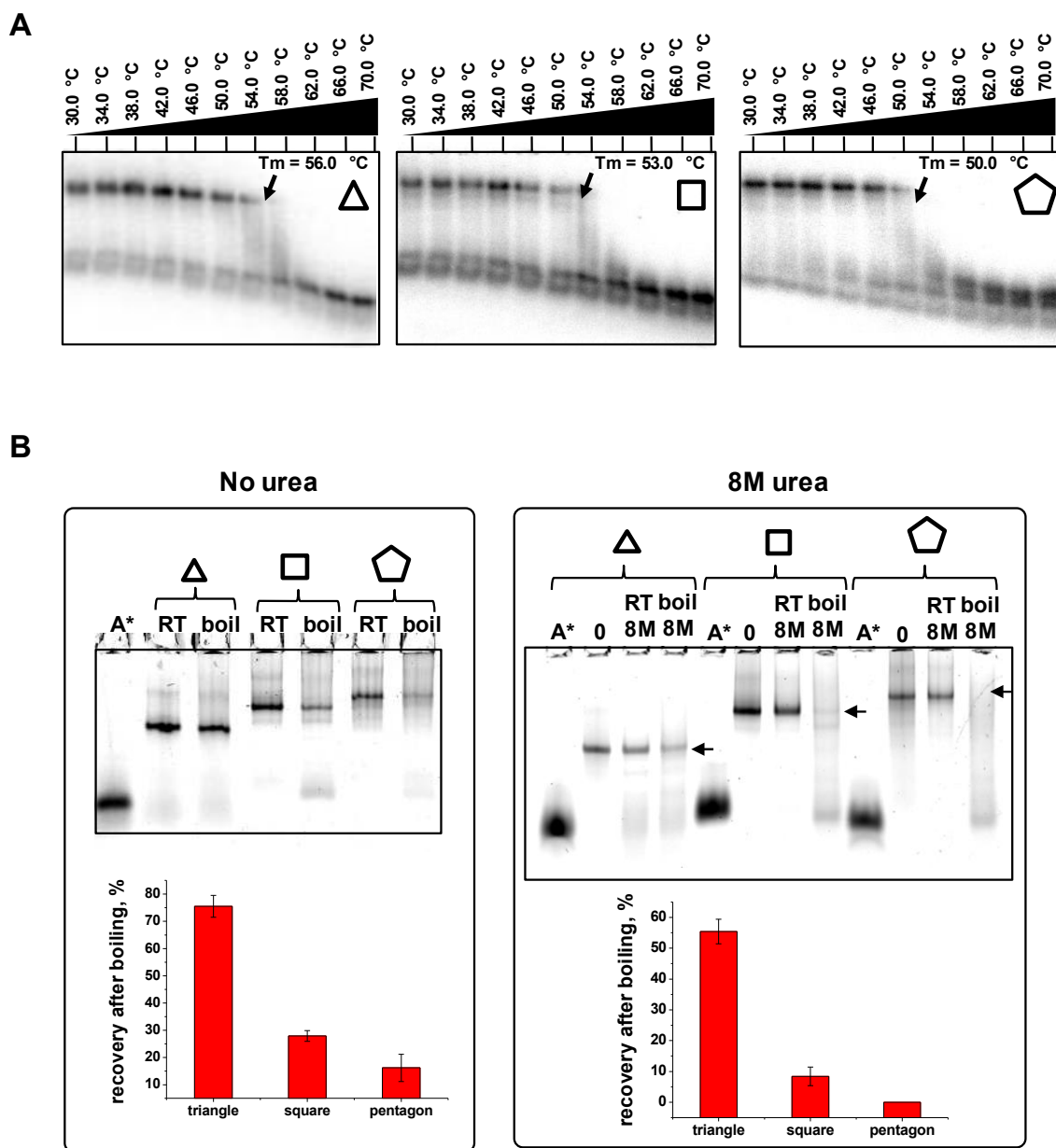


Figure 2.6. Comparison of polygon stabilities. (A) Melting temperatures of triangle, square, and pentagon measured by 7% perpendicular TGGE and boiling resistance assay in absence (B) and presence (C) of 8 M urea. Calculated percentage of recovery for polygons after boiling is shown below the each gel with error bars calculated from several independent experiments.

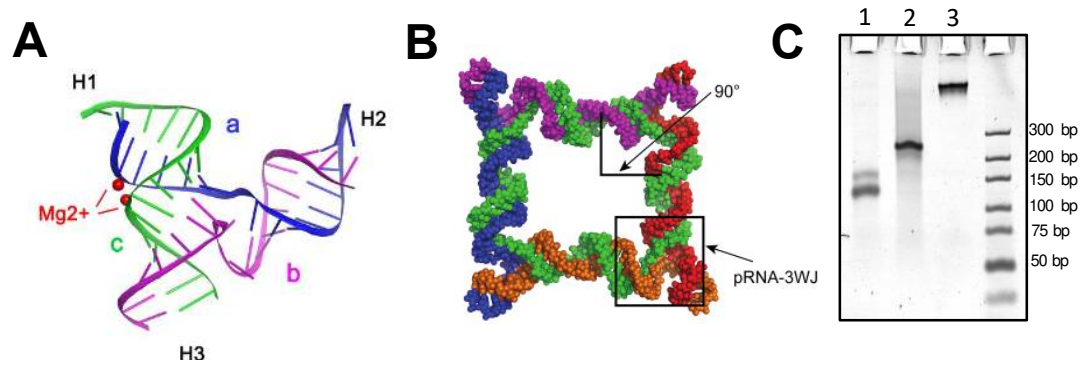


Figure 2.7. Design and assembly of the RNA squares. (A) Crystal structure of pRNA-3WJ showing the three component strands of the pRNA-3WJ, 3WJ-a (blue), 3WJ-b (purple), and 3WJ-c (green). (B) Three-dimensional structure of square shaped nanoparticle modeled on Swiss PDB Viewer, based on pRNA-3WJ. (C) Native PAGE assembly gel with ethidium bromide total RNA staining showing assembly of each square structure: Lane 1 is 5 nm square, Lane 2 is 10 nm square, and Lane 3 is 20 nm square.

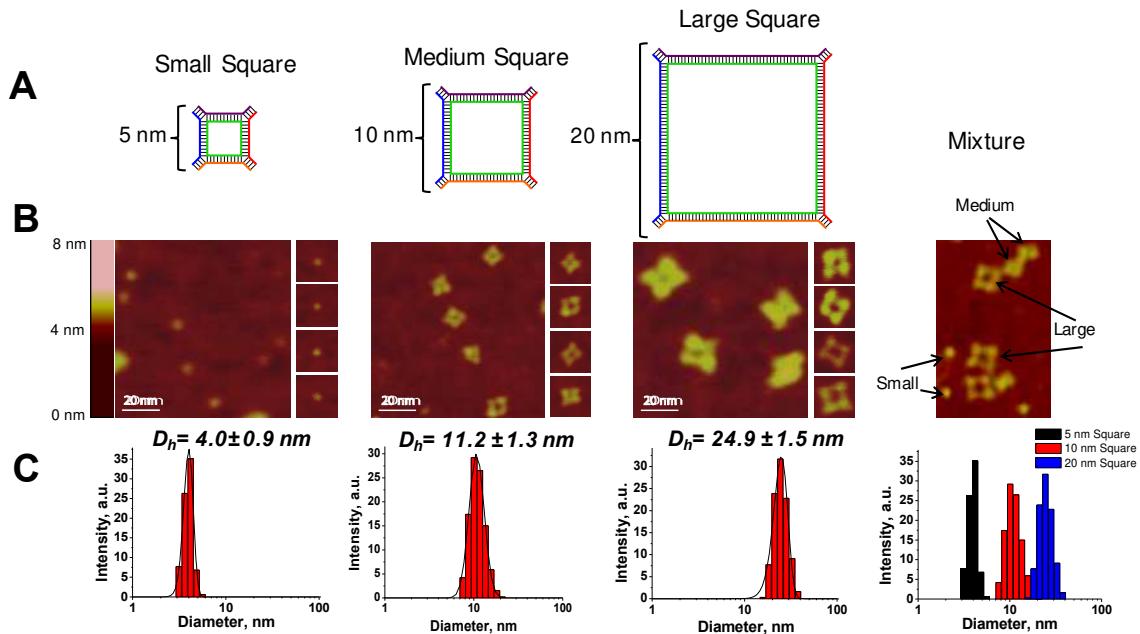


Figure 2.8. Physical Properties of the squares. (A) Schematic of small, medium, and large squares drawn to scale for size comparison. Four external strands (blue, purple, red, orange) are complimentary to the core internal strand (green). (B) AFM imaging of small, medium, and large RNA squares. Zoomed pictures of individual squares located on the right. On the far right is a mixture of squares, each square is indicated by arrows. (C) Dynamic light scattering (DLS) to determine the size of square nanoparticles. Far right panel shows comparison of all three square constructs.

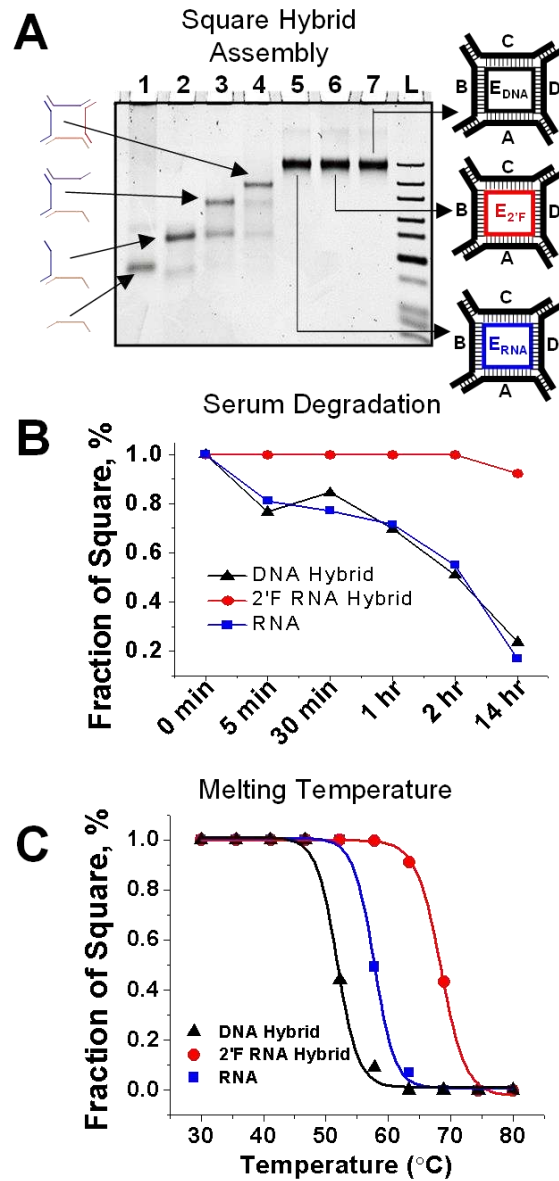


Figure 2.9. Comparison of RNA, 2’F-RNA, and DNA core strand hybrids. (A) Structure and native PAGE assembly of square nanoparticle hybrids. Blue strands represent RNA, red strands represent 2’F-RNA, black strands represent DNA. Lane 1 through 4 show the stepwise assembly from monomer to tetramer. **(B)** Nanoparticle stability in serum was compared among the square hybrid constructs **(C)** TGGE melting temperature profiles of square RNA nanoparticle along with 2’F and DNA core strand hybrids.

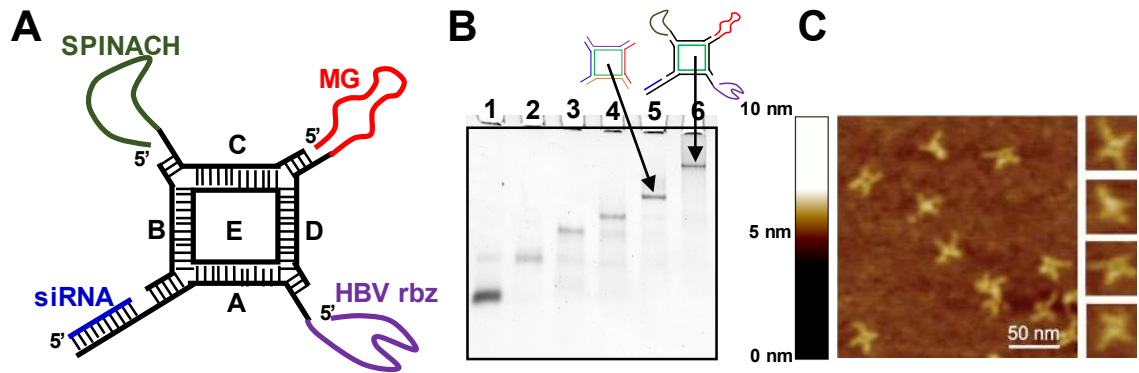


Figure 2.10. Design and assembly of multifunctional square. (A) Illustration of square structure with Spinach (SPIN) aptamer, malachite green (MG) aptamer, hepatitis B virus (HBV) ribozyme, and Luciferase siRNA incorporated into the square. (B) Assembly of the square nanoparticle and multi-functional square assessed by 7% native PAGE. (C) AFM images of multi-functional square nanoparticle with functional moieties visible on the corners of the nanoparticles.

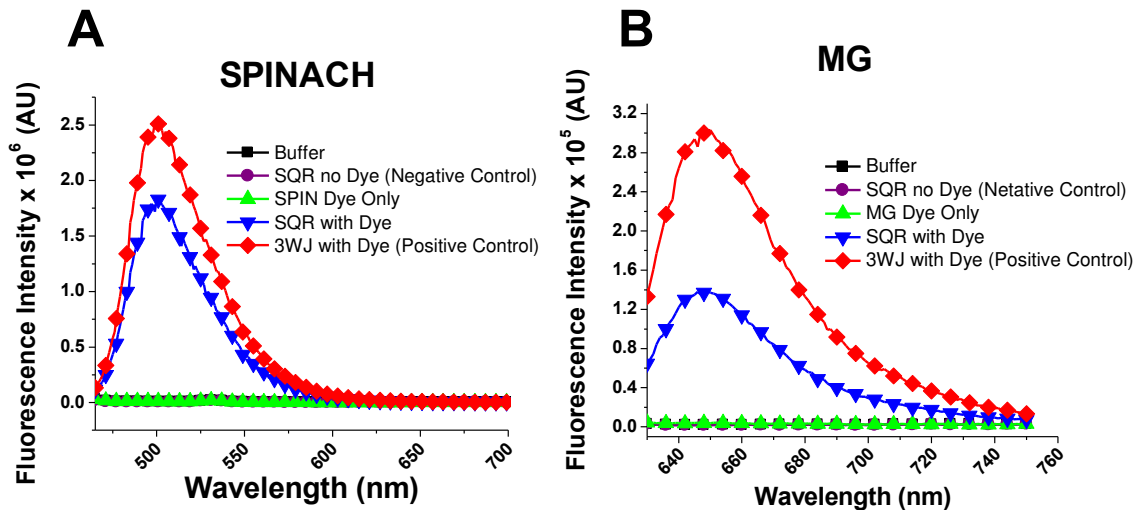


Figure 2.11. Fluorescence assays for multi-functional square. (A) Spinach aptamer assay. Increased fluorescence is shown upon incubation with DFHBI dye. **(B)** Malachite green aptamer assay. Increased fluorescence is shown upon incubation with malachite green dye.

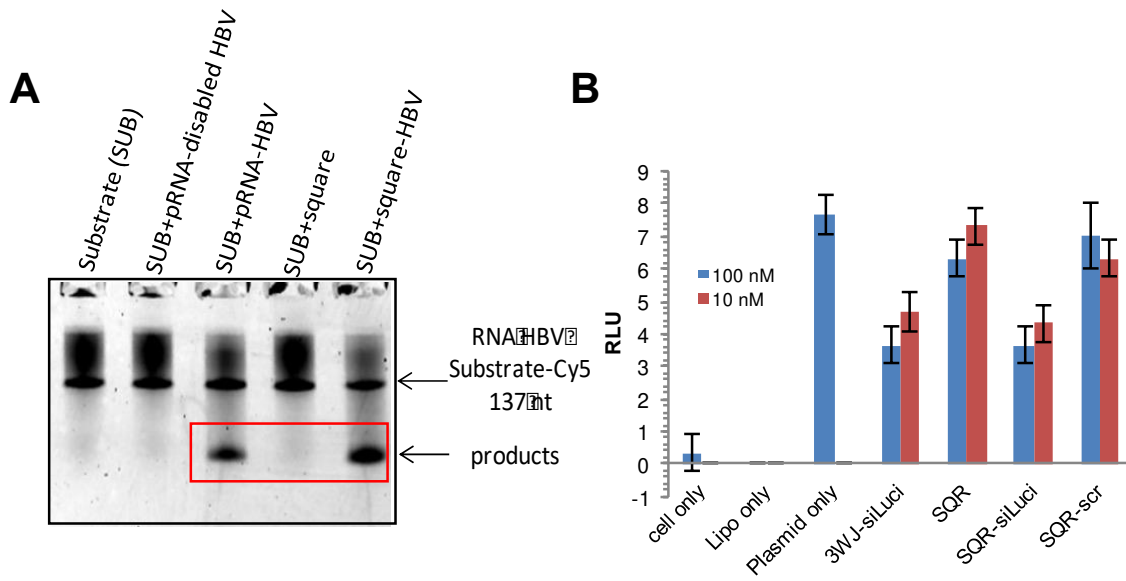


Figure 2.12. Ribozyme and siRNA activity assay. (A) Catalytic activity of the HBV ribozyme. Cleaved products are boxed. pRNA-HBV-Rbz was used as a control (B) Luciferase siRNA activity assay. Gene knockdown was measured by a decrease in luminescence. Cell only, Lipofectamine(Lipo) only and plasmid only were used as controls. Plasmid only control will exhibit the highest luminescence as the cells are only transfected with plasmid and no RNA. For a positive control 3WJ-siRNA showing knockdown was used. As negative control, naked square (no luciferase siRNA) and a scrambled siRNA sequence fused onto square were used. The square tested contained all four functional moieties. RLU is relative luminescence units.

Chapter 3: Effect of Nanoparticle Size, Shape, and Physical Properties on Biodistribution in Mouse Tumor Models

Chapter 3 was reproduced (with some modification) with permission from: Jasinski, DL; Li, H; and Guo, P. “The Effect of Size and Shape of RNA Nanoparticles on Biodistribution.” *Molecular Therapy. Under Revision*. Copyright 2017 Elsevier Inc.; Jasinski, DL; Yin H; Li, Z; and Guo P. “The Hydrophobic Effect from Conjugated Chemicals or Drugs on *in Vivo* Biodistribution of RNA Nanoparticles.” *Human Gene Therapy. Under Revision*. Copyright 2017 Mary Ann Liebert Publishing.

Special thanks to Dr. Hui Li for preparation of extended 3WJ samples for AFM images in figure 3.6 and help with IV injection and imaging of animal data in Chapter 3.1. Special thanks to Hongran Yin and Zhefeng Li for IV injection and imaging of animal data in Chapter 3.2. Thanks to Mario Vieweger for insightful discussion about hydrophobicity scale analysis in Chapter 3.2. Also, special thanks to Dr. Luda S. Shlyakhtenko and Dr. Yuri Lyubchencko for AFM images in figure 3.6.

Chapter 3.1: The Effect of RNA Nanoparticle Size and Shape on Biodistribution

INTRODUCTION:

The past decades have seen the emergence of nanotechnology as the next potential solution for advancing the field of medicine (13,14). Diverse types of nanoparticle platforms have been developed (3,4,7-12) that display distinct advantages over traditional treatments due to their increased circulation time, high therapeutic payload, and ability to harbor multiple functional groups (15,16). When combined with targeting ligands,

peptides, or aptamers, nanoparticles possess the potential for cell-specific drug delivery (29,32). The enhanced permeability and retention (EPR) effect allows even non-targeted nanoparticles to accumulate in tumor tissue due to the large amount of vascularization at the tumor site (216). However, many nanoparticles, while effectively targeting tumor and cancerous cells, accumulate non-specifically in healthy tissues, causing toxicity and off target effects (132). Non-biocompatible materials cause toxicity as they are never fully excreted from the body. Particles that do not cause toxicity, such as DNA and lipid based particles, then suffer from low stability *in vivo*.

Size and shape have been shown to greatly affect pharmacokinetics and biodistribution profiles of nanoparticles (127,128,134). Small particles (< 5 nm) are filtered by the kidneys and excreted in the urine (129). Large particles are engulfed by macrophages or sequestered in healthy tissue, never successfully navigating to the desired target (130). Many nanoparticles currently under investigation are rigid in nature, allowing no deformation from their size and shape. Rigid nanoparticles cannot penetrate pores smaller than themselves in size, resulting in low amounts of nanoparticles at the tumor site, which is normally heterogeneous in its structure. Alternatively, large, rigid particles that get stuck in healthy organs cannot escape, remaining trapped.

RNA nanotechnology, where the scaffold and ligands are composed solely of RNA, is an emerging technology that has shown promise to overcome several current challenges in nanotechnology (55,90). RNA nanoparticles can be engineered to diverse size and shape while retaining high thermostability necessary for *in vivo* applications (50,103,126,150). Simple sequence engineering can be used to employ the same RNA motif for construction of multiple RNA nanoparticles, reducing the number of single stranded RNA oligomers

needed for the construction of myriad of RNA nanoparticles. Furthermore, modifications to the ribose sugar (such as 2' fluorine, 2'F) of RNA bases confers stability in serum for more than 24 hours (h) (64,217). The unique base pairing mechanism that occurs during the assembly of RNA nanoparticles leads to consistent assembly properties, resulting in defined size nanoparticles with a narrow size distribution. Thus, a particular RNA nanoparticle will display homogeneity from batch to batch of assembly. In order to optimize drug delivery, it is important to have nanoparticles that are consistent in assembly that will display a narrow size distribution, as this will lead to consistent pharmacokinetic and biodistribution *in vivo* (218). Furthermore, RNA is a flexible biomaterial by nature, therefore allowing some structure deformity, unlike many rigid nanoparticles under development (219,220).

The pRNA three-way junction (3WJ) derived from the packaging RNA (pRNA) of bacteriophage phi29 has recently been shown to display high thermostability (55,63), fast kinetic assembly (62), and has been successfully used *in vivo* for miRNA and siRNA delivery and tumor growth suppression (56-58). The addition of aptamers and targeting ligands allow the 3WJ to successfully enter tumor cells specifically. Interestingly, 3WJ particles have repeatedly displayed little to no accumulation in healthy tissue, including the liver, kidneys, lung, and spleen (55,57,58). Despite the small size of the nanoparticles (<5 nm), total clearance by the kidneys does not occur while accumulation in tumor tissue is still observed (56-58).

The effects of RNA nanoparticle size and shape on biodistribution were investigated using previously constructed and characterized RNA triangles, squares, and pentagons (103,150). Analysis by fluorescence imaging of whole mice and their organs

demonstrated a strong correlation between increased size and increased circulation time using RNA nanosquares. However, shape showed to have less of an effect on biodistribution, despite the appearance of different elimination routes. Unlike many nanoparticle systems where it is hard to study size and shape independently, RNA nanoparticle size and shape is precisely controlled from nanoparticle conception. Therefore, in this study, different size nanoparticles that have identical shape could be studied.

MATERIALS AND METHODS:

RNA Nanoparticle Synthesis and Assembly

RNA strands were prepared as previously detailed (105) by either T7 *in vitro* transcription (strands longer than 70 nucleotides) or typical phosphoramidite oligonucleotide chemical synthesis (strands shorter than 70 nucleotides) using an automated oligo-synthesizer. DNA strands used as primers for dsDNA transcription templates were ordered from Integrated DNA Technologies (IDT). Assembly was carried out by mixing equimolar amounts of RNA strands followed by thermal denaturation at 85°C for 5 minutes and then slow cooling to 4 °C over one hour. For each nanoparticle, one strand was fluorescent labeled with AlexaFluor647 for fluorescent tracking *in vivo*.

In Vivo Biodistribution Experiments

KB cells were cultured *in vitro* and subcutaneously injected under the skin of 4-week old male nude mice (NU/NU, Taconic). A total of 2×10^6 cells were injected into each mouse. Tumors were grown for 2 weeks before mice were injected IV through the tail vein. Mice were administered with PBS as a blank control. Mice were imaged for whole body fluorescence at time points of 0.5, 1, 2, 4, 8, 12, and 24 h with an *In Vivo* Imaging

System (IVIS) imager (Caliper Life Sciences, Waltham, MA). For this study, two mice were used for the 0.5 through 12 h time points. At the 12 h time point, one mouse was sacrificed and its organs removed. At 24 h the second mouse was sacrificed and its organs removed and imaged. Tumors, hearts, kidneys, livers, spleen, and lungs were collected and imaged on the IVIS system.

Serum Stability Assays

2'F nanosquares were assembled and purified using polyacrylamide gel electrophoresis prior to serum degradation testing. After purification, 0.5 μ M fluorescently labeled squares were incubated at 37°C in 10% fetal bovine serum (FBS). Enzymatic degradation was stopped by freezing on dry ice at 0, 1, 2, 4, 8, 16, and 32 h. Samples were then analyzed using 2% agarose gel electrophoresis. Gels were then scanned for AlexaFluor647 fluorescent signal. Gel band intensity was integrated using ImageJ software (169). Values were normalized to initial band intensity and then plotted using OriginPro.

RESULTS:

Design and assembly of RNA polygons with variable size and shape

In vivo biodistribution studies of RNA nanoparticles was carried out using previously designed, constructed, and characterized RNA polygons (150). The nanosquares tested were designed to be 5, 10, and 20 nm along each edge (**Fig 3.1A**), and were previously measured by dynamic light scattering (DLS) to be 4.0 ± 0.9 , 11.2 ± 1.3 , and 24.9 ± 1.5 nm (150) while RNA triangle, square, and pentagons were each designed to be 10 nm along each edge (**Fig 3.1B**) (103). Throughout this paper, the nanosquares will be referred to by their designed edge length (5, 10, 20 nm). As previously described, RNA polygon size is determined by selecting the number of base pairs between each 3WJ at each

vertex, and the shape is determined by selecting the number of total 3WJs in the particle (103,126,150). Each polygon is constructed from multiple single stranded (ss) RNA oligonucleotides: short external strands (one along each edge), and one long core strand connecting each external strand. RNA strands were chemically synthesized with fluorine modifications at the 2' sugar position of cytosine and uracil, which confers enzymatic and thermodynamic stability (64). Polygons were assembled by mixing equimolar amounts of each strand in buffer followed by thermal denaturation at 85 °C and slow cooling to 4 °C over one hour.

A bi-partite fluorophore labeling approach, where only one of five strands was fluorescently labeled with AlexaFluor 647, was used to confirm that the particles were not dissociating *in vivo*. It has been shown previously that single stranded 2'F RNA is eliminated within five minutes after intravenous (IV) injection (184). Therefore, if the nanosquares were indeed dissociating, signal would have been lost within five minutes of polygon injection.

In vivo biodistribution of RNA polygons with variable sizes

Subcutaneous xenograft tumors were developed in male nude mice with KB cells. After tumors were fully developed (~2 weeks), 100 µL of 15 µM nanosquares harboring chemically conjugated AlexaFluor647 were injected IV *via* the tail vein. Whole body fluorescent images were taken at 0.5, 1, 2, 4, 8, 12, and 24 h (**Fig 3.2**). A diverse set of biodistribution profiles is seen when comparing different size 2'F nanosquares. 20 nm nanosquare fluorescence is observed throughout the mice at four hours, while both the 5 and 10 nm nanosquares are mainly sequestered in the tumor. As seen previously, the 3WJ nanoparticle shows no accumulation in vital organs in mice (55-58).

The same trend is seen from the organ images as from whole body scans of the mice. At 12 and 24 h, mice were sacrificed and their liver (Li), spleen (S), kidneys (K), heart (H), lung (Lu), and tumors (T) were collected (**Fig 3.3**). The 5 nm nanosquare is eliminated quickly from vital organs, localizing in only the tumor after 12 h. For the 10 and 20 nm nanosquares, fluorescence is much more intense in organs, especially after 12 h. However, 10 nm nanosquares localize only to the tumor after 24 h. Some fluorescence is still seen in the liver and kidneys of mice injected with 20 nm nanosquares after 24 h, however, we expect at longer time points the nanosquares would circulate out of all healthy organs.

Serum degradation testing was performed on the 2'F nanosquares (**Fig 3.4**). Nanosquares labeled with AlexaFluor647 were incubated at 37 °C in 10% fetal bovine serum (FBS) solution and time points were taken by immediately freezing the samples on dry ice to stop enzymatic degradation. After incubation, nanosquares were analyzed using 2% agarose gels scanned for AlexaFluor647 fluorescent signal (**Fig 3.4A**). ImageJ was used to quantify gel band intensity and values were plotted (**Fig 3.4B**). Gel band intensity was normalized to the well displaying highest fluorescence intensity. The results indicate half-lives in excess of 12 h for all nanosquare constructs. It is important to note that the half-lives of each nanoparticle are far greater than their apparent fluorescent half-lives seen during *in vivo* biodistribution experiments.

In Vivo Biodistribution of RNA polygons with variable shapes

Next, we investigate the role that shape plays in biodistribution profiles of RNA nanoparticles using previously constructed RNA polygons: triangle, square, and pentagon. The shape of RNA nanoparticles is easily controlled by modulating the inner angle of the

3WJ motif, which was used as the module for polygon construction. The inner angle is increased by extending the core strand by 22 nt, corresponding to two helix turns of A-type RNA duplex, and adding one external strand (103). RNA polygons were assembled using the same method as the nanosquares, mentioned above. 2'F modified polygons were used for *in vivo* biodistribution analysis.

Subcutaneous xenograft tumors were developed in male nude mice with KB cells. After tumors were fully developed (~2 weeks), 100 μ L of 15 μ M 2'F polygons harboring chemically conjugated AlexaFluor647 were injected IV *via* the tail vein. After 12 and 24 h, mice were sacrificed, their organs collected, and imaged for AlexaFluor647 signal (**Fig 3.5**).

It is evident that shape plays some part in the excretion routes and times of 2'F nanoparticles. Triangular nanoparticles appear to clear the fastest, showing only low fluorescent signal in the kidneys after 12 h, and only fluorescence in the tumor after 24 h. Square shaped nanoparticles show high fluorescent signal in the kidneys and low fluorescent signal in the spleen after 12 h. However, after 24 h fluorescent signal only remains in the tumor. Pentagon shaped nanoparticles show low signal in the kidneys after 12 h, with higher fluorescence seen in the spleen. Importantly, pentagonal, along with triangular and square- shaped nanoparticles only show fluorescence in the tumors after 24 h of circulation.

DISCUSSION:

Effect of Size on RNA Nanoparticle Biodistribution

In cancer treatment, nanoparticles accumulate at solid tumors by taking advantage of the EPR effect. However, EPR is principally affected by the circulation time of

nanoparticles (216). Larger nanoparticles generally show much higher circulation times, allowing them to capitalize on the EPR effect. Therefore, size is an important factor for nanoparticles that rely on the EPR effect to localize at tumors.

RNA nanoparticle size is easily controlled, and the assembly process is highly reproducible and homogenous, resulting in narrow size distributions and batch-to-batch reproducibility. This is an advantage of RNA nanoparticles over other systems, whose assembly processes are less controlled. Demonstrated by *in vivo* biodistribution results, the size of RNA nanoparticles greatly affects circulation time and accumulation in healthy organs and tumors. A strong correlation between increased nanosquare size and increased circulation time is seen, indicated by higher fluorescent signal in whole body and organ images of mice (**Fig 3.2, 3.3**). There are numerous reasons for these observations. Particles less than 15 nm, such as the 5 nm nanosquare, are excreted primarily through the kidneys, a quicker route of elimination compared to liver excretion (129). Larger particles up to 100 nm, such as the 10 and 20 nm nanosquares, have more interaction with macrophages, and are excreted more slowly through the liver (130). Another reason for different observed rates of RNA nanoparticle clearance is protein binding to the nanosquares, referred to as the protein corona (138). Differences in nanoparticle size have shown to dictate the amount and identity of proteins bound to nanoparticles, affecting their circulation time and excretion pathways (218). It is possible that differences in protein binding to the nanosquares greatly effects their elimination routes and therefore how long they stay in circulation.

Due to the high-fidelity assembly of RNA nanoparticles, they have a high likelihood to display consistent and controllable *in vivo* properties. Therefore, the same

nanoparticle system can be employed, easing nanoparticle preparation strategies, while displaying diverse but controllable *in vivo* properties. Based on the trend found in this study, it is possible that the construction of larger RNA nanoparticles would extend their circulation times even further.

Effect of Shape on RNA Nanoparticle Biodistribution

While size is a determining factor of *in vivo* circulation properties of nanoparticles, shape is also very important. Like size, the shape of RNA nanoparticles can be easily tuned. In this study, RNA polygons of different shape but same size along each edge, were analyzed in mouse models. The organ biodistribution was similar among the particles after 24 h, however, after 12 h there appears to be differences in biodistribution, per the intensity of fluorescent signal in different organs (**Fig 3.5**). For example, nanosquares show high fluorescence in kidneys after 12 h, while the triangle shows none, and the pentagon very little. And in the spleen, the highest fluorescence is seen in mice injected with pentagon nanoparticles.

Different shaped nanoparticles interact very differently with the *in vivo* environment (134). The protein corona is drastically changed by the shape of nanoparticles, which will affect the elimination pathways of nanoparticles. Additionally, previous studies have shown that symmetric nanoparticles can increase interaction with the immune system and trigger toxicity due to similarity in size and shape to pathogenic microorganisms (221). While RNA nanoparticles have been proven to trigger very low immune responses (103), shape is still something to consider and each nanoparticle should be tested to determine immune responses.

Additionally, when considering entry into cells, both size and shape will be very important. Cell receptors vary in size and shape, and it will be beneficial to design nanoparticles that can fit precisely into the receptor binding pockets, enhancing recognition and uptake (222). This is an area where RNA nanoparticles could potentially excel, as size, shape, and properties of RNA nanoparticles can be controlled and finely tuned to fit specific receptors.

CONCLUSIONS:

Herein, we have shown that size of RNA nanoparticles have a large effect on circulation time and biodistribution *in vivo*. A strong correlation between increased size and increased circulation time was observed, evidenced by the increased duration of fluorescent signal in whole body images of tumor bearing nude mice over 24 h. Despite increased size, there was still minimal fluorescent signal in healthy organs such as the liver and kidneys after 24 h compared to tumors. Here, shape was seen to have less effect on the biodistribution of RNA nanoparticles. However, fluorescent signal after 12 h suggests that elimination pathways could be different based on the shape of RNA nanoparticles. This study demonstrates a unique property of RNA nanoparticles that allows them to evade accumulation in healthy organs while still accumulating in tumor tissue by the EPR effect. Importantly, we have shown that the circulation time of RNA nanoparticles can be tuned simply by modulating their size. Circulation time is an important factor in drug delivery, as sometimes a short-lived particle is preferred to reduce toxicity, and other times a long circulating particle could be beneficial for slow acting therapies. RNA is an advantageous biomaterial for nanoparticle construction, as the base pairing self-assembly mechanism results in defined size and shape nanoparticles. Thus, *in vivo* drug delivery attributes, such

as circulation time, can be controlled from the conception of the design of a nanoparticle. It will be possible to utilize this unique property of RNA nanoparticles to enhance the current state of nucleic acid nanotechnology and drug delivery.

ACKNOWLEDGEMENTS:

The research in P.G.'s lab was supported by NIH grants R01EB019036, U01CA151648 and U01CA207946. The authors would like to thank Mario Vieweger and Daniel W. Binzel for their insight during manuscript preparation. P.G.'s Sylvan G. Frank Endowed Chair position in Pharmaceutics and Drug Delivery is funded by the CM Chen Foundation. PG is the consultant of Oxford Nanopore Technologies and Nanobio Delivery Pharmaceutical Co. Ltd, as well as the cofounder of Shenzhen P&Z Bio-medical Co. Ltd and its subsidiary US P&Z Biological Technology LLC.

Chapter 3.2: The Effect of RNA Nanoparticle Hydrophobicity on Biodistribution

INTRODUCTION:

Interactions of nanoparticles with their *in vivo* environment is an important factor and affects nanoparticle characteristics such as protein binding, toxicity, pharmacokinetics, and biodistribution (127,128,131-133,137,141,142). Accumulation of nanoparticles in healthy organs, such as the liver, kidneys, spleen, and lungs can lead to toxicity and lower efficacy of the administered dose of nanoparticles. While researchers are attempting to overcome this challenge with myriad of different nanoparticle systems, generally, less than 2% of the administered dose reaches the treatment site with the remaining dose sequestered by filtration organs, which leads to toxicity and off-target drug effects (132).

Recently, RNA nanoparticles derived from the packaging RNA (pRNA) of bacteriophage phi29 have seen increased use as an *in vivo* delivery system (50,55-58,103,126,148,150). RNA was once thought to have little potential for *in vivo* use due to biological and thermodynamic stability issues. However, these issues have been solved systematically by: (1) Finding of a thermodynamically stable three-way junction (3WJ) motif (55); (2) Findings that chemical modifications to RNA nanoparticles confer enzymatic stability *in vivo* (64); and (3) Finding that RNA nanoparticles exhibit little to no immunogenicity *in vivo* (103). RNA nanoparticles are also water soluble and anionic due to the charged phosphate backbone. RNA nanoparticles show no accumulation in healthy organs, navigating to tumors after four hours of circulation (55,57,58).

It is well known that a nanoparticle's size, shape, and physical properties affect interactions *in vivo*, and will therefore play a large role in determining their pharmacokinetics and biodistribution(128,134,140). Thus, tremendous efforts are made by nanoparticle engineers to overcome inherent downfalls in nanoparticle construction. For example, polyethylene glycol (PEG) is frequently used to increase water solubility of otherwise insoluble nanoparticles (143,144).

Conjugation of chemicals, such as fluorophores, drugs, and targeting ligands, is a popular method to decorate nanoparticles with functional moieties. However, many studies using hydrophobic fluorophores (fluors) show nanoparticle accumulation in vital organs such as the liver, kidneys, lung, and spleen (223-227). It is possible that the hydrophobic conjugates, in this case fluors, are promoting interaction with cell membranes and plasma proteins, causing accumulation of the nanoparticles in organs. In order for a nanoparticle

to display low toxicity and low accumulation in vital organs, it is important to understand how conjugation of chemicals to nanoparticles affects their *in vivo* properties.

Previous *in vivo* studies using pRNA nanoparticles were carried out using charged and water soluble fluors to make sure the properties of the nanoparticles were not changed drastically (55,57,58,228). However, as RNA nanotechnology progresses it will be important to know to what extent an RNA nanoparticle can be decreased in water solubility before accumulating in vital organs. Many potential applications such as chemical drug delivery and ligand based targeting involve conjugation of chemical groups to RNA nanoparticles. When chemicals are conjugated externally and not encapsulated, the impact of the conjugate is likely to be more significant.

To investigate this, three fluors of different hydrophobicities were conjugated to the 3WJ RNA nanoparticle to serve as model chemicals: Cyanine5.5 (C5.5); Sulfonated-Cyanine 5.5 (SC5.5); and AlexaFluor700 (A700). All three fluors display similar excitation and emission spectra, despite minimal differences in their structures and solubility (229,230). HPLC analysis demonstrated that conjugation of the fluors increased RNA nanoparticle hydrophobicity to differing extents. Hydrophobicity induced by chemical conjugates resulted in higher accumulation of RNA nanoparticles in vital organs of mice. Additionally, we observed weaker organ accumulation for hydrophobic chemicals after they were conjugated to RNA nanoparticles, suggesting that RNA can increase the solubility of hydrophobic chemicals. To offer a physical explanation for *in vivo* results, predictive compound logP (ClogP) values of the fluors and 3WJs were compared to experimentally determined hydrophobicity scales of amino acids, which are used to predict trans-membrane protein residues (231-234). This study offers insight into drug

development concerning the reduction of organ accumulation and drug toxicity or side effects of nanoparticles that are modified with chemical conjugates such as targeting ligands, fluors for tracking, and chemical drugs.

MATERIALS AND METHODS:

RNA Synthesis and Fluor Conjugation

RNA oligomers were chemically synthesized using typical phosphoramidite chemical synthesis on an automated oligo synthesizer. Following synthesis, oligomers were deprotected and desalted using conventional methods (235). Each 3WJ strand was synthesized using 2'-fluorinated cytidine and uracil. 3WJ-c strand was 5' modified with a primary amine (Cat. No: 10-1947-90, Glen Research). Cyanine5.5-NHS ester and Sulfo-Cyanine5.5-NHS ester were purchases from Lumiprobe. AlexaFluor700-NHS Ester was purchased from Molecular Probes. Conjugation reactions were carried out by mixing a 1:10 molar ratio of primary amine labeled 3WJ-c: NHS Ester-Fluorophore in 0.1 M sodium bicarbonate buffer, pH = 8.5. The conjugation reactions were incubated at room temperature for 16 hours while protected from light. Following incubation, the reactions were ethanol precipitated and washed twice with cold 75% ethanol to remove the majority of unreacted fluorophore, facilitating purification.

HPLC Purification and Analysis of RNA-Fluor Conjugates

Samples were purified using IPRP-HPLC. Due to different hydrophobicities of each RNA-fluor conjugate, different HPLC gradient methods were used for each conjugate. Buffer A was 0.1 M triethylamine acetate (TEAA) (Glen Research) in water and buffer B was 0.1 M TEAA in 75% acetonitrile and 25% water. All purifications were performed using an Agilent 1260 HPLC and Agilent PLRP-S HPLC column (Agilent Cat. No:

PL1512-5500). A flow rate of 1.5 mL/min was used throughout all HPLC methods and absorbance was monitored at 260 nm (RNA), 675 nm (C5.5, SC5.5), and 700 nm (A700). 3WJ-c-C5.5 was purified by a 5-100% gradient of buffer B over 15 minutes. 3WJ-c-SC5.5 was purified by 5-18% gradient of buffer B over five minutes followed by an 18-39% gradient over 15 minutes. 3WJ-c-A700 was purified by 5-18% gradient of buffer B over five minutes followed by an 18-38% gradient over 15 minutes. Fractions were collected when RNA absorbance and fluor absorbance eluted simultaneously. After fraction collection, RNA-fluor conjugates were dried to completion under vacuum.

For %ACN elution comparison, an identical gradient of 5-100% buffer B over 20 minutes was used to analyze 3WJ-fluor nanoparticles, 3WJ-c-fluor conjugates, and fluors. %ACN elution was calculated based on elution times of RNA oligoes or 3WJ complexes. Delay time was calculated by injection of an RNA sample in a high hydrophobic environment (100% acetonitrile) to prevent interaction with the column. The experimentally determined delay time was then subtracted from sample elution time, which was then used to calculate %ACN elution.

Chromatograms were plotted using OriginPro. Plots comparing 3WJ %ACN elution show 3WJ absorbance at 260 nm, 3WJ-Cy5.5 and 3WJ-SCy5.5 absorbance at 675 nm, and 3WJ-A700 absorbance at 700 nm. Comparison of %ACN elution of dye species were values taken from analysis chromatograms of dye species (**Fig A.2.1B, C, D**). Values were plotted and then slope determined using a linear fit.

Determination of Predictive ClogP Values

ChemDraw Professional 16 was used to predict ClogP values of amino acids, fluors, and nucleotide-fluor conjugates. Amino acids, fluors, and nucleotide-fluor

conjugates were drawn with charges analogous to their charged state at physiological pH = 7.4. Only the side chains of the amino acids were used for predictive ClogP calculations. Predicted ClogP values of amino acid side chains were then plotted versus previously published hydrophobicity scales of amino acids (233,234,236,237). Four different hydrophobicity scales were chosen for comparison (**Fig A.2.2**) and it was found that the Cornette hydrophobicity scale was the best match to predictive ClogP values. The Cornette scale is based on 28 published scales and demonstrates one of the best overall scales of amino acid hydrophobicity. High values indicate higher degree of hydrophobicity.

In vivo Biodistribution

Male BALB/c mice, 5 weeks old, (Taconic) were injected intravenously (IV) through the eye using retroorbital injection (238). At 1, 4, and 8 hours mice were sacrificed and their hearts, kidneys, livers, spleen, and lungs collected and imaged for Cy5.5, SCy5.5, and A700 fluorescent signal using an *In Vivo* Imaging System (IVIS) imager (Caliper Life Sciences). Mice were administered PBS as a blank control. 100 μ L of 20 μ M nanoparticle sample or dye sample were injected. It is important to note that the concentrations of dyes was kept consistent in all *in vivo* experiments.

RESULTS AND DISCUSSION:

3WJ-fluor HPLC analysis

The 3WJ is composed of three component RNA oligomers: 3WJ-a, 3WJ-b, and 3WJ-c (**Fig 3.6A**). Mixing equimolar amounts of each component strand at room temperature in physiological buffer yields homogeneous RNA nanoparticles (**Fig 3.6B**) (55). To fluorescently label the 3WJ nanoparticles, NHS-Ester derivatives of C5.5, SC5.5,

and A700 were conjugated to primary amine labeled 3WJ-c strand (**Fig 3.6C**). Fluor conjugated oligomers were purified from un-labeled RNA by IPRP-HPLC.

Following assembly of fluor labeled 3WJ nanoparticles (3WJ-C5.5, 3WJ-SC5.5, 3WJ-A700), polyacrylamide (PAGE) gel analysis was used to determine assembly efficiency. A decrease in migration rate of fully assembled 3WJ nanoparticles compared to monomer and dimer species indicates successful formation at high yield (**Fig 3.7A**). Gels were stained with ethidium bromide (EB) for total RNA visualization followed by scanning for EB and fluor signal. Co-migration of EB and fluor signal indicates successful incorporation of fluor-labeled oligomers into 3WJ nanoparticles.

3WJ particles were then analyzed by IPRP-HPLC to compare elution times and %ACN elution (**Fig 3.7B**). Table 3.1 shows a summary of nanoparticle elution times and %ACN elution. There is a strong correlation between the number of charged sulfate groups per fluor and the %ACN elution. 3WJ-C5.5 has the highest %ACN elution of 46.39 followed by 3WJ-SC5.5 at 22.72% and finally 3WJ-A700 at 21.49%. 3WJ with no fluor eluted at 14.13 %ACN. HPLC analysis indicates that different chemicals conjugated to RNA nanoparticles will increase the nanoparticle's hydrophobicity to differing degrees.

Fluorophore hydrophobicity vs biodistribution

Following HPLC analysis, the fluors were injected retroorbitally into mice and fluorescent signal was whole body imaged 1, 4, and 8 h post-injection. Mice were then sacrificed and their organs collected and imaged for fluorescent signal. Fluorescent signal from whole body images show low fluorescent signal for A700 and SC5.5 and higher fluorescent signal for C5.5 (**Fig 3.8A**). Organ images of the mice injected with the fluors

all show fluorescent signal after 8 h (**Fig 3.8B**). These observations correlate well with the increased hydrophobicity of C5.5 over both SC5.5 and A700.

3WJ-fluor hydrophobicity vs biodistribution

The *in vivo* properties of the 3WJ-fluor nanoparticles were analyzed by testing their biodistribution profiles in mice. Mice were injected retroorbitally and sacrificed at 1, 4, and 8 h post-injection. Organs were collected and scanned for fluorescent signal. Whole body images indicate faster clearance of 3WJ-SC5.5 and 3WJ-A700 compared to and 3WJ-C5.5 (**Fig 3.8**). 3WJ-C5.5 showed high fluorescent signal in the organs compared to mice injected with PBS as a blank, primarily accumulating in the liver and kidneys after 8 h (**Fig 3.8B**). 3WJ-SC5.5 does show fluorescence in organs after 8 h, albeit much less intense than observed for 3WJ-C5.5. 3WJ-A700 shows no fluorescence in organs after 8 h. These *in vivo* results demonstrate a strong correlation between the increased hydrophobicity of the fluorophore and increased accumulation of nanoparticles in organs. Furthermore, these results show the ability of the 3WJ nanoparticle to increase the solubility of the fluors as less accumulation in vital organs of 3WJ-fluor nanoparticles is seen when compared to fluors.

Physical basis for hydrophobicity effect on biodistribution

After *in vivo* results, we sought a physical explanation for our observations. One likely explanation for accumulation of the nanoparticles is interaction with proteins and cell membranes *in vivo*. It is our hypothesis that the increased hydrophobicity of the fluors conjugated to the 3WJ nanoparticles initiates interaction with the hydrophobic regions of proteins and cell membranes, causing the nanoparticles to accumulate in organs. Many studies have been done on the hydrophobicity of proteins and how the amino acid

arrangement creates pockets of hydrophobicity and hydrophilicity (231-234,236,237). These studies have generated amino acid hydrophobicity scales, which are used to predict hydrophobic regions in proteins and determine trans-membrane protein regions.

We hypothesized that the increased hydrophobicity of 3WJ-C5.5 was increasing the strength of the interactions between the hydrophobic regions of proteins and cell membranes and the nanoparticles. Because the RNA nanoparticles are extremely hydrophilic with a hydrophobic fluor attached, we expect them to exhibit an amphipathic property. This is akin to trans-membrane proteins, which are amphipathic to cross cell membranes.

A logP (partition coefficient) value is the ratio of a compounds solubility in two immiscible solvents, normally octanol: water, and is a good indication of hydrophobicity. Additionally, logP values are useful in estimating the biodistribution of drugs. More hydrophobic logP values generally indicate accumulation of drugs in hydrophobic areas such as the lipid bilayers of cells, while more hydrophilic logP values indicates accumulation of drugs in hydrophilic regions such as blood serum (239). A ClogP value uses experimentally determined logP values of small fragments, and then adds these values together with correction factors to obtain a ClogP value (240). When dealing with complex molecules, such as those containing aromaticity, ClogP values tend to be quite accurate.

ChemDraw version 16.0 was used to predict the ClogP values of the amino acids (**Tbl 3.2**). These values were then plotted alongside hydrophobicity values from different hydrophobicity scales (**Fig A.2.2**). We chose the Cornette(233) hydrophobicity scale as we observed the best correlation between predicted ClogP values and Cornette values (**Fig 3.9A**). A dotted line represents a neutral value of 0.

Next, ClogP values of C5.5, SC5.5, and mono, di, and trinucleotide derivatives of the fluors were predicted (**Tbl 3.2**). The structure of A700 is proprietary, and no structural information was available, however, SC5.5 and A700 demonstrate similar hydrophobicity based on IPRP-HPLC. The ClogP values were then plotted alongside ClogP values of amino acids (**Fig 3.9B**). Interestingly, C5.5 displays a high ClogP value while SC5.5 displays an extremely low ClogP value. Only when C5.5 is in trinucleotide form does the ClogP value reduce to near zero. ClogP values beyond trinucleotide form could not be predicted due to the increased number of atoms and software limitations. However, we expect as more nucleotides are added (54 in one 3WJ nanoparticle), the ClogP value would drastically decrease.

Importantly, comparison of the predicted ClogP values of the amino acids with the fluors and their nucleotide derivatives provides some insights into the effect of hydrophobicity on cell membrane interaction. We see a highly-correlated trend between high ClogP value and organ accumulation *in vivo*. We also see a highly-correlated trend between high ClogP value and high value in the Cornette hydrophobicity scale. This shows that conjugates with high predicted ClogP values conjugated to a nanoparticle may cause interaction with the cell membrane, much like trans-membrane proteins.

Interestingly, while 3WJ-SC5.5 and 3WJ-A700 display similar %ACN elution by HPLC analysis, they demonstrate different behaviors *in vivo*. This suggests that the interaction of the nanoparticle conjugate with cell membranes is determining organ accumulation, not the overall hydrophobicity of the nanoparticle conjugate. Also, factors other than hydrophobicity, such as structure of the conjugate, could contribute to entrapment in vital organs.

RNA nanoparticles solubilize hydrophobic chemicals

The hydrophilic property of RNA nanoparticles enables them to solubilize many hydrophobic chemicals. IPRP-HPLC demonstrates an increase in solubility (decrease in %ACN elution) from fluor alone to 3WJ-c-fluor to 3WJ-fluor (**Fig A.2.1B-D**). Interestingly, we see a much larger decrease in %ACN elution for the hydrophobic Cy5.5 fluor than for both hydrophilic fluors, indicated by more negative slope for Cy5.5 (**Fig 3.10**). The effect of RNA nanoparticles increasing solubility is evidenced by decreased fluorescent signal in vital organs when comparing 3WJ-fluor to fluor alone (**Fig 3.8B**).

However, despite the high overall hydrophilicity, we still see both increased %ACN elution and accumulation with hydrophobic cell membranes when using a hydrophobic conjugate. This once again leads us to believe that the conjugate itself is interacting with cell membranes, and if the interaction of the conjugate with the cell membrane is strong enough it can overcome the hydrophilic nature of the RNA nanoparticle and the anionic property of RNA. Thus, not only is the overall hydrophilicity of the nanoparticle important, but so are the specific surface properties of the nanoparticle.

While this study uses fluors to demonstrate how hydrophobicity affects nanoparticles *in vivo*, we expect it to extend to other conjugates such as chemical drugs or targeting ligands. For future use, it will be beneficial to determine beforehand if a conjugate will or will not cause nanoparticles to accumulate non-specifically *in vivo*. It is possible that using a screening method, such as the one presented in this study, will greatly benefit nanoparticle engineers looking to optimize their nanoparticle's physical properties. Specifically, for RNA nanoparticles, it could be beneficial to use encapsulation methods to

protect the hydrophobic molecules from strong interactions with cell membranes or other proteins (148).

CONCLUSIONS:

Our study demonstrates a strong correlation between increased hydrophobicity of an external conjugate and increased accumulation of nanoparticles in vital organs. Comparison of ClogP values of C5.5, SC5.5, and A700 to amino acids showed a strong correlation between hydrophobic dyes, which accumulate *in vivo*, to amino acids that are commonly seen in hydrophobic regions of trans-membrane proteins. Our results demonstrate a method to pre-screen nucleic acid based nanoparticle conjugates for their hydrophobic properties using a common method of HPLC analysis. As shown here, careful consideration must be taken when choosing to externally conjugate chemical drugs, fluors, or targeting ligands to water soluble nanoparticles, as their effect on water-solubility, and in turn *in vivo* biodistribution, could be detrimental to the safety of patients in future clinical settings. This study offers some insight into drug development concerning the reduction of organ accumulation of nanoparticles and reduction of drug toxicity and side effects.

ACKNOWLEDGEMENTS:

The research in P.G.'s lab was supported by NIH grants R01EB019036, U01CA151648 and U01CA207946. We thank Mario Vieweger and Daniel W. Binzel for their insight in manuscript preparation. P.G.'s Sylvan G. Frank Endowed Chair position in Pharmaceutics and Drug Delivery is funded by the CM Chen Foundation. PG is the consultant of Oxford Nanopore Technologies and Nanobio Delivery Pharmaceutical Co. Ltd, as well as the cofounder of Shenzhen P&Z Bio-medical Co. Ltd and its subsidiary US P&Z Biological Technology LLC.

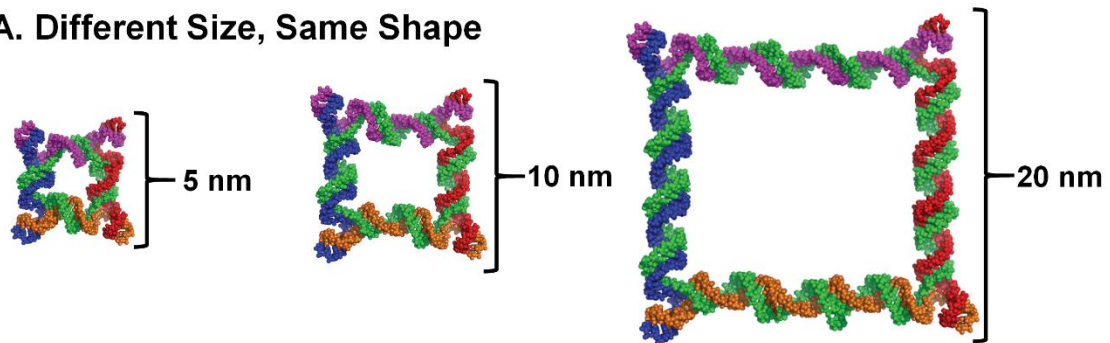
Table 3.1. Elution Times and %ACN Elution of Fluorophore Species.

RNA-Dye Conjugate	Elution Time (min)	%Acetonitrile Elution	In vivo Result	# of Sulfate Groups
Cy5.5	22.29/26.14	55.41/69.13	High in organs	0
SCy5.5	13.10/16.20	22.69/33.69	Low in organs	4
A700	13.19/15.07	22.97/29.68	Low in organs	?
2'F-3WJ-C	11.48	16.90	-	-
2'F-3WJ-C-Cy5.5	20.58	49.31	-	2
2'F-3WJ-C-SCy5.5	13.67	24.72	-	4
2'F-3WJ-C-A700	13.27	23.26	-	?
2'F-3WJ	10.70	14.13	-	-
2'F-3WJ-Cy5.5	19.76	46.39	High in organs	0
2'F-3WJ-SCy5.5	13.11	22.72	Low in organs	2
2'F-3WJ-A700	12.77	21.49	No Organs	?

Table 3.2. Amino Acid Hydrophobicity Comparisons to Fluorophore Species.

	Amino Acid	Cornette	ClogP	%ACN Elution
D	Aspartic Acid	-3.10	-4.19	-
K	Lysine	-3.10	0.96	-
Q	Glutamine	-2.80	-0.59	-
P	Proline	-2.20	0.83	-
T	Threonine	-1.90	-0.24	-
E	Glutamic Acid	-1.80	-3.67	-
N	Asparagine	-0.50	-1.11	-
S	Serine	-0.50	-0.76	-
G	Glycine	0.00	-1.32	-
A	Alanine	0.20	1.10	-
H	Histidine	0.50	0.36	-
W	Tryptophan	1.00	2.63	-
R	Arginine	1.40	-0.45	-
Y	Tyrosine	3.20	1.97	-
C	Cysteine	4.10	0.65	-
M	Methionine	4.20	1.37	-
F	Phenylalanine	4.40	2.64	-
V	Valine	4.70	2.28	-
I	Isoleucine	4.80	2.81	-
L	Leucine	5.70	2.68	-
	SCy5.5-NHS-Ester	-	-11.59	22.69/33.69
	SCy5.5-MonoNT	-	-14.22	-
	SCy5.5-DiNT	-	-16.06	-
	SCy5.5-TriNT	-	Highly Neg.	-
	Cy5.5-NHS-Ester	-	7.66	69.13
	Cy5.5-MonoNT	-	5.43	-
	Cy5.5-DiNT	-	3.59	-
	Cy5.5-TriNT	-	0.90	-
	A700-NHS	-	??	22.97/29.68
	MonoNT	-	-4.67	-
	DiNT	-	-7.16	-
	TriNT	-	-9.85	-
	3WJ-SCY5.5	-	Highly Neg.	22.72
	3WJ-Cy5.5	-	Neut to Neg.	46.39
	3WJ-A700	-	Highly Neg.	21.49

A. Different Size, Same Shape



B. Different Shape, Same Size

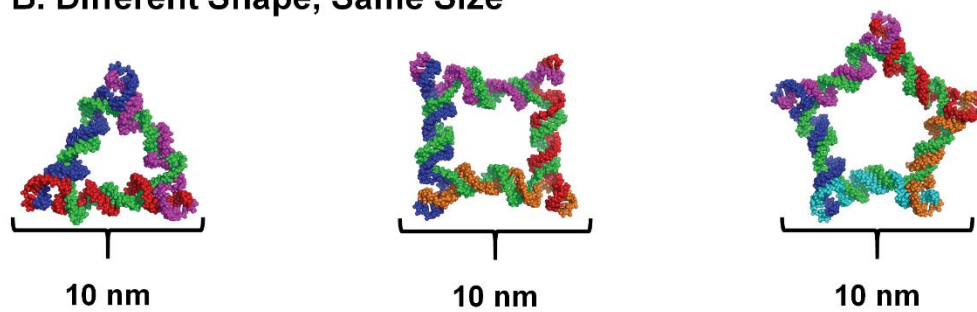


Figure 3.1. (A) Structures of the 5, 10, and 20 nm 2'F nanosquares. (B) Structures of 10 nm RNA triangle, square, and pentagon

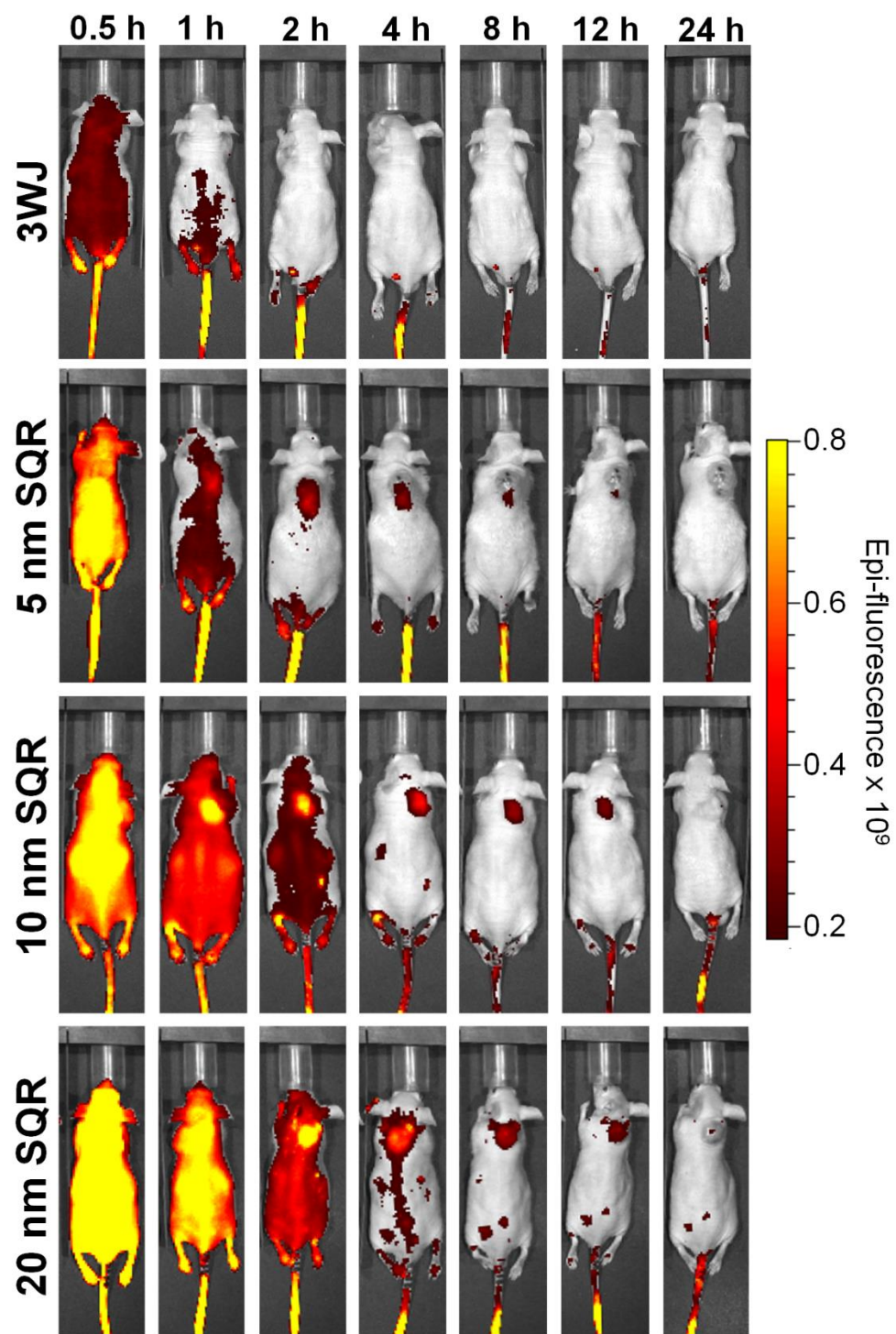


Figure 3.2. *In vivo* biodistribution time course fluorescence images of 5, 10, and 20 nm 2'F nanosquares. Mice were imaged for fluorescent signal using an *in vivo* imaging system (IVIS) scanning for AlexaFluor647 signal.

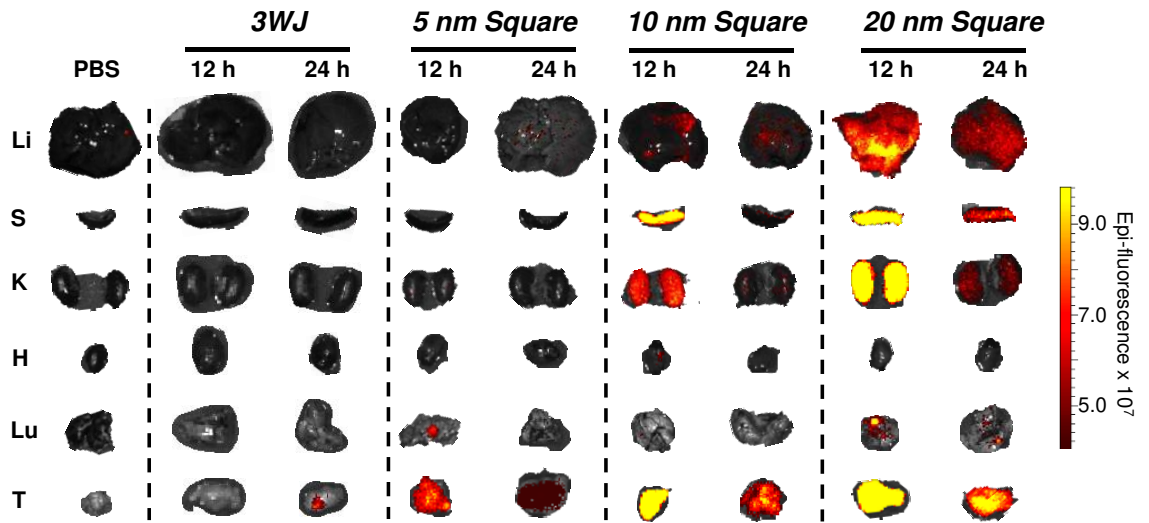


Figure 3.3. Organ images of 5, 10, and 20 nm 2'F nanosquares after 12 and 24 h. Organs were fluorescently imaged using an *in vivo* imaging system (IVIS) scanning for AlexaFluor647 signal.

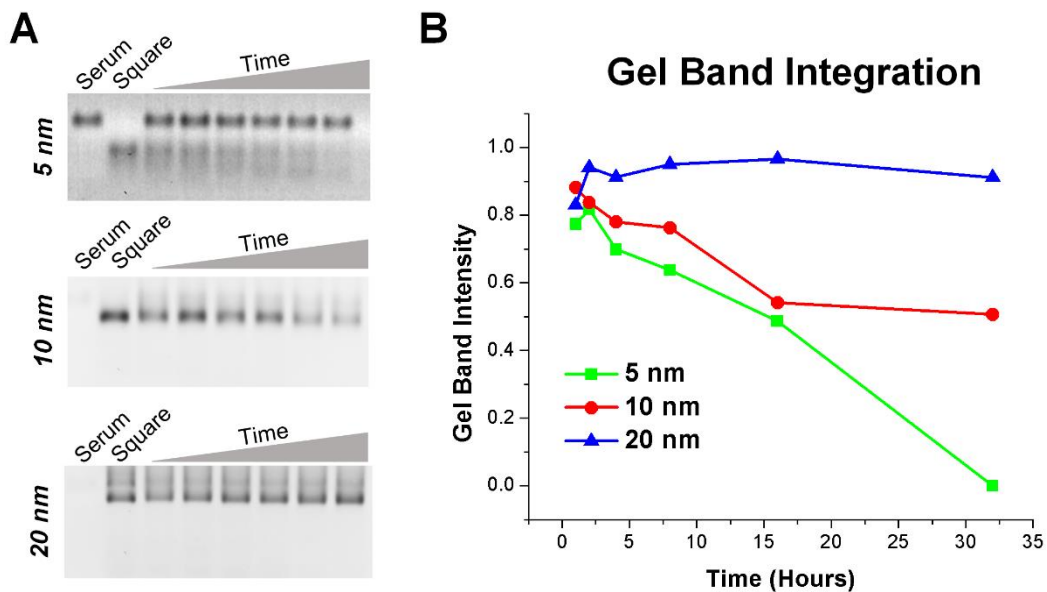


Figure 3.4. (A) Gel images of serum degradation of 5, 10, and 20 nm 2'F nanosquares. (B) Plots of gel band intensity from serum degradation gels of 5 (green), 10 (red), and 20 (blue) nm 2'F nanosquares.

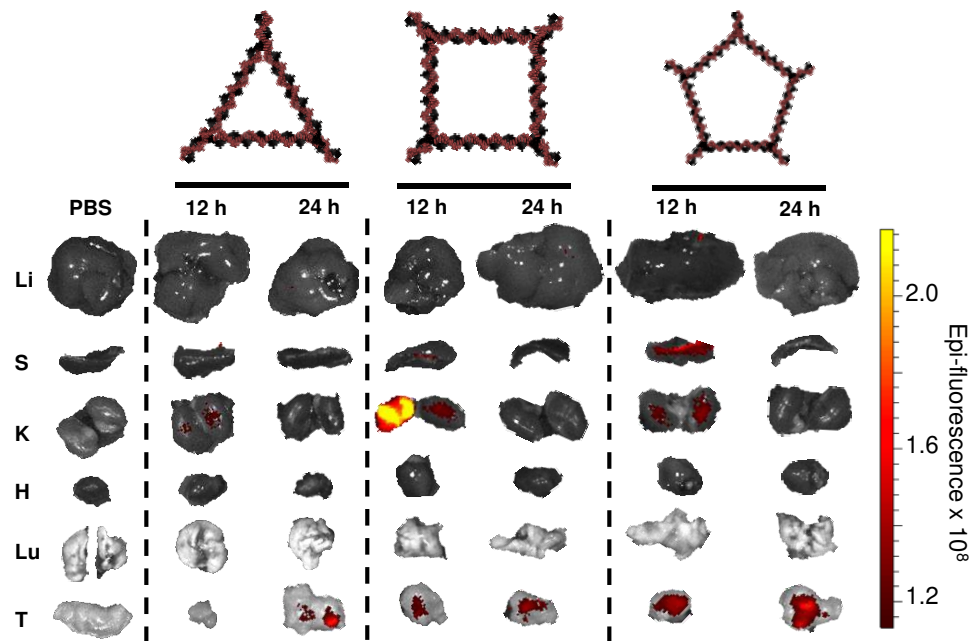


Figure 3.5. Organ images of 2'F RNA polygons after 12 and 24 h. Organs were fluorescently imaged using an *in vivo* imaging system (IVIS) scanning for AlexaFluor647 signal.

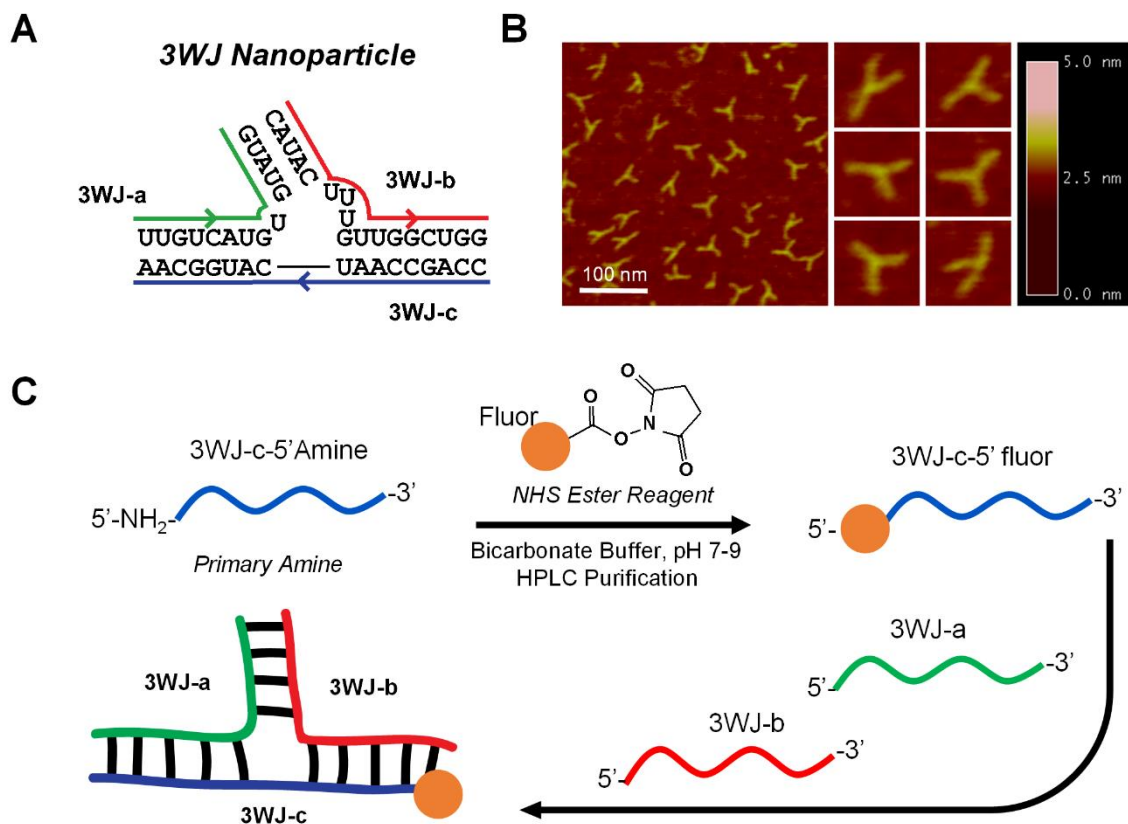


Figure 3.6. 3WJ Introduction and Dye Conjugation. (A) pRNA-3WJ secondary structure and sequences. (B) Atomic force microscopy images of pRNA-3WJ with 60 base pair extensions from each helix to show overall shape. (C) Reaction and assembly scheme of fluorescently labeled 3WJ nanoparticles.

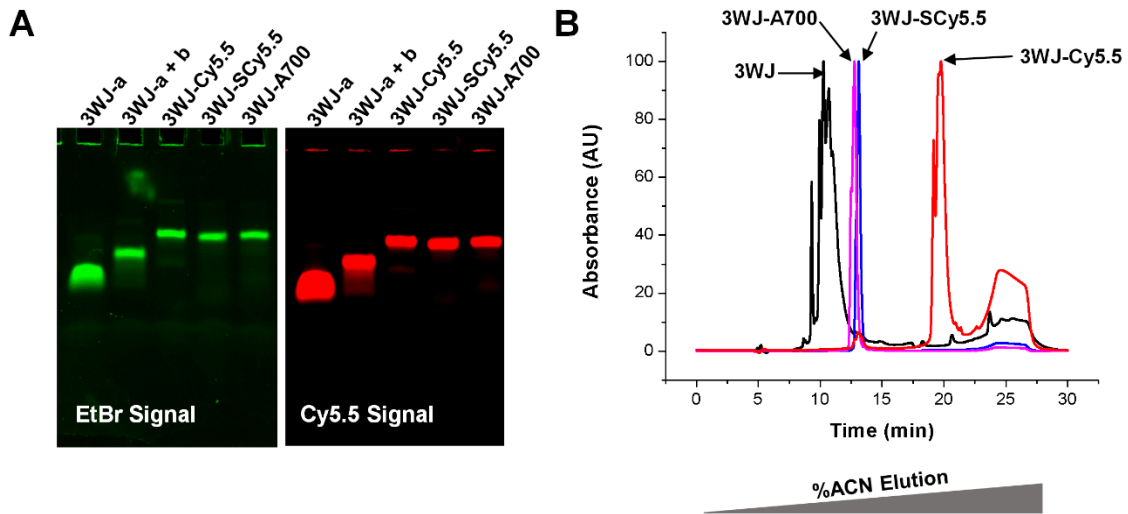


Figure 3.7. 3WJ Assembly and HPLC Analysis. (A) Native PAGE assembly gels of fluorescently labeled 3WJ nanoparticles. (B) IPRP-HPLC chromatograms of fluorescently labeled nanoparticles. Demonstrates the effect of the fluorophore conjugation on hydrophobicity of the nanoparticles.

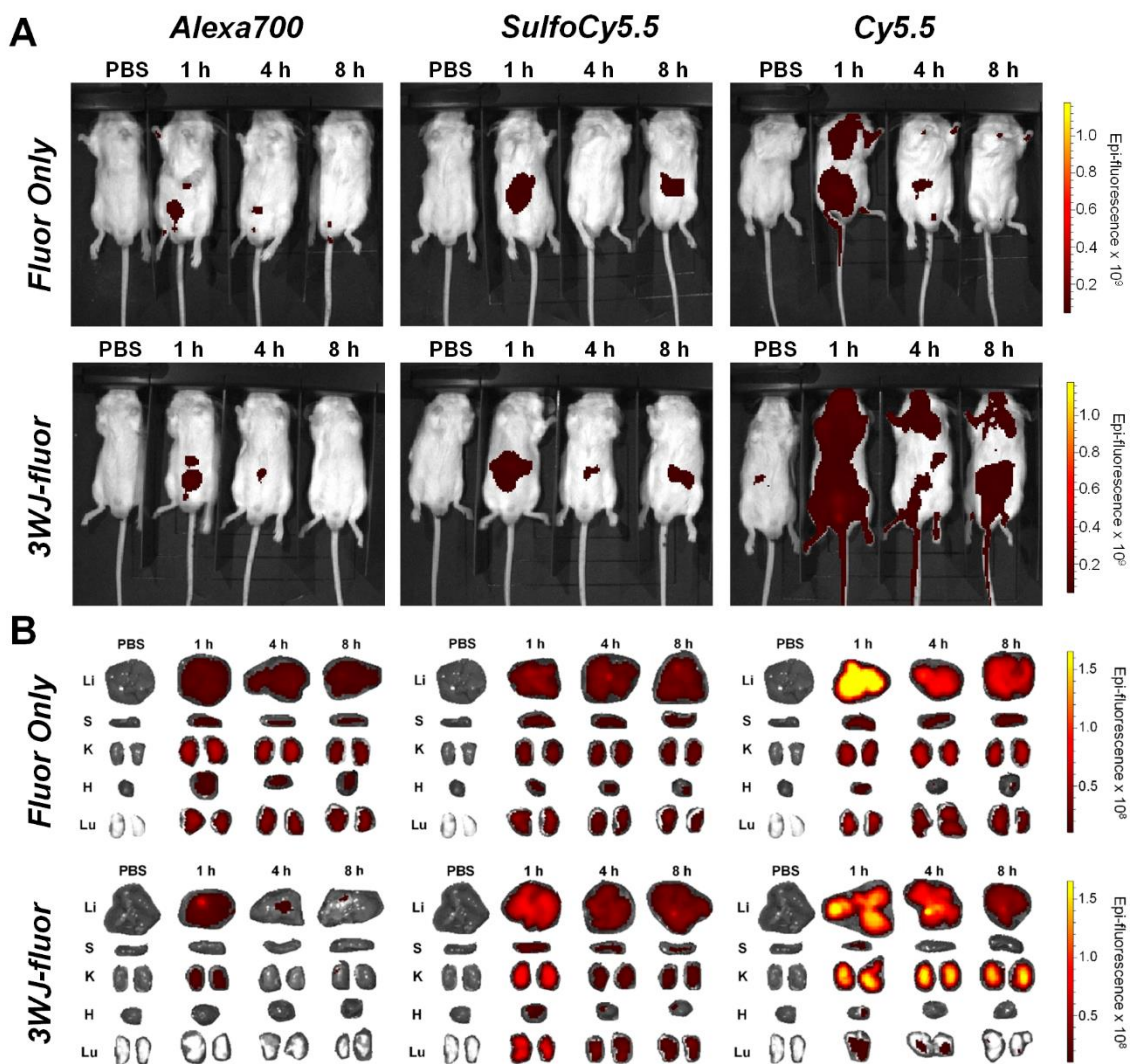


Figure 3.8. Biodistribution in Mice. (A) Whole body fluorescent images of mice IV injected with C5.5, SC5.5, A700, 3WJ-C5.5, 3WJ-SC5.5, and 3WJ-A700. Mice were scanned after 1, 4, and 8 h of circulation. (B) Fluorescent scans of organs.

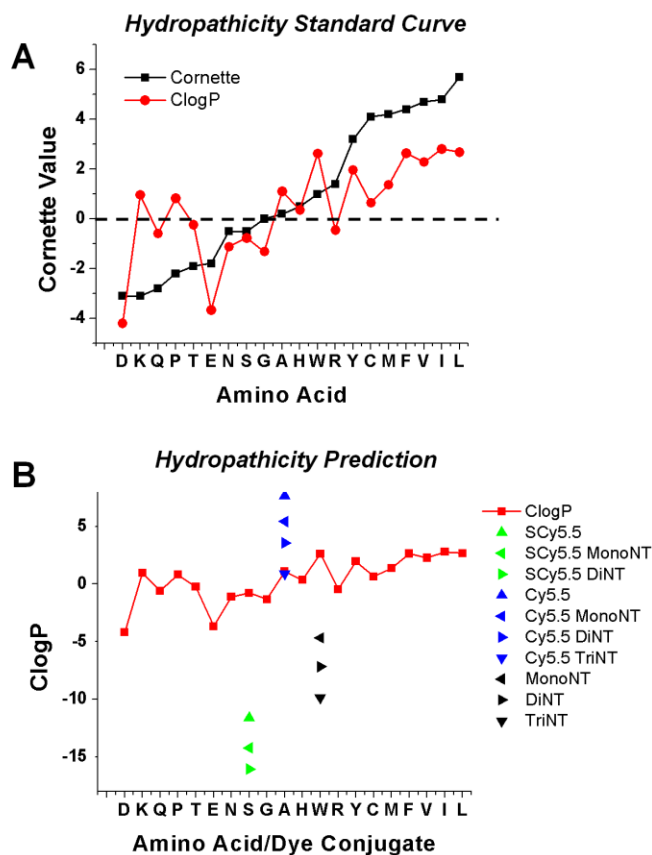
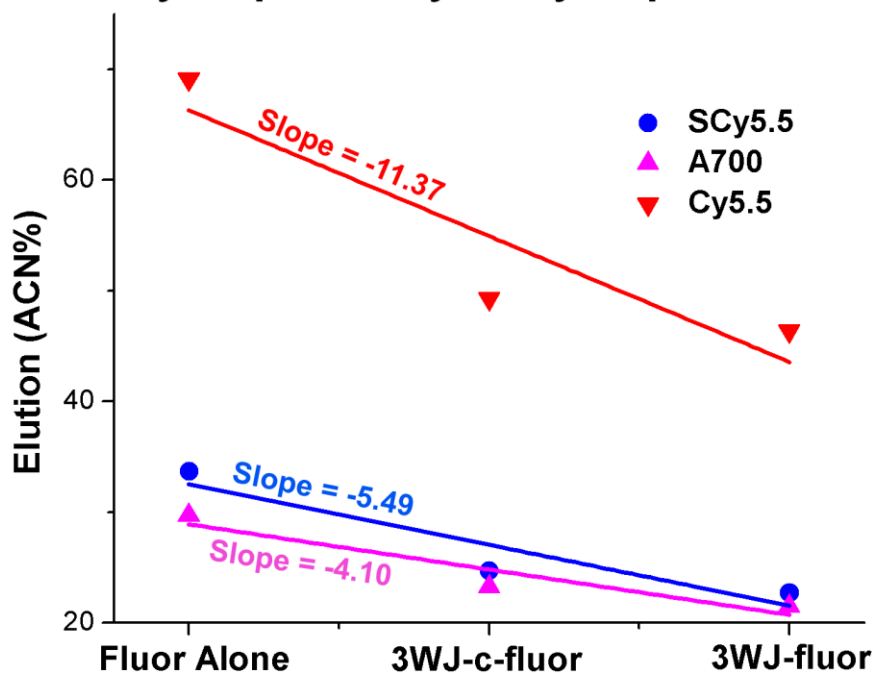


Figure 3.9. Hydrophobicity Comparison. (A) Plots of Cornette hydrophobicity scale values along with predicted ClogP values of the amino acids. A strong correlation is seen between the previously determined Cornette hydrophobicity scale and predicted ClogP values of the amino acids. The dotted line is a value of zero. (B) ClogP values were predicted for SulfoCy5.5 and their mono- and di-nucleotide derivatives (green), Cy5.5 and their mono- and di-nucleotide derivatives (blue), and mono-, di-, and tri-nucleotides (black).

Hydrophobicity of Dye Species



Hydrophobicity of Dye Species			
	Slope	Standard Error	R-Squared
Cy5.5	-11.37	4.88	0.69
SCy5.5	-5.49	2.01	0.76
A700	-4.10	1.34	0.81

Figure 3.10. RNA nanoparticles solubilize hydrophobic ligands. Each colored line represents a different fluorophore: SulfoCy5.5 (blue), AlexaFluor700 (pink), and Cy5.5 (red). Three species of each fluorophore were plotted: fluorophore alone, 3WJ-c-fluorophore, and 3WJ-fluorophore. A decreasing %ACN elution is seen as more nucleotides are added. Linear fitting was performed for each fluorophore. A more negative slope is seen for Cy5.5, indicating the RNA nanoparticle can help to solubilize the hydrophobic ligand.

Chapter 4: Development of Three-Dimensional RNA Nanocages with Novel Small Molecule Encapsulation and Release Mechanism

Chapter 4 was reproduced (with some modification) with permission from Khisamutdinov, EF*; Jasinski, DL*; Li, H; Zhang, K; Chiu, W; and Guo, P. “Fabrication of RNA 3D Nanoprisms for Loading and Protection of Small RNAs and Model Drugs.” *Advanced Materials*, 2016. 28(45), 9996-20004. DOI: 10.1002/adma.201603180. Copyright 2016 Wiley Publishing.

Special thanks to: Dr. Emil F. Khisamutdinov for help in preparation of data for these figures; and to Dr. Luda S. Shlyakhtenko and Dr. Yuri Lyubchenko for AFM images in figures 4.2; and to Dr. Kaiming Zhang and Dr. Wah Chiu for cryo-em images and reconstructions in figure 4.2; and to Dr. Hui Li for cell data and confocal images in figure 4.8.

INTRODUCTION:

In RNA Nanotechnology, canonical Watson-Crick pairs combined with non-canonical base pair interactions create a large variety of RNA structural building blocks or motifs such as multi-way junctions (55,68,73,90,109), kissing loops (12,100,101,162,241,241,241,242), and sticky ends (104,104,126) that have been utilized to create two-dimensional (2D) RNA structures (243). Combining diverse RNA connectivity into one nanostructure imparts complexity and allows for the addition of a third dimension in nanoparticle design. As a result, three-dimensional (3D) RNA nanoarchitectures have been explored (116,117,124,244). 3D nanostructures are of

particular interest as they hold tremendous potential for the encapsulation of small molecule drugs and therapeutic RNAs. Importantly, encapsulation may hold the distinct ability for controlled release of therapeutic modalities. Previously reported 3D DNA cages such as tetrahedrons, cubes, icosahedrons, and triangular prisms have been used as nanocontainers to hold proteins (245,246), gold nanoparticles (247,248), as well as organic molecules (249). Although construction of 3D RNA nanocages has been previously reported, their potential to encapsulate small reporter molecules, drugs, and proteins is yet to be realized.

RNA aptamers are important candidates for therapeutic and diagnostic applications as they display high affinity and specificity for their target molecules. Binding of malachite green (MG), a triphenylmethane dye, to its respective RNA aptamer, the malachite green aptamer (MGA), causes a drastic increase in MG fluorescence (212,250). This fluorophore/RNA complex has been widely utilized as a marker in the construction of functional RNA nanoparticles (108,124,126,152,201,251). However, the application of MGA *in vivo* is limited due to RNA specific exo- and endonucleases inside cells. To prevent this, ribose ring modification at 2'-C/U in RNA is a common strategy to enhance RNA's nuclease resistance (160). However, due to either structural hindrance or redistribution of the nearest neighbor landscape, 2' ribose sugar or other chemical modifications can hamper the activities of aptamers selected with native RNA libraries. For example, 2'-fluorine (2'F) modification to the MGA eliminates binding of the fluorophore (201). Protection of RNA aptamers would be beneficial as their lifetimes could be significantly increased, thereby increasing their utility *in vivo*. One possibility to extend their lifetimes is encapsulation inside nuclease resistant nanocages.

One advancement utilized for constructing RNA architectures was the finding of an unusually thermostable three-way junction (3WJ) derived from the pRNA of bacteriophage phi29 DNA packaging motor (55). The 3WJ can be used as a vehicle to integrate multiple functional RNA modules into one nanoparticle while retaining folding and function *in vivo* (12,55). Utilizing the crystal structure of the 3WJ (168), various RNA nanoparticles including triangles, squares, and pentagons were constructed (252). Upon systemic injection in mice, the RNA nanoparticles bind to xenograft and metastatic cells specifically and strongly with little or no accumulation in the liver or other healthy organs (253).

Herein, we describe a strategy to fabricate 3D RNA nanocages resembling triangular prisms based on pRNA 3WJ. Importantly, this 3D nanoparticle was used to demonstrate encapsulation of a small fluorescent dye, MG, while increasing its fluorescence half-life in an RNA unfriendly environment. The modularity of the triangular nanoprism design also allowed single strand oligonucleotide-drug conjugates to be positioned precisely inside the inner cavity of the RNA complex. The functional properties of the RNA nanocage to simultaneously carry 5 folate ligands for cell targeting were further evaluated *in vitro*. This work paves the way towards the application of RNA based nanocaging as a delivery system for small reporter or therapeutic molecules.

MATERIALS AND METHODS:

RNA sequence design and 3D modeling

RNA sequences were optimized using RNA 2D folding software Mfold (www.mfold.bioinfo.rpi.edu) prior to synthesis. Computer models of the RNA prism were assembled from two copies previously constructed RNA triangles (126). The vertices of

the triangles were assembled by overlapping helical domains of the triangular "arms" to position them at the correct angle and distance using the 'autofit' tool in Swiss-PDB Viewer (www.spdbv.vital-it.ch) and manual adjustment. The detailed procedure for the triangle design can be found in our previous reports (126). Each triangle vertex contains a 21 nt ssRNA tethered to the 3'-end using a poly-uracil (poly-U) linker. The poly-U is inserted to provide a hinge allowing for the flexibility of the ssRNA when hybridized with its complementary sequence of another triangle. The resulting 21 bp RNA duplexes were chosen to have similar lowest free-energy secondary structures (calculated $\Delta G = -39.0 \pm 2.0$ kcal/mol). The sequence of the RNA MGA module was extracted from the PDB databank (www.pdb.org), PDB ID: 1F1T (212). Detailed 2D structures and sequence of the nanoprisms as well as synthetic oligonucleotides containing conjugates are provided in Tables A.3.1, A.3.2, and A.3.3.

RNA synthesis, purification and assembly

Templates for RNA transcription were prepared by standard protocols described in detail elsewhere (105). Briefly, PCR was used to prepare transcription templates using PCR reaction kit (Promega Corporation, GoTaq® FlexiDNA Polymerase) for the amplification of DNA primers (IDT). Following purification of DNA templates on spin columns (QIAGEN), the RNA strands or 2'-F-U/C modified RNA strands were transcribed using home-made T7 RNA polymerase. The RNA was precipitated with cold ethanol, then the pellets dried and resuspended in ddH₂O. Homogeneity of individual RNA strands is checked by denaturing 10% PAGE. For assembly assays, equimolar RNA strands (0.5 μ M each) were mixed in 1 X TMS buffer. The RNA mixture was heated to 80 °C for 5 min and slowly cooled to 4 °C over one hour in a thermocycler. RNA assembly products were

checked on native 6% or 7% PAGE (29:1 acrylamide: bis-acrylamide ratio) in 1 X TBM running buffer. All native PAGE experiments were run at 4°C at constant 90 V for 2 hours. Gels were stained in Ethidium Bromide buffer for total RNA strand visualization or in MG binding buffer (20 μ M MG dye, 10 mM HEPES pH = 7.4, 100 mM KCl, 5mM MgCl₂) for detection of MG aptamer signal as previously reported (103).

Cryo-electron microscopy

2 μ l of RNA triangular prism nanoparticle solution (1 mg/ml) was applied onto a glow-discharged 200-mesh R1.2/1.3 Quantifoil grid. The grids were blotted for 3 s and rapidly frozen in liquid ethane using a Vitrobot Mark IV (FEI). Then the grids were transferred to JEM2200FS cryo-electron microscope (JEOL) operated at 200 kV with in-column filter for screening. Micrographs of 10 nm RNA prism were recorded with a direct detection device (DDD) (DE-20 4k \times 5k camera, Direct Electron, LP) operating in movie mode at a recording rate of 25 raw frames per second at 25,000 \times microscope magnification (corresponding to a calibrated sampling of 2.51 \AA per pixel) and a dose rate of \sim 20 electrons per second per \AA^2 with a total exposure time of 3 s. Micrographs of 5 nm RNA prism were recorded with a 4k \times 4k CCD (Gatan) at 80,000 \times microscope magnification (corresponding to a calibrated sampling of 1.36 \AA per pixel) and a dose rate of \sim 20 electrons per second per \AA^2 with a total exposure time of 3 s. A total 52 images of 10 nm RNA prism and 30 images of 5 nm RNA prism were collected with a defocus range of 2~4 μ m.

Single particle image processing and 3D reconstruction

The image processing software package EMAN2 was used for the micrograph evaluation, particle picking, CTF correction, 2-D reference-free class averaging, initial

model building and 3-D refinement of the cryo-electron microscopy data. We boxed total 2340 particles for 10 nm RNA prism and 2206 particles for 5 nm RNA prism to generate the 2D class averages for building the initial models. Finally, 1514 particles for the 10 nm RNA prism and 1648 particles for the 5 nm RNA prism were used for final refinement, applying the D3 symmetry. The resolution for the final maps was estimated by the 0.143 criterion of FSC curve without any mask. 25 Å and 22 Å Gauss low-pass filter were applied to the final 3D maps displayed in the Chimera software package.

AFM images

For all samples, specially modified mica surfaces (APS mica) were used. The APS mica was obtained by incubation of freshly cleaved mica in 167nM 1-(3-aminopropyl) silatrane following previously reported protocol (171). The RNA samples were diluted with 1 × TMS buffer to a final concentration of 3 - 5 nM. Then, 5-10 µL was immediately deposited on APS mica. After 2min incubation on the surface, excess samples were washed with DEPC treated water and dried under a flow of Argon gas. AFM images in air were acquired using MultiMode AFM NanoScope IV system (Veeco/Digital Instruments, Santa Barbara, CA) operating in tapping mode.

Dynamic light scattering

The hydrodynamic diameter of the RNA nanoprisms was determined at a concentration of 10 µM in 50 µL TMS buffer using a Zetasizer nano-ZS (Malvern Instrument, LTD) at 25°C.

Prism MG degradation assay

The function of the MGA within the triangular prism nanoparticles was assayed by mixing the RNA complex at a concentration of 0.1 µM with 1µM MG dye in 1X TMS

buffer. The solutions were allowed to equilibrate at room temperature for 10 minutes. The fluorescence emission spectrum (recorded from 630 – 750 nm) of the complexes was measured using a fluorospectrophotometer (Horiba Jobin Yvon) with an excitation wavelength positioned at 615 nm. 1 μL of 500 U/μL RNase T1 (Thermo Scientific) was added to 99 μL of the above RNA-MG complex directly in a fluorometer cuvette. Fluorescence at $\lambda_{\text{max}} = 650$ nm was immediately recorded and monitored every 1 sec for a total time of 3600 sec. Fluorescence life time measurements were performed by the software integrated within the fluorometer. The obtained data were fit using exponential decay function $I(t) = I_0 e^{(-t/\tau)}$, where I_0 is the initial intensity (at time zero) and τ is the mean life time defined as the time for the intensity to drop by $1/e$ or to ~37%. All fluorescence decay experiments were conducted in triplicate with indication of \pm for mean standard error (SEM).

RESULTS AND DISCUSSION:

Computer-aided rational design and fabrication of 3D RNA nanoprism from planar pRNA 3WJ geometry

The triangular nanoprism was designed employing the structural information of pRNA 3WJ following a bottom-up approach (90). As such, two helices of three adjacently arranged 3WJs were connected with duplex RNA to form flat triangular nanoparticles, a nanoparticle construction method devised previously (126). To extend 2D triangle particles into a 3D RNA complex, two triangular nanoparticles (T1 and T2) containing 21 nucleotide (nt) single stranded (ss) complementary linker (L) regions on each vertex were tethered (**Fig 4.1A, Fig A.3.1**). Each ssL region was designed to interact specifically with its complement strands L1-L1', L2-L2', L3-L3' forming RNA-RNA duplex of 21 bp. To

provide structural flexibility and allow the linkers to bend to a 90° angle necessary for triangular prism complex, poly uracils (poly-U_s) were embedded between the ssL and triangle vertices. This resulted in the formation of a "face-to-face" dimer with a total of 8 RNA strands. The overall geometry was manually computed using SwissPDB Viewer software (254), the structure resembling triangular prism geometry with the pRNA 3WJ motif at the corners. The 3D RNA model displays a size of ~11 nm, measured from one vertex to an adjacent vertex, and a size of ~10 nm measured from one vertex to its nearest edge, as measured by the modeling software (**Fig 4.1B**). The largest diameter of the inner cavity of the prism was measured to be ~7 nm while the height was ~ 6 nm. Based on these dimensions, we assume that the central cavity of the prism could accommodate a spherical object of approximately 6 nm in diameter.

Assembly efficiency of the RNA strands into the desired conformation was first assayed by 6% native polyacrylamide gel electrophoresis (PAGE). Upon addition of each of eight component strands, a step-wise decrease in electrophoretic migration can be clearly seen, indicating association of each complimentary ssRNA oligomer into the complex RNA structure (**Fig 4.2A**). The distinct band in lane 7 indicates the formation of a stable RNA complex containing all 8 RNA strands. Integration of the intensity of gel bands results in an estimated assembly yield of $43.0 \pm 3.1\%$. A large fraction of RNA aggregates are localized in the top of lane 7. Presumably, this is due to non-specific interactions between the 21nt RNA single stranded sticky ends. Interestingly, the RNA complex with no D and d' stands has much a higher assembly efficiency with estimated yield of 90% (**Fig 4.2A, Lane 6**).

DLS was utilized to measure the apparent dimensions of the purified RNA prism. As measured by DLS, the hydrodynamic diameter of the RNA complex is 11.5 ± 1.6 nm, consistent with the 3D model structure of the nanoprism (**Fig 4.2B**). AFM imaging of the pure RNA complex revealed that the particles do in fact display prismatic-like architecture (**Fig 4.2C**). AFM is 2D observation of the 3D RNA prism and cannot be used to conclusively indicate the formation of the triangular prism geometry, nevertheless, the particles do resemble the designed triangular prism in two dimensional projections.

Cryo-EM imaging studies revealed triangular prism geometry

To address the concern whether the folding of 8 RNA stands resulted in 3D geometry, the purified RNA complex was visualized by single-particle cryo-electron microscopy (cryo-EM) (**Fig 4.2D, E**). Cryo-electron microscopy is a useful method to show the true 3D nature of the RNA nanoprisms, as AFM analysis causes distortion of 3D nanoparticles imaged in 2D (255). The 3D reconstruction of the RNA nanoparticles was achieved implementing single-particle reconstruction using the EMAN2 approach as described in the methods section. Reconstruction of the 3D structure of the RNA complex were determined at a resolution of 2.5 nm (10 nm RNA prism) and 2.2 nm (5nm RNA prism), and demonstrated that the RNA particles have average sizes of 10 nm and 5nm, respectively, in agreement with DLS and AFM results. More importantly, the overall geometry is similar to computer modeled 3D RNA prisms. It is important to note that the reconstruction of the RNA prism by Cryo-EM clearly demonstrates the presence of an inner cavity. Collectively, the data from native PAGE, DLS, AFM, and Cryo-EM clearly indicate the formation of closed and compact RNA nanoprisms.

Design and construction of RNA aptamer encapsulated nanoparticle

The MGA is a commonly used tool in biochemistry for structure-function verification (50,103,153). This is attributed to its unique properties as free MG dye in solution displays little to no fluorescent signal, yet when bound to MGA the photoemission increases more than 2000-fold (211,256). However, fluorescence can only occur if the RNA MGA folds into its authentic 3D conformation. Previous attempts to achieve fluorescence using 2'F modified RNA bases resulted in little to no fluorescence (201). Therefore, for RNA MGA to remain a useful tool within a cellular environment, it must be placed into a container that will protect the RNA. This is a common problem among many small RNAs and small molecule drugs with therapeutic utility. Using 2'F modified RNA to construct the prism's frame (2'-fluoro uridine (2'F-U) and 2'-fluoro cytosine (2'F-C)), which are known to display resistance to a degrading environment (150), we hypothesize that the RNA MGA will be protected when positioned inside the 2'F modified nanocage.

As a proof-of-principle, we employed the MGA RNA sequence by embedding it within the "D" and "d'" strands at their 3' ends. Throughout this chapter, we refer to the stable RNA complex formed by six 2'F modified RNA strands without D or d' strands as a "frame". It was interesting to find that this complex is highly stable with apparent melting temperature (T_M) of 74 °C, with the assembly efficiency being Mg^{2+} dependent (**Fig A.3.2**).

Using SwissPDB Viewer, we first modeled the complex structure of the RNA nanocage with encapsulated MGA by positioning the 3D structure of the MGA inside the inner cavity formed by the Nanoprism. This allowed us to estimate the distance constraint in base pairs required to mount the RNA MGA (extracted from PDB ID: 1F1T (212)) into the inner cavity of the prism. The complexation of the RNA MGA within the nanocage was evaluated on native PAGE (**Fig 4.3**). The apparent gel shift of the band localized in

lane 4 (2'F-RNA frame with MGA) compared to lane 1 (2'F-RNA frame only) shows complexation of the MGA sequences with the frame structure detected by total RNA stain with Ethidium Bromide (EB). Staining of the same gel in the presence of MG dye resulted in strong fluorescence emission from the distinct band on lane 4, indicating correct folding of the RNA MGA (**Fig 4.3**). We performed additional control experiments based on migration properties of the closed (compact) and open (relaxed) 3D RNA complexes as it is generally accepted that more compact RNA structures migrate faster in comparison to relaxed RNA conformations. To fabricate the open 3D prism conformation, the interaction of one of the complementary sticky ends linking two RNA triangles together were intentionally disrupted through sequence design. Comparing migration of the open RNA prism to the closed version revealed slight differences in migration distance (**Fig 4.3: Lanes 4 and 5, Fig A.3.3**). This indicates that the prism is closed and that the MGA was located, presumably, within the inner cavity of the nanocage. Data obtained from the mobility shift assay alone do not provide a concrete conclusion whether the RNA MGA formed inside of the closed cage; additional data supporting our assumption comes from RNase T1 cleavage experiments as described below.

RNase T1 protection assay confirmed the encapsulation of the MG RNA aptamer by the nanocage

Encapsulation of an RNA module inside the negatively charged RNA nanoprism is challenging due to the repulsion forces caused by the negatively charged phosphodiester backbone of both the inner cavity of the RNA cage and the RNA MGA. Development of a method to overcome this challenge would be exceptionally beneficial as the activity of functional RNA modules could be retained by protecting them from enzymatic degradation

in vivo. To further confirm that the RNA MGA was localized inside the cavity of the nanocage, we treated the RNA complex with endonuclease RNase T1, which specifically cleaves unpaired guanosine (Gs) nucleotides (257). While the single stranded Gs are absent from the 2'F-RNA prismoidal construct, there are several ss Gs present in the RNA MGA itself that are essential for MG binding. Thus, we hypothesize that RNase T1 will cleave the exposed Gs of the MGA sequence resulting in the loss of fluorescence. However, if the cage were to restrict RNase T1 access to the MG aptamer within the nanoprism, fluorescence emission would be retained or decay at a slower rate.

According to the modeled 3D structure of the prism, the estimated average dimensions of the inner cavity of the prism could accommodate a spherical object of about 6 nm. The average size of the RNase T1 structure was measured (PDB ID: 1YGW) to be 3.7 nm in diameter (258) (**Fig 4.4**) allowing RNase T1 to easily access the inner cavity and quench the fluorescence of the MGA. To address this obstacle, a nanoprism having a smaller cavity size of 3 nm was designed by decreasing the length of the RNA prism helical regions by one half. The schematic design of the experiment is summarized in Figure 4.5B. The smaller prism is expected to insulate the MGA from RNase T1 cleavage, thus extending fluorescence activity.

The assembly of the small prism is highly efficient, and RNA MGA is functional according to native PAGE analysis (**Fig 4.5C: Lanes 1 and 2**). Next, we carried out time-dependent MG fluorescence decay in the presence of RNase T1 to test the activity of the MGA embedded inside the large and small nanoprisms. Figure 4.5D shows the fluorescence decay profiles of the large (black squares) and small (red circles) nanoprisms. The calculated lifetimes (τ) were found to be 445.5 sec and 781.4 seconds (s) for the large

and small nanoprisms respectively. The small prism displayed a half-life almost double that of the large prism, suggesting that RNase T1 has limited access to MGA encapsulated inside of the small nanoprism. Complete protection against RNase T1 has not been observed presumably due to the dynamic nature of the interacting linker arms of two triangles. This is also supported by AFM images where fractions of prisms are in an open state, which allows RNase T1 to digest the MGA. Notably, fluorescence emission of the small prism was still observed after 1 hour of incubation with RNase T1 while fluorescence in the large prism was negligible (**Fig 4.5E**). Additional control experiments were performed using a variety of other RNA control complexes containing RNA MGA. The calculated values of τ are summarized in Table 4.1. Mean lifetime comparison of the small RNA prism to the controls demonstrates that no control construct has greater τ than the small prism. Thus, the RNase T1 cleavage assay indicates the successful encapsulation of MGA encapsulated in both the small and large nanocages. More importantly, we have shown that by tuning the size of the inner cavity, fluorescence half-life can be significantly increased. This is synonymous with increasing the release time of a drug that can be potentially used an *in vivo* system.

Encapsulation of oligonucleotide-drug conjugates inside the nanocage

Taking advantage of the programmability of the D and d' prism strands, we next demonstrated the encapsulation of single stranded oligodeoxynucleotides (ssODN) containing functional moieties such as fluorescence reporters and drugs. To this end, one long ssRNA was designed to connect D and d' strands through a 22 nt linker. The resulting RNA sequence will be referred as a “core” RNA strand. While the 5'- and 3'-ends of the core RNA strand interact with the triangular edges of the prism, its single stranded middle

region is designed to localize inside the nanocage. The portion of the core strand inside the prism was utilized for encapsulation of either ssDNA or ssRNA carrying different functional groups *via* base pair hybridizations (**Fig 4.6A**). Hence, we anticipate that the encapsulation of the functional moieties will prevent them from enzymatic degradation and increase their cellular life-time. Alternatively, this principle can be applied as a safety mechanism. For instance, carrying highly toxic compounds that should be released only upon reaching its target.

Due to the programmable nature of the RNA prism, the size of the nano-container can be adjusted by simply increasing or decreasing the sides of the prism by complete helical turns as shown previously (150,228). This is advantageous as the capacity of the RNA nano-container can be controlled enabling encapsulation of diverse size biomolecules or inorganic nanoparticles, as well as increase the payload of a single nano-container for increased detection sensitivity and increased efficacy in the treatment of disease. Moreover, from a medical point of view, size alternation of the nano-prism imparts differences in toxicity, cellular binding and internalization, renal clearance, physicochemical features, as well as pharmacokinetic and biodistribution profiles. As such, the prismoidal nano-container provides a unique system to further exploit these factors.

The principle behind chemical drug encapsulation relies on the conjugation of a drug at the 3'/5'-end or at both ends of DNA /RNA oligonucleotides, followed by hybridization of this conjugate inside the cavity of the RNA nanoprism. To demonstrate this in practice, short DNA sequences (22nt) labeled at the 5'-end with different chemicals including folic acid (FA), cyclodextrin, taxol, Cy5 fluorophore, and biotin. To verify the formation of the RNA nanoparticle with the conjugated DNA sequence, prism strands and

corresponding DNA oligonucleotides were assembled in one-pot by mixing at equimolar concentrations, followed by native PAGE analysis (**Fig 4.6B**). Formation of distinct bands corresponding to the frame structure and frame containing the core RNA sequence are shown in Figure 4.6, lanes 1 and 2, respectively. The additional lanes correspond to loaded nanocage with the 22nt DNA containing a variety of small molecules. Based on the slower rate and almost identical distance of all five loaded cargoes as compared to the bands in lanes 1 and 2, we can conclude that the conjugated ssDNA were successfully hybridized inside the nanocage structure. Additionally, co-migration of Cy5 and EB signal of Cy5 loaded nanocage indicates correct assembly.

To demonstrate incorporation and function of the DNA-biotin conjugate within the RNA 3D cage, biotin-streptavidin binding was utilized (259) (**Fig 4.6C**). To separately visualize the biotin-nanoprism and the streptavidin, the DNA-biotin conjugate was tagged with Cy5 and the streptavidin with Cy3. The ensuing gel shift assay demonstrated complexation between the encapsulated biotin and streptavidin as the complex migrates much slower than the biotin-nanoprism or streptavidin alone (**Fig 4.6C: Lane 1 vs Lane 2 and 5**). Co-localization of EB (RNA), Cy3 (streptavidin), and Cy5 (DNA-biotin) signals in the distinct band in lane 1 reveals the functional properties of the encapsulated molecule (**Fig 4.6C**). Although PAGE results cannot directly confirm whether the functionalities were located inside the nanocage, results based on computer modeling and fluorescence functional assays are a strong indication of the encapsulation mechanism. Utilizing the programmability of RNA D and d' strands as well as modularity of the ssDNA-drug conjugates we were able to demonstrate feasibility of the encapsulation approach, in addition to RNA MGA aptamer encapsulation, for caging of small molecules and proteins.

Varying RNA Chemical Modifications Allows Control over Nanoprism Serum Stability and Drug Release

One potential advantage of RNA 3D nanocontainers is the ability to safely deliver and release encapsulated drugs in a fine-tunable fashion. Development of controlled release is extremely challenging yet highly desirable in RNA nanotechnology (90). To release the encapsulated drug(s), one approach is to use the help of naturally occurring nucleases to break down RNA 3D nanoscaffold. It was our hypothesis that changing the percentage of 2'F nucleotides in the nanoprism scaffold would result in diverse degradation profiles. To change the amount of 2'F nucleotides in the nanoprisms, the ratio of 2'F cytidine triphosphate (CTP) and uridine triphosphate (UTP) nucleotides to unmodified CTP and UTP were adjusted during *in vitro* transcription reactions to 4:0, 3:1, 2:2, 1:3, and 0:4, respectively. After transcription and purification, five different nanoprisms were assembled with 2'F-C/U modifications of approximately 100%, 75%, 50%, 25%, and 0%. The degradation profiles of each nanoprism were observed over the course of one hour in 2% fetal bovine serum (FBS) solution at a final concentration of 200 nM and analyzed on 3% agarose gel (**Fig 4.7A**). Gel band intensity was integrated using ImageJ software and intensity at each time point was compared to initial gel band intensity for each individual nanoprism (**Fig 4.7B**). As shown by the time course plot, decreasing the percentage of 2'F nucleotides increases the digestion rate of the nanoprism scaffold. This approach shows feasibility of controlled drug release by degradation of the partially 2'F modified nanocontainer, which can be fine-tuned to the scale of minutes.

In vitro cell binding studies revealed high binding affinity to cancer cells by RNA nanocage carrying ssDNA-Cy5.

The ability of the RNA nano-container to successfully bind and deliver drugs or reporter molecules into cancer cells would tremendously benefit the advancement of nanomedicine. To investigate whether the RNA nanocage can serve as a container to deliver small molecules, the 2'F RNA frame structure was decorated with 5 copies of DNA oligonucleotide-folate conjugates and 1 copy of DNA-Cy5, as shown in Figure 4.8 (**Assembly in Fig A.3.4**). Folate-containing nanoconstructs are known to have a strong affinity to cancer cells of epithelial origin as these types of cancer cells overexpress folate-binding protein receptors (260). After incubation of the folate functionalized RNA nanoprism with KB cells, strong binding of the RNA complex with the cells was observed (**Fig 4.8A**) in comparison to control complex having the same RNA 3D nanostructure but lacking folate molecules. This result demonstrates applicability of the 3D RNA system for detection and delivery of the reporter molecules.

CONCLUSIONS:

The proof-of-concept for a technique to construct 3D RNA nanocontainers to encapsulate small RNA molecules and a method for loading the nanocontainers with model drugs was demonstrated. The assembly of RNA triangular nanoprism utilizes pRNA 3WJ motifs positioned at the prism vertices, imparting stability into the system and allowing for future *in vivo* delivery. Loading the container with model drugs (MG) was accomplished *via* diffusion of the model drug into the container with subsequent immobilization by RNA receptors (MGA) pre-encapsulated within the nanoprism. The concept of RNA aptamer encapsulation is a promising platform for exploring new applications in pharmaceutical and materials science. The RNA-directed triangular prism brings together the functionality,

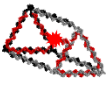

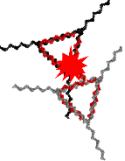


biocompatibility, and self-assembly potential with fine control of geometry, positioning, and the responsive characteristic of RNA nanoparticles.

ACKNOWLEDGMENTS:

E.F.K. and D.L.J. contributed equally to this work. This research was supported by NIH Grant Nos. R01EB019036 and U01CA151648 to P.G. The cryo-EM work was supported by NIH Grant Nos. P41GM103832 and P50 GM103297 to W.C. We would like to thank Luda Shlyakhtenko and Yuri Lyubchencko for the AFM imaging. The AFM work was supported by NIH Grant No. P01GM091743 to Yuri Lyubchencko. Service of Shared Resource Facilities was provided by University of Kentucky Markey Cancer Center NIH Grant No. P30CA177558. P.G.'s Sylvan G. Frank Endowed Chair position in Pharmaceutics and Drug Delivery is funded by the C.M. Chen Foundation. P.G. is a consultant of Oxford Nanopore, Nanobio Delivery Pharmaceutical Co., Ltd., and NanoBio RNA Technology Co. Ltd. His inventions at the University of Kentucky have been licensed to Matt Holding and Nanobio Delivery Pharmaceutical Co., Ltd. The Content is solely the responsibility of the authors and does not necessarily represent the official views of the NIH. Data repository: Cryo-EM maps of the RNA nanoprisms have been deposited to EMDDataBank (5 nm RNA nanoprism: EMD-8366, 10 nm RNA nanoprism: EMD-8365).

Table 4.1. Fluorescence half-lives of prism constructs and control constructs. ^a The analysis of the electrophoretic migration of controls 2 and 3 are shown in Figure A.3.4.

^bThe standard error of the mean was obtained from three independent experiments.

Nanoparticle type and structure					
	Triangle prism	Control 1	Control 2	Control 3	Small prism
Life time τ , sec ^b	445.5 \pm 50.0	352.3 \pm 47.8	273.2 \pm 39.3	386.5 \pm 45.6	781.4 \pm 43.0

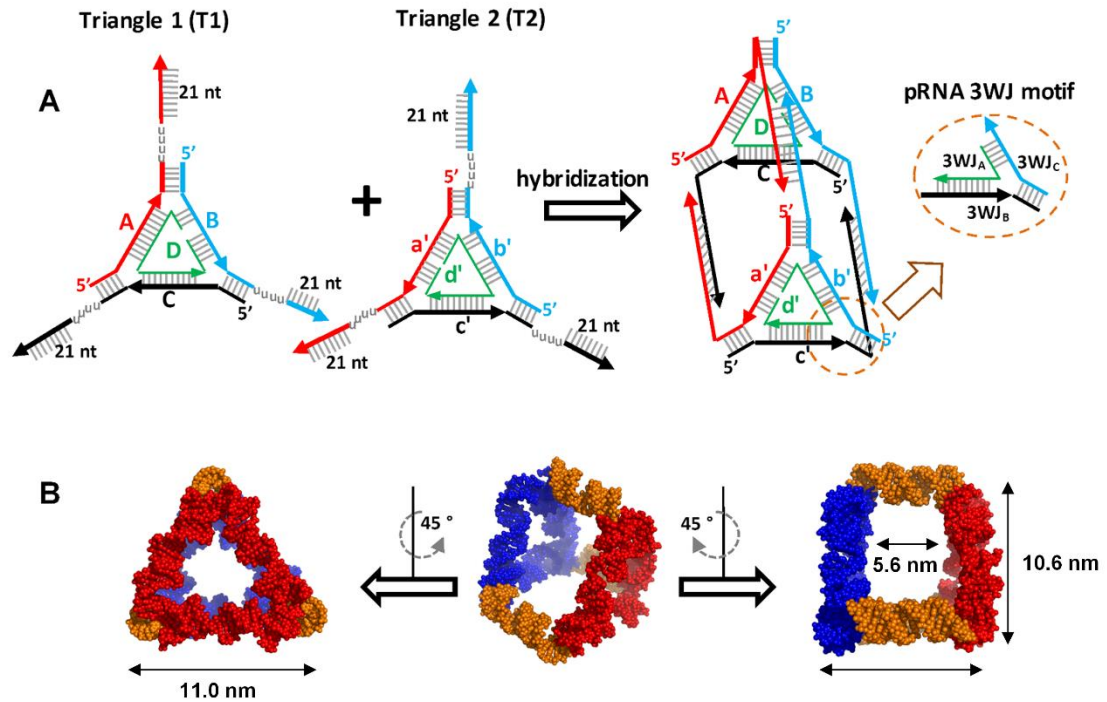


Figure 4.1. Triangular Nanoprism design and 3D model structure. (A) Fabrication of the triangle nanoprism from two planar equilateral RNA triangles. The triangle prism nanostructure forms by hybridization of the flexible 21 nt ssRNA “linkers” of each triangle. The overall prismoidal construct contains the preserved geometry of the pRNA 3WJ structural building block. (B) Computer model structure of the triangular nanoprism demonstrating its average dimension in 3D space.

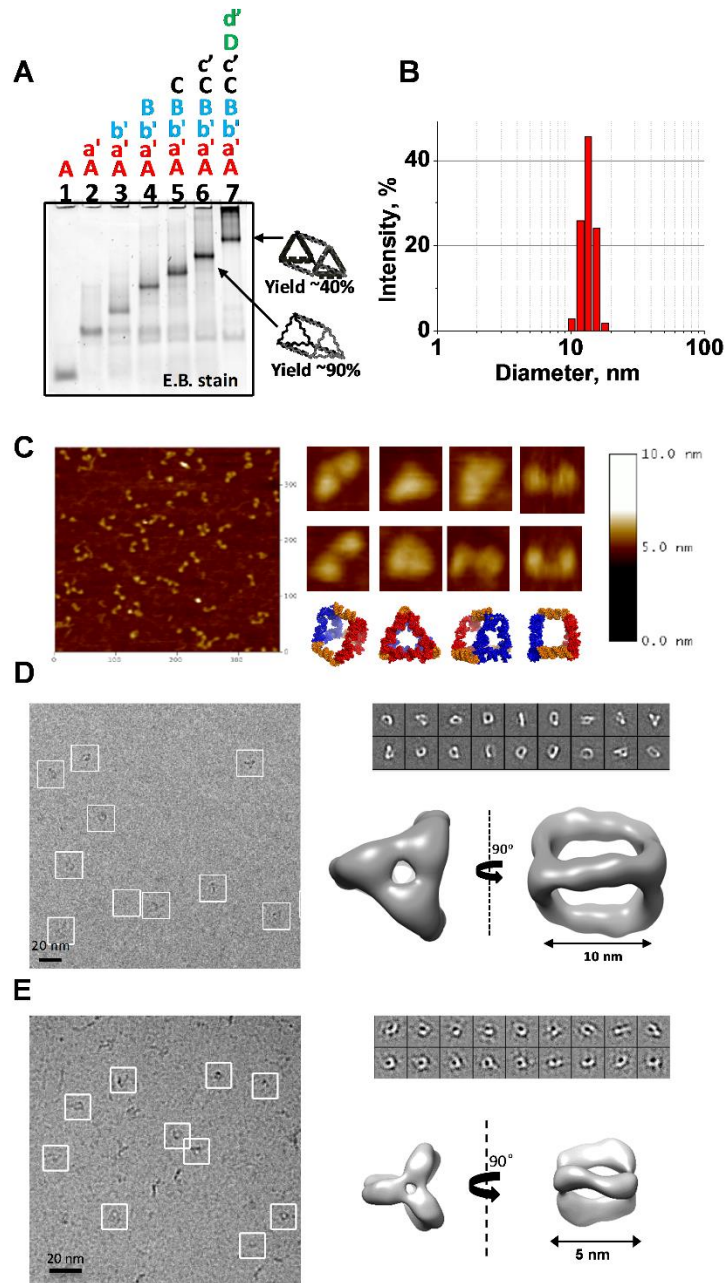


Figure 4.2. RNA Triangular nanoprism self-assembly and characterization. (A) Assembly efficiency of the RNA triangle nanoprism complex evaluated by 6% native polyacrylamide gel electrophoresis (PAGE). Step-wise association of the 8 RNA strands ($0.5 \mu\text{M}$ each) into the final complex was conducted in 1 X TMS buffer using one-pot assembly. (B) Typical dynamic light scattering (DLS) data demonstrating average

hydrodynamic diameter of the prism. **(C)** Atomic force microscopy (AFM) images of the triangle nanoprism (5 nM) taken in air. **(D)** CryoEM image of the large (10 nm) triangular RNA prism. Each white box indicates an individual RNA complex. Class averages of RNA nanoprisms as observed by cryo-EM. Reconstructed three-dimensional nanoprism at 2.5 nm resolution. **(E)** CryoEM image of the small (5 nm) triangular RNA prism. Each white box indicates an individual RNA complex. Class averages of RNA nanoprisms as observed by cryo-EM. Reconstructed three-dimensional nanoprism at 2.2 nm resolution.

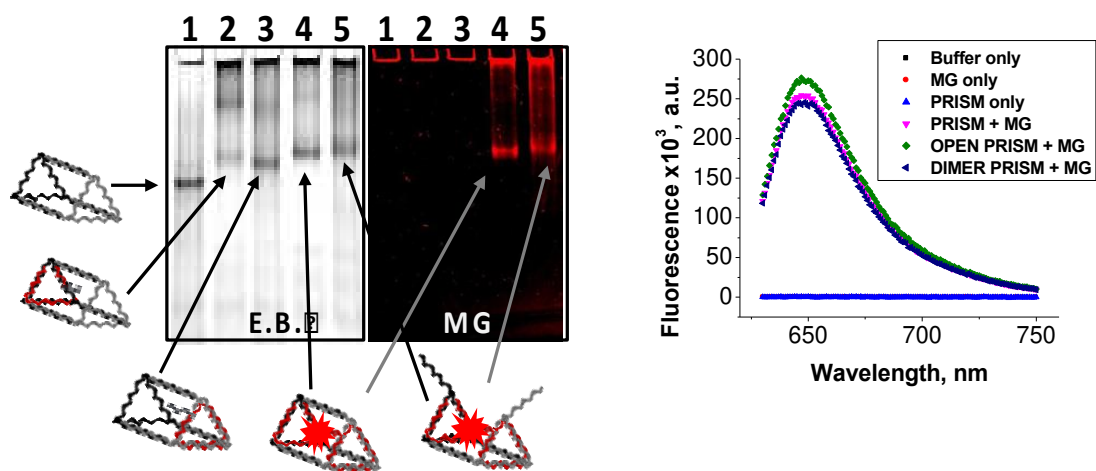


Figure 4.3. Assembly of triangular prism and MG fluorescence assay. Fluorescence emission in lane 4, and faster migration than in lane 5, indicates the formation of compact triangular nanoprisms with encapsulated MG aptamer.

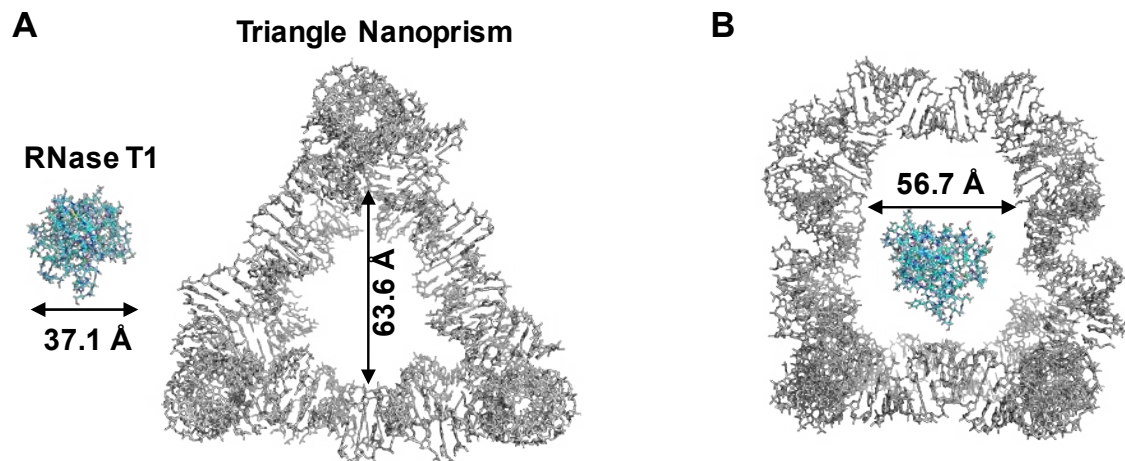


Figure 4.4. Swiss PDB viewer was used to fit RNase T1 inside the designed 3D nanoprism. The inner cavity of the large prism will fit RNase T1 inside, allowing digestion of the MG aptamer. RNase T1 cannot fit inside the small prism, enhancing the fluorescence half-life of MG.

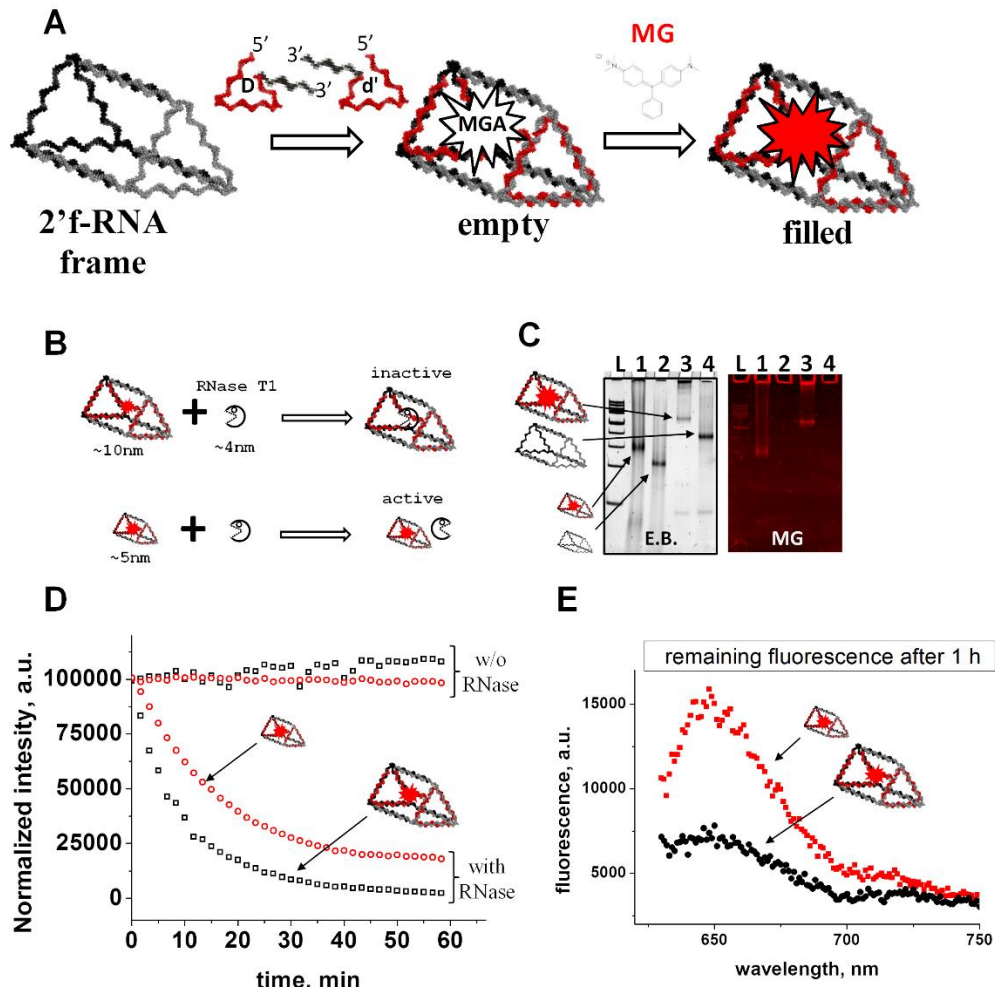
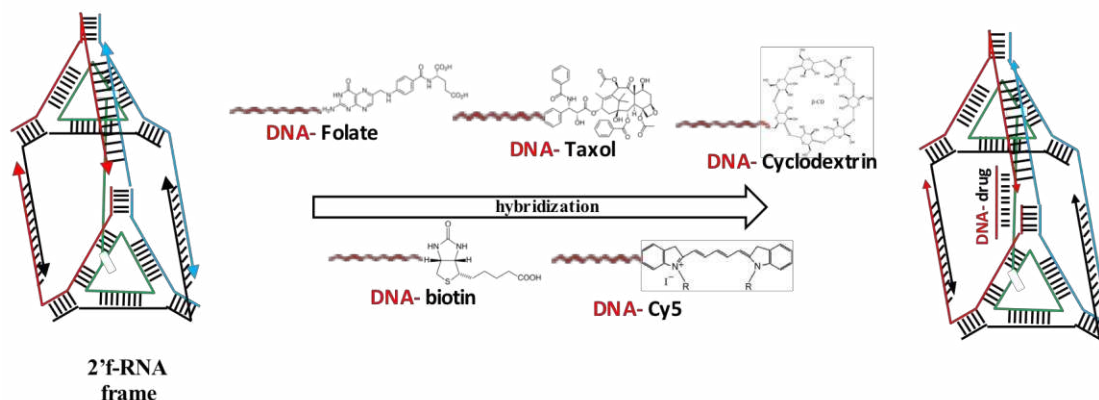


Figure 4.5. Encapsulation of the RNA MGA and fluorescence assay. (A) Schematic design approach for the RNA MGA encapsulation. The RNA MGA sequence is embedded within the 3'-end of D and d' strands. Upon hybridization MGA folds into native conformation. (B) Schematic representation of the RNase T1 protection experiment demonstrating the relative dimensions of RNase T1 and nanoprisms. (C) Assembly efficiency and relative migration of the triangle prisms on native 6% PAGE. The smaller RNA prism migrates much faster compared to the regular prism and emits fluorescence signal indicating proper folding of the functional RNA complex. Lane "L" is 100 bp DNA ladder (Thermo Scientific). (D) Time-dependent fluorescence emission profile of the 0.1

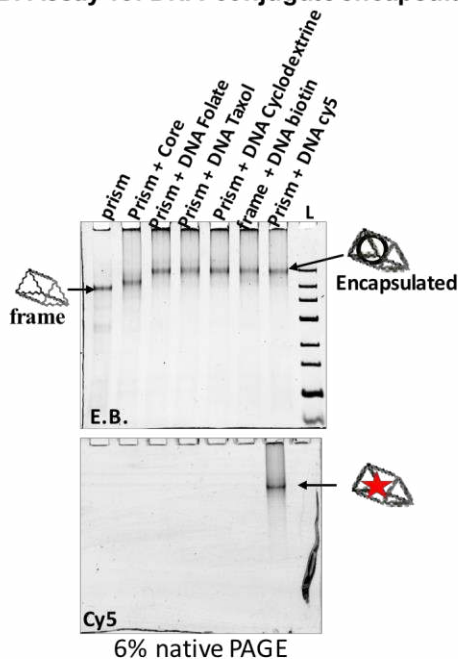
μ M RNA MGA aptamer in the presence of 500U of RNase T1 and its absence (control).

(E) The remaining fluorescence signal of the triangle prisms after one hour of RNase T1 treatment.

A. DNA-conjugates encapsulation scheme



B. Assay for DNA-conjugate encapsulation



C. Functional assay for biotin

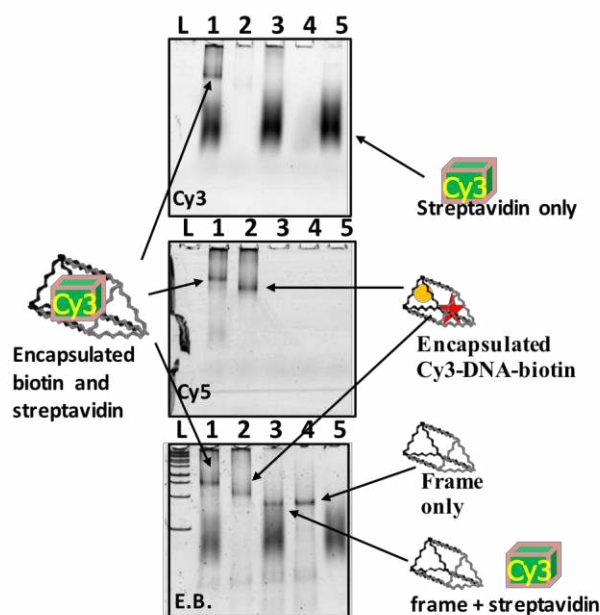


Figure 4.6. (A) Schematic of ssDNA and ssRNA oligonucleotides with functional modules encapsulation inside of the triangular nanoprism. (B) Assembly of encapsulated functional modules conjugated to ssRNA and ssDNA oligonucleotides. (C) Encapsulation and functional assays of streptavidin encapsulation inside the triangular nanoprism.

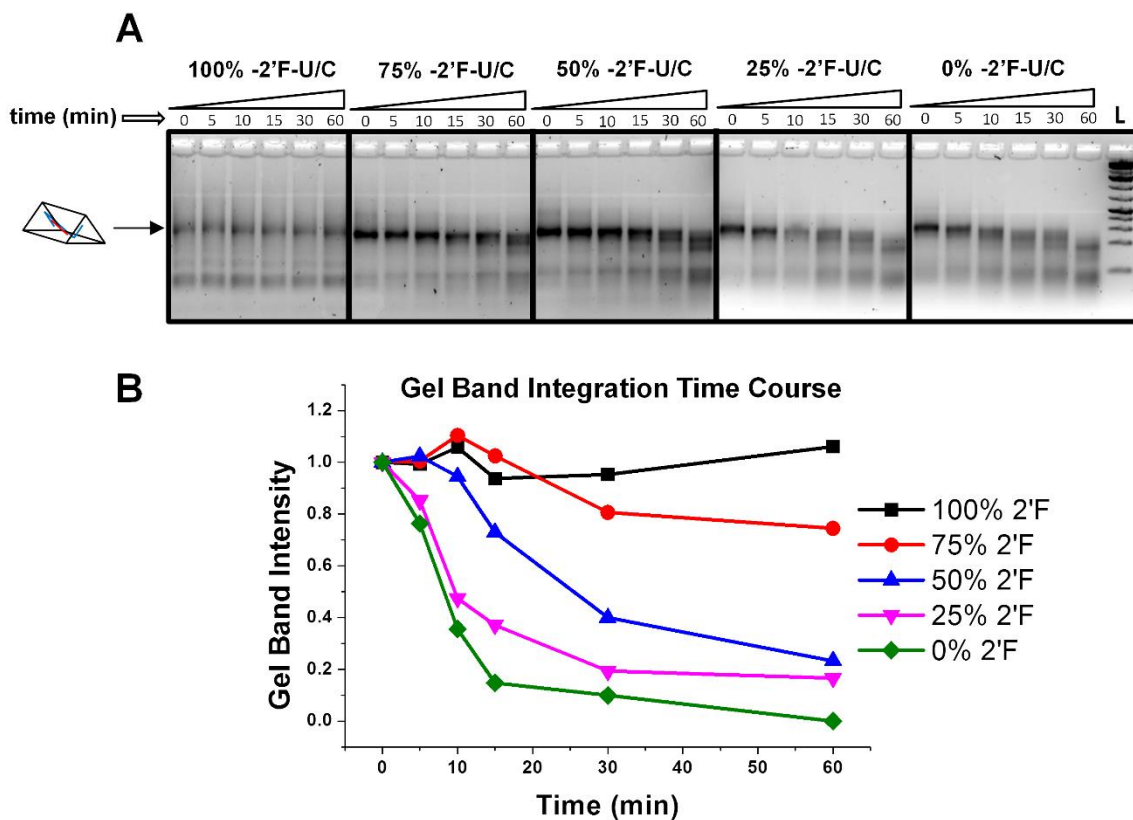


Figure 4.7. Tuning degradation profile of nanoprism in fetal bovine serum. (A) Gel images of nanoprisms with different percentages of 2'F modified pyrimidines used during assembly. Nanoprisms of 200 nM concentration were incubated in 2% FBS solution and analyzed by 3% agarose gel. **(B)** Prism relative gel band intensity plotted versus time. The intensity of each band was normalized to the zero time point for each nanoprism.

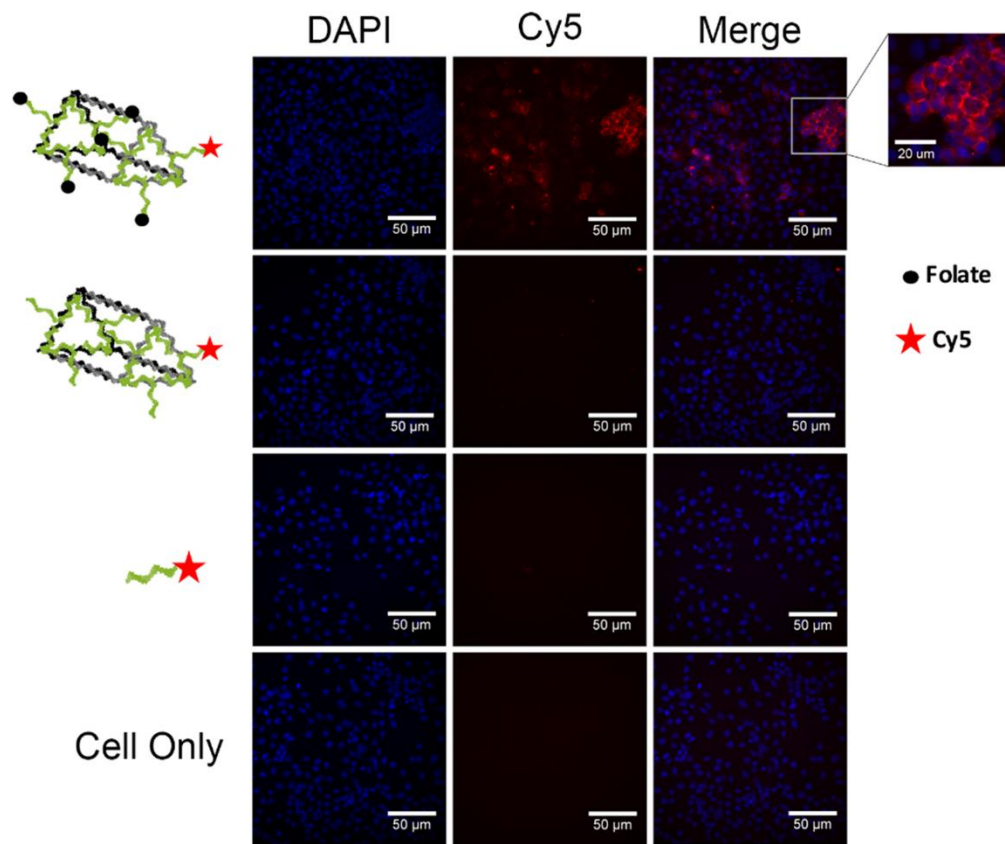


Figure 4.8. Evaluation of the RNA triangle prism to carry functional moieties. Confocal microscopy images of KB cells incubated with RNA nanoprism decorated with 5 folates as targeting modules.

Chapter 5: Large-scale *In Vitro* Synthesis and Purification of RNA Nanoparticles using Rolling Circle Transcription (RCT)

Chapter 5 was reproduced (with some modification) with permission from Jasinski, DL; and Guo, P. “Co-Transcriptional Assembly of RNA Nanoparticles *via* Rolling Circle Transcription of Fully Double Stranded Circular DNA.” *Currently under submission* and Jasinski, DL; Schwartz, CT; Haque, F; and Guo, P. “Large scale purification of RNA nanoparticles by preparative ultracentrifugation.” *Methods in Molecular Biology*. 2015. 1297, 67-82. DOI: 10.1007/978-1-4939-2562-9_5.

Chapter 5.1: Co-Transcriptional Assembly of RNA Nanoparticles *via* Rolling Circle Transcription of Fully Double Stranded Circular DNA

INTRODUCTION:

RNA nanotechnology is an emerging field that has grown in complexity and diversity, as RNA is an attractive material to construct nanostructures with defined physical properties (38,90,126,261-263). Many apparent issues of RNA instability were overcome to achieve a nanoparticle platform with potential for treatment of disease, especially cancer (62-64,90). Targeting aptamers and functional RNAs such as siRNA, miRNA, ribozymes, and riboswitches are available to construct diverse multi-functional nanoparticles. Development of RNA nanotechnology has been accelerated by the finding of an unusually stable three-way junction (3WJ) RNA motif from the packaging RNA (pRNA) of the phi29 DNA packaging motor (55). The 3WJ has been used for targeted delivery of therapeutic

modalities to multiple cancer types and has been used as a scaffold for the construction of RNA nanoparticles with controllable size and shape (56,60,103,148,150,264-266).

In a lab setting, RNA is most commonly synthesized by two methods: *in vitro* run-off transcription and chemical synthesis. While useful and widespread, both methods have their limitations. Chemical synthesis is hindered by limits on length and low RNA coupling efficiency while *in vitro* run-off transcription is limited by yield and time efficiency due to delayed RNA polymerase binding and initiation (219,267-269).

Isothermal amplification of nucleic acids, rolling circle amplification (RCA) for DNA and rolling circle transcription (RCT) for RNA, are gaining popularity due to the simplified processes for amplification and the unique capabilities of RCA and RCT (125,270,271). Isothermal reactions can be carried out in conjunction with other biological processes or in the presence of sensitive enzymes that would otherwise be destroyed by heating during thermocycling. Sensitive detection systems using padlock probes and fluorescent nucleic acid sequences have also been used for the detection of antigens or nucleic acids such as mRNA or miRNA (272,273).

RCT is especially useful as there are many functional RNA motifs, such as aptamers, miRNA, siRNA, and ribozymes that can be continually synthesized in a normal RCT reaction. Short single stranded (ss) circular DNAs encoding for ribozymes that self-process into unit length functional ribozymes have been synthesized. These ribozymes show biological functionality *in trans*, cleaving HIV-1 RNA targets (274,275). RCT has been used to synthesize siRNA loaded microsponges that show successful gene knockdown *in vivo* (38,270,276). Showing the versatility of RCT, nanowires (277), millimeter sized

RNA membranes (278), mRNA nanoparticles (279), and tandem repeats of fluorogenic RNA aptamers have all been synthesized (280).

While functional RNA motifs are useful in therapeutic settings, RNA biology could be implemented to produce defined RNA oligomers during RCT by, for example, using self-cleaving ribozymes (281-283). Previous methods to create defined RNA oligomers include the use of ssDNA oligomers and RNaseH during RCT, allowing site-specific cleavage (284). Encoding for a self-cleaving ribozyme in the DNA template for RCT will allow simpler experimental processes and more widespread application. Additionally, *in vivo* expression of specific RNA oligomers and RNA nanoparticles could be possible.

Increased use of nucleic acids in nanoparticle applications necessitates the development of high yield synthesis methods other than those available today. RCT's increased transcription efficiency over traditional run-off transcription could help to increase the production yield of RNA oligomers and RNA nanoparticles (125). *In vitro* transcription is not limited by length and one-strand or multi-strand nanoparticle assembly can occur co-transcriptionally, which has been shown to increase assembly efficiency (191,285).

However, traditional methods of circular DNA preparation for RCT are not amenable for DNA templates displaying stable secondary structure. Bacterial RNA polymerases are sensitive to secondary structure, falling off template DNA when encountering stable DNA hairpins and loops (125,274,286). Ribozymes have a stable secondary structure and when combined in the same ssDNA template as an RNA nanoparticle sequence, the ΔG of the DNA template is quite low. For successful transcription of a circular DNA encoding for self-cleaving ribozymes and nanoparticle

sequences, it was necessary to develop a new method for the construction of short circular dsDNA for transcription to process in an RCT reaction. While other short dsDNA molecules have been constructed through click chemistry, we questioned if disturbing the phosphate backbone could cause polymerase stalling and dissociation (287).

Herein, we describe a method for the construction of short circular dsDNA templates that code for self-cleaving ribozymes and RNA oligomers or RNA nanoparticles. Upon *in vitro* transcription, the ribozymes self-cleave with high efficiency, producing large amounts of target RNA. The phi29 pRNA 3WJ was assembled from its three component strands both co-transcriptionally and by self-assembly after RNA oligomer purification. Also, single strand RNA nanoparticles were synthesized *via* RCT by addition of loops to link adjacent 3WJ strands. The malachite green fluorogenic RNA aptamer (MGA) was fused to one helix of the 3WJ and malachite green dye (MG) fluorescence was observed in real time during *in vitro* transcription. SYBR GreenII fluorescence, a dsRNA specific fluorophore that fluoresces only upon binding to RNA, was also used to monitor transcription in real time. Fluorescent signals from transcription reactions using circular dsDNA were 8-10 times higher compared to identical sequences in linear dsDNA, indicative of the increased efficiency of the RCT reaction.

MATERIALS AND METHODS:

Sequence Design

Sequences for target oligomers were derived from the pRNA-3WJ nanoparticle as reported previously (55). Additional nucleotides were added to the 5' and 3' ends of the native 3WJ sequences, 5'-GAC-3' and 5'-GUC-3' respectively, aiding in ribozyme stability and cleavage efficiency. For the synthesis of single stranded RNA nanoparticles,

loops (5'-GAGA-3') were used to join adjacent 5' and 3' ends of the multi-strand RNA nanoparticles. Ribozyme sequences were adapted from previously solved structures of the hammerhead ribozyme (283). For ribozyme efficiency assays, ribozyme sequences were mutated to abolish activity as previously described (283). The malachite green aptamer sequence was adapted from previously published sequences (212). All sequences are summarized in Table A.4.1.

DNA and RNA Preparation

RNA oligomers were prepared *in vitro* using T7 RNA polymerase from linear and circular dsDNA containing the T7 promoter. Linear dsDNA was prepared by PCR using ssDNA primers purchased from Integrated DNA Technologies (IDT). Circular dsDNA was prepared from ultramer oligomers purchased from IDT. The assembly method of circular dsDNA is detailed in Figure 5.1. ssDNA anti-sense to the RNA strand (including T7 promoter, ribozymes, and target RNA) was self-cyclized intramolecularly using Epicentre CircLigase following the manufacturer's protocol. Remaining linear ssDNA was removed by addition of DNA Exonuclease I. ssDNA complementary to the cyclized ssDNA was annealed by thermal denaturation at 85°C for five minutes followed by slow cooling to 4°C at over one hour at 4 μ M concentration. Following annealing, T4 DNA ligase closed the nick in the circular dsDNA. Ligations were performed at a DNA concentration of 2.5 μ M in 1 X DNA ligase buffer, 5% (w/v) PEG4000, and a ligase concentration of 0.25 U/ μ L. The ligation mixture was incubated at 25°C for 4 hours followed by heating at 65°C to heat denature the enzyme. Control constructs without T4 ligation were also assembled.

Gel Analysis and Quantification

Assembly of linear and circular dsDNA constructs and RNA products was confirmed using 10% (29:1) PAGE in a buffer containing 50 mM TRIS, 100 mM NaCl, and 5 mM EDTA, and DNA or RNA was stained using ethidium bromide (EB) solution or MG dye solution (final concentration of 5 μ M MG Dye, HEPES pH=7.4, 100 mM KCl, 5 mM MgCl₂).

Ribozyme Cleavage Efficiency

Time course experiments were run to analyze ribozyme cleavage efficiency. A typical transcription reaction was quenched at specific time points by addition of DNase. Equal aliquots of each time point were then analyzed on PAGE and gel band intensity was integrated using ImageJ software (169). Cleavage efficiency was calculated by dividing band intensity of the cleaved fractions by total band intensity per lane. Cleavage percentage versus time was then plotted using OriginPro.

Gel Analysis of Transcription Kinetics

dsDNA constructs, both linear and circular, were transcribed following typical T7 *in vitro* transcription protocols with a 250 nM final DNA concentration. At 0.5, 1, 2, and 4 hours, transcription reactions were stopped using DNase. Equal aliquots of transcription from each time point were analyzed on PAGE and target RNA bands were integrated using ImageJ software. Gels were stained separately for total RNA (EB) and MG fluorescence. Gel band intensity versus time was then plotted using OriginPro. Gel assays were carried out in triplicate with standard deviations indicated by error bars.

Fluorescence Monitoring of RNA Transcription

To monitor transcription in real time, MG dye or SYBR GreenII were added at a final concentration of 5 μ M to transcription reactions. Solutions were incubated at 37°C in

96 well plates and fluorescent signal was monitored every 15 minutes using a BioTek Synergy 4 Microplate Reader. MG signal was read from excitation and emission wavelengths of 590 nm and 630 nm, respectively. SYBR GreenII fluorescence was read from excitation and emission wavelengths of 496 nm and 520 nm, respectively. OriginPro was used to plot fluorescent signal versus time. Transcription analysis was performed at DNA concentrations of 10, 100, and 250 nM.

Large-Scale Purification Using Gel Electrophoresis Column

Transcription reactions were purified on a BioRad model 491 Prep Cell using continuous-elution gel electrophoresis following the manufacturer's standard protocol. 20 mL of 8% polyacrylamide gel were prepared in a buffer containing 50 mM TRIS, 100 mM NaCl, and 5 mM EDTA. The gel was polymerized and to a column height of 5.5 centimeters and pre-run at 300 V for 1 hour. Large-scale, 1 mL transcriptions with final DNA concentration of 250 nM, transcriptions were diluted to 2 mL with 2X gel loading dye and loaded onto the column. After two hours of electrophoresis at 300 V, fractions were collected at a rate of .25 mL/min for 4 minutes for a total fraction volume of 1 mL. A total of 60 fractions were collected for four hours. Fractions were analyzed by adding 20 μ L of 10 X MG binding buffer (final concentration of 5 μ M MG Dye, HEPES pH=7.4, 100 mM KCl, 5 mM MgCl₂) to 180 μ L of each fraction. Fluorescence was analyzed as described previously. RNA concentrations were measured by reading absorbance at 260 nm.

RESULTS:

Sequence Design and Ribozyme Optimization Using Linear dsDNA

Due to the processive nature of RCT, long RNA concatamers are the result, unless a strategy is devised to reduce the products into defined oligomers. In our case, the goal was to produce short RNA oligomers that would then then fold into higher order RNA nanoparticles. Thus, self-cleaving ribozymes were incorporated into the sequences to cleave the RNA during transcription, resulting in short RNA oligomers. However, as it was necessary to optimize ribozyme sequence to obtain high cleavage efficiency, sequences were first optimized using traditional run-off transcription of linear dsDNA templates. These sequences were then used in the circular constructs, as described in a later section.

Linear dsDNA containing the T7 RNA polymerase promoter sequence, self-cleaving ribozymes 5' and 3' of the target RNA sequence, and the target RNA sequence were designed and constructed using PCR (sequence layout in **Fig 5.1**). The initial goal was the assembly of the pRNA-3WJ, as it is well characterized in our lab. Therefore, the target RNA sequences for ribozyme optimization were 3WJ-a, 3WJ-b, and 3WJ-c (55). Hammerhead ribozyme sequences were chosen as they are well characterized and display high cleavage efficiency (281,283,288,289). Ribozyme sequence optimization was carried out experimentally by gel analysis using linear dsDNA. While active site bases of the ribozyme sequence must be conserved to maintain cleavage, non-active site duplex sequences can be modified, aiding in self-cleavage optimization (281,283).

Size controls were transcribed to represent the possibilities of RNA transcript length with and without cleavage. Failed 5' and 3' ribozyme cleavage, failed 5' ribozyme cleavage only, failed 3' ribozyme cleavage only, and ribozyme only were used as RNA size controls (**Fig A.4.1A**). Ribozyme activity was abolished in RNA size controls by sequence mutation (283) to maintain identical sequences in RNA size controls. Target

RNA strands were chemically synthesized as size and assembly controls. Cleavage efficiency was calculated by comparing target RNA band intensity to total band intensity per lane over two-hour time course experiments (**Fig A.4.1B**). ImageJ software was used to integrate the gel band intensity. Cleavage kinetics assays were done using truncated versions of the dsDNA. For example, 5' ribozyme efficiency was assayed using dsDNA template with no 3' ribozyme. The cleavage efficiency of each ribozyme, 5' and 3' of the target RNA, was calculated independently. Kinetics of full length constructs with ribozymes 5' and 3' of the target RNA were also assayed (**Fig A.4.1B**).

The first iteration of ribozyme sequences contained a two base-pair (bp) “closing” duplex resulting in cleavage efficiencies ranging from 36% - 65% cleavage. Upon lengthening the “closing duplex” to five bp (**Fig A.4.1C**), to increase the stability of the ribozyme sequence, cleavage efficiencies increased to 65% - 78%. When full length constructs with both active ribozymes were tested, cleavage efficiencies were more than 80% (**Tbl A.4.2**).

Circular dsDNA Construction and RCT Reaction

Circular and fully double stranded DNA templates were prepared for the RCT reaction (**Fig 5.1**). Ribozyme sequences used in circular dsDNA were identical to those optimized previously using linear dsDNA. First, phosphorylated ssDNA complimentary to the T7 polymerase promoter, 5' and 3' ribozymes, and target RNA sequences was self-ligated intramolecularly using Epicentre ssDNA Circ Ligase to form circular ssDNA. To confirm cyclization, non-denaturing polyacrylamide gel electrophoresis (PAGE) was used to visualize DNA bands before and after ssCirc ligation (**Fig 5.2A**). Upon self-cyclization,

an increase in migration rate is seen presumably due to the compact structure of the now self-folded ssDNA.

To form circular dsDNA, the cyclized ssDNA and phosphorylated ssDNA complement were mixed in equimolar concentrations. ssDNA strands were thermally denatured at 85°C for five minutes to remove any secondary structure, and then cooled to 4°C over one hour. Assembly of the complement strands was confirmed using PAGE analysis. Assembly of the complement strands resulted in a dramatic decrease in migration rate, indicating successful hybridization (**Fig 5.2A**). Importantly, compared to linear dsDNA controls, circular dsDNA migrates much slower, indicating circular conformation. After assembly, T4 DNA ligase was used to ligate the nicked circular dsDNA (**Fig 5.2A**). No apparent shift is observed by gel analysis after T4 ligation. Successful T4 ligation can be confirmed using *in vitro* transcription.

To prove RCT was occurring, ribozyme activity was abolished by sequence mutation on one circular dsDNA construct (**Fig 5.2B**) (283). No ribozyme activity will result in template length RNA using linear dsDNA template and long concatemeric RNA using circular dsDNA template. The target RNA sequence in this assay was 3WJ-a for both active and inactive ribozyme constructs. After *in vitro* transcription and termination by DNase, denaturing PAGE analysis was used to analyze RNA transcripts (**Fig 5.2B**). Significant accumulation of long RNA transcripts is seen from the RCT reaction (**Fig 5.2B, Lane 5**) compared to transcription of both the linear dsDNA template (**Fig 5.2B, Lane 3**) and the nicked circular dsDNA template (**Fig 5.2B, Lane 4**), indicating successful construction of circular dsDNA and successful RCT reaction. When ribozyme activity was restored, successful cleavage and release of target RNA strand was observed (**Fig 5.2B,**

Lanes 6-8), evidenced by the appearance of short RNA transcripts not seen in inactivated ribozyme constructs. Assembly confirmation of all circular dsDNA constructs is shown in Figure A.4.2.

Co-Transcriptional Assembly of 3WJ Nanoparticles

RNA nanoparticles have the unique ability to self-assemble co-transcriptionally, as they are being transcribed, under isothermal conditions (191,285). To assemble the pRNA 3WJ co-transcriptionally, 3WJ-b and 3WJ-c were incorporated into separate circular dsDNA constructs. The transcription of both 3WJ-b and 3WJ-c constructs were confirmed using PAGE analysis. Both constructs demonstrated correct cleavage and release of their target RNA in both linear and circular form (**Fig 5.2C, red box**). Compared to linear dsDNA controls, the band patterns of circular dsDNA are identical. Size controls of failed transcripts and resulting ribozyme sequences migrate much slower than the target RNA, further showing evidence of target RNA release (**Fig 5.2C**). Additionally, target RNA strands are equal in size to that of their chemically synthesized size controls, indicating cleavage and release of correct size ssRNA target sequences (**Fig A.4.3A**). To confirm the sequence of released ssRNA was correct, each fragment was isolated by gel purification. Assembly of the pRNA-3WJ from the ssRNA fragments isolated from the RCT reactions indicates cleavage specificity and target RNA release (**Fig A.4.3B**).

pRNA 3WJ nanoparticles were assembled co-transcriptionally by mixing 3WJ-a, c, and c dsDNA constructs in an equimolar ratio followed by *in vitro* transcription. PAGE analysis of both linear and circular co-transcription products indicates successful assembly of 3WJ nanoparticles when compared to the assembled 3WJ from gel purified RCT product (**Fig 5.2D**).

Alternatively, 3WJ nanoparticles were co-transcriptionally assembled from one ssRNA oligomer. Circular dsDNA encoding for the full sequence of the pRNA-3WJ, with the helix ends closed with loops or aptamer sequences, was constructed (**Fig 5.3A**). To facilitate monitoring of transcription and RNA folding, the MGA was incorporated on one of the helix loops (**Fig 5.3B**). Following transcription, the RCT reaction mixture was analyzed by non-denaturing PAGE (**Fig 5.3C**). Total RNA staining with ethidium bromide indicates correct size RNA oligomers compared to the DNA ladder. RCT-3WJ assembled from purified 3WJ monomers and one piece 3WJ with loops were used as size controls. The one-stranded nanoparticles migrate slower due to increased size from the incorporation of loop sequences used to connect helix ends. Additionally, gel staining with MG shows binding of the MG-3WJ nanoparticle to its fluorophore, indicating correct sequence and folding of the MG-3WJ as the MGA must fold correctly to produce MG fluorescence. No MG signal from the 3WJ, which lacks the MGA, indicates specific binding of MG to MGA in the MG-3WJ. Higher order concatamers (dimers, trimers, etc.) are present in the RCT reactions, indicating that ribozyme cleavage is not 100%.

Real-Time Monitoring of Transcription by Fluorescence

Fusion of the MGA onto the 3WJ allows for monitoring and comparison of transcription kinetics between traditional run-off transcription and RCT (**Fig 5.4A**). Gel assays were used to compare the transcription rate of linear and circular dsDNA (**Fig 5.4B**). After *in vitro* transcription was commenced, DNaseI was added at 0.5, 1, 2, and 4 hours to terminate the transcription reaction. After termination, an equal aliquot of transcription reaction was analyzed by PAGE. Gels were separately stained for total RNA, ethidium bromide (EB), and for MG signal. ImageJ software was used to integrate gel and intensity.

The integration results clearly show that RCT generates RNA nanoparticles much faster with a higher yield than that of run-off transcription (**Fig 5.4C**).

To monitor transcription rates in real-time, transcription was analyzed using a BioTek plate reader monitoring transcription kinetics in a 96-well plate. MGA fluorescence was monitored by adding MG dye to a final concentration of 5 μM in the transcription mixture while total RNA production was monitored by adding SYBR GreenII, an RNA specific probe which fluoresces only upon binding to RNA, to a final concentration of 1 X to the transcription mixture. Fluorescence measurements were taken every 15 minutes and fluorescence intensity was plotted versus time using OriginPro (**Fig 5.4D, E**). Among three different DNA template concentrations of 10(\blacktriangle), 100 (\blacksquare), and 250 (\bullet) nM, the RCT reactions (red lines) consistently outperformed run-off transcription (black lines) in both nanoparticle production rate and overall transcription yield. Across the three DNA template concentrations, RCT produced on average 10 times more RNA at the termination of the transcription reaction, consistent with previous findings on the rate of RCT (125,280). Interestingly, circular dsDNA template with a nick present, without T4 ligation, is similar in transcription rate to linear dsDNA at the same concentration, suggesting that T7 polymerase does not proceed to RCT with nicked circular dsDNA (**Fig 5.4D, E**).

Next, substrate (DNA template) concentration dependent kinetics of total RNA transcription was analyzed by comparing SYBR GreenII fluorescence values at different time points among different DNA template concentrations (values from **Fig 5.4E**). Time points from 60 – 165 minutes were chosen as these were during and after the highest increase of observed fluorescence. Fluorescence values from 10, 100, and 250 nM concentrations at each time point were plotted and fit linearly ($y = mx + b$) (**Fig A.4.4A,**

B). A strong linear correlation is seen between different DNA template concentrations relative to their RNA output, represented by SYBR GreenII fluorescence (**Fig A.4.4C**). Interestingly, the slope (x) values for circular DNA template, x average equal to 5.27, are much higher than those observed for linear DNA template, x average equal to 1.27. These values can be correlated to fluorescence output per nM (RFU/nM) of DNA template. Thus, these results support that RCT reaction results in an apparent increase in transcription efficiency. At these DNA template concentrations, the relationship appears to be linear. However, as biological systems are quite complicated, it is possible that higher DNA concentrations could saturate the transcription reaction.

Large-Scale Purification Post RCT

Purification of the MG-3WJ nanoparticles was carried out using a prep-scale version of typical gel electrophoresis. The BioRad Model 491 Gel Electrophoresis Prep Cell was used to purify large-scale transcription products of RNA nanoparticles transcribed from circular dsDNA encoding for the MG-3WJ. Fractions were analyzed for both MG fluorescent signal and absorbance at 260 nm (**Fig 5.5A**). Three distinct peaks were seen by MG fluorescence: fractions 5-7 (peak 1), 7-23 (peak 2), and 25-32 (peak 3). PAGE analysis was used to determine the identity of each peak compared to crude transcription mixture. Each lane was loaded with ~200 ng of RNA sample, based on absorbance at 260 nm. Peak 1 was smaller in size than the target RNA, peak 2 contained the target RNA, and peak 3 contained both the target RNA and larger RNA bands. Gel bands were integrated to determine purity with peaks 2 and 3 giving averages of 93.6% and 84.2%, respectively. Of note is the large absorbance value of the first fractions, which has been attributed to remaining nucleotides from the transcription mixture, as no band was seen by gel analysis.

DISCUSSION:

RCT offers many advantages over traditional *in vitro* transcription methods including higher transcription rate (125,280), template DNA economy, and the potential for *in vivo* expression of artificial RNA sequences and RNA nanoparticles (153). The most popular method for circular DNA preparation contains a long ssDNA phosphorylated at the 5' end, which is assembled to a splint ssDNA followed by DNA ligation, resulting in circular DNA with double stranded promoter region and single stranded regions complementary to the target RNA sequence. Alternatively, ssDNA templates with no promoter region can also be transcribed. While this method is amenable for ssDNA templates with little secondary structure (ΔG of self-folding close to zero or a positive value, **Tbl A.4.3**) (125,275,290,291) or stable dumbbell sequences (38,270,280,292), it was not amenable for ssDNA templates encoding for 3WJ based nanoparticles. The ΔG of self-folding for the ssDNA templates constructed here range from -11.6 kcal/mol to -27 kcal/mol (**Tbl A.4.3**), resulting in stable secondary structures. Transcriptions using current methods for preparing circular DNA template were attempted, however the stable secondary structure of the sequences hindered transcription, despite successful ligation, even in the presence of single stranded binding proteins and elevated transcription temperatures at 42°C (data not shown).

Therefore, a new method for circular DNA template preparation was conceived using dsDNA throughout the entire template DNA. While it well known that RCT transcribes much faster than run-off, the real novelty lies in the preparation of dsDNA that codes for nanoparticles with stable secondary structure, something that would not have and did not work with the traditional DNA preparation method. Removing the issue of stable

secondary structure in the DNA template was only possible by making the entire circular template double stranded. Making circular dsDNA is a widespread procedure in molecular biology with the construction of artificial DNA plasmids, in most cases multiple kilobases long, using cloning and other techniques. While the RNA nanoparticle sequence could have been cloned directly into a plasmid, complications arise from the inclusion of extra DNA such as the origin sequence, antibiotic resistant sequences, among others. Because the goal of this method was for *in vitro* synthesis, these sequences were not necessary and in fact would hamper reaction efficiency due to transcription of useless RNA. The most straightforward method to make circular dsDNA starting with two long, but identical length, phosphorylated ssDNAs, as depicted in **Figure 5.1**.

RCT results in the synthesis of long concatamers of ssRNA due to the progressive nature of the polymerase around the circular dsDNA. In this study, RNA oligomers and RNA nanoparticles with defined sequences were desired, so a cleavage method was devised to release the target RNA sequence from the rest of the transcript. Ribozymes are RNA motifs that cleave RNA, and can be engineered to cleave a specific sequence and even self-cleave. Their catalytic property was implemented to self-cleave co-transcriptionally and release specific RNA sequences, in this case those target sequences being 3WJ-a, b, and c (**Fig 5.2C**). This allows a hands-off method for the transcriptional production of short and defined RNA oligomers in high yield without the use of additional enzymes and will aid in the future scale up of this method for large-scale synthesis of RNA nanoparticles *in vitro* and *in vivo*.

The real power of RCT coupled with release of defined RNA oligomers is the ability of RNA nanoparticles to fold co-transcriptionally. As soon as each RNA monomer is

released by ribozyme cleavage, it can find its partner sequences in the transcription mixture and assemble isothermally into the nanoparticle. This is evidenced by comparison of purified monomers assembled into the 3WJ to the co-transcriptional reactions (**Fig 5.2D**).

To increase nanoparticle assembly yield, a second approach was taken to co-transcriptionally assemble RNA nanoparticles. Alternate to assembling the nanoparticle from three individual RNA monomers, loop sequences were used to join the 5' and 3' ends of adjacent monomers resulting in a nanoparticle from one RNA strand (**Fig 5.3A**). To demonstrate this concept, 3WJ with loops was synthesized as well as 3WJ with one loop and the other helix being closed by the malachite green fluorogenic aptamer. Including an aptamer in the sequence serves two purposes: (1) monitoring transcription kinetics by fluorescence; (2) shows accurate cleavage and correct folding of the RNA nanoparticle, as MG will not bind to MGA unless the sequences is correct. A decrease in gel migration rate compared to 3WJ assembled from cleaved 3WJ ssRNA "RCT-3WJ" and the 3WJ assembled from one RNA piece, "3WJ-Loop," of the MG-3WJ indicates increased size from the addition of the MGA (**Fig 5.3C**). Both linear and circular constructs show identical size. It is important to note that the MG-3WJ from RCT shows upper bands, indicating cleavage is not 100%.

The advantage to preparing circular dsDNA for transcription is the hypothesis that RCT will result in higher amounts of RNA nanoparticles from the same starting DNA concentrations, therefore being more efficient and faster in nanoparticle production. To test this hypothesis, we performed two methods of transcriptional kinetics monitoring using one piece MG-3WJ in linear and circular dsDNA. The first was by gel analysis and band intensity comparison. Gel band intensity indicates a much higher rate of transcription and

overall RNA production yield, both by total RNA staining and MG staining (**Fig 5.4B, C**). This supports the hypothesis that RCT will result in higher production of RNA nanoparticles. The results are also the same for real-time fluorescence monitoring (**Fig 5.4D, E**). While the ribozyme cleavage for circular dsDNA is not 100%, gel staining represents an accurate comparison of production of RNA nanoparticles as the gel band that was quantified was the target RNA nanoparticle. Fluorescence monitoring of the actual transcription mixture monitors the entire transcription reaction, including non-cleaved RNAs, reflecting slightly less accurate quantification of RNA nanoparticle production yield.

In both cases, a leveling of RNA transcription is observed. We hypothesized that buildup of magnesium salts from transcription byproducts or loss of enzyme activity could be the cause. To test this, separate transcriptions were performed with the addition of inorganic pyrophosphatase enzyme and additional T7 polymerase after two hours of transcription. In both cases, the same quenching of transcription occurred (data not shown). It is possible that the buildup of significant amounts of RNA in the transcription mixture could abolish enzyme activity, due to increased viscosity of the solution.

Failed ribozyme cleavage during circular transcription leads to long RNA stands, which are multimers of the desired RNA product. These impurities are observed by gel analysis (**Fig 5.4C**). It is important to remove unwanted products as nanomedical applications require a high degree of product purity. In this application, the most efficient method was purification by gel electrophoresis due to somewhat close size of products (impurities are as close as only two times larger than desired product). However, typical gel set ups are not amenable to large-scale purification due to large sample volumes

required for transcription and loss of sample during elution from gels. A continuous elution gel electrophoresis apparatus was, therefore, ideal for purification. After purifying of transcription samples, a purity of 93.6% was achieved, compared to 44.8% in the crude product.

While this procedure produces native RNA, most applications with RNA nanotechnology implement modified nucleotides, such as 2'-fluorine modification to the ribose sugar of purines (cytosine and uracil). Modifications increase thermodynamic and *in vivo* stability allowing their use in medical applications. Transcriptions with modified nucleotides, using mutant polymerase, were attempted, and while transcription processed normally ribozyme cleavage failed resulting in no release of target RNA oligomers. Presumably, this is due to the hydrolytic mechanism of ribozyme cleavage, requiring a 2' hydroxyl at the cleavage site (281). The sequence design used contains a cytosine at the cleavage site, which contains a fluorine at the 2' site in modified transcription. This sequence was mutated to adenine at the cleavage site and, despite the presence of a 2' hydroxyl, ribozyme cleavage failed (**Fig A.4.5**). It is apparent that duplex structure is extremely important for this ribozyme to maintain activity. Modification of the nucleotides to 2'F RNA changes the duplex structure, abolishing ribozyme activity. While this is a current challenge in the large-scale production of modified RNA nanoparticles, work is underway to find alternate cleavage methods to implement RCT for large-scale synthesis using modified nucleotides. Nonetheless, RNA nanoparticles show increased enzymatic stability over ssRNA and other endogenous dsRNA due to increased size and their complex structure protecting 5' and 3' ends from exonucleases.

CONCLUSIONS:

DNA template used for RCT reactions is generally made up of long ssDNA regions with dsDNA in the promoter region for RNA template binding. However, if long stretches of ssDNA in the template code for RNA displaying stable structure, such as RNA nanoparticles, the ssDNA template will also have stable secondary structure due to the complementary mechanism of transcription. Therefore, a new method was devised to construct fully double stranded and circular DNA encoding for RNA nanoparticles with extremely stable secondary structure. The method for circular dsDNA preparation is broadly applicable to the field of RNA nanotechnology as functional nanoparticles, in most cases, are stable by nature due to base pairing of complimentary nucleotides within the nanoparticle. To release RNA nanoparticles transcribed during RCT, self-cleaving ribozymes were coded for in the template allowing release of the target sequence and assembly co-transcriptionally. Furthermore, RCT produced eight times as much RNA than traditional transcription from dsDNA templates of identical sequence. RNA nanotechnology has been emerging as a new drug delivery platform and shows great promise to help advance the current state of nanomedicine. The methods introduced here allow large-scale production of RNA nanoparticles and will be needed for future clinical applications of RNA nanotechnology. As well as large-scale batch synthesis, *in vivo* expression and production of RNA nanoparticles could be possible using the methods introduced here, helping to solve the current challenges of scale and cost in RNA nanoparticle production.

ACKNOWLEDGEMENTS:

The research in P.G.'s lab was supported by NIH grants R01EB019036, U01CA151648 and U01CA207946. P.G.'s Sylvan G. Frank Endowed Chair position in Pharmaceutics and Drug Delivery is funded by the CM Chen Foundation. PG is the consultant of Oxford Nanopore and Nanobio RNA Technology Co, Ltd. He is the cofounder of P&Z Biology Medical Co. Ltd.

Chapter 5.2: Large-scale Purification of RNA Nanoparticles using Preparative Ultracentrifugation

INTRODUCTION:

Since the first example of RNA nanotechnology in 1998 (12), RNA has shown to be a promising therapeutic delivery system to target cancers, viral infections, and genetic diseases (91,293). Recent advances in RNA nanotechnology have led to the construction of diverse nanoparticles with varying sizes and structural features (50,64,103,105,126,150,152,190). Many of these nanoparticles have the potential for imaging, disease diagnosis, and drug and therapeutic RNA delivery (91,293-297). RNA is a polymer made up of four different nucleotides: adenine (A), cytosine (C), guanine (G), and uracil (U). Much like DNA, RNA can be easily manipulated to form precise structures, while at the same time retaining flexibility in structure and diversity in function much like proteins (90).

RNA nanoparticles assemble with high efficiencies; however, fully assembled and contamination-free nanocomplexes are required for most *in vitro* and *in vivo* applications. Besides HPLC, in many cases, purification is performed by polyacrylamide gel

electrophoresis (PAGE) or agarose gel electrophoresis (AGE), through which the correctly folded structures migrate in a sharp and distinct band and are separated from the faster migrating single stranded (ss) RNA and the slower migrating misfolded and aggregate structures (105,298). While these methods have proven to be effective, there are downsides to using PAGE and AGE. After electrophoresis, the RNA must be extracted from the gel, which is labor intensive and often requires an additional purification step to remove contaminating gel residue. Also, some nanoparticles do not enter PAGE and AGE gels efficiently due to the large branched structures of these complexes. Finally, PAGE and AGE lack the scalability needed to purify large quantities of nanostructures. HPLC is often used for the purification of chemically synthesized and chemically modified oligonucleotides, however HPLC is not conducive to large RNA nanoparticles (299). Ultracentrifugation is a useful method for the scalable and efficient purification of RNA supramolecular complexes on the large scale (300-302). Here, we describe a scalable, cost-effective, and contamination-free method to purify RNA synthesized by *in vitro* transcription and supramolecular RNA nanoparticles by preparative ultracentrifugation (303-305).

While analytical ultracentrifugation is used to study molecular interactions, and define the properties of the analyte, such as molecular weights, sedimentation coefficient, shape, and conformation, preparative ultracentrifugation is primarily used to isolate and purify specific particles. There are three main types of preparative ultracentrifugation: differential (also known as pelleting), rate-zonal, and density-equilibrium (also known as isopycnic). Differential centrifugation separates based on size or molecular weight in a process in which successive pelleting steps allows researchers to recover the particle of

interest. Rate-zonal centrifugation again resolves particles by size and shape dependent on run time but the particle of interest remains isolated in the gradient and is typically fractionated and recovered. Equilibrium density centrifugation, however, separates entirely on density, independent of run time. In the methods introduced in this chapter, equilibrium density and rate zonal gradients are employed. Equilibrium density gradient ultracentrifugation is used in the CsCl gradient purification of ssRNA oligomers and rate-zonal is employed in the sucrose gradient purification of supramolecular RNA nanoparticles.

Post *in vitro* transcription, RNA is separated from unincorporated nucleotides and protein impurities by CsCl equilibrium density gradient ultracentrifugation (**Fig 5.6**). Exploiting the differences in density between proteins, RNA nucleotides, and synthesized RNA oligonucleotides enables the large-scale purification of ssRNA, which are then used to form multi-strand supramolecular RNA nanoparticles.

RNA nanoparticles are then constructed from the purified ssRNA oligonucleotides. The RNA nanoparticles are purified from misfolded and aggregated complexes and unincorporated ssRNA by sucrose gradient rate-zonal ultracentrifugation (**Fig 5.7**). Post centrifugation, fractions are collected and examined on non-denaturing AGE and stained with ethidium bromide (EtBr) (**Fig 5.8**).

To demonstrate the expected results utilizing this procedure, synthesis and purification of RNA nanoparticles utilizing the packaging RNA (pRNA) (306) from the phi29 bacteriophage DNA packaging motor was performed. The native pRNA structure has previously been engineered to assemble into many nanostructures including dimers, trimers, tetramers, hexamers, and larger supramolecular complexes utilizing hand-in-hand

and foot-to-foot interactions (12,50,104,105,200). As an example, we show here the purification of pRNA monomer and dimer constructs from two distinct pRNA monomers, Ab' and Ba' (151). Monomers were purified by CsCl equilibrium density gradient ultracentrifugation and monomer and dimer constructs were purified by 5-20% sucrose gradient rate-zonal ultracentrifugation. The Ab' and Ba' pRNA monomers assemble to form dimer constructs, a size difference that can be confirmed by traditional native PAGE analysis. Despite a size difference of only 120 nucleotides between monomer and dimer, the two species can be resolved by sucrose gradient ultracentrifugation. Furthermore, the recovered fractions exhibited comparable dimer assembly to RNA nanoparticles purified by PAGE (**Fig 5.9**).

MATERIALS:

Prepare all solutions using Millipore water (prepared by purifying deionized water to attain a sensitivity of $18.2 \text{ M}\Omega \text{ cm}^{-1}$ at 25°C) that has been incubated at 37°C overnight with diethylpyrocarbonate (DEPC) and then autoclaved. All reagents used should be analytical grade and RNase and DNase free as RNA is extremely sensitive to RNase degradation. All glassware, tubes, and pipette tips used in preparation of reagents and buffers should be autoclaved to ensure sterilization. Gloves and lab coats should be worn at all times. All waste disposal regulations should be carefully followed. Prepare and store reagents at room temperature (RT) unless otherwise noted.

2.1. For Gradient Preparation

- 1) Diethylpyrocarbonate (DEPC) aqueous solution: 0.05% solution in millipore water (v/v): Add 5 mL DEPC to 995 mL millipore water and shake the solution vigorously. Incubate the solution overnight at 37°C and then autoclave to remove DEPC.

- 2) CsCl Ultracentrifugation Buffer: 1X Tris-EDTA (TE) Buffer (10 mM Tris-HCl, 1 mM ethylenediaminetetraacetate (EDTA)). Add about 100 mL water to a 1-L glass beaker with a magnetic stir bar (*see Note 1*). Weigh 1.21 g Tris-HCl, and 0.000292 g EDTA (*see Note 2*) and transfer to the glass beaker. Bring the volume to 900 mL with water and then adjust the pH to 8.0 with HCl (*see Note 4*). Bring the final volume to 1 L and autoclave.
- 3) Sucrose Ultracentrifugation Buffer: 1X Tris-magnesium saline (TMS) Buffer (50 mM Tris-HCl, 100 mM NaCl, and 10 mM MgCl₂). Add about 100 mL water to a 1-L glass beaker with a magnetic stir bar. Weigh 6.05 g Tris base, 5.844 g sodium chloride, and 2.03 g MgCl₂ hexahydrate and transfer to the glass beaker. Bring the volume to 900 mL with water and then adjust the pH to 8.0 with HCl. Bring the final volume to 1 L and autoclave.
- 4) CsCl Solutions: $d=1.65$ (0.790 g/mL). Dissolve 79.0 g molecular biology grade CsCl in 50 mL of 1X TE buffer in a glass beaker and mix with a magnetic stir bar. Once dissolved, dilute to 100 mL with 1X TE buffer in a graduated cylinder. $D=1.95$ (1.230 mg/mL). Follow same procedure as before with 116.73 grams of CsCl. Additional 1.745 g CsCl for sample preparation. (*see Note 5*)
- 5) Sucrose solution: 5%, 10%, 15%, 20% (w/v). To prepare sucrose solutions, dilute respective amount of sucrose (e.g. 5 g for 5% w/v) to 100 mL final volume with 1X TMS Buffer. Mix in glass beakers and stir with a magnetic beaker. (*see Note 5*)
- 6) Ultracentrifugation tubes: Beckman #326819, 5-mL.
- 7) Automated Gradient Maker: BioComp Gradient Master Model 106 (BioComp Instruments) gradient maker.

- 8) Long Neck Pipette tips: Bio-Rad 223-9916. 1-200 μ L pipette tip for gel loading.
- 9) Syringe and Needle: 5-mL BD Syringe, Fisher Scientific. Reusable non-sterile hypodermic needle, 3.5 in, Fisher Scientific.
- 10) Mild detergent: Alconox Detergent, Fisher Scientific #NC9003111.
- 11) Pipette: 1000 μ L and 200 μ L pipette, Denville Scientific Inc.
- 12) Vortexer: VWR Analog Vortex Mixer.

2.2. For Ultracentrifugation

- 1) Analytical Balance: Mettler Toledo AB204-S Analytic Balance.
- 2) Ultracentrifuge: Beckman Coulter L-80 Ultracentrifuge (Beckman #392051) (*see Note 6*).
- 3) Ultracentrifuge Rotor: Beckman Coulter SW 55 Ti Rotor (Beckman #342194) (*see Note 7*).
- 4) Ultracentrifugation Bucket: Swinging Bucket for SW 55 Ti Rotor (Beckman #342194) (*see Note 8*).
- 5) Ultracentrifugation Bucket Rack: Bucket rack for swinging bucket SW 55 Ti Rotor (Beckman #331313).
- 6) Ultracentrifugation Spinkote Lubricant: Lubricant for ultracentrifuge (Beckman #306812) (*see Note 9*).
- 7) Ultracentrifugation Vacuum Grease: Vacuum seal grease (Beckman #335148) (*see Note 10*).

2.3. For Fractionation and Sample Analysis

- 1) Tubes: Fisherbrand Premium Microcentrifuge tubes, 1.5 mL. Catalog No: 05-408-120. Autoclaved.

- 2) Pipette: 200 μ L pipette, Denville Scientific Inc. and sterile pipette 200 μ L pipette tips
- 3) Fraction Collector (Optional): Beckman Coulter Fraction Recovery System, No: 343890. (*see Note 11*)
- 4) Agarose: Low-melting, molecular biology grade. Fisher BioReagents. Catalog No: BP165-25.
- 5) Agarose Gel Buffer/Running Buffer: 1X TAE (40 mM Tris-acetate, 1 mM EDTA) with 10 mM $MgCl_2$. Add about 100 mL water to a 1-L glass beaker with a magnetic stir bar. While stirring, add 0.00725 g Tris-acetate, 0.000292 g EDTA, and 2.03 g $MgCl_2$ hexahydrate and transfer to the glass beaker. Bring the volume to 1-L.
- 6) Microwave
- 7) Imaging System: Typhoon FLA 7000 imaging system, GE Healthcare.
- 8) Agarose Gel Electrophoresis System, mini-sub cell GT system, Bio-Rad.
- 9) Ethidium Bromide: 1% Solution, Molecular Grade. Fisher BioReagents Catalogue No: BP1302-10.
- 10) Sample Concentration: Amicon Ultra 0.5 mL Centrifugal Filters, Millipore.

METHODS:

Carry out all procedures at RT unless otherwise specified.

3.1: CsCl Equilibrium Density method RNA Purification

This method details the purification of RNA prepared by *in vitro* transcription using T7 RNA polymerase as described in detail previously (105). CsCl centrifugation will remove unincorporated nucleotides as well as proteins and other impurities from the transcription reaction mixture based on differences in density. The sample being used for

centrifugation in the following procedure can be used directly after *in vitro* transcription without further modification (Figure 1).

3.1.1: Preparation of d=1.65-1.95 CsCl Gradient

1. Prepare two CsCl solutions with densities of 1.65 (0.790 g/mL) and 1.95 (1.23 g/mL) as detailed previously. (*see Note 5*)
2. Prepare CsCl sample solution with density equal to 1.75 (1.164 g/mL). Dilute the sample from RNA transcription to 1.0 mL (maximum sample volume for 5 mL centrifuge tube is 1.0 mL) with 1X TE buffer. To the diluted sample add 1.7452 g CsCl and mix thoroughly with a vortexer (*see Note 5*). Adjust the final volume to 1.5 mL.
3. Pipette the 1.5 mL sample in CsCl solution, $d=1.75$, into a 5.0 mL ultracentrifuge tube (Beckman #326819).
4. Using a syringe and long needle, pipette the $d=1.95$ CsCl solution to the bottom of the ultracentrifuge tube, below the sample CsCl solution
5. On top of the sample solution, pipette 1.5 mL of $d=1.65$ CsCl solution.
6. Cap the centrifuge tube. (*see Note 12*)

3.1.2: Ultracentrifugation Procedure

At all times, be gentle when handling the tubes with the prepared CsCl gradients. Too rough of handling will disturb the gradient and affect the sample purification.

- 1) Place the ultracentrifuge tube into the centrifugation buckets.
- 2) Using an analytical balance, measure and record the weight of each bucket and respective bucket top with the tube inside. It is extremely important to equilibrate weights of buckets that will be across from each other when attached to the rotor (*see Note 13*). To make the weights equal, use water to match weights between the pairs of

- buckets. For each 0.01 gram of difference, pipette 10 μ L of water into the bucket with less weight (*see Note 14*).
- 3) Once the buckets are balanced, tightly secure the tops of the buckets to prevent leaking. Finally, secure the buckets onto the swinging-bucket rotor (Beckman SW Ti 55) (*see Note 15*).
 - 4) Holding onto the base and the top of the rotor, carefully place the rotor into the ultracentrifuge (Beckman L-80 ultracentrifuge) (*see Note 16*).
 - 5) Bring the temperature down to 4.0°C and turn on the vacuum to equilibrate the rotor and sample. Wait until the final temperature and lowest pressure (<20 microns) are reached before commencing rotation (*see Note 17*).
 - 6) Spin the rotor (Beckman SW 55 Ti) at 45,000 RPM (246, 078 x g) for 16 hours. (*see Note 18*).
 - 7) After centrifugation, wait for the rotor to come to a complete stop and the RPM reading on the ultracentrifuge reaches "0." Once the rotor has stopped, release the vacuum and open the lid. Carefully grabbing the base and the top of the rotor, remove the rotor from the ultracentrifuge and place it back on the rotor stand.
 - 8) Remove the rotor buckets and place them back in the bucket holder rack. Remove the tubes and place them in a sample rack. It is important to now thoroughly clean and dry the buckets as excess moisture can cause damage to the buckets.
 - 9) Proceed to section 3.3 for fractionation and sample analysis.

3.2: Rate-zonal sucrose gradient for Nanoparticle Separation or cushioned Rate-Zonal Sucrose Gradient

This method details the separation of the final nanoparticle assembly from incorrect structures such as misformed aggregates and unincorporated strands. The RNA assemblies should be annealed prior to purification by ultracentrifugation in 1X TMS buffer. Maximum sample volume for ultracentrifugation is 500 μ L.

3.2.1: Preparation of 5-20% (v/v) sucrose density gradient preparation

3.2.1.1: Gradient preparation by gradient maker

- 1) Prepare two sucrose solutions, 5% and 20% (w/v), in 1X TMS buffer by diluting 5 g and 20 g, respectively, of sucrose to 100 mL volume in a graduated cylinder. Transfer to a glass beaker and use a magnetic stir bar to thoroughly mix the solutions.
- 2) Into a 5.0 mL polypropylene (Beckman #326819) ultracentrifuge tube, cleaned with a mild detergent and thoroughly dried, pipette 2.4 mL of 5% sucrose solution. In a 5-mL syringe with a long tip needle, carefully syringe 2.4 mL of 20% (w/v) sucrose solution to the bottom of the ultracentrifuge tube. Insert the cap of the centrifuge tube into the top of the tube (*see Note 12*).
- 3) In this method, the gradient was made using the BioComp Gradient Master Model 106 (BioComp Instruments) gradient maker (*see Note 19*). For the specified gradient, 5%-20% sucrose (w/v), set the gradient maker to spin for one minute and thirteen seconds at an angle of 86° at 16 RPM. After the gradient maker is done, remove the ultracentrifuge tube and place in a sample holder rack (*see Note 20*).

3.2.1.2: Gradient preparation by manual layering (if gradient maker not available)

This method details the procedure to make the 5%-20% (w/v) sucrose gradient if there is no automated gradient maker available.

- 1) By the same procedure previously detailed, make 5%, 10%, 15%, and 20% (w/v) sucrose solutions.
- 2) Using the prepared solutions, layer from most dense (20%) to least dense (5%) with 1.2 mL of each solution. Carefully layer the solutions into a 5.0-mL (Beckman #326819) ultracentrifuge tube using a long-tip hypodermic needle. (*see Note 21*)
- 3) Incubate the tube overnight at 4°C to form a continuous gradient, ideally in a cold room (*see Note 22*).

3.2.2: Sample loading and ultracentrifugation procedure

At all times, be gentle when handling the tubes with the prepared sucrose gradients. Too rough of handling will disturb the gradient and affect the sample purification.

1. Before being loaded, ensure the sample is in its native annealing buffer (*see Note 23*).
To load the sample, slowly pipette a maximum volume of 100 µL on top of the previously prepared sucrose gradient (*see Note 24*).
2. Using an analytical balance, measure and record the weight of each bucket and respective cap with the tube inside. It is extremely important to equilibrate weights of buckets that will be across from each other when attached to the rotor (*see Note 13*).
Use water to equal bucket weights. For each 0.01 gram of difference, pipette 10 µL of water into the bucket with less weight (*see Note 14*).
3. Once the buckets are balanced, tightly secure the tops of the buckets to prevent leaking.
Finally, secure the buckets onto the swinging-bucket rotor (Beckman SW Ti 55) (*see Note 15*).
4. Holding onto the base and the top of the rotor, carefully place the rotor into the ultracentrifuge (Beckman L-80 ultracentrifuge) (*see Note 16*).

5. Bring the temperature down to 4.0°C and turn on the vacuum to equilibrate the rotor and sample. Wait until the final temperature and lowest pressure (<20 microns) are reached before commencing rotation (*see Note 17*).
6. Spin the rotor (Beckman SW 55 Ti) at 50,000 RPM (303, 800 x g) for 7 hours. (*see Note 18*).
7. After centrifugation, wait for the rotor to come to a complete stop and the RPM reading on the ultracentrifuge has reached "0." Once the rotor has stopped, release the vacuum and open the lid. Carefully grabbing the base and the top of the rotor, remove the rotor from the ultracentrifuge and place it back on the stand.
8. Remove the rotor buckets and place them back in the bucket holder rack. Remove the tubes and place them in a sample rack. It is important to now thoroughly clean and dry the buckets as excess moisture can cause damage to the buckets.

3.2.3 Preparation of Cushioned Sucrose Gradient for Rate-Zonal Purification of RNA Nanoparticles

This method details the use of a high-density sucrose “cushion” at the bottom of the gradient during the rate-zonal purification of RNA nanoparticles (**Fig 5.9E**). Utilizing a cushion has multiple advantages. For low amounts of sample, the sample can be run to the bottom of the gradient and then stopped at the cushion. This allows the samples to be collected at a higher concentration (fewer fractions) while avoiding pelleting. Pelleting can sometimes lead to damage of sensitive samples during resuspension. Additionally, using a cushion enhances the collection of nanoparticles that display multiple conformations, which would otherwise spread to multiple fractions. Importantly, when purifying nanoparticles that contain small molecule therapeutics or reporter molecules, a cushion will

help to purify the nanoparticle complex from free small molecules by allowing large separation between the two species. The size of the complex can easily separate from free drug due to the buoyancy of the small molecule, which will prevent the small molecule from co-localizing in the denser (lower) portion of the gradient.

1. First prepare the 5-20% sucrose gradient as described earlier in section 3.2.1. However, when using the BioComp gradient maker reduce the volume of each solution to 2.3 mL and when manually layering each solution decrease the volume of each solution to 1.15 mL. This will account for the additional volume needed for the high-density sucrose cushion.
2. After preparation of the 5-20% sucrose gradient, with decreased volume, use a pipette to load .2 mL of 60% sucrose solution to the bottom of the gradient. Slowly pipette the 60% sucrose solution down the side of the ultracentrifuge tube, from the top of the gradient. Because of the high density of the solution, it will fall to the bottom of the tube forming a sucrose cushion.
3. Let the cushion settle for 5 minutes being careful not to disturb the solution in the tube.
4. For sample loading and fractionation follow the same procedures detailed for sucrose gradient rate-zonal ultracentrifugation without use of the cushion.

3.3: Fractionation and sample analysis/recovery (Same for CsCl and Sucrose)

During this step it is important to keep track of each fraction when removing it from the tubes. Pre-label autoclaved tubes to ensure accuracy of fractions.

- 1) To remove fractions, use a pipette to remove 200 μ L from the very top of the CsCl or sucrose gradient and place in a pre-labeled tube to ensure accuracy of fraction numbers (*see Note 25*).

- 2) Continue to remove 200 μ L fractions from the very top of the tube until the tubes are completely empty (*see Note 26*).
- 3) Prepare a 2.0% non-denaturing agarose gel containing 1X EtBr gel stain (2.0 grams agarose, diluted to 100 mL in 1X TAE Buffer containing 10 mM-Mg) (*see Note 27*).
- 4) Into each well of the agarose gel load 10 μ L aliquots of each fraction. Run for 30 minutes at 120 V at RT in 1 X TAE buffer with 10 mM MgCl₂.
- 5) After the gel has finished running, scan on a Typhoon FLA 7000 laser scanner for EtBr signal. Similar gel scanning devices can also be used. (*see Note 28*)
- 6) Combine the fractions containing the desired products and reconstitute into the native folding buffer, 1X TMS, using Amicon Ultra 0.5 mL centrifugal filters (*see Note 29*).

EXPECTED RESULTS:

Synthesis and purification of RNA nanoparticles utilizing the pRNA from the phi29 bacteriophage was performed. In nature, the pRNA forms a hexameric ring that is used in gearing the phi29 DNA packaging motor (12,306). Previously, the native pRNA structure was engineered to assemble into diverse RNA nanoparticles including dimers, trimers, tetramers, hexamers, and larger supramolecular complexes utilizing hand-in-hand and foot-to-foot interactions (12,50,104,105,200). As demonstration of expected results, we show here the purification of pRNA monomer and dimer constructs from two different pRNA monomers, Ab' and Ba' (151). Monomers were purified by CsCl density gradient ultracentrifugation and dimer constructs by 5-20% sucrose gradient rate-zonal ultracentrifugation. The Ab' and Ba' pRNA monomers assemble *via* hand-in-hand kissing loops to form dimer constructs (**Fig 5.9A**). CsCl density gradient ultracentrifugation was used to purify RNA directly after *in vitro* transcription from the proteins and DNA template

using the procedures detailed here. Post *in vitro* RNA transcription, the reaction mixture contains proteins and DNA template, which are undesired products. The DNA template is degraded by DNase enzyme and the proteins are easily separated from the RNA product by the difference in their densities. The high density of RNA results in the products migrating to the densest portion of the gradient. Despite a small size difference between monomers and dimer, ~120 nucleotide monomer and ~240 nucleotide dimer, the monomer and dimer can be separated by sucrose density gradient ultracentrifugation following the procedures detailed here (**Fig 5.9C**). The recovered fractions demonstrated comparable dimer assembly to RNA nanoparticles purified by PAGE (**Fig 5.9D**).

NOTES:

- 1) Adding reagents to already circulating water helps to dissolve them easily. If there is trouble dissolving the reagents the glass beaker can be heated gently to 37°C. However, pH must be adjusted at room temperature.
- 2) Use caution when handling EDTA. EDTA is a skin, eye, and respiratory tract irritant
- 3) MgCl₂ will absorb moisture from the air. Be sure to handle as quickly as possible and then recap the reagent bottle tightly to prevent moisture absorption.
- 4) Use caution when handling concentrated HCl. HCl is a strong acid and is very corrosive. HCl is a strong eye, skin, and respiratory tract irritant. HCl can cause severe burns, be sure to handle with gloves and wear splash goggles to prevent it from getting in eyes.
- 5) Be sure to mix vigorously enough to have a homogeneous mixture of CsCl or sucrose and 1X TE buffer.

- 6) Be sure regular maintenance has been carried out on the ultracentrifuge to ensure proper operation and safety for the user.
- 7) Before use, inspect rotor to make sure there are no cracks or disfigurements, use of damaged buckets could result in danger to the user and damage to the ultracentrifuge.
- 8) Before use inspect buckets for cracks and/or disfigurements, use of damaged buckets could result in danger to the user and damage to the ultracentrifuge.
- 9) Before using the ultracentrifuge, be sure the rotation bearings are properly lubricated.
- 10) Prior to ultracentrifugation ensure the vacuum seal is properly greased. A badly greased vacuum seal will not allow the proper low-pressure environment to be reached and ultracentrifugation will not be able to commence.
- 11) The Beckman Coulter Fraction Recovery System works by puncturing a hole in the bottom of the ultracentrifugation tube and collection occurs from the bottom of the tube. This system can be a viable alternative to the method described here, however this equipment is optional.
- 12) When capping the ultracentrifuge tube make sure to cap at an angle to prevent air bubbles from forming in the gradient. Keep air bubbles out while preparing the gradient. When syringing higher density CsCl or sucrose do so slowly and with extreme care to avoid mixing the high density with the low-density solutions. The gradient used will not be identical for all complexes. In some cases the ideal gradient to use must be experimentally determined.
- 13) Each bucket is labeled with a number 1-6, 1 is across from 4, 2 from 5, 3 from 6. It is important that each pair be identical in weight and are placed across from each other

- on the rotor. Also, even if six samples are not being run, it is important that all buckets be in place during centrifugation and run with equal weight.
- 14) Do not pipette into the ultracentrifuge tube, pipette into the space surrounding the tube inside the bucket.
 - 15) Before beginning ultracentrifugation, make sure each bucket is securely fixed to the rotor. Do this by gently but firmly tugging down on each bucket once it is attached to the rotor. However, while doing this do not disturb the gradient and sample in the tube.
 - 16) The rotor must rotate freely to ensure proper function of the ultracentrifuge. Ensure that the connection is sufficiently greased (Beckman #306812) and test by rotating the rotor clockwise by hand. If it moves freely it is sufficiently lubricated.
 - 17) A proper vacuum seal is required to hold the vacuum constant. Make sure the seal is sufficient, if not apply grease to ensure a proper seal (Beckman #335148).
 - 18) The optimal centrifugation time depends on the exact mass and shape of the RNA complex. This should be experimentally determined. Avoid excessive centrifugation as this may lead to sample pelleting at the bottom of the tube, which will negatively affect the purification of the RNA assembly. Pelleting time, or k-factor, can be calculated quickly by equation $t=k/s$, where t is run time in hours required to pellet a particle of known sedimentation coefficient s (in Svedberg units, S). The k-factor is a function of the maximum and minimum radius of a rotor and the run speed in RPM. The k-factor for the SW-55 Ti rotor at 45,000 RPM is 72.4. After determining the sedimentation coefficient of the particle of interest, the pelleting time can be calculated and a shorter time should be used.

- 19) This exact model of gradient maker is not required. Follow the gradient maker protocol for correct angle, speed, and duration.
- 20) Always prepare gradients with location in mind. Try to move the formed gradients as little as possible as moving the gradients can disturb the final density gradient.
- 21) Pipette as carefully as possible when stacking the different densities of CsCl or sucrose. Taking care not to mix the different gradients will lead to a better quality gradient.
- 22) A cold room is preferred over a refrigerator. Repeated opening and closing of a refrigerator door will disturb the gradient during its equilibration.
- 23) Sample should be in its native annealing buffer, 1X TMS.
- 24) When pipetting the sample onto the top of the gradient take great care to pipette slowly and get as narrow a band as possible of the sample. This will lead to higher resolution during ultracentrifugation.
- 25) 200 μ L may not be an ideal volume for every purification situation. In a case where the RNA complex is not as well separated a lower fraction volume may be ideal, in cases where resolution is high larger fraction volumes may be ideal. This should be experimentally determined.
- 26) Be sure to use a new pipette tip with each fraction to avoid contamination.
- 27) Be careful handling EtBr, it is thought to act as a mutagen because it intercalates with dsDNA and dsRNA.
- 28) Be sure to include a molecular weight marker in the agarose gel to determine which fractions are the correctly formed complexes.
- 29) Follow the manufacturer's protocol. The size of the RNA complex being purified will determine the specific filter to be used. Centrifugal force less than 4500g should be

used in order to minimize sample damage and loss. Typically this will result in 50-100 μL of purified RNA complex.

ACKNOWLEDGEMENTS:

The research was supported by NIH grants R01-EB003730 and U01-CA151648 to P.G. The content is solely the responsibility of the authors and does not necessarily represent the official views of NIH. Funding to Peixuan Guo's Endowed Chair in Nanobiotechnology position is from the William Fairish Endowment Fund.

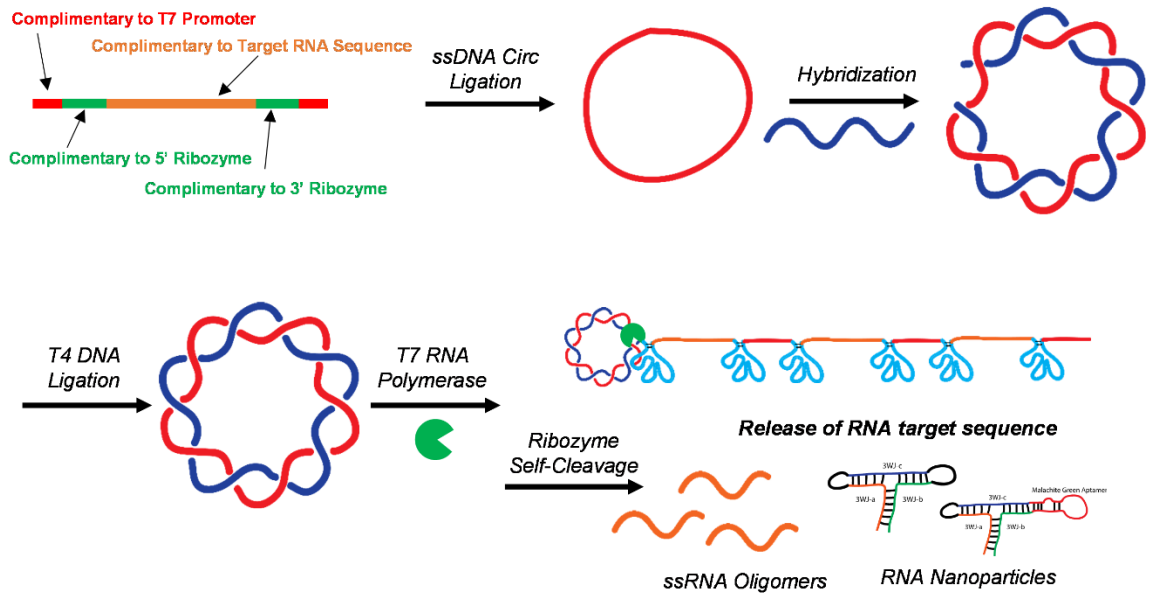


Figure 5.1: Scheme for Circular dsDNA Assembly. ssDNA CircLigase is first used to self-cyclize a phosphorylated ssDNA. Following hybridization of the complementary strand, T4 DNA ligase is used to close the nick. T7 RNA polymerase transcribes the sequence, which contains self-cleaving ribozymes to release the target RNA sequence. The target RNA sequence can be a defined RNA oligomer or nanoparticle sequence.

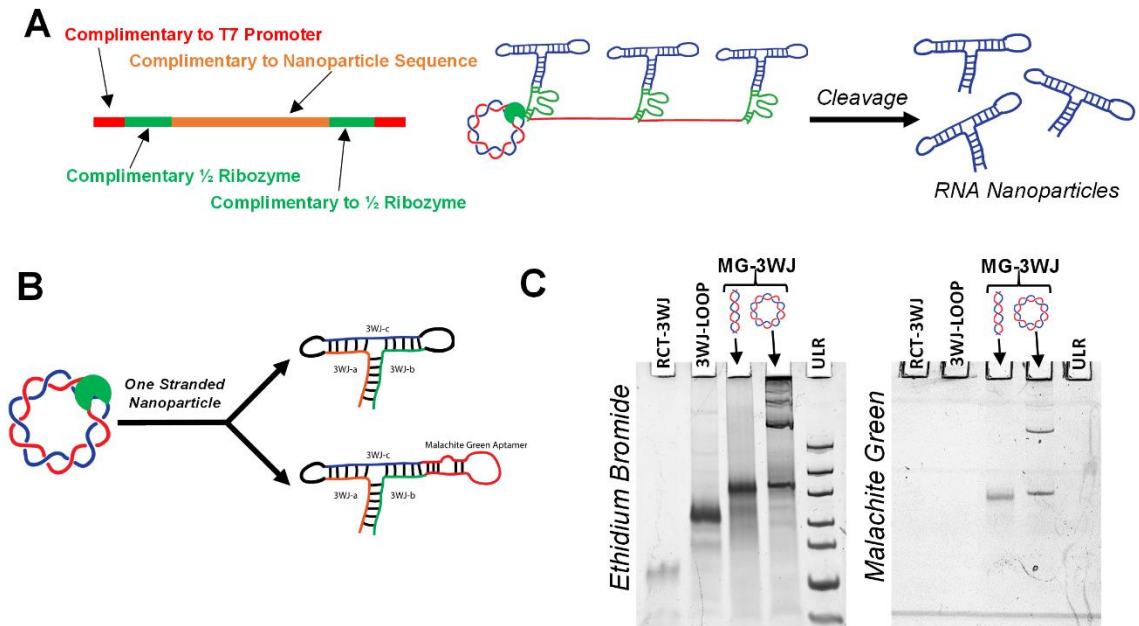


Figure 5.3: One-Strand RNA Nanoparticle Assembly. (A) Schematic for modified design of self-cleaving ribozyme. A portion of one ribozyme is positioned 5' of the nanoparticle sequence while the other portion is located 3' of the nanoparticle sequence. Self-cleavage occurs after transcription of the entirety of the dsDNA template. (B) Circular dsDNA was assembled to code for the 3WJ and MG-3WJ nanoparticles assembled from one long piece of RNA. (C) PAGE gels showing assembly of the one-stranded nanoparticles. Gels were stained with both ethidium bromide (total RNA) and MG dye, which shows correct folding and release of the nanoparticles.

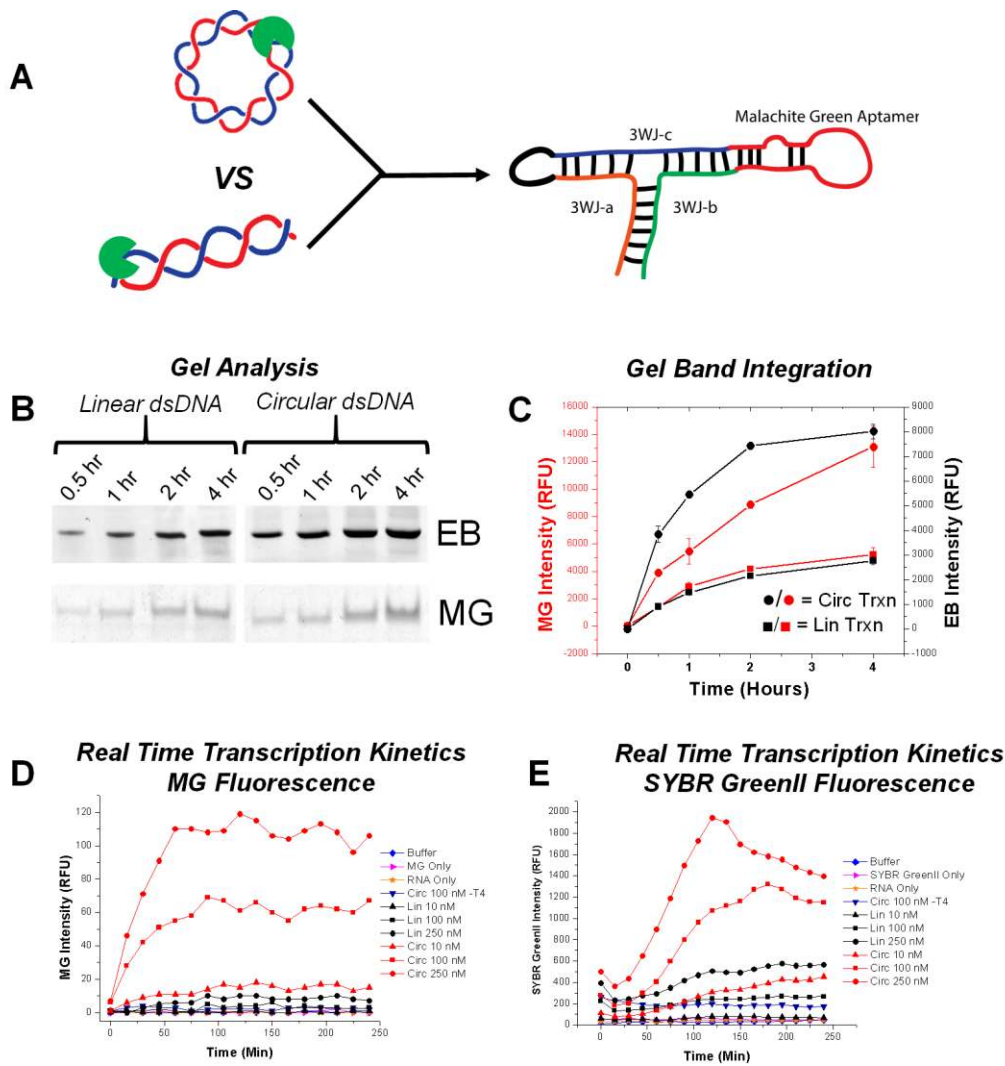


Figure 5.4: Transcription Kinetics. (A) Comparison of linear transcription and circular transcription. MG-3WJ was used as fluorescence can be an indicator for the progression of transcription. (B, C) Gel analysis of transcription. Bands were integrated and plotted. (D, E) Monitoring of transcription using MG fluorescence (specific to nanoparticle folding, panel D) and SYBR GreenII (RNA specific, panel E).

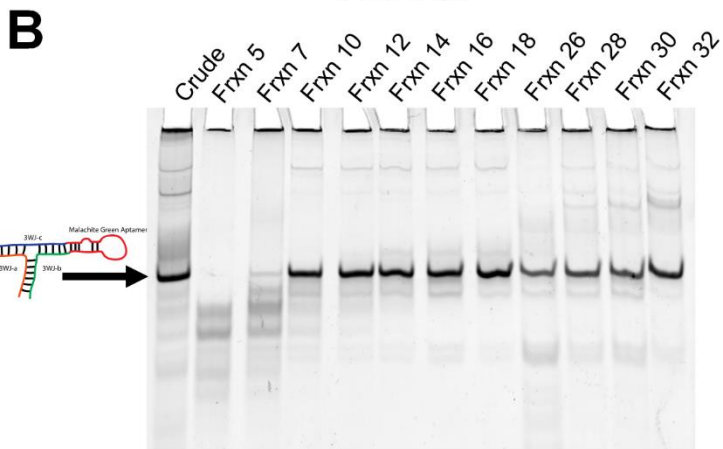
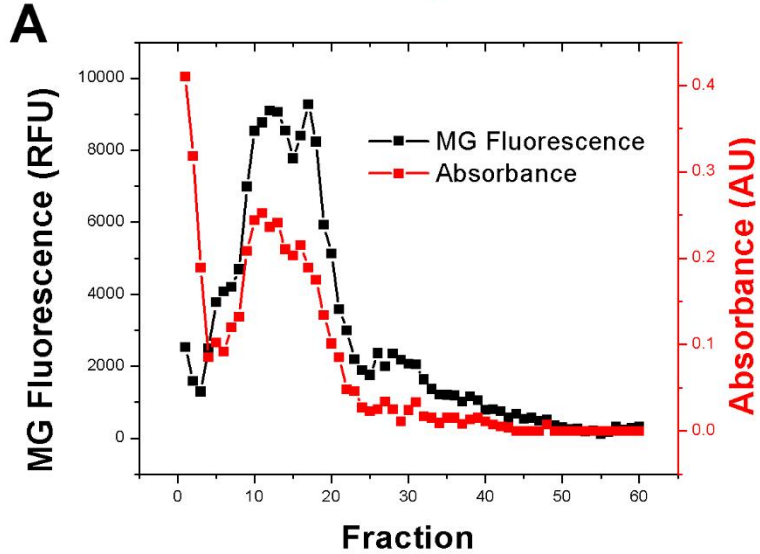
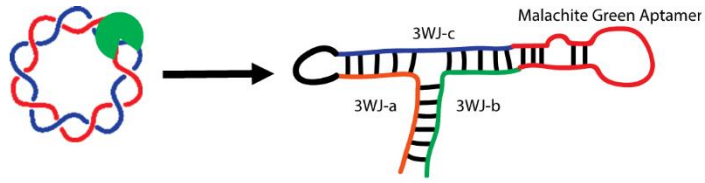


Figure 5.5: Gel-electrophoresis Column Purification. (A) MG fluorescence and absorbance at 260 nm were used to analyze fractions after purification. (B) PAGE gel analysis determines the identity of the peaks from fluorescence and absorbance analysis.

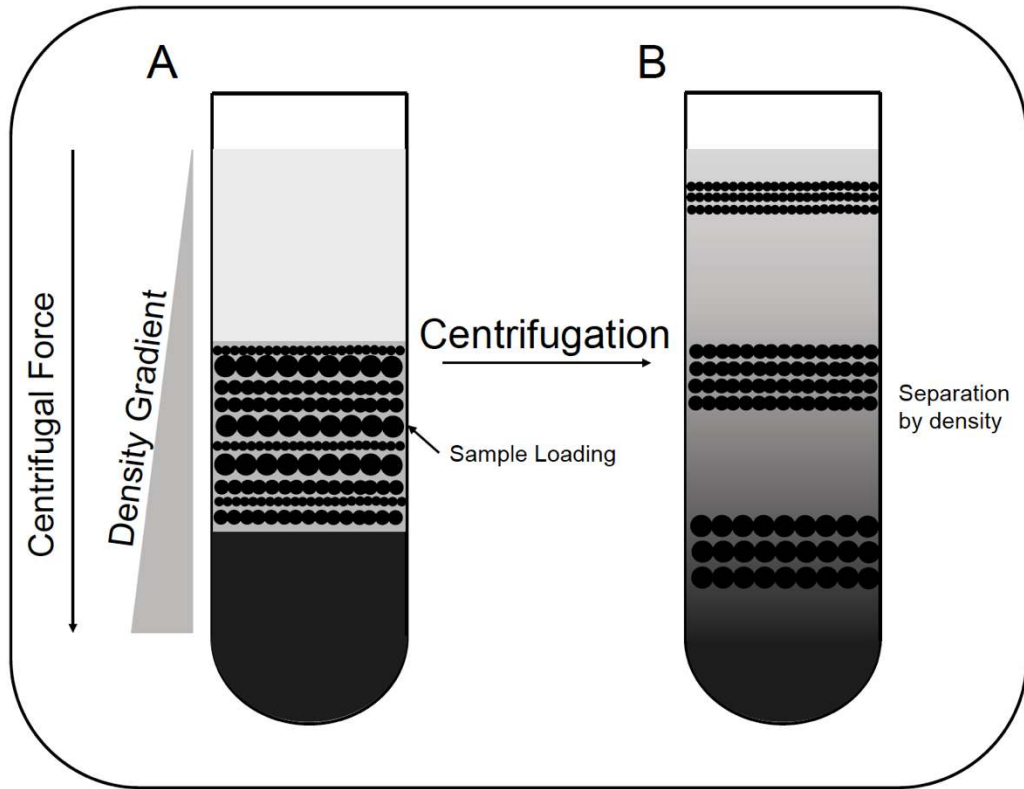


Figure 5.6. Mechanism for CsCl equilibrium density gradient. (A) Different densities of CsCl salt solution are loaded into centrifuge tube with sample in medium density solution. (B) Post centrifugation, when equilibrium is reached, a gradient is formed with the migration of particles separating by their density (specific gravity).

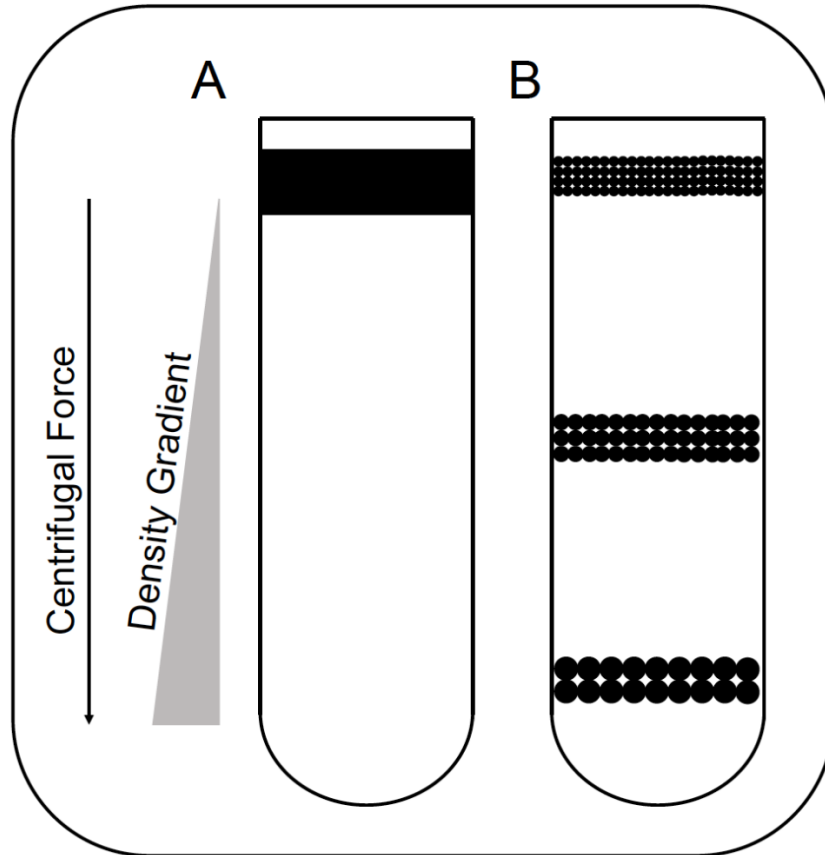


Figure 5.7. Mechanism of separation for sucrose gradient rate-zonal ultracentrifugation. (A) Before centrifugation, the sample is loaded on the top of the gradient in a thin band. (B) After centrifugation, the particles separate based on shape and mass. Higher mass particles migrate faster to the higher density portion of the gradient and lower mass particles stay in the lower density portion at the top of the gradient.

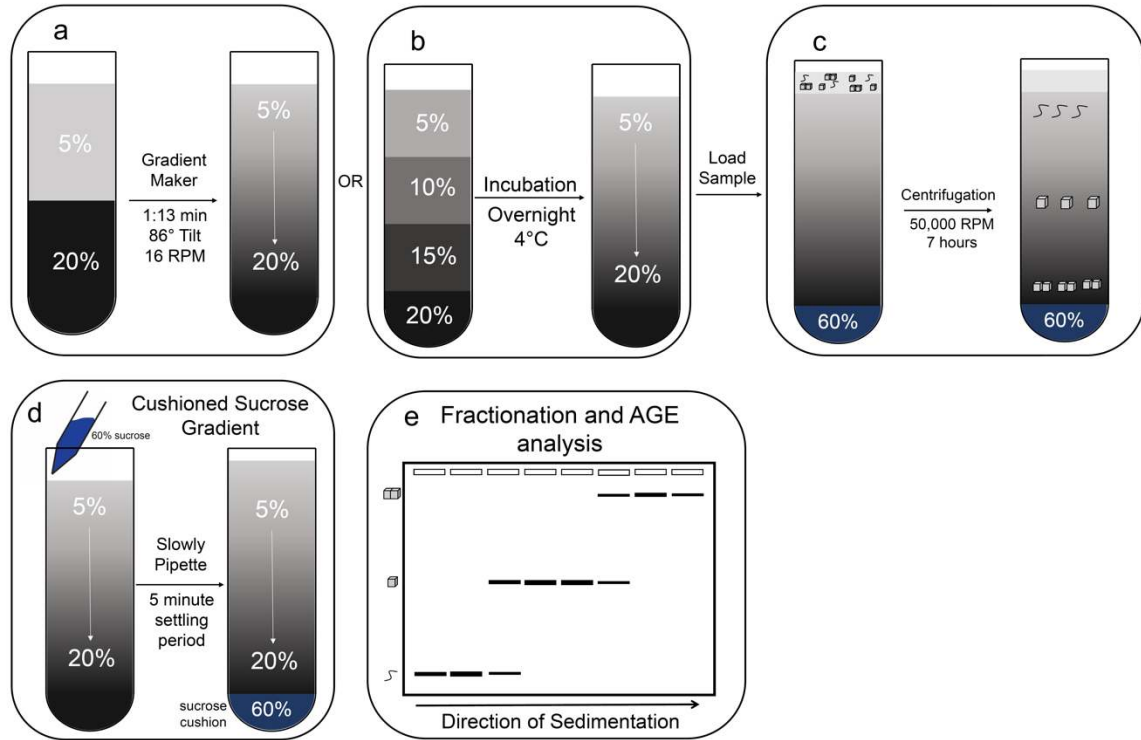


Figure 5.8. Gradient formation, sample loading and analysis scheme of sucrose gradient rate-zonal ultracentrifugation and expected results. (A) Formation of gradient by automated gradient maker. **(B)** Formation of gradient by manual layering. **(c)** Sample is loaded in a thin band on top of the gradient. After centrifugation the particles are separated by size. **(D)** Alternate method for the formation a cushioned sucrose rate-zonal density gradient using 60 % sucrose solution pipetted to the bottom of a preformed sucrose gradient. **(E)** Expected AGE analysis results. AGE analysis reveals the identity of each fraction. After AGE analysis the target particle fractions are combined and concentrated.

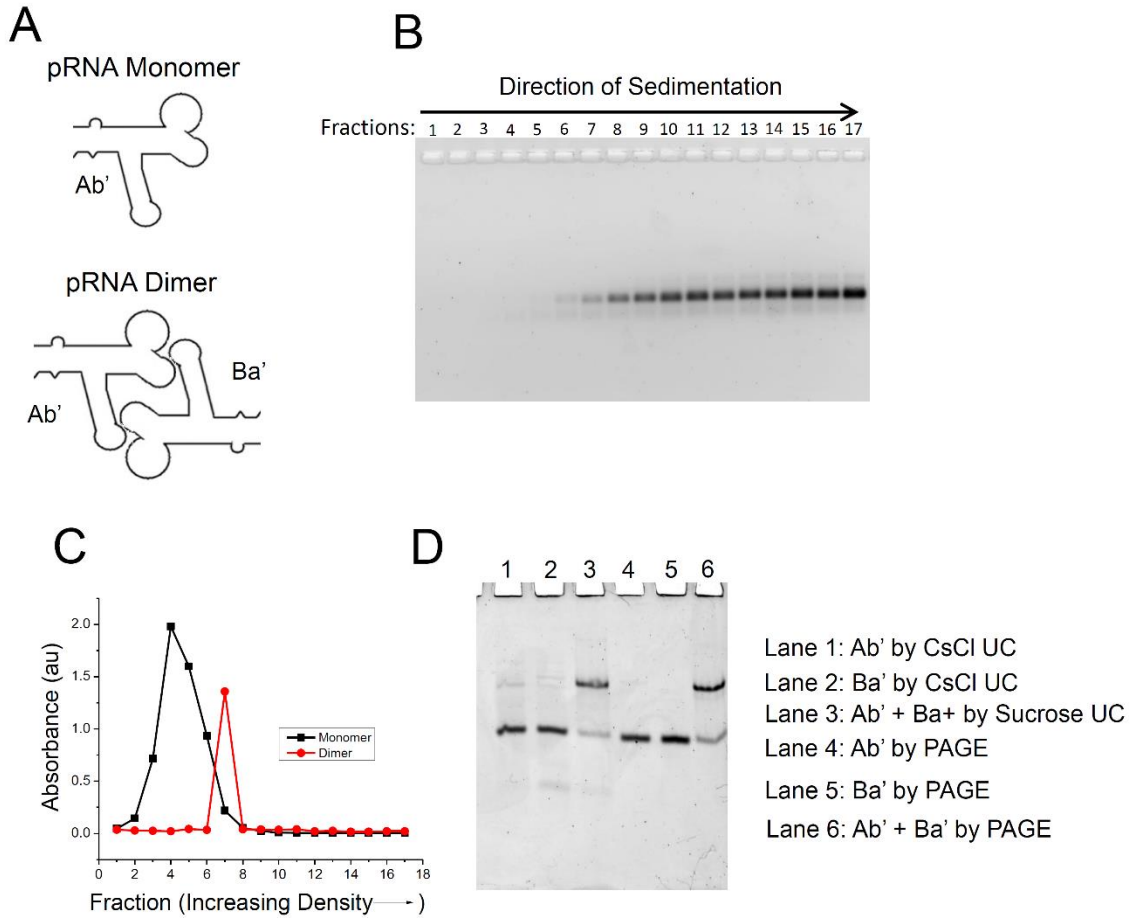


Figure 5.9. pRNA monomer and dimer purification. (A) Schematic Representation of pRNA monomer (Ab' and Ba') and dimer complex (Ab'-Ba'). The pRNA dimer is formed by two distinct pRNA monomers, termed Ab' and Ba' (B) The two pRNA monomers are purified by CsCl density gradient ultracentrifugation and analyzed by agarose gel electrophoresis. The monomer sedimented toward the bottom of the tube, an example of differential centrifugation. (C) 5–20 % sucrose gradient was used to purify the pRNA dimer complex (*red*). As a reference, pRNA monomer was also examined under the same conditions (*black*). (D) Post centrifugation, fraction 7 was recovered and native PAGE was used to examine the assembly of pRNA dimers purified by ultracentrifugation (UC, *Lane 3*) compared to those purified by PAGE (*Lane 6*). *Lanes 1* and *2* are pRNA monomers

purified by CsCl ultracentrifugation, used as size controls in the gel; *Lanes 4 and 5* were purified by PAGE as a comparison to results obtained by purification using ultracentrifugation. Comparable assembly of the pRNA dimer complex is observed between each method

Chapter 6: Summary of Thesis Achievements and Outlook

This chapter was reproduced (with some modification) with permission from Jasinski, D; Haque, F; Binzel, DW; and Guo, P. “Advancement of the Emerging Field of RNA Nanotechnology.” *ACS Nano*, 2017. DOI: 10.1021/acsnano.6b05737. Copyright 2017 American Chemical Society.

SUMMARY:

This thesis work describes the development of RNA nanoparticles with diverse and controllable sizes, shapes, and physical properties. Before this work, RNA nanotechnology was somewhat limited in its diversity of nanoparticles. As mentioned previously, size and shape diversity are paramount for *in vivo* drug delivery systems, since these properties have profound effects on biodistribution, circulation time, toxicity, and interactions with the *in vivo* environment. Thermodynamically stable and serum resistant 2'F RNA triangles, squares, and pentagons were constructed using a modular design approach with the pRNA-3WJ as the base unit. The same angle of the 3WJ was used to construct the nanoparticles, displaying diversity in shape from one RNA motif. Nanosquares were tuned in size by modulating RNA duplex length between adjacent 3WJ modules. The nanosquares displayed homogeneous size and narrow size distribution, as evidenced by DLS measurements. Upon IV administration of the diverse size RNA nanosquares, differences in biodistribution profiles were seen. A strong correlation between increased size of nanosquares and increased circulation time is evident by time course fluorescent images of mice whole body and organs. While triangle, square, and pentagon RNA nanoparticles

demonstrated similar biodistribution after 24 h, different fluorescent intensities in organs at 12 h suggest diverse elimination pathways. The tunable nature of RNA nanoparticles lends this platform advantages when precise control over size, and therefore *in vivo* properties, is desired. Additionally, 3D RNA nanoprisms were constructed and used for a unique small molecule encapsulation technique. A fragile RNA aptamer enclosed within the stable frame of the nanoprism protected the small molecule cargo from degradation and prevented leaking of the small molecule drug. Finally, a method for the large scale *in vitro* production of RNA nanoparticles was developed. Rolling circle transcription (RCT) was used to transcribe fully double stranded circular DNA encoding for self-cleaving ribozymes to release target RNA. The target RNA was either single stranded RNA oligomers, which co-transcriptionally assembled into RNA nanoparticles, or one-stranded RNA nanoparticles, which also folded co-transcriptionally and produced functional RNA nanoparticles.

RNA NANOTECHNOLOGY OUTLOOK:

RNA nanotechnology for drug delivery has garnered much attention recently as it has tremendous potential to help treat many diseases. Certainly, improvements are necessary to push this innovative platform towards clinical trials and bring the product to the market. Some of the challenges and possible solutions are discussed below.

Limited therapeutic payload

Currently, RNA nanoparticles have limited small molecule drug loading capacity. Single drugs can be labeled onto the terminal ends of RNA strands and incorporated into RNA nanoparticles. Whole chain labeling methods can increase chemical drug payload, but can cause misfolding of RNA nanoparticles due to steric hindrance and compromise

the release of the drugs. Computational approaches can help to identify locations where drugs can be introduced without disrupting the folding of the nanoparticle. Ensuring the drugs are orientated out of plane from the RNA nanostructure can also minimize any structural defects in the scaffold.

Intercalation is another viable approach to increase drug loading capacity, but drug release profiles need to be closely evaluated as premature release of the drug leads to non-specific side effects. For instance, if the pRNA-3WJ nanoparticle is used as a delivery vector for targeting solid tumors, the projected half-life of the intercalated drug release should be more than 4 h, as extensive biodistribution studies revealed that the vast majority of the systemically administered pRNA-3WJ nanoparticles localize in the tumor site within 1-4 hrs.

RNAi is considered the next frontier of cancer therapy, and is thought by many to have potential to “drug the undruggable.” However, like chemical drug conjugation, RNA nanoparticles are limited in the number of RNAi molecules that can be delivered to cells. However, this limitation may not be an issue as studies report that there are only about 10^3 – 10^5 Dicer molecules per cell and oversaturation of therapeutic RNAs can lead to non-specific binding and off-target gene knockdown (308). Too much shRNA delivered to cells can cause cytotoxic effects (309), thus, a lower payload of RNAi may not be an issue in the end. However, nanoparticle systems such as RNA microsponges have the potential for delivering high payloads of siRNAs (38) and their utility in broader preclinical studies will be improved if the particle size can be reduced to avoid organ accumulation.

Endosome escape to fulfill the promise of RNAi

Like most nanoparticle platforms, RNA nanoparticles enter cells through receptor-mediated endocytosis. Thus, intracellular RNA nanoparticle trafficking becomes the next challenge. Early endosomal vesicles are the first destination of RNA nanoparticles. Once sorted, RNA nanoparticles are transferred to late endosomes and lysosomes, where they are trapped without reaching their intended target. Fortunately, endosomal escape using small 8-nt anti-miRNA LNA fragments in RNA nanoparticle delivery was successful and cancer regression efficient (58), but the efficacy of endosomal escape of siRNA in RNA nanoparticles is still unknown as cancer regression after siRNA delivery *via* receptor mediated endocytosis is relatively low (56,310). To date, there is very limited knowledge on different cellular endocytosis or internalization pathways that govern subsequent intracellular processing and endosomal escape of RNA nanoparticles. Nevertheless, there are well-characterized tools available to enhance endosome escape such as chemical functional groups including acid-cleavable and pH sensitive (311). The pH-sensitive materials undergo high amounts of protonation thereby inducing an influx of ions into the endosome, resulting in osmosis and endosome rupture - referred to as 'proton-sponge' effect.

Large-scale production and purification of RNA nanoparticles

One of the major bottlenecks for future clinical applications is the large-scale production, large-scale purification, and cost of RNA nanoparticle production. Typically, RNA nanoparticles are designed to be modular composed of multiple short strands that are well within the limits of chemical synthesis (maximum of 80 nt). Over the years, the cost of RNA oligo synthesis has progressively decreased due to improvements in chemical synthesis efficiency. However, large-scale purification remains a challenge. HPLC and gel

electrophoresis purification have limited capabilities with somewhat low yields. Due to the special nature of RNA nanotechnology, the size of the assembled nanoparticle is significantly different from its building blocks, thus, preparative ultracentrifugation has recently been employed (312) and looks to be a promising approach for purification of fully assembled RNA nanoparticles with high yield.

CONCLUSIONS:

RNA nanotechnology has come a long way since its inception in 1998 (12). Some of the most exciting advancements happened only within the last five years. The design of elegant nanostructures with precise arrangement of functional modules in 3D space and self-assembly in a programmable 4D structure with controlled manner have greatly advanced the field. Progress in the understanding of the principle for structure-based design will enhance the capacity to make more intricate RNA nanoparticles with diverse function that one day can mimic naturally occurring RNA nanomachines like the ribosome. RNA nanoparticles display many advantages over other nanoparticle systems; however, the development of RNA nanoparticles as drugs lags behind that of liposome and polymer systems, which have been in clinical trials for years. To reach clinical applications, the development of RNA nanoparticles should broaden beyond that of just their construction and focus more on applying the advantages of RNA nanotechnology.

FUTURE STUDIES:

Chapter 2 details a novel modular design technique for constructing RNA nanoparticles followed by a unique multi-strand assembly process that results in stable and tunable nanoparticle scaffolds. This method has been well developed, and the construction of RNA nanoparticles with tunable size, shape, and stabilities has been realized. This

system allows a platform for studying how nanoparticle properties affect *in vivo* PK/PD properties.

However, further development and optimization of this nanoparticle platform is still preferable. For example, stretching of the 3WJ angle was shown to decrease stability, despite increasing the number of base pairs and theoretical stability based on nearest neighbor parameters. In-depth investigation of this phenomenon is desirable. It is apparent that the stretching of the 3WJ angle is causing the decrease in stability, therefore, modifying the 3WJ could be one possibility to retain stability despite angle stretching. One possible way in which this could be accomplished is adding flexibility to the inner angles of the 3WJ by addition of unpaired uracil bases, a common bulge seen in RNA structures that imparts flexibility into their 3D conformations.

In addition to increasing flexibility of the 3WJ, and in turn increasing the stability of the nanoparticles constructed from this 3WJ, nanoparticle rigidity has been shown to influence interactions with the immune system. We believe these nanoparticles to be relatively rigid and locked into their geometrical configurations. By imparting flexibility into the 3WJ module, it is possible that flexibility could be introduced into the higher order nanostructures, thus reducing interaction with the immune system and possible toxicity caused by the nanoparticles *in vivo*.

Future work utilizing these nanoparticles also lies on the biological side. That is, a systematic study utilizing this platform could result in a full set of size/shape/property relationships with other factors such as biodistribution, cellular entry pathways, and drug delivery efficacies. More work needs to be done studying how physical properties can influence the way in which RNA nanoparticles enter cells, as cell entry pathways go a long

way in determining therapeutic effect. By studying a property-efficacy relationship, it could be possible to optimize the drug delivery pathways for numerous cell and cancer types.

While the biodistribution studies in this thesis demonstrate a clear relationship between increased size of RNA nanoparticles and their increased circulation time, fluorescence is not a quantitative measure. Despite using near-infrared fluorophores, which have shown potential penetration depths of up to 5-7 mm (307), quantitative labeling, such as radiolabeling, could show statistical differences in nanoparticle accumulation in organs and tumors among diverse nanoparticles. Additionally, more investigation to reveal a molecular basis for different biodistributions of different size and shape RNA nanoparticles would be extremely beneficial for our understanding of RNA nanoparticle interaction with the *in vivo* environment.

The overall goal of nanotechnology is to increase delivery efficacy of the administered dose of therapeutic, whether it be chemical drug, protein therapeutic, or RNAi. However, as nanoparticles have significant size, the immune system recognizes nanoparticles as foreign objects, thus engulfing them in macrophages, filtering them out through the kidneys, or if they enter cells, sequestering them in organelles such as endosomes and lysosomes, where they are eventually degraded. This drastically reduces the amount of therapeutic that can be effective. To this point, the cellular trafficking pathways of RNA nanoparticles is not known. Due to the fact that many RNA nanoparticles use chemical ligands or RNA aptamers to enter cells, it is assumed that the particles enter the cells *via* receptor mediated endocytosis, where they are most likely trafficked to endosomes and degraded by the acidic environment. It is a necessary step to determine how

RNA nanoparticles are trafficked. Once this step has been taken, it will be possible to examine how nanoparticles with different sizes, shapes, and physical properties (ie stability, hydrophobicity, solubility, charge, etc) enter cells, and which particles show the largest advantages in regards to drug delivery efficacy. With all these factors taken into consideration, it could be possible to optimize which particles to use to maximize cellular entry and drug efficacy. According to literature on other nanoparticle systems, the smaller particles will enter cells to a higher degree. However, as shown in this thesis, the smaller particles appear to circulate out of the body faster. Thus, a balance should be struck between circulation time, cellular entry and entrapment, and accumulation in healthy organs such as the liver, spleen, and kidneys.

In this thesis was also demonstrated a novel method for the protection of a small molecule model drug by binding to a fragile RNA aptamer inside a stable RNA nanoparticle frame. This study is the first to show encapsulation of a small molecule within an RNA nanocage. However, the increase in half-life needs to be extended to at least 4 hours, as this is the time it takes for RNA nanoparticles to circulate to tumors and accumulate in an amount high enough to be therapeutically relevant. Other techniques, such as developing more stable aptamers to hold their small molecule cargo more tightly, or construction techniques to prevent breathing of the stable frame and invasion by nucleases, could help to overcome this challenge. It is possible that this system could be extremely helpful in the delivery of vaccines and other protein cargoes to specified targets. Preventing off target effects of proteins is extremely important as some potent proteins can cause high immune responses *in vivo*.

Finally, this thesis demonstrated a method for large-scale *in vitro* synthesis and purification of RNA oligomers and RNA nanoparticles. This method overcame the hurdle of transcribing a ssDNA sequence with stable secondary structure by constructing circular double stranded DNA. Despite this advancement, the resulting nanoparticles will be susceptible to degradation *in vivo*, as they are not chemically modified after the RCT and ribozyme cleavage process. Currently, there are no ribozymes available that are both 2'F modified and can cleave 2'F RNA. It is conceivable that this type of ribozyme could be made by *in vitro* selection (SELEX). Following the selection of a modified ribozyme, this process would result in the production of a high yield of RNA nanoparticle that could be used in nanomedicine and biomedical applications. Additionally, this method is currently challenged by the cost of synthesizing long single stranded DNA oligoes. A new method of double stranded circular DNA synthesis, such as the assembly of multiple short DNA oligoes into circular double stranded DNA, would be beneficial to reduce cost of DNA preparation.

It is possible that the increased production of RNA nanoparticles could decrease their folding efficiency. Certain downstream steps of nanoparticle synthesis could be necessary to produce the high-quality RNA nanoparticles constructed from traditional methods. This could be achieved by thermal denaturation followed by a typical annealing procedure. Thus, all mis-folding occurring from expedited transcription rates would be avoided.

In addition to *in vitro* methods for RNA nanoparticle synthesis, the RCT method developed in this thesis will also lend itself to *in vivo* production of stable RNA nanoparticles. This would allow RNA nanoparticles to be produced by bacterial cells, thus

drastically increasing production scale and drastically decreasing cost. However, to produce 2'F modified nanoparticles for use in nanomedicine, bacterial cells would need to be modified in order to produce and incorporate modified nucleotides. While the challenge of this project is significant, it is not at all impossible due to the increased knowledge and techniques of bacterial engineering and molecular engineering. If this bacterial engineering project were to be achieved, the cost and scale-up challenges of RNA nanoparticle production would be eliminated, thus allowing a clear path to clinical translation and testing of RNA nanoparticles.

Appendix 1: Supplemental Data for Chapter 2

Appendix 1 was reproduced (with some modification) with permission from: Khisamutdinov, EF*; Li, H*; Jasinski, DL*; Chen, J; Fu, J; and Guo, P. “Enhancing immunomodulation on innate immunity by shape transition among RNA triangle, square, and pentagon nanovehicles.” *Nucleic Acids Research*, 2014. 42(15), 9996-20004. DOI: 10.1093/nar/gku516. Copyright 2014 Oxford Publishing; Jasinski, DL; Khisamutdinov, EF; Lyubchenko, YL; and Guo P. “Physicochemically tunable polyfunctionalized RNA square architecture with fluorogenic and ribozymatic properties.” *ACS Nano*. 2014. 8(8), 7620-7629. DOI: 10.1021/nm502160s. Copyright 2014 American Chemical Society. Chemical Society. Special thanks to Dr. Emil F. Khisamutdinov for help in preparation of data for figures A.1.3.

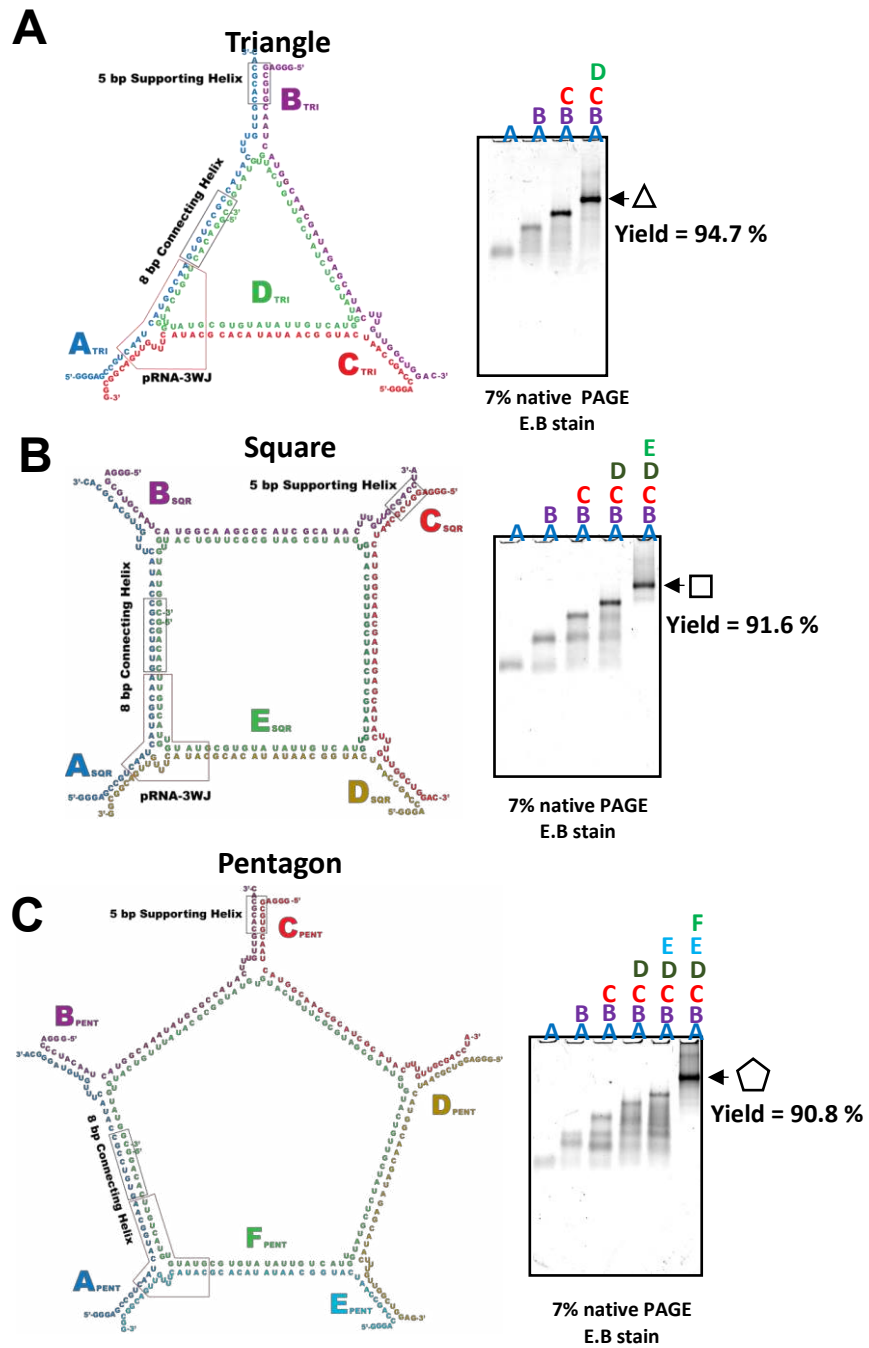


Figure A.1.1. Sequences and secondary structures of RNA polygons. RNA polygons and quantified assembly yields (a) triangle, (b) square and (c) pentagon.

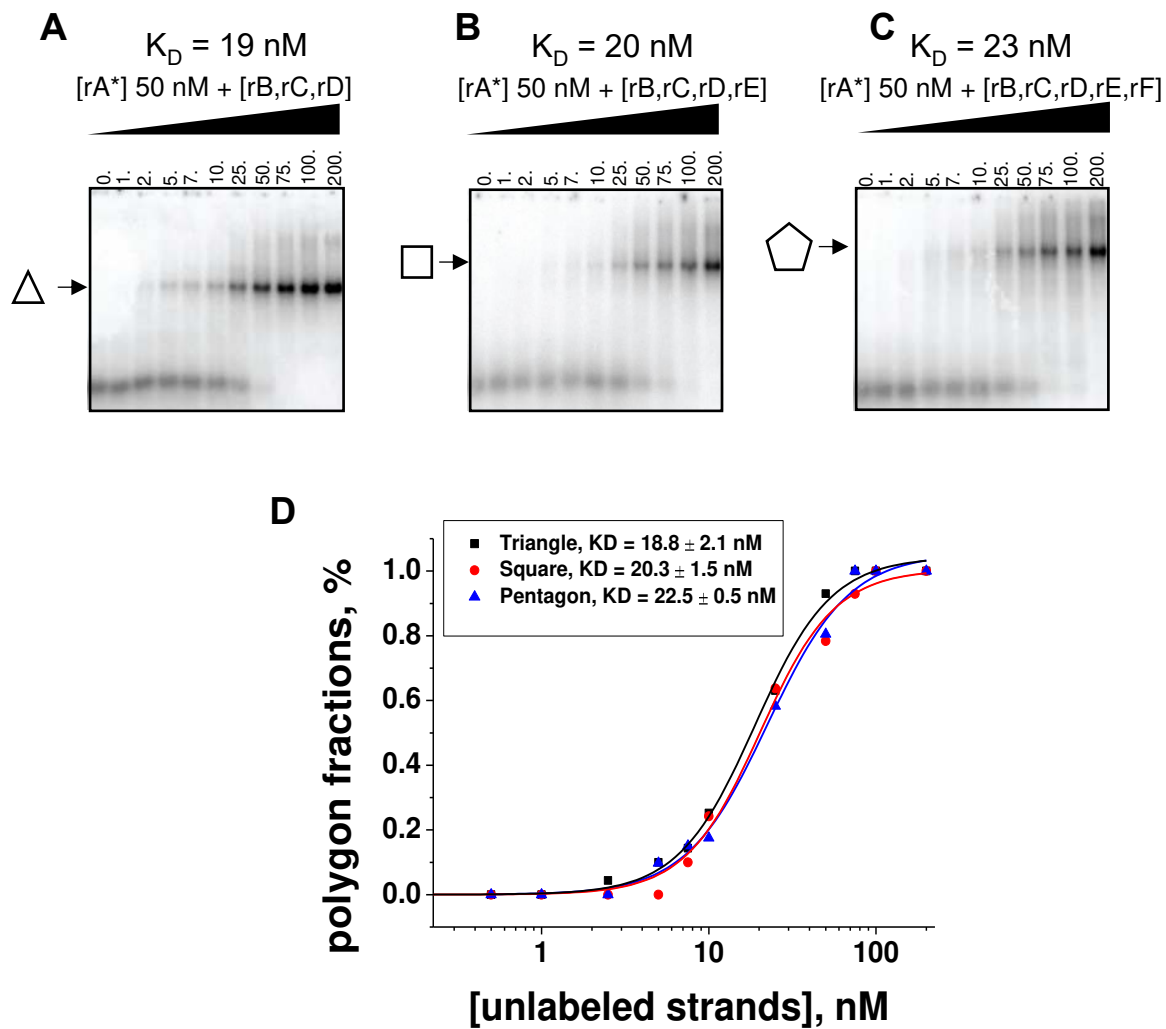


Figure A.1.2. RNA polygons dissociation constant determination. From left to right, 7% Native PAGE gels titration data for formation of triangle, square, and pentagon polygons. Below, the gels is the plot used to determine the equilibrium concentration for each polygon which were then used to calculate the apparent dissociation constant.

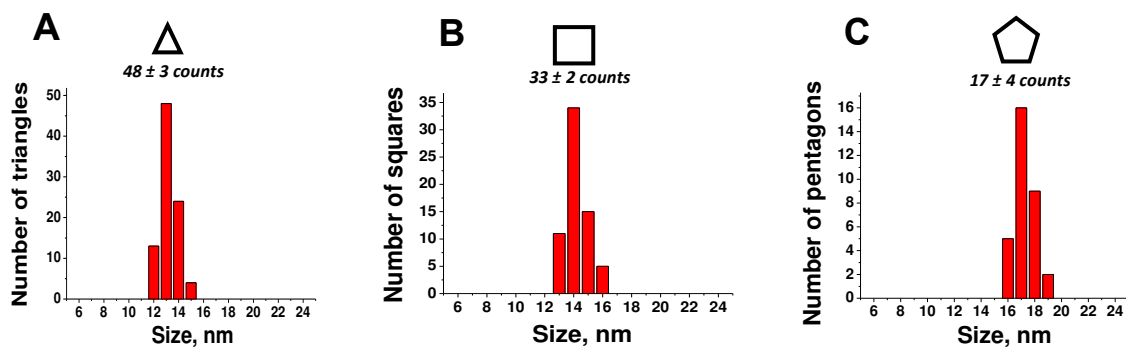


Figure A.1.3. AFM images of RNA polygons. Population distribution of RNA triangle (a), square (b), and pentagon (c) polygons per 0.5 mm^2 of mica surface obtained from AFM analysis.

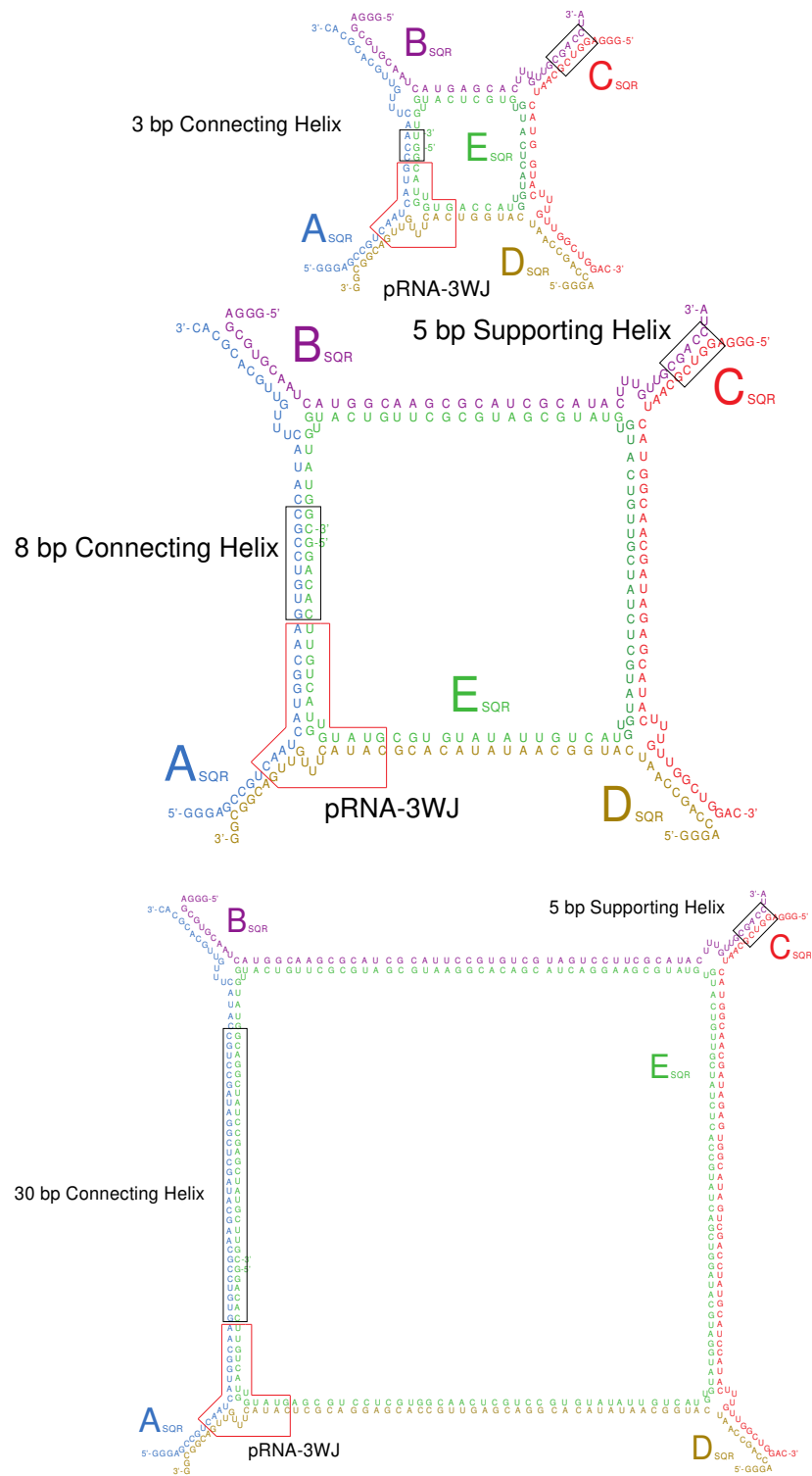


Figure A.1.4. Secondary structure and sequences for 5, 10, and 20 nm RNA nanosquares.

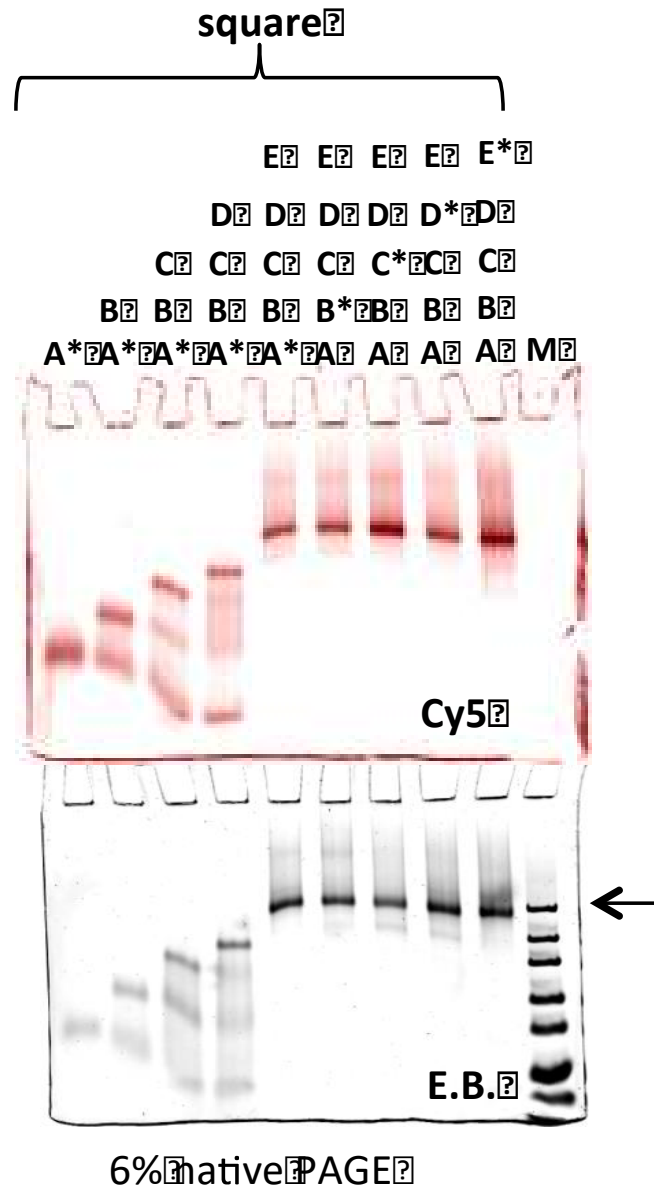


Figure A.1.5. Total strand participation in square assembly. 7% native PAGE and whole chain Cy5 labeling were used to confirm the participation of each strand in the assembly of the square nanoparticle. Each strand was individually end radiolabeled and the radiolabeled strand was varied for each sample. The “*” denotes which strand is labeled. The first four lanes show the stepwise assembly of the RNA square.

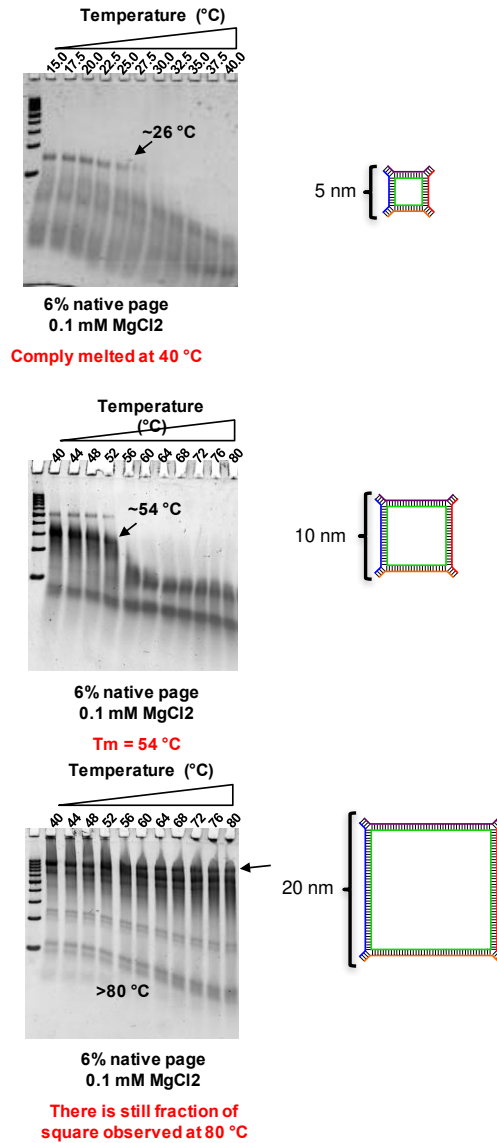


Figure A.1.6. Melting temperature profiles of small, medium, and large squares.

Melting temperature = 50% Square Formation). The small square (top panel) melted at ~26 °C, the medium square (middle panel) melted at 54 °C, and the large square (bottom panel) still showed square fractions at 80 °C, indicating melting temperature above 80 °C.

All nanoparticles were assembled in Tris-HCl buffer containing 100 mM NaCl and 0.1 mM MgCl₂ at 0.5 μM RNA concentrations.

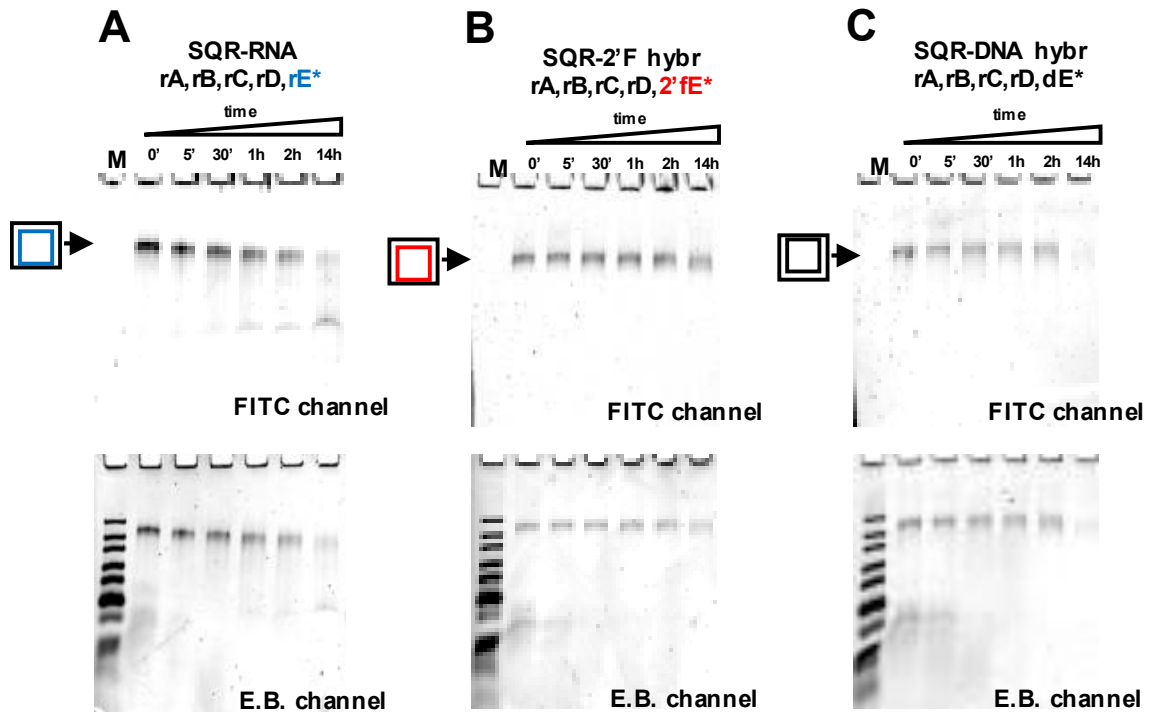


Figure A.1.7. Fetal bovine serum (FBS) degradation testing of square nanoparticle hybrids: RNA (A), 2'F Hybrid (B), DNA Hybrid (C). The top row of gels is scanned for FITC signal and bottom row gels are scanned for total RNA by ethidium bromide staining. ImageJ software was used to integrate the intensities of the FITC bands and then compared to untreated integration to calculate the percent degradation of each hybrid at specified time points.

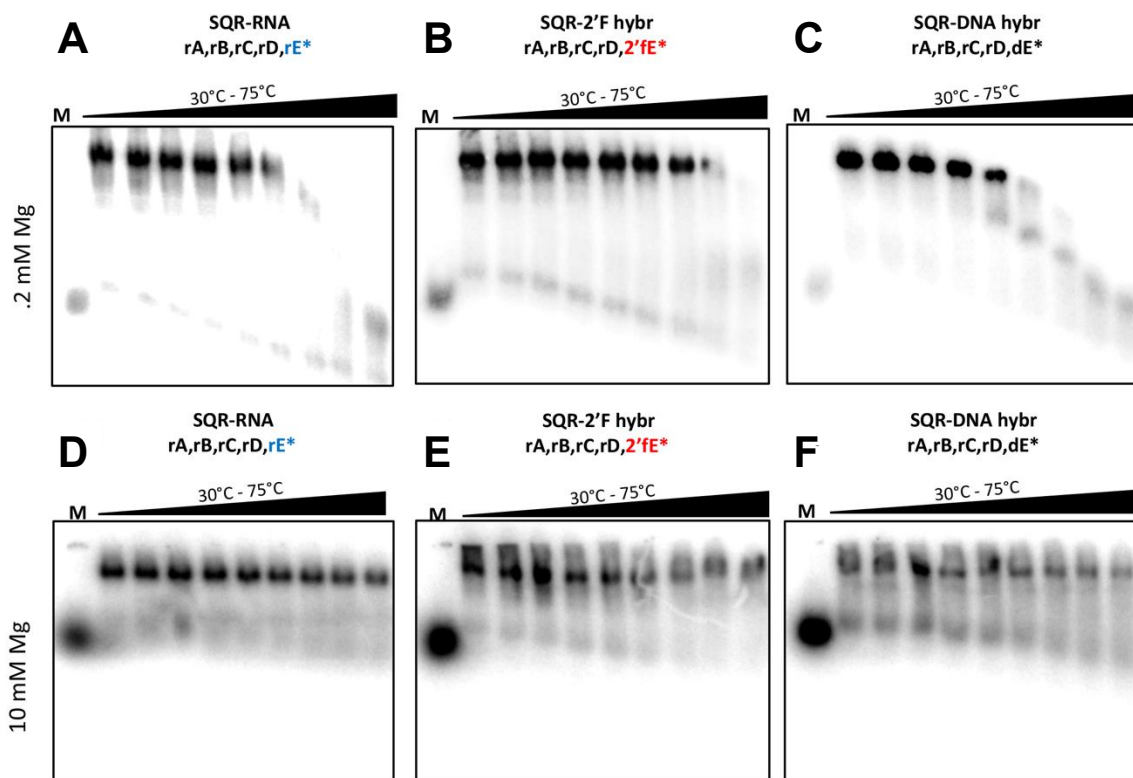


Figure A.1.8. Temperature gradient gel electrophoresis (TGGE) analysis of total RNA square (A, D), 2'F RNA hybrid square (B, E), and DNA hybrid square (C,F). A, B, and C were carried out under .2 mM Mg ion concentration conditions and D, E, and F were carried out under 10 mM Mg ion conditions. A temperature gradient, perpendicular to electric current, of 30°C - 75°C was used to determine the melting temperature of the three square nanoparticles. ImageJ software was used to analyze the gels and integrate the intensities of the bands. Melting temperatures were taken to be 50% square formation compared to 100% formation in lane two. Lane one in each gel represents a single short strand monomer RNA strand. 5'-[γ -³²P]-ATP labeling was used with a total RNA concentration of 80 nM. In D, E, and F no melting temperature is reached under 10 mM Mg ion conditions.

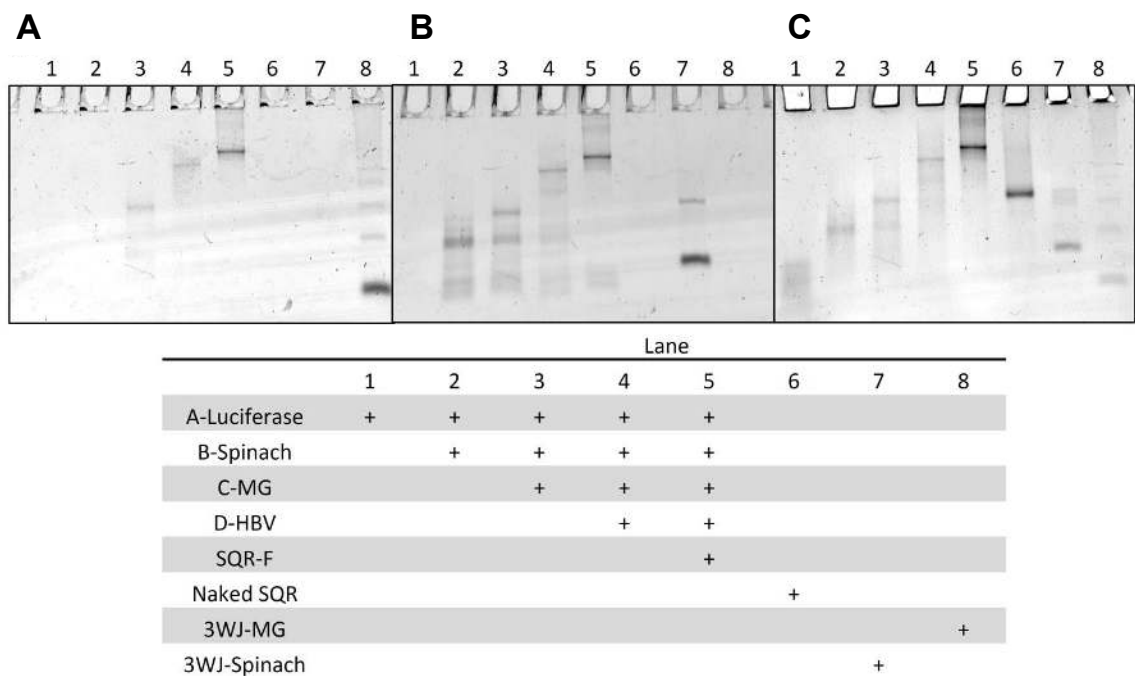


Figure A.1.10. Fluorescence signal testing in native PAGE. MG dye stain (A), Spinach dye stain (B), and total RNA by ethidium bromide staining (C). 7% native PAGE was run with stepwise assembly of the multifunctional square nanoparticle. The gel was then simultaneously stained with MG and Spinach dyes and scanned for both signals separately. The gel was then total RNA stained with ethidium bromide and scanned for ethidium bromide signal.

Appendix 2: Supplemental Data for Chapter 3

Appendix 2 was reproduced (with some modification) with permission from: Jasinski, DL; Li, H; and Guo, P. “The Effect of Size and Shape of RNA Nanoparticles on Biodistribution.” *Molecular Therapy. Under Revision*. Copyright 2017 Elsevier Inc.; Jasinski, DL; Yin H; Li, Z; and Guo P. “The Hydrophobic Effect from Conjugated Chemicals or Drugs on *in Vivo* Biodistribution of RNA Nanoparticles.” *Human Gene Therapy. Under Revision*. Copyright 2017 Mary Ann Liebert Publishing.

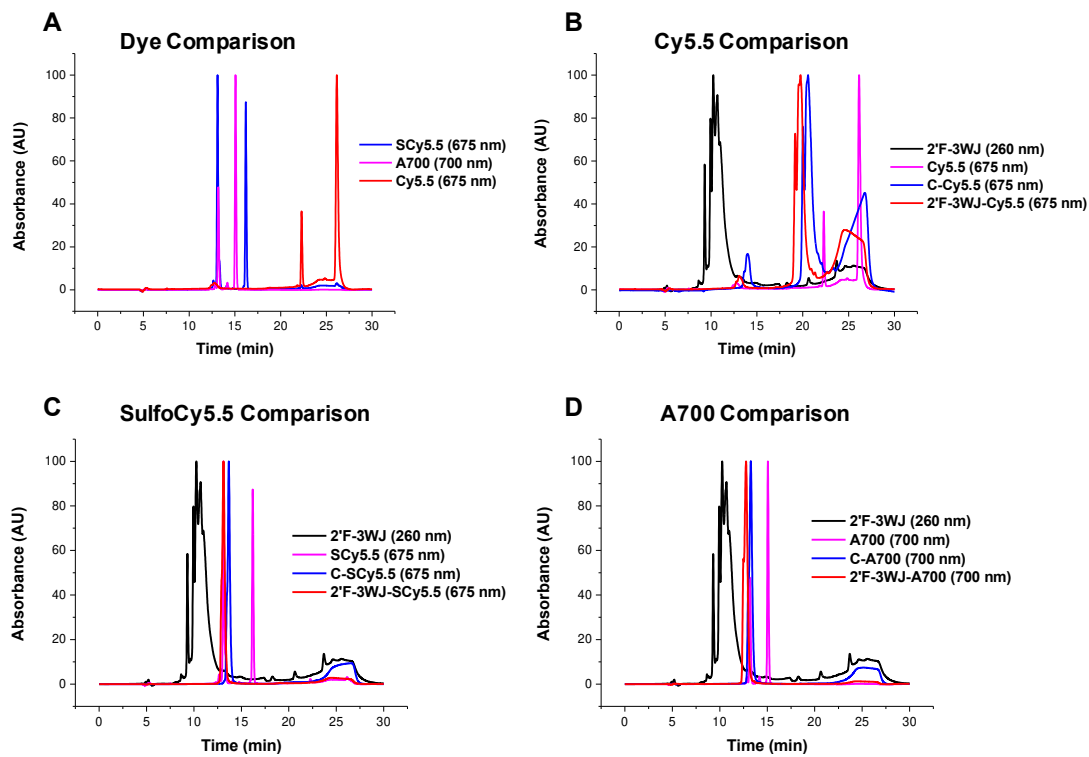


Figure A.2.1. HPLC Hydrophobicity Comparisons. %ACN elution for fluorophores alone (A), Cy5.5 species (B), SulfoCy5.5 species (C), and AlexaFluor700 species (D).

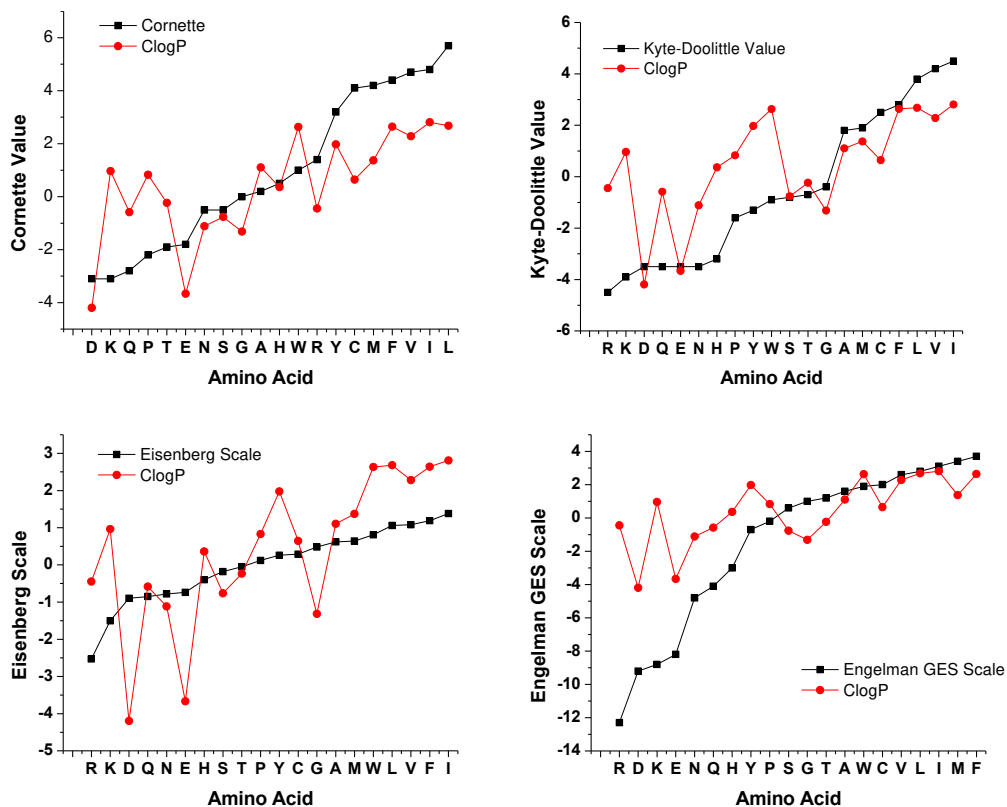
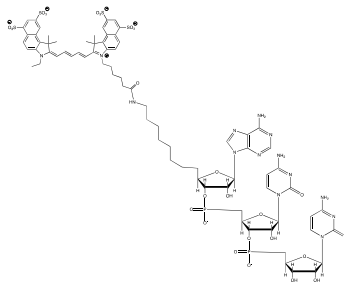
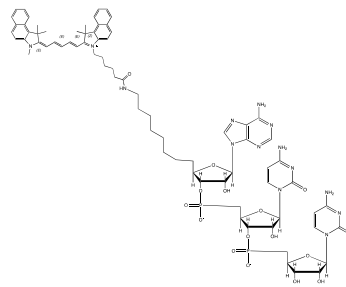


Figure A.2.2. Amino Acid Hydrophobicity Comparison Plots. Predicted ClogP values, determined using ChemDraw Pro 16, were compared to four different previously determined hydrophobicity scales of amino acids. Cornette scale (233) (A), Kyte-Doolittle scale (236) (B), Eisenberg Scale (234) (C), and the Engelman GES scale (237) (D).

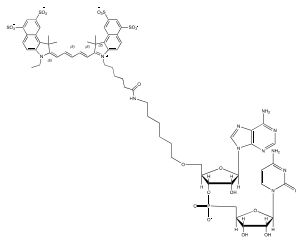
A. Cy5.5 Tri-Nucleotide



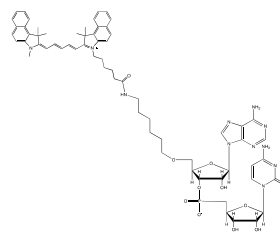
A. SCy5.5 Tri-Nucleotide



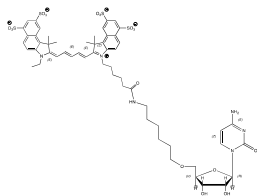
B. Cy5.5 Di-Nucleotide



B. SCy5.5 Di-Nucleotide



C. Cy5.5 Mono-Nucleotide



C. SCy5.5 Mono-Nucleotide

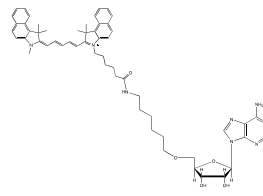


Figure A.2.3. Chemical Structures of Fluorophores and Nucleic Acids. The chemical structures of Cy5.5 and SulfoCy5.5 mono-, di-, and tri-nucleotide derivatives.

Appendix 3: Supplemental Data for Chapter 4

Appendix 3 was reproduced (with some modification) with permission from Khisamutdinov, EF*; Jasinski, DL*; Li, H; Zhang, K; Chiu, W; and Guo, P. “Fabrication of RNA 3D Nanoprisms for Loading and Protection of Small RNAs and Model Drugs.” *Advanced Materials*, 2016. 28(45), 9996-20004. DOI: 10.1002/adma.201603180. Copyright 2016 Wiley Publishing. Special thanks to Dr. Emil F. Khisamutdinov for help in preparation of data for these figures.

Table A.3.1. Prism sequences and control construct sequences.

RNA triangle prism ^A	Nucleic Acid sequence 5' → 3'	
	A	GGCCAGCGAAUCAUGGCCUACGAUUACCAUACUUUGUUAUCGCGUUUUGCGAC UUGUCCACUGCAGGCC
	B	GGCGCGAAUAAUCAUGGCCGUCUCCAGCAUACUUUGUUGAGACCUUUUGAGAC GUACCACGAGCGUACC
	C	GGUCUCAAUCAUGGCACCUACCACGCAUACUUUGUUCGCGUGUUUUUCCAGCU GGCAAGCGCAUUAU
	2xD/d'	GGACACUUGUCAUGUGUAUGCGUGUAUAUUGUCAUGUGUAUGCUCUAUCGUU UCAUGUGUAUGGC
	a'	GGCGUCAAUCAUGGCAAGUGUCCGCCAUACUUUGUUGAGCCUUUUUAUAGCC CUUGCCAAGCUGGG
	b'	GGAAUCAAUCAUGGCAAUUACACGCAUACUUUGUUGAGCGCCUUUUGGCCUGC AGUGGACAACUCGC
	c'	GGGCUCAAUCAUGGCAACGAUAGAGCAUACUUUGUUGAUUCCUUUUGGUACGC UCGUGGUACGUCUC
Prism with RNA MGA		
	A	GGCCAGCGAAUCAUGGCCUACGAUUACCAUACUUUGUUAUCGCGUUUUGCGAC UUGUCCACUGCAGGCC
	B	GGCGCGAAUAAUCAUGGCCGUCUCCAGCAUACUUUGUUGAGACCUUUUGAGAC GUACCACGAGCGUACC
	C	GGUCUCAAUCAUGGCACCUACCACGCAUACUUUGUUCGCGUGUUUUUCCAGCU GGCAAGCGCAUUAU
	D-MGA	GGAAGACGGUCAUGUGUAUGGUAUUCGUAGGUAUGUGUAUGCUGGUUAGGU UCAUGUGUAUGCUUUUUUCGAGGAUCCCGACUGGCAUAG
	a'	GGCGUCAAUCAUGGCAAGUGUCCGCCAUACUUUGUUGAGCCUUUUUAUAGCC CUUGCCAAGCUGGG
	b'	GGAAUCAAUCAUGGCAAUUACACGCAUACUUUGUUGAGCGCCUUUUGGCCUGC AGUGGACAACUCGC
	c'	GGGCUCAAUCAUGGCAACGAUAGAGCAUACUUUGUUGAUUCCUUUUGGUACGC UCGUGGUACGUCUC
d'-MGA	GGACACUUGUCAUGUGUAUGCGUGUAUAUUGUCAUGUGUAUGCUCUAUCGUU UCAUGUGUAUGGCCUUUUUCAUGCCAGGUAACGAAUGGAUCCUCG	
Control open prism #1		
	A	GGCCAGCGAAUCAUGGCCUACGAUUACCAUACUUUGUUAUCGCGUUUUGCGAC UUGUCCACUGCAGGCC
	B	GGCGCGAAUAAUCAUGGCCGUCUCCAGCAUACUUUGUUGAGACCUUUUGAGAC GUACCACGAGCGUACC
	C	GGUCUCAAUCAUGGCACCUACCACGCAUACUUUGUUCGCGUGUUUUUCCAGCU GGCAAGCGCAUUAU
	D-MGA	GGAAGACGGUCAUGUGUAUGGUAUUCGUAGGUAUGUGUAUGCUGGUUAGGU UCAUGUGUAUGCUUUUUUCGAGGAUCCCGACUGGCAUAG
	a'	GGCGUCAAUCAUGGCAAGUGUCCGCCAUACUUUGUUGAGCCUUUUUAUAGCC CUUGCCAAGCUGGG
	B	GGCGCGAAUAAUCAUGGCCGUCUCCAGCAUACUUUGUUGAGACCUUUUGAGAC GUACCACGAGCGUACC
	c'	GGGCUCAAUCAUGGCAACGAUAGAGCAUACUUUGUUGAUUCCUUUUGGUACGC UCGUGGUACGUCUC
d'-MGA	GGACACUUGUCAUGUGUAUGCGUGUAUAUUGUCAUGUGUAUGCUCUAUCGUU UCAUGUGUAUGGCCUUUUUCAUGCCAGGUAACGAAUGGAUCCUCG	
Small prism with RNA MGA		
	A	GGCCAGCGAAUCCUACGACCUUUUGUUAUCGCGUUUUGCGAGUUGUC
	B	GGCGCGAAUAAUCCGUCUCCUUUGUUGAGACCUUUUGAGACGUACC
	C	GGUCUCAAUCAUGGCCACUUUGUUCGCGUGUUUUUCCAGCUUGG
	D-MGA	GACGGUGGUCGUAGGUGUGGUAUGUGGAA UUUUUU GCGUCCGACAUC
	a'	GGCGUCAAUUCUGCCGCCUUUGUUGAGCCUUUUUCAAGCUGGG
	b'	GGAAUCAAUCAUACACCUUUUGUUGAGCGCCUUUUGACAACUCGC
	c'	GGGCUCAAUCAUGAGGCUUUUGUUGAUUCCUUUUGGUACGUCUC
d'-MGA	GACAGUGGUGUAUAGUGCUCUAUCGUGGCG UUUUU GGAUGGUAACGAAUGACGC	

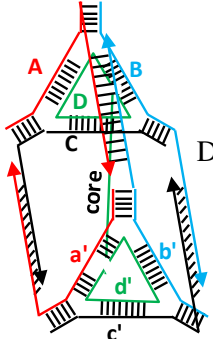
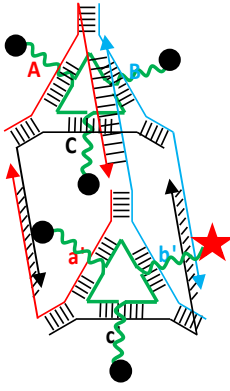
?

Table A.3.2. Sequences of Prism Control Constructs

Control open prism #2		
	2xA	GGCCAGCGAAUCAUGGCCUACGAUUACCAUACUUUGUUAUCGCGUUUUUGCGAC UUGUCCACUGCAGGCC
	2xB	GGCGCGAUAUAUCAUGGCCGUCUCCAGCAUACUUUGUUGAGACCUUUUGAGAC GUACCACGAGCGUACC
	2xC	GGUCUCAAUCAUGGCCACCUACCACGCAUACUUUGUUCGUGUUUUUCCAGCU GGCAAGCGCAUUAU
	D-MGA	GGAAGACGGUCAUGUGUAUGGUAUUCGUAGGUCAUGUGUAUGCGUGGUAGGU UCAUGUGUAUGCUUUUUUCGAGGAUCCCGACUGGCAUAG
	d'-MGA	GGACACUUGUCAUGUGUAUGCGUGUAUUAUUGUCAUGUGUAUGCUCUAUCGUU UCAUGUGUAUGGCCUUUUUCUAUGCCAGGUAACGAAUGGAUCCUCG
Control open prism #3 (dimer)		
	2xA	GGCCAGCGAAUCAUGGCCUACGAUUACCAUACUUUGUUAUCGCGUUUUUGCGAC UUGUCCACUGCAGGCC
	2xB	GGCGCGAUAUAUCAUGGCCGUCUCCAGCAUACUUUGUUGAGACCUUUUGAGAC GUACCACGAGCGUACC
	2xC	GGUCUCAAUCAUGGCCACCUACCACGCAUACUUUGUUCGUGUUUUUCCAGCU GGCAAGCGCAUUAU
	D-MGA	GGAAGACGGUCAUGUGUAUGGUAUUCGUAGGUCAUGUGUAUGCGUGGUAGGU UCAUGUGUAUGCUUUUUUCGAGGAUCCCGACUGGCAUAG
	d'-MGA	GGACACUUGUCAUGUGUAUGCGUGUAUUAUUGUCAUGUGUAUGCUCUAUCGUU UCAUGUGUAUGGCCUUUUUCUAUGCCAGGUAACGAAUGGAUCCUCG
	2xD/d'	GGACACUUGUCAUGUGUAUGCGUGUAUUAUUGUCAUGUGUAUGCUCUAUCGUU UCAUGUGUAUGGC
	2xa'	GGCGUCAAUCAUGGCCAAGUGUCCGCCAUACUUUGUUGAGCCUUUUUAUAGCC CUUGCCAAGCUGGG
	2xb'	GGAAUCAAUCAUGGCCAAUAUACACGCAUACUUUGUUGAGCCUUUUUGGCCUG AGUGGACAACUCGC
	2xc'	GGGCUCAAUCAUGGCCAACGAUAGAGCAUACUUUGUUGAUUCCUUUUUGGUACG UCGUGGUACGUCUC

?

Table A.3.3. Prism sequences and control construct sequences.

2'F-RNA frame + Core^B		
	2'f-A	GGCCAGCGAAUCAUGGCCUACGAUUACCAUACUUUGUUAUCGCGUUUUGCGAC UUGUCCACUGCAGGCC
	2'f-B	GGCGCGAUAUAUCAUGGCCGUCUCCAGCAUACUUUGUUGAGACCUUUUGAGAC GUACCACGAGCGUACC
	2'f-C	GGUCUCAAUCAUGGCACCUACCACGCAUACUUUGUUCGCUUGUUUUCCAGCU GGCAAGCGCAUUAU
	D/d'-core	GGACACUUGUCAUGUGUAUGCGUGUAUAUUGUCAUGUGUAUGCUCUAUCGUU UCAUGUGUAUGGCCUUUUUUAAUCCCGCGGCCAUGGCGGCCGGGAGUUUUUUGC ACACUUGUCAUGUGUAUGCGUGUAUAUUGUCAUGUGUAUGCUCUAUCGUUUGU AUGUGUAUGGC
	2'f-a'	GGCGUCAAUCAUGGCAAGUGUCCGCCAUACUUUGUUGAGCCUUUUUAUAGCC CUUGCCAAGCUGGG
	2'f-b'	GGAAUCAAUCAUGGCAAAUACACGCAUACUUUGUUGAGCCUUUUGGCCUGC AGUGGACAACUCGC
	2'f-c'	GGGCUCAAUCAUGGCAACGAUAGAGCAUACUUUGUUGAUUCCUUUUGGUACGC UCGUGGUACGUCUC
2'F-RNA frame + DNA-FA^C		
	1DNA-FA	GTATGGTAATCGTAGGTCATGTTTTATCCCGCGGCCATGGCGGCCGGGAG
	2DNA-FA	GTATGCGTGTATATTGTCATGTTTTATCCCGCGGCCATGGCGGCCGGGAG
	3DNA-FA	GTATGCGTGGTAGGTGTCATGTTTTATCCCGCGGCCATGGCGGCCGGGAG
	4DNA-FA	GTATGCTCTATCGTGTGTCATGTTTTATCCCGCGGCCATGGCGGCCGGGAG
	5DNA-FA	GTATGCTGGAAGACGGTTCATGTTTTATCCCGCGGCCATGGCGGCCGGGAG
	6DNA-FA	GTATGGCGGACACTGTGTCATGTTTTATCCCGCGGCCATGGCGGCCGGGAG
	1xDNA-Cy5	GTATGCGTGGTAGGTGTCATGTTTTATCCCGCGGCCATGGCGGCCGGGAG-Cy5
	2'f-A	GGCCAGCGAAUCAUGGCCUACGAUUACCAUACUUUGUUAUCGCGUUUUGCGAC UUGUCCACUGCAGGCC
	2'f-B	GGCGCGAUAUAUCAUGGCCGUCUCCAGCAUACUUUGUUGAGACCUUUUGAGAC GUACCACGAGCGUACC
	2'f-C	GGUCUCAAUCAUGGCACCUACCACGCAUACUUUGUUCGCUUGUUUUCCAGCU GGCAAGCGCAUUAU
2'f-a'	GGCGUCAAUCAUGGCAAGUGUCCGCCAUACUUUGUUGAGCCUUUUUAUAGCC CUUGCCAAGCUGGG	
2'f-b'	GGAAUCAAUCAUGGCAAAUACACGCAUACUUUGUUGAGCCUUUUGGCCUGC AGUGGACAACUCGC	
2'f-c'	GGGCUCAAUCAUGGCAACGAUAGAGCAUACUUUGUUGAUUCCUUUUGGUACGC UCGUGGUACGUCUC	
ssDNA conjugates complementary to the core		
DNA-folate	FA-TCCCGGCCGC CATGGCCGCG GGATT	
DNA-cyclodextrin	TCCCGGCCGC CATGGCCGCG GGATT-CLDXT	
DNA-biotin	TCCCGGCCGC CATGGCCGCG GGATT-biotin	
DNA-taxol	TCCCGGCCGC CATGGCCGCG GGATT-TXL	
DNA-Cy5	TCCCGGCCGC CATGGCCGCG GGATT-Cy5	
Cy3-DNA-biotin	Cy3-TCCCGGCCGC CATGGCCGCG GGATT-biotin	

^A Triangle prism can be formed using RNA as well as 2'F U/C modified RNA strands. The sequence for the complementary linkers are underlined

^B The D/d'-core RNA sequence locating inside of the prism is underlined. This underlined sequence portion is complementary to the ssDNA-drug conjugates.

^C The RNA complementary sequences for the 3'-end labeled DNA-FA is underlined

^D The bolded nucleotides correspond to CpG motif

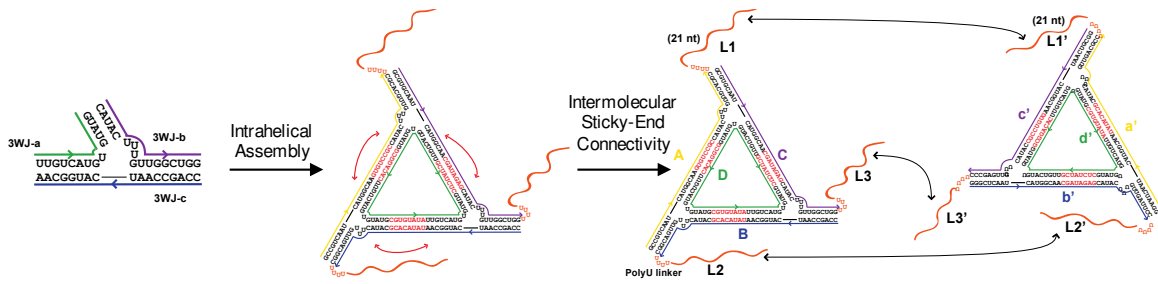


Figure A.3.1. Detailed sequence design and schematic for the assembly of 3D triangular nanoprisms from previously designed flat RNA triangle nanoparticles.

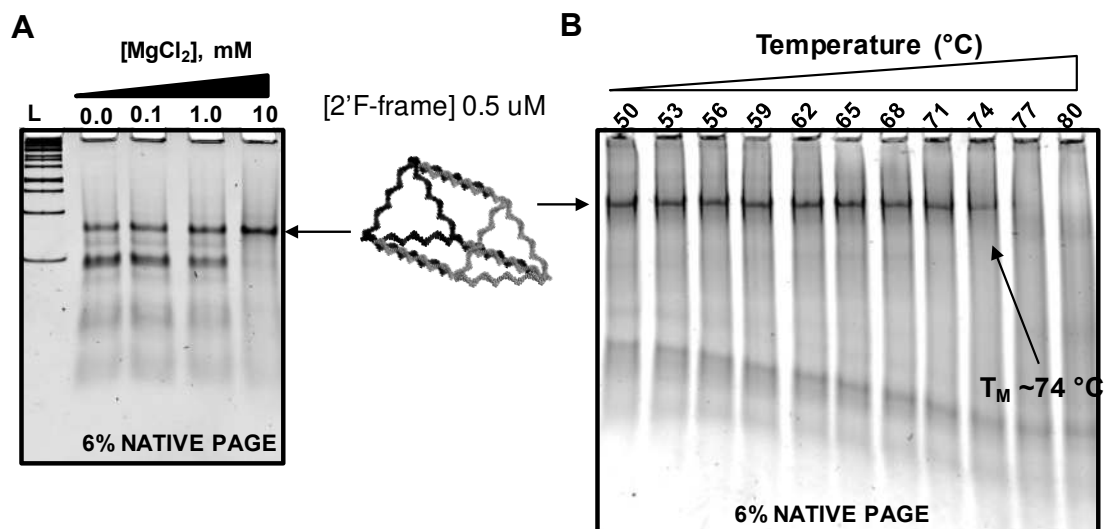


Figure A.3.2. (A) Magnesium effect on assembly of triangular nanoprism. Higher concentrations of magnesium ions dictate higher assembly efficiencies. (B) TGGE melting gel analysis of 2'F prism frame. Melting temperature is taken to be 50% assembled nanoparticle.

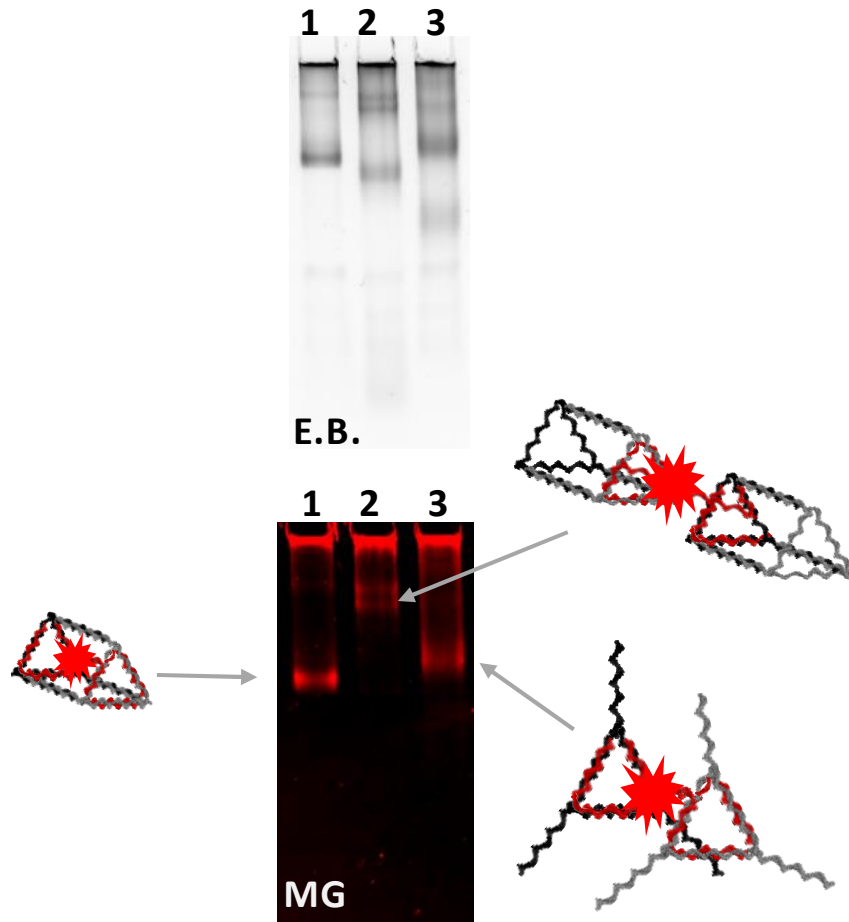


Figure A.3.3. Control PAGE experiments excluding prism dimer and open prism constructs from gel shift assembly experiments. Decrease in migration in lanes 2 and 3 indicate that the prism dimer and open prism, formed by sequence engineering, will migrate much slower than the closed prism, as expected.

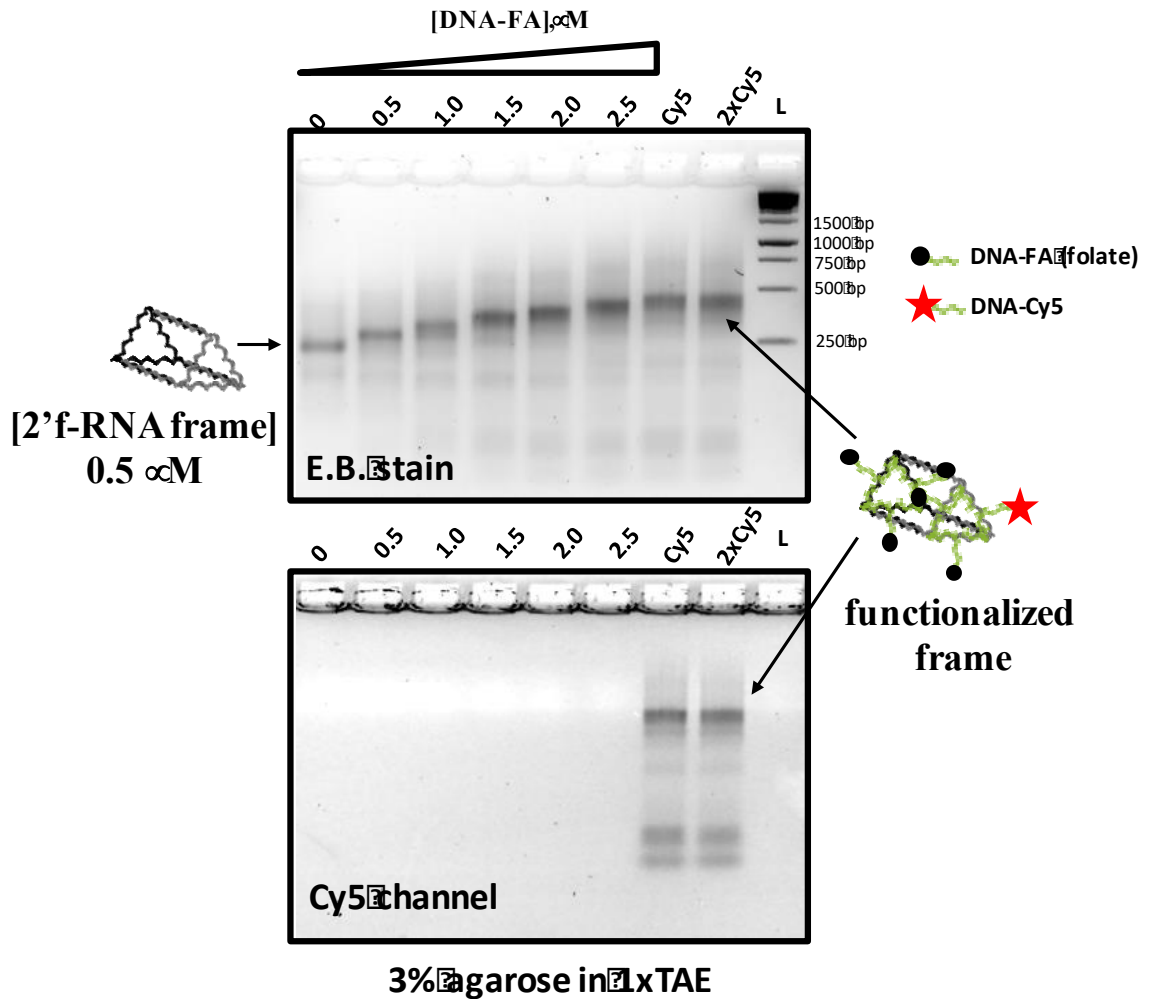


Figure A.3.4. Analysis of the 2'f-RNA frame hybridization with DNA-folate and DNA-Cy5 strands. Experiments were conducted on 6% native PAGE. The same gel was first scanned using Cy5 channel to detect signal from Cy5 fluorophore following staining in EB for total nucleic acid visualization. Lane Cy5 contains the following complex: 0.5 μM 2'f-RNA frame, 2.5 μM DNA-FA, and 0.5 μM DNA-Cy5; L = DNA ladder Thermo Scientific O'GeneRuler 1 kb

Appendix 4: Supplemental Data for Chapter 5

Appendix 4 was reproduced (with some modification) from Jasinski, DL; and Guo, P. “Co-Transcriptional Assembly of RNA Nanoparticles *via* Rolling Circle Transcription of Fully Double Stranded Circular DNA.” *Under Submission* and Jasinski, DL; Schwartz, CT; Haque, F; and Guo, P. “Large scale purification of RNA nanoparticles by preparative ultracentrifugation.” *Methods in Molecular Biology*. 2015. 1297, 67-82. DOI: 10.1007/978-1-4939-2562-9_5.

Table A.4.1. Sequence of constructs.

Sequences for Linear dsDNA	
	Promoter, 5'Ribozyme, 3WJ Target RNA, 3'Ribozyme
RCT-1.0-3WJ-A	TAATACGACTCACTATAAGGAGCCTGATGAGTCCGTGAGGACGAAACCGCGTATATCGCGGTCGCTTGCCATGTG TATGTGGGTCGCGCGTATATCGCGCCTGATGAGTCCGTGAGGACGAAAC
RCT-1.0-3WJ-B	TAATACGACTCACTATAAGGAGCCTGATGAGTCCGTGAGGACGAAACCGCGTATATCGCGGTCGCCCCACATACT TTGTTGATCCGTCGCGCGTATATCGCGCCTGATGAGTCCGTGAGGACGAAAC
RCT-1.0-3WJ-C	TAATACGACTCACTATAAGGAGCCTGATGAGTCCGTGAGGACGAAACCGCGTATATCGCGGTCGCGGATCAATCA TGGCAAGTCGCGCGTATATCGCGCCTGATGAGTCCGTGAGGACGAAAC
RCT-1.0-3WJ-A-InactiveRbz	TAATACGACTCACTATAAGGAGCCTAATGAGTCCGTGAGGACGAAACCGCGTATATCGCGGTCGCTTGCCATGTG TATGTGGGTCGCGCGTATATCGCGCCTAATGAGTCCGTGAGGACGAAAC
RCT-1.1-3WJ-A	TAATACGACTCACTATAAGGAAAGTCCTGATGAGTCCGTGAGGACGAAACCGCGTATATCGCGGTCGACTTGCCCA TGTGTATGTGGCGTCCCGCATATAGCGGCTGATGAGTCCGTGAGGACGAAACGCCAC
RCT-1.1-3WJ-B	TAATACGACTCACTATAAGGAGCCTCCTGATGAGTCCGTGAGGACGAAACCGCGTATATCGCGGTCGACGCCACA TACTTTGTTGATCCGTCCCGCATATAGCGGCTGATGAGTCCGTGAGGACGAAACGGATC
RCT-1.1-3WJ-C	TAATACGACTCACTATAAGGAGCCTCCTGATGAGTCCGTGAGGACGAAACCGCGTATATCGCGGTCGACGGATCA ATCATGGCAAGTCGCGCATATAGCGGCTGATGAGTCCGTGAGGACGAAACCTTGCC
RCT-1.1-3WJ-A-InactiveRbz	TAATACGACTCACTATAAGGAAAGTCCTAATGAGTCCGTGAGGACGAAACCGCGTATATCGCGGTCGACTTGCCCA GTGTATGTGGCGTCCCGCATATAGCGGCTAATGAGTCCGTGAGGACGAAACGCCAC
RCT-Mut-2'F-Activity-Test	TAATACGACTCACTATAAGGAGCCTCCTGATGAGTCCGTGAGGACGAAACCGCGTATATCGCGGTCGACGCCACA TACTTTGTTGATCCGTACCGCATATAGCGGCTGATGAGTCCGTGAGGACGAAACGGATC
Sequences for Circular dsDNA	
	Promoter, 5'Ribozyme, 3WJ Target RNA, 3'Ribozyme
RCT_1.1_3WJ-A_In_Circ_AntiSense	Phos-ATAGTGAGTCGATTAGTGGCGTTTCGTCTCACGGACTCATTAGCCGCTATATGCGGGA CGCCACATACACATGGCAAGTCGACCGCGATATACCGGTTTCGTCTCACGGACTCATTAGGACTTTCT
RCT_1.1_3WJ-A_In_Circ_Sense	Phos-AGGAAAGTCCTAATGAGTCCGTGAGGACGAAACCGCGTATATCGCGGTCGACTTGCCATGT GTATGTGGCGTCCCGCATATAGCGGCTAATGAGTCCGTGAGGACGAAACGCCACTAATACGACTCACTAT
RCT_1.1_3WJ-A_Circ_AntiSense	Phos-ATAGTGAGTCGATTAGTGGCGTTTCGTCTCACGGACTCATTAGCCGCTATATGCGGGA CGCCACATACACATGGCAAGTCGACCGCGATATACCGGTTTCGTCTCACGGACTCATTAGGACTTTCT
RCT_1.1_3WJ-A_Circ_Sense	Phos-AGGAAAGTCCTGATGAGTCCGTGAGGACGAAACCGCGTATATCGCGGTCGACTTGCCATGT GTATGTGGCGTCCCGCATATAGCGGCTGATGAGTCCGTGAGGACGAAACGCCACTAATACGACTCACTAT
RCT_1.1_3WJ-B_Circ_AntiSense	Phos-ATAGTGAGTCGATTAGTCCGTTTCGTCTCACGGACTCATTAGCCGCTATATGCGGGACGG ATCAACAAAGTATGTGGCGTCGACCGCGATATACCGGTTTCGTCTCACGGACTCATTAGGACGCTCCT
RCT_1.1_3WJ-B_Circ_Sense	Phos-AGGAGCGTCCGTGATGAGTCCGTGAGGACGAAACCGCGTATATCGCGGTCGACGCCACATACTT TGTTGATCCGTCCCGCATATAGCGGCTGATGAGTCCGTGAGGACGAAACGGATCAATACGACTCACTAT
RCT_1.1_3WJ-C_Circ_AntiSense	Phos-ATAGTGAGTCGATTAGGCAAGTTTCGTCTCACGGACTCATTAGCCGCTATATGCGGGA CTTGCCATGATTGATCCGTCGACCGCGATATACCGGTTTCGTCTCACGGACTCATTAGGACGGTCTC
RCT_1.1_3WJ-C_Circ_Sense	Phos-AGGACCGTCCGTGATGAGTCCGTGAGGACGAAACCGCGTATATCGCGGTCGACGGATCAAT CATGGCAAGTCCCGCATATAGCGGCTGATGAGTCCGTGAGGACGAAACCTTGCCTAATACGACTCACTAT
3WJ_OnePiece_Circ_AntiSense	Phos-ATAGTGAGTCGATTAGTGGCGTTTCGTCTCACGGACTCATTAGCCGCTATATGCGGGACGG GATTGATCCTCTCGGATCAACAAAGTATGTGGCTCTCGCCACATACACATGGCAAGACCGGTCCT
3WJ_OnePiece_Circ_Sense	Phos-AGGAGCGGTCCTTGCCATGTGTATGTGGCGAGAGCCACATACTTTGTTGATCCG AGAGGATCAATCATGGCAACTGATGAGTCCGTGAGGACGAAACCGCGTAATACGACTCACTAT
MG-3WJ_OnePiece_AntiSense	Phos-ATAGTGAGTCGATTAGCAGGTTTCGTCTCACGGACTCATTAGTTGCCATGATTGATCCTCT CGGATCAACAAAGTATGTGGCGGATCCATTCTGTTACCTGGCTCTCGCCAGTCGGATCCGCCA
MG-3WJ_OnePiece_Circ_Sense	Phos-AGGACCGGTCCTTGCCATGTGTATGTGGCGGATCCCGACTGGCGAGAGCCAGGTAACG AATGGATCCGCCACATACTTTGTTGATCCGAGAGGATCAATCATGGCAACTGATGAGTCCGTGA GGACGAAACCGCGTAATACGACTCACTAT
3WJ Sequences	
3WJ-A-RCT	GACUUGCCAUUGUUAUGUGGCGUC
3WJ-B-RCT	GACGCCACAUACUUUGUUAUCCGUC
3WJ-C-RCT	GACGGAUCAUUAUGGCAAGUC

Table A.4.2. Table summarizing the cleavage efficiencies of the ribozymes in each of the sequences, broken down for 5' and 3' ribozyme of each sequence, as well as total cleavage efficiency of the full-length constructs (those containing both 5' and 3' ribozymes)

	RCT 1.0		RCT 1.1	
	3WJ-A		3WJ-A	
Time (minutes)	5' Rbz	3' Rbz	5'Rbz	3'Rbz
0	0.00%	0.00%	0.00%	0.00%
5	56.7%	25.6%	55.48%	43.54%
15	60.0%	35.5%	61.97%	50.35%
30	61.4%	37.6%	64.04%	50.93%
60	62.9%	49.7%	64.22%	57.94%
120	65.7%	53.3%	68.12%	71.86%
	3WJ-B		3WJ-B	
Time (minutes)	5'Rbz	3'Rbz	5'Rbz	3'Rbz
0	0.00%	0.00%	0.00%	0.00%
5	52.69%	56.35%	63.53%	56.91%
15	50.55%	55.70%	68.33%	66.85%
30	47.18%	56.83%	69.77%	69.66%
60	50.08%	63.56%	71.88%	72.48%
120	47.25%	65.77%	75.37%	77.99%
	3WJ-C		3WJ-C	
Time (minutes)	5'Rbz	3'Rbz	5'Rbz	3'Rbz
0	0.00%	0.00%	0.00%	0.00%
5	16.18%	15.80%	47.43%	45.38%
15	20.89%	16.15%	55.98%	52.39%
30	22.21%	24.59%	56.82%	56.94%
60	25.80%	30.05%	58.45%	59.93%
120	30.20%	36.72%	65.35%	64.66%
Full Length Cleavage				
Construct			Cleavage %	
RCT-1.1-3WJ-A			87.12%	
RCT-1.1-3WJ-B			85.76%	
RCT-1.1-3WJ-C			80.83%	

Table A.4.3. Summary of sequences used in publications with RCT reactions (38,125,270,275,280,290-292). The DeltaG of most templates are close to 0 or positive, indicating unstable secondary structure, which is suitable for transcription using bacterial polymerases. Besides dumbbell sequences (denoted by a “*” before the reference), which have previously been shown as suitable substrates for transcription. Templates from this manuscript display a large negative DeltaG value, demonstrating the need for a fully double stranded circular DNA template.

Parameters:	Sequence set to circular, 25 mM NaCl, 6 mM Mg, 37C	mFold Calculation
Publication	Sequence	Delta G (kcal/mol)
Diegelman, NAR, 1998	ACAACGTGTGTTTCTCTGGTTGACTTCTCTGCTTGCAGGACTGTCAGGAGGTACCAGGTAATA TACC	2.63
Diegelman, NAR, 1998	TTGAAAACAGGACTGTCAGGAGGTACCAGGTAATATACCACAACGTGTGTTTCTCTGGTTGACT TCTCTGTTTC	-0.59
Diegelman, NAR, 1998	TGGAACAGAAACAGGACTGTCATCGAGTACCAGGTAATATACCAACGTGTGTTTCTCTGGT TGACTTCTCTGTTTC	-3.4
Diegelman, NAR, 1998	CGAAAACCTGGACTACAGGGAGGTACCAGGTAATGTACCACAACGTGTGTTTCTCTGGTCTGC TTCTCAGGAAT	4.71
Lindstrom, Biochemistry, 2002	CACTCCACTCACAAACATCCACACCTCACACTCAACTCCAACACACTCACTCACTCCT	NO FOLDING POSSIBLE
Lindstrom, Biochemistry, 2002	CCCTAACCCCTAACCCCTAACCCCTAACCCCTAACCCCTAACCCCTAACCCCTAACCCCTAA	9.12
Lindstrom, Biochemistry, 2002	CCCACACCCACACCCCTAACCCCTAACCCCTAACCCCTAACCCCTAACCCCTAACCCCTAA	9.12
Hartig, ChemBioChem, 2005	TAGGGTTAGGGTTAGGGTTAGGGTTAGGGTTAGGGTTAGGGTTAGGGTTAGGGTTAGGGT	8.2
Hartig, ChemBioChem, 2005	TAGGGTTAGGGTTAGGGTTAGGGTTAGGGTTAGGGTTAGGGTTAGGGTTAGGGTTAGGGT	8.52
Hartig, ChemBioChem, 2005	TAGGGTTAGGGTTAGGGTTAGGGTTAGGGTTAGGGTTAGGGTTAGGGTTAGGGTTAGGGT	8.77
Daubendiek, JACS, 1995	CCTTCTTTCTTTTCCGATCCTTTCTTTCTTCTCCT	7.24
Daubendiek, JACS, 1995	CTTTTTTTTTTTCACACTTTTTTTTTTTCACA	NO FOLDING POSSIBLE
*Hammond, 2012, Nat. Mat.	ATAGTGAGTCGTATTAACGTA CCAACAACCTACGCTGAGTACTTCGATTACTTGAATCGAAGTACTCAGCGTAAGTTTAGAGGC ATATCCCT	-16.73
*Jang, 2015, Nat. Comm.	ATAGTGAGTCGTATTAACGTAACCAAGAGAGTTCAAGTCCATCTCAATCTAAAAAGGGTG GGTGTGACCCCTAAAAAGTAGATGGACTTGAACCTTTAGAGGCATATCCCT	-11.27
*Jang, 2015, Nat. Comm.	ATAGTGAGTCGTATTAACGTAACCAAGAGAGTTCAAGTCCATCTCAATCTAAAAAGGGTG GGTGTGACCCCTAAAAAGTAGATGGACTTGAACCTTTAGAGGCATATCCCT	-12.36
*Roh, 2015, Angew. Chem Int. Ed.	ATAGTGAGTCGTATTAACGTAACCAAGAGAGTTCAAGTCCATCTCAATCTAAAAAGGGTG A TGAACCTCAGGGTCAGCTTGTAGAGGTTAAGCTACATATCCCT	-19.56
*Roh, 2015, Angew. Chem. Int. Ed.	ATAGTGAGTCGTATTAACGTAACCAAGAGAGTTCAAGTCCATCTCAATCTAAAAAGGGTG AGAGTTCAAGTCCATCTACATAGAGGCCACAACGTGCAATATCCCT	-11.56
*Furukawa, Bio. Med.Chem. Lett., 2008	GGCCACAGGATCCATTCTGTTACCTGGCTCTGCCAGTCGGGATCCACGTACC	-0.64
This manuscript Sequences		
3WJ-A	ATAGTGAGTCGTATTAAGTGGCGTTTCGTCTCACGGACTCATTAGCCGCTATATGCGGGACG CCACATACACATGGCAAGTCGACCGCGATATACGCGGTTTCGTCTCACGGACTCATTAGGA CTTTCTCCT	-11.67
3WJ-A-Inactive-Rbz	ATAGTGAGTCGTATTAAGTGGCGTTTCGTCTCACGGACTCATTAGCCGCTATATGCGGGACG CCACATACACATGGCAAGTCGACCGCGATATACGCGGTTTCGTCTCACGGACTCATTAGGA CTTTCTCCT	-11.58
3WJ-B	ATAGTGAGTCGTATTAAGTGGCGTTTCGTCTCACGGACTCATTAGCCGCTATATGCGGGACG GATCAACAAAGTATGTGGCGTCGACCGCGATATACGCGGTTTCGTCTCACGGACTCATTAGGA GACGCTCCT	-10.81
3WJ-C	ATAGTGAGTCGTATTAAGTGGCGTTTCGTCTCACGGACTCATTAGCCGCTATATGCGGGACT TGCCATGATTGATCCGTCGACCGCGATATACGCGGTTTCGTCTCACGGACTCATTAGGACG GTCCT	-10.86
3WJ-One Piece	ATAGTGAGTCGTATTAAGTGGCGTTTCGTCTCACGGACTCATTAGCCGCTATATGCGGGACT CGGATCAACAAAGTATGTGGCGTCGACCGCGATATACGCGGTTTCGTCTCACGGACTCATTAGGA CTTTCTCCT	-17.87
3WJ-MG One Piece	ATAGTGAGTCGTATTAAGTGGCGTTTCGTCTCACGGACTCATTAGCCGCTATATGCGGGACT CGGATCAACAAAGTATGTGGCGTCGACCGCGATATACGCGGTTTCGTCTCACGGACTCATTAGGA CTTTCTCCT	-27.04

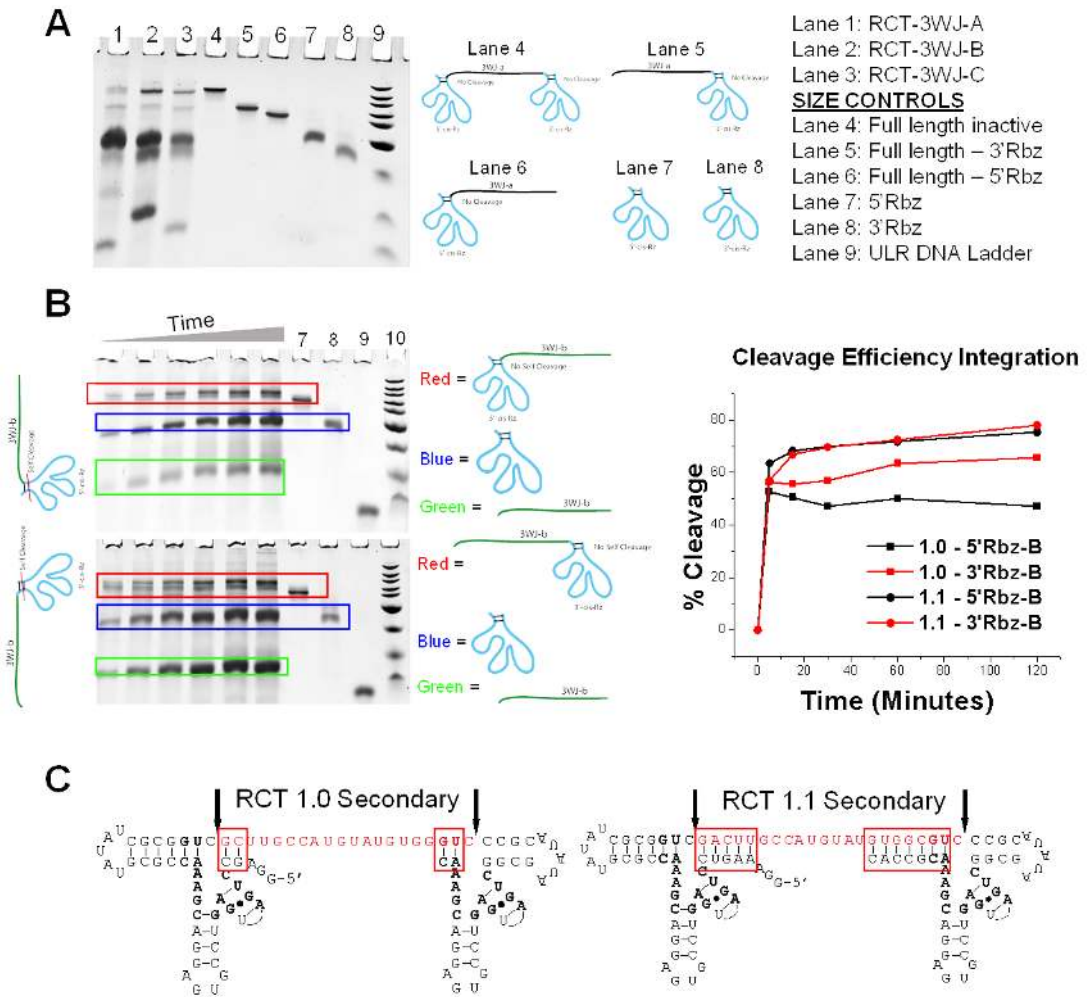


Fig A.4.1. (A) PAGE analysis shows active RCT constructs along with size controls of inactivated ribozyme constructs. Size controls allow confirmation of ribozyme cleavage and release of target RNA oligomers. **(B)** Typical experiment run to determine cleavage efficiency of self-cleaving ribozymes. The target sequence (green box) intensity was added with the cleaved ribozyme (blue box) intensity and then divided by the total band intensity (red + blue + green box) per well. A plot on the right shows the ribozyme cleavage efficiency over time, comparing first generation design (RCT-1.0) to the second generation design (RCT-1.1). The construct containing 3WJ-B sequence is shown here. While a better curve was desired for ribozyme cleavage kinetics, ribozymes self-cleave as they are being

transcribed, making it difficult to obtain time points of low percent cleavage. (C) An increase in ribozyme efficiency is attributed to increasing the length of the duplex in the “closing” region of the ribozyme sequence, shown in red boxes.

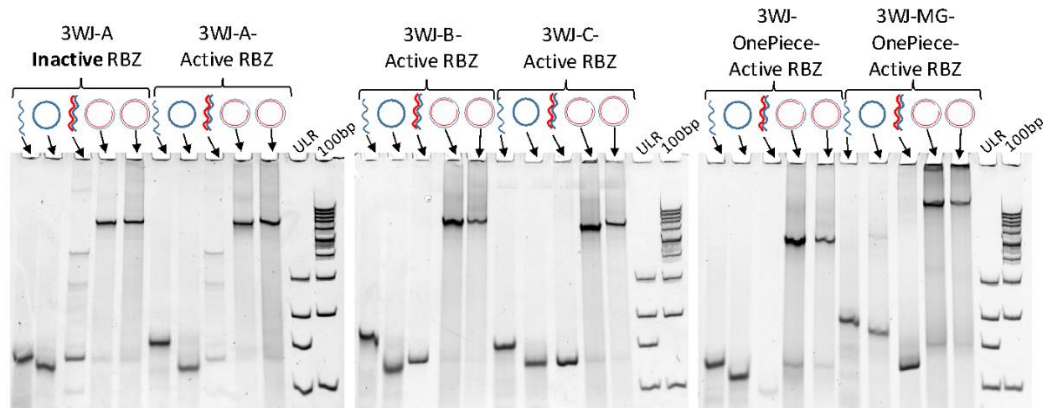


Figure A.4.2. PAGE analyzing the assembly of circular dsDNA constructs containing the T7 promoter used for transcription reactions.

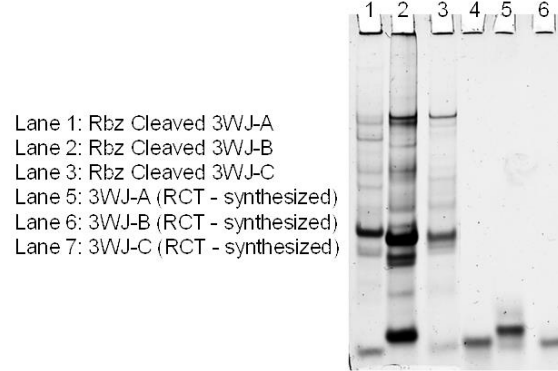
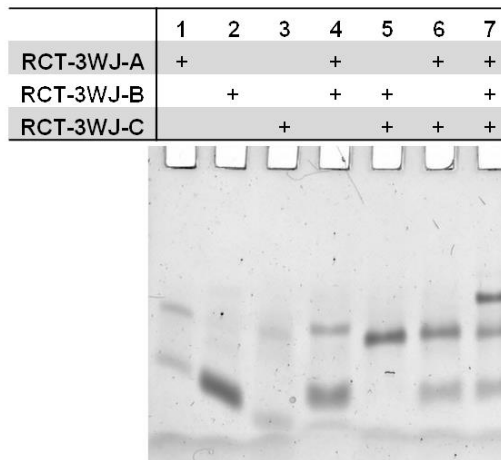
A**B**

Figure A.4.3. (A) Ribozyme cleaved 3WJ ssRNA oligomers were compared to chemically synthesized sequences identical to those of the target sequence. Evidenced by identical migration rate, we can conclude that the cleaved RNA oligomers are the same size as chemically synthesized controls. **(B)** RCT cleaved 3WJ ssRNA oligomers were purified by PAGE band isolation. After elution from gel pieces assembly was tested on native PAGE. A stepwise assembly from monomer to dimer and finally trimer complex demonstrate the ssRNA from RCT reactions are indeed the correct sequences.

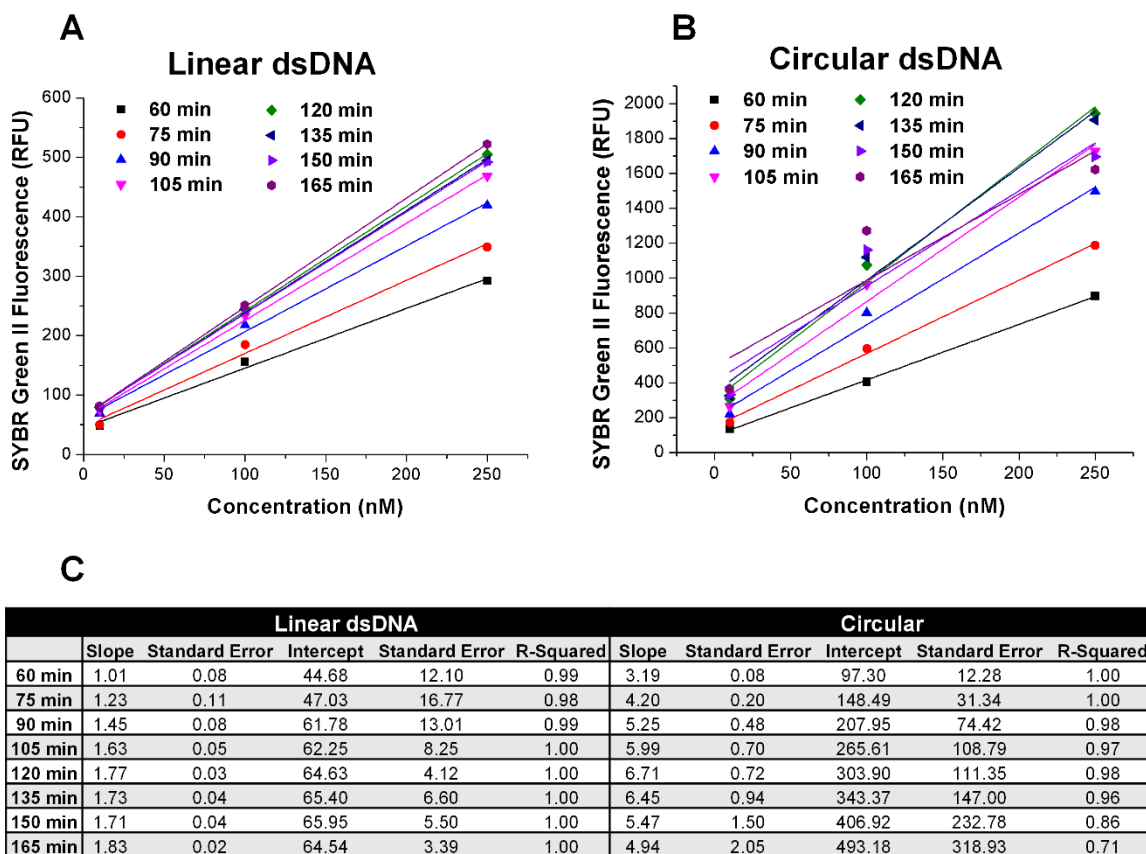


Figure A.4.4. (A/B) Plots and linear fitting of DNA template concentration, x-axis, versus RNA output, as monitored by SYBR GreenII fluorescence. **(C)** Values of slope and intercept, along with their standard errors and R-Squared values of the fits.

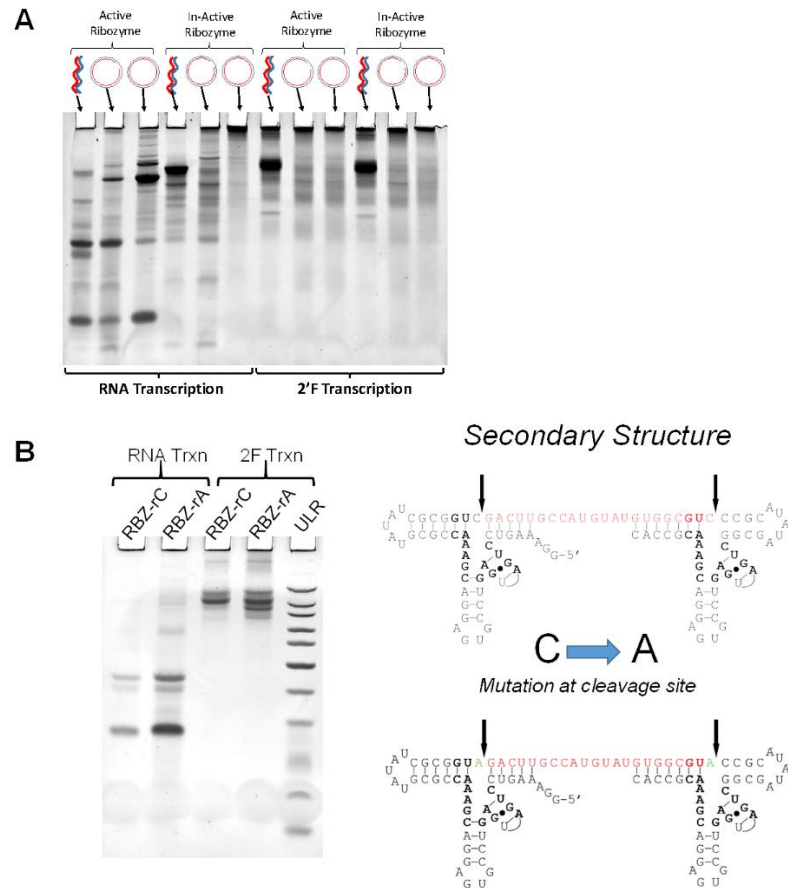


Figure A.4.5. (A) Ribozyme cleavage with native sequences was attempted with modified nucleotides, fluorine substitution on the 2' hydroxyl of the ribose sugar (2'F) of C and U bases, the pyrimidines. As evidenced by no short RNA fragments after gel analysis, the 2'F modifications abolish ribozyme activity. **(B)** Because hammerhead ribozymes proceed by a hydrolysis mechanism, we hypothesized that removal of the 2'OH hindered ribozyme activity. Therefore, the C at the cleavage site was replaced with an A, thus the 2'OH would still be present, as only pyrimidines are modified with 2'F. However, cleavage activity was still zero. It is apparent that modification to the duplex structure by the 2'F modification stops ribozyme activity.

References

1. Feynman RP (1960) There's Plenty of Room at the Bottom---An Invitation to Enter a New Field of Physics (Dec. 29, 1959 at the Ann Meet Amer Phys Soc, Caltech's *Engineering and Science*, December issue:
2. Feynman RP & Sykes C (1995) No Ordinary Genius: The Illustrated Richard Feynman. *W. W. Norton & Company* 175
3. Westesen K, Siekmann B, & Koch MHJ (1993) Investigations on the Physical State of Lipid Nanoparticles by Synchrotron-Radiation X-Ray-Diffraction. *International Journal of Pharmaceutics* 93: 189-199
4. Quintanar-Guerrero D, Allemann E, Fessi H, & Doelker E (1998) Preparation Techniques and Mechanisms of Formation of Biodegradable Nanoparticles From Preformed Polymers. *Drug Development and Industrial Pharmacy* 24: 1113-1128
5. Weber C, Coester C, Kreuter J, & Langer K (2000) Desolvation Process and Surface Characterisation of Protein Nanoparticles. *International Journal of Pharmaceutics* 194: 91-102
6. Klem MT, Willits D, Young M, & Douglas T (2003) 2-D Array Formation of Genetically Engineered Viral Cages on Au Surfaces and Imaging by Atomic Force Microscopy. *J. Am. Chem. Soc.* 125: 10806-10807
7. Wang XS, Li QQ, Xie J, Jin Z, Wang JY, Li Y, Jiang KL, & Fan SS (2009) Fabrication of Ultralong and Electrically Uniform Single-Walled Carbon Nanotubes on Clean Substrates. *Nano Letters* 9: 3137-3141
8. Eigler DM & Schweizer EK (1990) Positioning Single Atoms With A Scanning Tunneling Microscope. *Nature* 344: 524-526
9. Munro CH, Smith WE, Garner M, Clarkson J, & White PC (1995) Characterization of the Surface of A Citrate-Reduced Colloid Optimized for Use As A Substrate for Surface-Enhanced Resonance Raman-Scattering. *Langmuir* 11: 3712-3720

10. Babes L, Denizot B, Tanguy G, Le Jeune JJ, & Jallet P (1999) Synthesis of Iron Oxide Nanoparticles Used As MRI Contrast Agents: A Parametric Study. *Journal of Colloid and Interface Science* 212: 474-482
11. Kallenbach N, Ma R, & Seeman N (1983) An Immobile Nucleic Acid Junction Constructed From Oligonucleotides. *Nature* 305: 829-831
12. Guo P, Zhang C, Chen C, Trottier M, & Garver K (1998) Inter-RNA Interaction of Phage Phi29 PRNA to Form a Hexameric Complex for Viral DNA Transportation. *Mol. Cell.* 2: 149-155
13. Duncan R (2003) The Dawning Era of Polymer Therapeutics. *Nat Rev. Drug Discov.* 2: 347-360
14. Ferrari M (2005) Cancer Nanotechnology: Opportunities and Challenges. *Nat Rev. Cancer* 5: 161-171
15. Morgen M, Bloom C, Beyerinck R, Bello A, Song W, Wilkinson K, Steenwyk R, & Shamblin S (2012) Polymeric Nanoparticles for Increased Oral Bioavailability and Rapid Absorption Using Celecoxib As a Model of a Low-Solubility, High-Permeability Drug. *Pharmaceutical Research* 29: 427-440
16. Mudshinge SR, Deore AB, Patil S, & Bhalgat CM (2011) Nanoparticles: Emerging Carriers for Drug Delivery. *Saudi Pharmaceutical Journal* 19: 129-141
17. Savjani KT, Gajjar AK, & Savjani JK (2012) Drug Solubility: Importance and Enhancement Techniques. *ISRN. Pharm.* 2012: 195727
18. De Jong WH & Borm PJA (2008) Drug Delivery and Nanoparticles: Applications and Hazards. *International Journal of Nanomedicine* 3: 133-149
19. Han HS, Thambi T, Choi KY, Son S, Ko H, Lee MC, Jo DG, Chae YS, Kang YM, Lee JY, & Park JH (2015) Bioreducible Shell-Cross-Linked Hyaluronic Acid Nanoparticles for Tumor-Targeted Drug Delivery. *Biomacromolecules* 16: 447-456
20. Banerjee R, Parida S, Maiti C, Mandal M, & Dhara D (2015) PH-Degradable and Thermoresponsive Water-Soluble Core Cross-Linked Polymeric Nanoparticles As Potential Drug Delivery Vehicle for Doxorubicin. *Rsc Advances* 5: 83565-83575

21. Chu KS, Schorzman AN, Finnis MC, Bowerman CJ, Peng L, Luft JC, Madden AJ, Wang AZ, Zamboni WC, & DeSimone JM (2013) Nanoparticle Drug Loading As a Design Parameter to Improve Docetaxel Pharmacokinetics and Efficacy. *Biomaterials* 34: 8424-8429

22. Pham E, Birrer MJ, Eliasof S, Garmey EG, Lazarus D, Lee CR, Man S, Matulonis UA, Peters CG, Xu P, Krasner C, & Kerbel RS (2015) Translational Impact of Nanoparticle-Drug Conjugate CRLX101 With or Without Bevacizumab in Advanced Ovarian Cancer. *Clinical Cancer Research* 21: 808-818

23. Mallick A, More P, Ghosh S, Chippalkatti R, Chopade BA, Lahiri M, & Basu S (2015) Dual Drug Conjugated Nanoparticle for Simultaneous Targeting of Mitochondria and Nucleus in Cancer Cells. *ACS applied materials & interfaces* 7: 7584-7598

24. Bartlett RL & Panitch A (2012) Thermosensitive Nanoparticles With PH-Triggered Degradation and Release of Anti-Inflammatory Cell-Penetrating Peptides. *Biomacromolecules*. 13: 2578-2584

25. Hatakeyama H, Murata M, Sato Y, Takahashi M, Minakawa N, Matsuda A, & Harashima H (2013) The Systemic Administration of an Anti-MiRNA Oligonucleotide Encapsulated PH-Sensitive Liposome Results in Reduced Level of Hepatic MicroRNA-122 in Mice. *J Control Release*

26. Kale AA & Torchilin VP (2007) "Smart" Drug Carriers: PEGylated TATp-Modified PH-Sensitive Liposomes. *J Liposome Res* 17: 197-203

27. Kyriakides TR, Cheung CY, Murthy N, Bornstein P, Stayton PS, & Hoffman AS (2002) PH-Sensitive Polymers That Enhance Intracellular Drug Delivery in Vivo. *J Control Release* 78: 295-303

28. Lv S, Tang Z, Zhang D, Song W, Li M, Lin J, Liu H, & Chen X (2014) Well-Defined Polymer-Drug Conjugate Engineered With Redox and PH-Sensitive Release Mechanism for Efficient Delivery of Paclitaxel. *J Control Release* 194C: 220-227

29. Lehto T, Simonson OE, Mager I, Ezzat K, Sork H, Copolovici DM, Viola JR, Zaghoul EM, Lundin P, Moreno PM, Mae M, Oskolkov N, Suhorutsenko J, Smith CI, & Andaloussi SE (2011) A Peptide-Based Vector for Efficient Gene Transfer in Vitro and in Vivo. *Mol. Ther.* 19: 1457-1467

30. Olson ES, Jiang T, Aguilera TA, Nguyen QT, Ellies LG, Scadeng M, & Tsien RY (2010) Activatable Cell Penetrating Peptides Linked to Nanoparticles As Dual Probes for in Vivo Fluorescence and MR Imaging of Proteases. *Proc. Natl. Acad. Sci. U. S. A* 107: 4311-4316
31. Schiffelers RM, Ansari A, Xu J, Zhou Q, Tang Q, Storm G, Molema G, Lu PY, Scaria PV, & Woodle MC (2004) Cancer SiRNA Therapy by Tumor Selective Delivery With Ligand-Targeted Sterically Stabilized Nanoparticle. *Nucleic Acids Res.* 32: e149
32. Ellington AD & Szostak JW (1992) Selection in Vitro of Single-Stranded DNA Molecules That Fold into Specific Ligand-Binding Structures. *Nature* 355: 850-852
33. Gold L (1995) The SELEX Process: a Surprising Source of Therapeutic and Diagnostic Compounds. *Harvey Lect.* 91: 47-57
34. Arvinte T, Wahl P, & Nicolau C (1987) Resonance Energy-Transfer and Fluorescence Intensity Studies of the Transport of Liposome-Encapsulated Molecules into Isolated Mouse Liver Nuclei. *Biochemistry* 26: 765-772
35. Gutierrez-Merino C, Bonini dR, I, Pietrasanta LI, & Barrantes FJ (1995) Preferential Distribution of the Fluorescent Phospholipid Probes NBD-Phosphatidylcholine and Rhodamine-Phosphatidylethanolamine in the Exofacial Leaflet of Acetylcholine Receptor-Rich Membranes From Torpedo Marmorata. *Biochemistry* 34: 4846-4855
36. Douglas SJ, Davis SS, & Illum L (1987) Nanoparticles in Drug Delivery. *Crit Rev. Ther. Drug Carrier Syst.* 3: 233-261
37. Moon MH & Giddings JC (1993) Size Distribution of Liposomes by Flow Field-Flow Fractionation. *J. Pharm. Biomed. Anal.* 11: 911-920
38. Lee JB, Hong J, Bonner DK, Poon Z, & Hammond PT (2012) Self-Assembled RNA Interference Microsponges for Efficient SiRNA Delivery. *Nat. Mater.* 11: 316-322
39. Duncan R (2011) Polymer Therapeutics As Nanomedicines: New Perspectives. *Curr. Opin. Biotechnol.* 22: 492-501

40. Manchester M & Singh P (2006) Virus-Based Nanoparticles (VNPs): Platform Technologies for Diagnostic Imaging. *Adv. Drug Deliv. Rev.* 58: 1505-1522
41. Rae CS, Khor IW, Wang Q, Destito G, Gonzalez MJ, Singh P, Thomas DM, Estrada MN, Powell E, Finn MG, & Manchester M (2005) Systemic Trafficking of Plant Virus Nanoparticles in Mice Via the Oral Route. *Virology* 343: 224-235
42. Weiner LM (1999) Monoclonal Antibody Therapy of Cancer. *Semin. Oncol.* 26: 43-51
43. Harrison J, Shi X, Wang L, Ma JK, & Rojanasakul Y (1994) Novel Delivery of Antioxidant Enzyme Catalase to Alveolar Macrophages by Fc Receptor-Mediated Endocytosis. *Pharm. Res* 11: 1110-1114
44. Li J, Pei H, Zhu B, Liang L, Wei M, He Y, Chen N, Li D, Huang Q, & Fan CH (2011) Self-Assembled Multivalent DNA Nanostructures for Noninvasive Intracellular Delivery of Immunostimulatory CpG Oligonucleotides. *ACS Nano* 5: 8783-8789
45. Lin C, Liu Y, Rinker S, & Yan H (2006) DNA Tile Based Self-Assembly: Building Complex Nanoarchitectures. *Chemphyschem.* 7: 1641-1647
46. Lo PK, Metera KL, & Sleiman HF (2010) Self-Assembly of Three-Dimensional DNA Nanostructures and Potential Biological Applications. *Current Opinion in Chemical Biology* 14: 597-607
47. Kang D, Wang J, Zhang W, Song Y, Li X, Zou Y, Zhu M, Zhu Z, Chen F, & Yang CJ (2012) Selection of DNA Aptamers Against Glioblastoma Cells With High Affinity and Specificity. *PLoS ONE* 7: e42731
48. Liu X, Yan H, Liu Y, & Chang Y (2011) Targeted Cell-Cell Interactions by DNA Nanoscaffold-Templated Multivalent Bispecific Aptamers. *Small* 7: 1673-1682
49. Henke E, Perk J, Vider J, de CP, Chin Y, Solit DB, Ponomarev V, Cartegni L, Manova K, Rosen N, & Benezra R (2008) Peptide-Conjugated Antisense Oligonucleotides for Targeted Inhibition of a Transcriptional Regulator in Vivo. *Nat Biotechnol.* 26: 91-100

50. Shu Y, Haque F, Shu D, Li W, Zhu Z, Kotb M, Lyubchenko Y, & Guo P (2013) Fabrication of 14 Different RNA Nanoparticles for Specific Tumor Targeting Without Accumulation in Normal Organs. *RNA* 19: 766-777
51. Schwartz C, De Donatis GM, Zhang H, Fang H, & Guo P (2013) Revolution Rather Than Rotation of AAA+ Hexameric Phi29 Nanomotor for Viral DsDNA Packaging Without Coiling. *Virology* 443: 28-39
52. Schwartz C, De Donatis GM, Fang H, & Guo P (2013) The ATPase of the Phi29 DNA-Packaging Motor Is a Member of the Hexameric AAA+ Superfamily. *Virology* 443: 20-27
53. Zhao Z, Khisamutdinov E, Schwartz C, & Guo P (2013) Mechanism of One-Way Traffic of Hexameric Phi29 DNA Packaging Motor With Four Electropositive Relaying Layers Facilitating Anti-Parallel Revolution. *ACS Nano* 7: 4082-4092
54. Schwartz C & Guo P (2013) Ultrastable PRNA Hexameric Ring Gearing Hexameric Phi29 DNA-Packaging Motor by Revolving Without Rotating and Coiling. *Current Opinion in Biotechnology* 24(4): 581-590
55. Shu D, Shu Y, Haque F, Abdelmawla S, & Guo P (2011) Thermodynamically Stable RNA Three-Way Junctions for Constructing Multifunctional Nanoparticles for Delivery of Therapeutics. *Nature Nanotechnology* 6: 658-667
56. Cui D, Zhang C, Liu B, Shu Y, Du T, Shu D, Wang K, Dai F, Liu Y, Li C, Pan F, Yang Y, Ni J, Li H, Brand-Saber B, & Guo P (2015) Regression of Gastric Cancer by Systemic Injection of RNA Nanoparticles Carrying Both Ligand and SiRNA. *Scientific reports* 5: 10726
57. Binzel D, Shu Y, Li H, Sun M, Zhang Q, Shu D, Guo B, & Guo P (2016) Specific Delivery of MiRNA for High Efficient Inhibition of Prostate Cancer by RNA Nanotechnology. *Molecular Therapy* 24: 1267-1277
58. Shu D, Li H, Shu Y, Xiong G, Carson WE, Haque F, Xu R, & Guo P (2015) Systemic Delivery of Anti-MiRNA for Suppression of Triple Negative Breast Cancer Utilizing RNA Nanotechnology. *ACS Nano* 9: 9731-9740
59. Rychahou P, Haque F, Shu Y, Zaytseva Y, Weiss HL, Lee EY, Mustain W, Valentino J, Guo P, & Evers BM (2015) Delivery of RNA Nanoparticles into

Colorectal Cancer Metastases Following Systemic Administration. *ACS Nano* 9: 1108-1116

60. Lee TJ, Haque F, Shu D, Yoo JY, Li H, Yokel RA, Horbinski C, Kim TH, Kim S-H, Nakano I, Kaur B, Croce CM, & Guo P (2015) RNA Nanoparticles As a Vector for Targeted SiRNA Delivery into Glioblastoma Mouse Model. *Oncotarget* 6: 14766-14776
61. Lee TJ, Haque F, Vieweger M, Yoo JY, Kaur B, Guo P, & Croce CM (2015) Functional Assays for Specific Targeting and Delivery of RNA Nanoparticles to Brain Tumor. *Methods Mol Biol* 1297: 137-152
62. Binzel D, Khisamutdinov EF, Vieweger M, Ortega J, Li GM, & Guo P (2016) Mechanism of Three-Component Collision to Produce Ultra-Stable PRNA Three-Way Junction of Phi29 DNA-Packaging Motor by Kinetic Assessment. *RNA* In Press.
63. Binzel DW, Khisamutdinov EF, & Guo P (2014) Entropy-Driven One-Step Formation of Phi29 PRNA 3WJ From Three RNA Fragments. *Biochemistry* 53: 2221-2231
64. Liu J, Guo S, Cinier M, Shlyakhtenko LS, Shu Y, Chen C, Shen G, & Guo P (2011) Fabrication of Stable and RNase-Resistant RNA Nanoparticles Active in Gearing the Nanomotors for Viral DNA Packaging. *ACS Nano* 5: 237-246
65. Laurenti E, Barde I, Verp S, Offner S, Wilson A, Quenneville S, Wiznerowicz M, MacDonald HR, Trono D, & Trumpp A (2010) Inducible Gene and ShRNA Expression in Resident Hematopoietic Stem Cells in Vivo. *Stem Cells* 28: 1390-1398
66. Hoepflich S, Zhou Q, Guo S, Qi G, Wang Y, & Guo P (2003) Bacterial Virus Phi29 PRNA As a Hammerhead Ribozyme Escort to Destroy Hepatitis B Virus. *Gene Ther.* 10: 1258-1267
67. Chang KY & Tinoco IJr (1994) Characterization of a "Kissing" Hairpin Complex Derived From the Human Immunodeficiency Virus Genome. *Proc Natl Acad Sci U. S. A.* 91(18): 8705-8709
68. Bindewald E, Hayes R, Yingling YG, Kasprzak W, & Shapiro BA (2008) RNAJunction: a Database of RNA Junctions and Kissing Loops for Three-

Dimensional Structural Analysis and Nanodesign. *Nucleic Acids Res.* 36: D392-D397

69. Wagner C, Ehresmann C, Ehresmann B, & Brunel C (2004) Mechanism of Dimerization of Bicoid mRNA: Initiation and Stabilization. *J. Biol. Chem.* 279: 4560-4569
70. Sugimoto N, Nakano S, Katoh M, Matsumura A, Nakamuta H, Ohmichi T, Yoneyama M, & Sasaki M (1995) Thermodynamic Parameters to Predict Stability of RNA/DNA Hybrid Duplexes. *Biochemistry* 34: 11211-11216
71. Searle MS & Williams DH (1993) On the Stability of Nucleic Acid Structures in Solution: Enthalpy-Entropy Compensations, Internal Rotations and Reversibility. *Nucleic Acids Res.* 21: 2051-2056
72. Lemieux S & Major F (2002) RNA Canonical and Non-Canonical Base Pairing Types: a Recognition Method and Complete Repertoire. *Nucleic Acids Res.* 30: 4250-4263
73. Leontis NB & Westhof E (2001) Geometric Nomenclature and Classification of RNA Base Pairs. *RNA.* 7: 499-512
74. Leontis NB, Lescoute A, & Westhof E (2006) The Building Blocks and Motifs of RNA Architecture. *Curr. Opin. Struct. Biol.* 16: 279-287
75. Leontis NB & Westhof E (2003) Analysis of RNA Motifs. *Curr. Opin. Struct. Biol.* 13: 300-308
76. Seeman NC (1982) Nucleic Acid Junctions and Lattices. *J. theor. Biol.* 99: 237-247
77. Jones MR, Seeman NC, & Mirkin CA (2015) Nanomaterials. Programmable Materials and the Nature of the DNA Bond. *Science* 347: 1260901
78. Seeman NC (2010) Nanomaterials Based on DNA. *Annu. Rev. Biochem.* 79: 65-87

79. Andersen ES, Dong M, Nielsen MM, Jahn K, Subramani R, Mamdouh W, Golas MM, Sander B, Stark H, Oliveira CL, Pedersen JS, Birkedal V, Besenbacher F, Gothelf KV, & Kjems J (2009) Self-Assembly of a Nanoscale DNA Box With a Controllable Lid. *Nature* 459: 73-76
80. Goodman RP, Heilemann M, Doose S, Erben CM, Kapanidis AN, & Turberfield AJ (2008) Reconfigurable, Braced, Three-Dimensional DNA Nanostructures. *Nat. Nanotechnol.* 3: 93-96
81. Yang YR, Liu Y, & Yan H (2015) DNA Nanostructures As Programmable Biomolecular Scaffolds. *Bioconjug. Chem.*
82. Rothmund PWK (2006) Folding DNA to Create Nanoscale Shapes and Patterns. *Nature* 440: 297-302
83. Ke Y, Sharma J, Liu M, Jahn K, Liu Y, & Yan H (2009) Scaffolded DNA Origami of a DNA Tetrahedron Molecular Container. *Nano. Lett.* 9: 2445-2447
84. Douglas SM, Bachelet I, & Church GM (2012) A Logic-Gated Nanorobot for Targeted Transport of Molecular Payloads. *Science* 335: 831-834
85. Dietz H, Douglas SM, & Shih WM (2009) Folding DNA into Twisted and Curved Nanoscale Shapes. *Science* 325: 725-730
86. Liedl T, Hogberg B, Tytell J, Ingber DE, & Shih WM (2010) Self-Assembly of Three-Dimensional Prestressed Tensegrity Structures From DNA. *Nature Nanotechnology* 5: 520-524
87. Zaug AJ, Grabowski PJ, & Cech TR (1983) Autocatalytic Cyclization of an Excised Intervening Sequence RNA Is a Cleavage-Ligation Reaction. *Nature* 301: 578-583
88. Jady BE & Kiss T (2001) A Small Nucleolar Guide RNA Functions Both in 2'-O-Ribose Methylation and Pseudouridylation of the U5 Spliceosomal RNA. *EMBO J.* 20: 541-551
89. Sundaram P, Kurniawan H, Byrne ME, & Wower J (2013) Therapeutic RNA Aptamers in Clinical Trials. *Eur. J Pharm. Sci.* 48: 259-271

90. Guo P (2010) The Emerging Field of RNA Nanotechnology. *Nature Nanotechnology* 5: 833-842
91. Guo P, Haque F, Hallahan B, Reif R, & Li H (2012) Uniqueness, Advantages, Challenges, Solutions, and Perspectives in Therapeutics Applying RNA Nanotechnology. *Nucleic Acid Ther.* 22: 226-245
92. Ellington AD & Szostak JW (1990) *In Vitro* Selection of RNA Molecules That Bind Specific Ligands. *Nature* 346: 818-822
93. Tuerk C & Gold L (1990) Systematic Evolution of Ligands by Exponential Enrichment: RNA Ligands to Bacteriophage T4 DNA Polymerase. *Science* 249: 505-510
94. Mulhbacher J, St-Pierre P, & Lafontaine DA (2010) Therapeutic Applications of Ribozymes and Riboswitches. *Curr. Opin. Pharmacol.* 10: 551-556
95. Serganov A (2009) The Long and the Short of Riboswitches. *Curr. Opin. Struct. Biol.* 19: 251-259
96. Fire A, Xu S, Montgomery MK, Kostas SA, Driver SE, & Mello CC (1998) Potent and Specific Genetic Interference by Double-Stranded RNA in *Caenorhabditis Elegans*. *Nature* 391: 806-811
97. Aagaard L & Rossi JJ (2007) RNAi Therapeutics: Principles, Prospects and Challenges. *Advanced Drug Delivery Reviews* 59: 75-86
98. Ni JZ, Chen E, & Gu SG (2014) Complex Coding of Endogenous siRNA, Transcriptional Silencing and H3K9 Methylation on Native Targets of Germline Nuclear RNAi in *C. Elegans*. *BMC Genomics* 15: 1157
99. Jaeger L, Westhof E, & Leontis NB (2001) TectoRNA: Modular Assembly Units for the Construction of RNA Nano-Objects. *Nucleic Acids Res.* 29: 455-463
100. Jaeger L & Leontis NB (2000) Tecto-RNA: One Dimensional Self-Assembly Through Tertiary Interactions. *Angew. Chem. Int. Ed Engl.* 39: 2521-2524

101. Westhof E, Masquida B, & Jaeger L (1996) RNA Tectonics: Towards RNA Design. *Folding & Design* 1: R78-R88
102. Watts JK, Deleavey GF, & Damha MJ (2008) Chemically Modified SiRNA: Tools and Applications. *Drug Discovery Today* 13: 842-855
103. Khisamutdinov E, Li H, Jasinski D, Chen J, Fu J, & Guo P (2014) Enhancing Immunomodulation on Innate Immunity by Shape Transition Among RNA Triangle, Square, and Pentagon Nanovehicles. *Nucleic Acids Res.* 42: 9996-10004
104. Shu D, Moll WD, Deng Z, Mao C, & Guo P (2004) Bottom-Up Assembly of RNA Arrays and Superstructures As Potential Parts in Nanotechnology. *Nano Lett.* 4: 1717-1723
105. Shu Y, Shu D, Haque F, & Guo P (2013) Fabrication of PRNA Nanoparticles to Deliver Therapeutic RNAs and Bioactive Compounds into Tumor Cells. *Nat. Protoc.* 8: 1635-1659
106. Petrov AI, Zirbel CL, & Leontis NB (2013) Automated Classification of RNA 3D Motifs and the RNA 3D Motif Atlas. *RNA* 19: 1327-1340
107. Abraham M, Dror O, Nussinov R, & Wolfson HJ (2008) Analysis and Classification of RNA Tertiary Structures. *RNA.* 14: 2274-2289
108. Grabow WW, Zakrevsky P, Afonin KA, Chworos A, Shapiro BA, & Jaeger L (2011) Self-Assembling RNA Nanorings Based on RNAI/II Inverse Kissing Complexes. *Nano Lett.* 11: 878-887
109. Chworos A, Severcan I, Koyfman AY, Weinkam P, Oroudjev E, Hansma HG, & Jaeger L (2004) Building Programmable Jigsaw Puzzles With RNA. *Science* 306: 2068-2072
110. Severcan I, Geary C, VE, CA, & Jaeger L (2009) Square-Shaped RNA Particles From Different RNA Folds. *Nano Lett.* 9: 1270-1277
111. Dibrov SM, McLean J, Parsons J, & Hermann T (2011) Self-Assembling RNA Square. *Proc. Natl. Acad. Sci. U. S. A.* 108: 6405-6408

112. Parlea L, Bindewald E, Sharan R, Bartlett N, Moriarty D, Oliver J, Afonin KA, & Shapiro BA (2016) Ring Catalog: A Resource for Designing Self-Assembling RNA Nanostructures. *Methods* 103: 128-137
113. Nasalean L, Baudrey S, Leontis NB, & Jaeger L (2006) Controlling RNA Self-Assembly to Form Filaments. *Nucleic Acids Res.* 34: 1381-1392
114. Geary C, Chworos A, & Jaeger L (2010) Promoting RNA Helical Stacking Via A-Minor Junctions. *Nucleic Acids Res.* 39: 1066-1080
115. Ishikawa J, Furuta H, & Ikawa Y (2013) RNA Tectonics (TectoRNA) for RNA Nanostructure Design and Its Application in Synthetic Biology. *Wiley. Interdiscip. Rev. RNA.* 4: 651-664
116. Severcan I, Geary C, Chworos A, Voss N, Jacovetty E, & Jaeger L (2010) A Polyhedron Made of TRNAs. *Nat. Chem.* 2: 772-779
117. Yu JW, Liu ZY, Jiang W, Wang GS, & Mao CD (2015) De Novo Design of an RNA Tile That Self-Assembles into a Homo-Octameric Nanoprism. *Nature Communications* 6: 5724-5729
118. Bindewald E, Grunewald C, Boyle B, O'Connor M, & Shapiro BA (2008) Computational Strategies for the Automated Design of RNA Nanoscale Structures From Building Blocks Using NanoTiler. *Journal of Molecular Graphics & Modelling* 27: 299-308
119. Jossinet F, Ludwig TE, & Westhof E (2010) Assemble: an Interactive Graphical Tool to Analyze and Build RNA Architectures at the 2D and 3D Levels. *Bioinformatics.* 26: 2057-2059
120. Martinez HM, Maizel JV, & Shapiro BA (2008) RNA2D3D: A Program for Generating, Viewing, and Comparing 3-Dimensional Models of RNA. *J. Biomol. Str. Dyn.* 25: 669-683
121. Busch A & Backofen R (2007) INFO-RNA--a Server for Fast Inverse RNA Folding Satisfying Sequence Constraints. *Nucleic Acids Res.* 35: W310-W313

122. Zadeh JN, Steenberg CD, Bois JS, Wolfe BR, Pierce MB, Khan AR, Dirks RM, & Pierce NA (2011) NUPACK: Analysis and Design of Nucleic Acid Systems. *J. Comput. Chem.* 32: 170-173
123. Yingling YG & Shapiro BA (2007) Computational Design of an RNA Hexagonal Nanoring and an RNA Nanotube. *Nano Letters* 7: 2328-2334
124. Afonin KA, Bindewald E, Yaghoubian AJ, Voss N, Jacovetty E, Shapiro BA, & Jaeger L (2010) In Vitro Assembly of Cubic RNA-Based Scaffolds Designed in Silico. *Nat. Nanotechnol.* 5: 676-682
125. Daubendiek S, Ryan K, & Took E (1995) Rolling-Circle RNA Synthesis: Circular Oligonucleotides As Efficient Substrates for T7 RNA Polymerase. *J. Am. Chem. Soc.* 117 (29): 7818-7819
126. Khisamutdinov EF, Jasinski DL, & Guo P (2014) RNA As a Boiling-Resistant Anionic Polymer Material to Build Robust Structures With Defined Shape and Stoichiometry. *ACS Nano.* 8: 4771-4781
127. Gustafson HH, Holt-Casper D, Grainger DW, & Ghandehari H (2015) Nanoparticle Uptake: The Phagocyte Problem. *Nano Today* 10: 487-510
128. Dobrovolskaia MA, Shurin M, & Shvedova AA (2016) Current Understanding of Interactions Between Nanoparticles and the Immune System. *Toxicol. Appl. Pharmacol.* 299: 78-89
129. Longmire M, Choyke PL, & Kobayashi H (2008) Clearance Properties of Nano-Sized Particles and Molecules As Imaging Agents: Considerations and Caveats. *Nanomedicine (Lond)* 3: 703-717
130. Hardonk MJ, Harms G, & Koudstaal J (1985) Zonal Heterogeneity of Rat Hepatocytes in the in Vivo Uptake of 17 Nm Colloidal Gold Granules. *Histochemistry* 83: 473-477
131. Sadauskas E, Danscher G, Stoltenberg M, Vogel U, Larsen A, & Wallin H (2009) Protracted Elimination of Gold Nanoparticles From Mouse Liver. *Nanomedicine* 5: 162-169

132. Wilheml S, Tavares AJ, Dai Q, Ohta S, Audet J, Dvorak HF, & Chan WCW (2016) Analysis of Nanoparticle Delivery to Tumours. *Nature Reviews Materials* 1: 1-12
133. Gratton SE, Ropp PA, Pohlhaus PD, Luft JC, Madden VJ, Napier ME, & DeSimone JM (2008) The Effect of Particle Design on Cellular Internalization Pathways. *Proc Natl Acad Sci U. S A* 105: 11613-11618
134. Canton I & Battaglia G (2012) Endocytosis at the Nanoscale. *Chem Soc Rev.* 41: 2718-2739
135. Champion JA & Mitragotri S (2006) Role of Target Geometry in Phagocytosis. *Proc Natl Acad Sci U. S A* 103: 4930-4934
136. Champion JA, Katare YK, & Mitragotri S (2007) Making Polymeric Micro- and Nanoparticles of Complex Shapes. *Proc Natl Acad Sci U. S A* 104: 11901-11904
137. Huang X, Li L, Liu T, Hao N, Liu H, Chen D, & Tang F (2011) The Shape Effect of Mesoporous Silica Nanoparticles on Biodistribution, Clearance, and Biocompatibility in Vivo. *ACS Nano* 5: 5390-5399
138. Gunawan C, Lim M, Marquis CP, & Amal R (2014) Nanoparticle-Protein Corona Complexes Govern the Biological Fates and Functions of Nanoparticles. *Journal of Materials Chemistry B* 2: 2060-2083
139. Wang AZ, Langer R, & Farokhzad OC (2012) Nanoparticle Delivery of Cancer Drugs. *Annu. Rev. Med.* 63: 185-198
140. Arvizo RR, Miranda OR, Moyano DF, Walden CA, Giri K, Bhattacharya R, Robertson JD, Rotello VM, Reid JM, & Mukherjee P (2011) Modulating Pharmacokinetics, Tumor Uptake and Biodistribution by Engineered Nanoparticles. *PLoS ONE* 6: e24374
141. Kim ST, Saha K, Kim C, & Rotello VM (2013) The Role of Surface Functionality in Determining Nanoparticle Cytotoxicity. *Acc. Chem Res* 46: 681-691
142. Moyano DF, Goldsmith M, Solfiell DJ, Landesman-Milo D, Miranda OR, Peer D, & Rotello VM (2012) Nanoparticle Hydrophobicity Dictates Immune Response. *J Am. Chem Soc* 134: 3965-3967

143. He Q, Zhang Z, Gao F, Li Y, & Shi J (2011) In Vivo Biodistribution and Urinary Excretion of Mesoporous Silica Nanoparticles: Effects of Particle Size and PEGylation. *Small* 7: 271-280
144. Liu Y, Hu Y, & Huang L (2011) Influence of Polyethylene Glycol Density and Surface Lipid on Pharmacokinetics and Biodistribution of Lipid-Calcium-Phosphate Nanoparticles. *Biomaterials* 35: 3027-3034
145. Zhang XD, Wu D, Shen X, Liu PX, Fan FY, & Fan SJ (2012) In Vivo Renal Clearance, Biodistribution, Toxicity of Gold Nanoclusters. *Biomaterials* 33: 4628-4638
146. Gaucher G, Asahina K, Wang J, & Leroux JC (2009) Effect of Poly(N-Vinyl-Pyrrolidone)-Block-Poly(D,L-Lactide) As Coating Agent on the Opsonization, Phagocytosis, and Pharmacokinetics of Biodegradable Nanoparticles. *Biomacromolecules* 10: 408-416
147. Dobrovolskaia MA, Aggarwal P, Hall JB, & McNeil SE (2008) Preclinical Studies to Understand Nanoparticle Interaction With the Immune System and Its Potential Effects on Nanoparticle Biodistribution. *Mol Pharm* 5: 487-495
148. Khisamutdinov EF, Jasinski DL, Li H, Zhang K, Chiu W, & Guo P (2016) Fabrication of RNA 3D Nanoprism for Loading and Protection of Small RNAs and Model Drugs. *Advanced Materials* 28: 10079-10087
149. Khisamutdinov EF, Bui MN, Jasinski D, Zhao Z, Cui Z, & Guo P (2015) Simple Method for Constructing RNA Triangle, Square, Pentagon by Tuning Interior RNA 3WJ Angle From 60 Degrees to 90 Degrees or 108 Degrees. *Methods Mol Biol* 1316: 181-193
150. Jasinski D, Khisamutdinov EF, Lyubchenko YL, & Guo P (2014) Physicochemically Tunable Poly-Functionalized RNA Square Architecture With Fluorogenic and Ribozymatic Properties. *ACS Nano* 8: 7620-7629
151. Shu D, Huang L, Hoepflich S, & Guo P (2003) Construction of Phi29 DNA-Packaging RNA (PRNA) Monomers, Dimers and Trimers With Variable Sizes and Shapes As Potential Parts for Nano-Devices. *J. Nanosci. Nanotechnol.* 3: 295-302

152. Haque F, Shu D, Shu Y, Shlyakhtenko L, Rychahou P, Evers M, & Guo P (2012) Ultrastable Synergistic Tetravalent RNA Nanoparticles for Targeting to Cancers. *Nano Today* 7: 245-257
153. Shu D, Khisamutdinov E, Zhang L, & Guo P (2013) Programmable Folding of Fusion RNA Complex Driven by the 3WJ Motif of Phi29 Motor PRNA. *Nucleic Acids Res.* 42: e10
154. Novikova IV, Hassan BH, Mirzoyan MG, & Leontis NB (2010) Engineering Cooperative Tecto-RNA Complexes Having Programmable Stoichiometries. *Nucleic Acids Res.* 39(7): 2903-2917
155. Ohno H, Kobayashi T, Kabata R, Endo K, Iwasa T, Yoshimura SH, Takeyasu K, Inoue T, & Saito H (2011) Synthetic RNA-Protein Complex Shaped Like an Equilateral Triangle. *Nat. Nanotechnol.* 6: 116-120
156. Jaeger L & Chworos A (2006) The Architectonics of Programmable RNA and DNA Nanostructures. *Curr Opin Struct Biol.* 16: 531-543
157. Shapiro BA, Bindewald E, Kasprzak W, & Yingling Y (2008) Protocols for the in Silico Design of RNA Nanostructures. *Methods Mol. Biol.* 474: 93-115
158. Guo P (2012) Rolling Circle Transcription of Tandem SiRNA to Generate Spherulitic RNA Nanoparticles for Cell Entry. *Mol Ther-Nucleic Acids* 1: e36
159. Leontis NB & Westhof E (2002) The Annotation of RNA Motifs. *Comp Funct. Genomics* 3: 518-524
160. Shu Y, Shu D, Diao Z, Shen G, & Guo P (2009) Fabrication of Polyvalent Therapeutic RNA Nanoparticles for Specific Delivery of SiRNA, Ribozyme and Drugs to Targeted Cells for Cancer Therapy. *IEEE/NIH Life Science Systems and Applications Workshop* 9-12
161. Garver K & Guo P (2000) Mapping the Inter-RNA Interaction of Phage Phi29 by Site-Specific Photoaffinity Crosslinking. *J Biol Chem* 275(4): 2817-2824
162. Chen C, Sheng S, Shao Z, & Guo P (2000) A Dimer As a Building Block in Assembling RNA: A Hexamer That Gears Bacterial Virus Phi29 DNA-Translocating Machinery. *J Biol Chem* 275(23): 17510-17516

163. Cayrol B, Nogues C, Dawid A, Sagi I, Silberzan P, & Isambert H (2009) A Nanostructure Made of a Bacterial Noncoding RNA. *J. Am. Chem. Soc.* 131: 17270-17276
164. Lescoute A & Westhof E (2006) Topology of Three-Way Junctions in Folded RNAs. *RNA*. 12: 83-93
165. Walter F, Murchie AI, Duckett DR, & Lilley DM (1998) Global Structure of Four-Way RNA Junctions Studied Using Fluorescence Resonance Energy Transfer. *RNA*. 4: 719-728
166. Lilley DM (2000) Structures of Helical Junctions in Nucleic Acids. *Q. Rev. Biophys.* 33: 109-159
167. Batey RT, Rambo RP, & Doudna JA (1999) Tertiary Motifs in RNA Structure and Folding. *Angew. Chem. Int. Ed Engl.* 38: 2326-2343
168. Zhang H, Endrizzi JA, Shu Y, Haque F, Sauter C, Shlyakhtenko LS, Lyubchenko Y, Guo P, & Chi YI (2013) Crystal Structure of 3WJ Core Revealing Divalent Ion-Promoted Thermostability and Assembly of the Phi29 Hexameric Motor PRNA. *RNA* 19: 1226-1237
169. Collins TJ (2007) ImageJ for Microscopy. *Biotechniques* 43: 25-30
170. Lyubchenko YL & Shlyakhtenko LS (2009) AFM for Analysis of Structure and Dynamics of DNA and Protein-DNA Complexes. *Methods* 47: 206-213
171. Lyubchenko YL, Gall AA, Shlyakhtenko LS, Harrington RE, Jacobs BL, Oden PI, & Lindsay SM (1992) Atomic Force Microscopy Imaging of Double Stranded DNA and RNA. *J Biomol Struct Dyn* 10: 589-606
172. Chadalavada DM & Bevilacqua PC (2009) Analyzing RNA and DNA Folding Using Temperature Gradient Gel Electrophoresis (TGGE) With Application to in Vitro Selections. *Methods Enzymol.* 468: 389-408
173. Afonin KA, Cieply DJ, & Leontis NB (2008) Specific RNA Self-Assembly With Minimal Paranemic Motifs. *J. Am. Chem. Soc.* 130: 93-102

174. Petrov AI, Zirbel CL, & Leontis NB (2011) WebFR3D--a Server for Finding, Aligning and Analyzing Recurrent RNA 3D Motifs. *Nucleic Acids Res.* 39: W50-W55
175. Sarver M, Zirbel CL, Stombaugh J, Mokdad A, & Leontis NB (2008) FR3D: Finding Local and Composite Recurrent Structural Motifs in RNA 3D Structures. *Journal of Mathematical Biology* 56: 215-252
176. Gu H, Chao J, Xiao SJ, & Seeman NC (2009) Dynamic Patterning Programmed by DNA Tiles Captured on a DNA Origami Substrate. *Nat. Nanotechnol.* 4: 245-248
177. Seeman NC (2003) DNA in a Material World. *Nature* 421: 427-431
178. Service RF (2002) Nanotechnology. Biology Offers Nanotech a Helping Hand. *Science* 298: 2322-2323
179. Craighead HG (2000) Nanoelectromechanical Systems. *Science* 290: 1532-1536
180. Fennimore AM, Yuzvinsky TD, Han WQ, Fuhrer MS, Cumings J, & Zettl A (2003) Rotational Actuators Based on Carbon Nanotubes. *Nature* 424: 408-410
181. Haque F, Lunn J, Fang H, Smithrud D, & Guo P (2012) Real-Time Sensing and Discrimination of Single Chemicals Using the Channel of Phi29 DNA Packaging Nanomotor. *ACS Nano* 6: 3251-3261
182. Gerion D, Parak WJ, Williams SC, Zanchet D, Micheel CM, & Alivisatos AP (2002) Sorting Fluorescent Nanocrystals With DNA. *J Am. Chem Soc.* 124: 7070-7074
183. Wendell D, Jing P, Geng J, Subramaniam V, Lee TJ, Montemagno C, & Guo P (2009) Translocation of Double-Stranded DNA Through Membrane-Adapted Phi29 Motor Protein Nanopores. *Nat. Nanotechnol.* 4: 765-772
184. Abdelmawla S, Guo S, Zhang L, Pulukuri S, Patankar P, Conley P, Trebley J, Guo P, & Li QX (2011) Pharmacological Characterization of Chemically Synthesized Monomeric PRNA Nanoparticles for Systemic Delivery. *Molecular Therapy* 19: 1312-1322

185. Wang S, Haque F, Rychahou PG, Evers BM, & Guo P (2013) Engineered Nanopore of Phi29 DNA-Packaging Motor for Real-Time Detection of Single Colon Cancer Specific Antibody in Serum. *ACS Nano* 7: 9814-9822
186. Kukowska-Latallo JF, Candido KA, Cao Z, Nigavekar SS, Majoros IJ, Thomas TP, Balogh LP, Khan MK, & Baker JR, Jr. (2005) Nanoparticle Targeting of Anticancer Drug Improves Therapeutic Response in Animal Model of Human Epithelial Cancer. *Cancer Res* 65: 5317-5324
187. Hansma HG, Oroudjev E, Baudrey S, & Jaeger L (2003) TectoRNA and 'Kissing-Loop' RNA: Atomic Force Microscopy of Self-Assembling RNA Structures. *J Microsc.* 212: 273-279
188. Reblova K, Strelcova Z, Kulhanek P, Besseova I, Mathews DH, Van Nostrand K, Yildirim I, Turner DH, & Sponer J (2010) An RNA Molecular Switch: Intrinsic Flexibility of 23S RRNA Helices 40 and 68 5'-UAA/5'-GAN Internal Loops Studied by Molecular Dynamics Methods. *Journal of Chemical Theory and Computation* 6: 910-929
189. Guo P (2005) RNA Nanotechnology: Engineering, Assembly and Applications in Detection, Gene Delivery and Therapy. *Journal of Nanoscience and Nanotechnology* 5(12): 1964-1982
190. Shu Y, Cinier M, Shu D, & Guo P (2011) Assembly of Multifunctional Phi29 PRNA Nanoparticles for Specific Delivery of SiRNA and Other Therapeutics to Targeted Cells. *Methods* 54: 204-214
191. Afonin KA, Kireeva M, Grabow WW, Kashlev M, Jaeger L, & Shapiro BA (2012) Co-Transcriptional Assembly of Chemically Modified RNA Nanoparticles Functionalized With SiRNAs. *Nano. Lett.* 12: 5192-5195
192. Afonin KA, Grabow WW, Walker FM, Bindewald E, Dobrovolskaia MA, Shapiro BA, & Jaeger L (2011) Design and Self-Assembly of SiRNA-Functionalized RNA Nanoparticles for Use in Automated Nanomedicine. *Nat. Protoc.* 6: 2022-2034
193. Jaeger L (2009) Defining the Syntax for Self-Assembling RNA Tertiary Architectures. *Nucleic Acids Symp. Ser. (Oxf)* 83-84

194. Feng L, Li SK, Liu H, Liu CY, LaSance K, Haque F, Shu D, & Guo P (2014) Ocular Delivery of PRNA Nanoparticles: Distribution and Clearance After Subconjunctival Injection. *Pharmaceutical Research* 31: 1046-1058
195. Moghimi SM, Hunter AC, & Andresen TL (2012) Factors Controlling Nanoparticle Pharmacokinetics: An Integrated Analysis and Perspective. *Annual Review of Pharmacology and Toxicology, Vol 52* 52: 481-503
196. Merkel TJ, Chen K, Jones SW, Pandya AA, Tian SM, Napier ME, Zamboni WE, & DeSimone JM (2012) The Effect of Particle Size on the Biodistribution of Low-Modulus Hydrogel PRINT Particles. *Journal of Controlled Release* 162: 37-44
197. Igarashi E (2008) Factors Affecting Toxicity and Efficacy of Polymeric Nanomedicines. *Toxicology and Applied Pharmacology* 229: 121-134
198. Zhang S (2003) Fabrication of Novel Biomaterials Through Molecular Self-Assembly. *Nat. Biotechnol.* 21: 1171-1178
199. Lyubchenko YL, Shlyakhtenko LS, & Ando T (2011) Imaging of Nucleic Acids With Atomic Force Microscopy. *Methods* 54: 274-283
200. Guo P, Shu Y, Binzel D, & Cinier M (2012) Synthesis, Conjugation, and Labeling of Multifunctional PRNA Nanoparticles for Specific Delivery of SiRNA, Drugs and Other Therapeutics to Target Cells. *Methods in Molecular Biology* 928: 197-219
201. Reif R, Haque F, & Guo P (2013) Fluorogenic RNA Nanoparticles for Monitoring RNA Folding and Degradation in Real Time in Living Cells. *Nucleic Acid Ther.* 22(6): 428-437
202. Zuker M (2003) Mfold Web Server for Nucleic Acid Folding and Hybridization Prediction. *Nucleic Acids Res.* 31: 3406-3415
203. Prabha S, Zhou WZ, Panyam J, & Labhasetwar V (2002) Size-Dependency of Nanoparticle-Mediated Gene Transfection: Studies With Fractionated Nanoparticles. *Int. J. Pharm.* 244: 105-115

204. Huang XL, Teng X, Chen D, Tang FQ, & He JQ (2010) The Effect of the Shape of Mesoporous Silica Nanoparticles on Cellular Uptake and Cell Function. *Biomaterials* 31: 438-448
205. Dash BC, Rethore G, Monaghan M, Fitzgerald K, Gallagher W, & Pandit A (2010) The Influence of Size and Charge of Chitosan/Polyglutamic Acid Hollow Spheres on Cellular Internalization, Viability and Blood Compatibility. *Biomaterials* 31: 8188-8197
206. Gratton SEA, Ropp PA, Pohlhaus PD, Luft JC, Madden VJ, Napier ME, & DeSimone JM (2008) The Effect of Particle Design on Cellular Internalization Pathways. *Proceedings of the National Academy of Sciences of the United States of America* 105: 11613-11618
207. Li Z, Wei B, Nangreave J, Lin CX, Liu Y, Mi YL, & Yan H (2009) A Replicable Tetrahedral Nanostructure Self-Assembled From a Single DNA Strand. *J. Am. Chem. Soc.* 131: 13093-13098
208. Goedken ER & Marqusee S (2001) Native-State Energetics of a Thermostabilized Variant of Ribonuclease HI. *J Mol Biol* 314: 863-871
209. Cuchillo CM, Nogues MV, & Raines RT (2011) Bovine Pancreatic Ribonuclease: Fifty Years of the First Enzymatic Reaction Mechanism. *Biochemistry* 50: 7835-7841
210. Paige JS, Wu KY, & Jaffrey SR (2011) RNA Mimics of Green Fluorescent Protein. *Science* 333: 642-646
211. Babendure JR, Adams SR, & Tsien RY (2003) Aptamers Switch on Fluorescence of Triphenylmethane Dyes. *J. Am. Chem. Soc.* 125: 14716-14717
212. Baugh C, Grate D, & Wilson C (2000) 2.8 Å Crystal Structure of the Malachite Green Aptamer. *J. Mol. Biol.* 301: 117-128
213. Zhu LF, Yi RD, Lu CD, Wang Y, & Qi Gr (1994) Ribozyme That Site-Specifically Cleaves the RNA Fragment Derived From Core Antigen Gene of Hepatitis B Virus in Vitro. *Chin J Biochem Biophy* 26: 239-249

214. Afonin KA, Danilov EO, Novikova IV, & Leontis NB (2008) TokenRNA: A New Type of Sequence-Specific, Label-Free Fluorescent Biosensor for Folded RNA Molecules. *Chembiochem* 9: 1902-1905
215. Morrissey DV, Lockridge JA, Shaw L, Blanchard K, Jensen K, Breen W, Hartsough K, Machemer L, Radka S, Jadhav V, Vaish N, Zinnen S, Vargeese C, Bowman K, Shaffer CS, Jeffs LB, Judge A, Maclachlan I, & Polisky B (2005) Potent and Persistent in Vivo Anti-HBV Activity of Chemically Modified SiRNAs. *Nat. Biotechnol.* 23: 1002-1007
216. Maeda H, Nakamura H, & Fang J (2013) The EPR Effect for Macromolecular Drug Delivery to Solid Tumors: Improvement of Tumor Uptake, Lowering of Systemic Toxicity, and Distinct Tumor Imaging in Vivo. *Adv. Drug Deliv. Rev.* 65: 71-79
217. Kawasaki AM, Casper MD, Freier SM, Lesnik EA, Zounes MC, Cummins LL, Gonzalez C, & Cook PD (1993) Uniformly Modified 2'-Deoxy-2'-Fluoro Phosphorothioate Oligonucleotides As Nuclease-Resistant Antisense Compounds With High Affinity and Specificity for RNA Targets. *J. Med. Chem.* 36: 831-841
218. Bae YH & Park K (2011) Targeted Drug Delivery to Tumors: Myths, Reality and Possibility. *J. Control Release* 153: 198-205
219. Lipfert J, Skinner GM, Keegstra JM, Hensgens T, Jager T, Dulin D, Kober M, Yu Z, Donkers SP, Chou FC, Das R, & Dekker NH (2014) Double-Stranded RNA Under Force and Torque: Similarities to and Striking Differences From Double-Stranded DNA. *Proc. Natl. Acad. Sci. U. S. A* 111: 15408-15413
220. Herrero-Galan E, Fuentes-Perez ME, Carrasco C, Valpuesta JM, Carrascosa JL, Moreno-Herrero F, & rias-Gonzalez JR (2013) Mechanical Identities of RNA and DNA Double Helices Unveiled at the Single-Molecule Level. *J. Am. Chem. Soc.* 135: 122-131
221. Fadee B (2012) Clear and Present Danger? Engineered Nanoparticles and the Immune System. *Swiss Medical Weekly* 142: w13609
222. Vindigni G, Raniolo S, Ottaviani A, Falconi M, Franch O, Knudsen BR, Desideri A, & Biocca S (2016) Receptor-Mediated Entry of Pristine Octahedral DNA Nanocages in Mammalian Cells. *ACS Nano* 10: 5971-5979

223. Owens EA, Hyun H, Dost TL, Lee JH, Park G, Pham DH, Park MH, Choi HS, & Henary M (2016) Near-Infrared Illumination of Native Tissues for Image-Guided Surgery. *J Med. Chem* 59: 5311-5323
224. Porcu EP, Salis A, Gavini E, Rassu G, Maestri M, & Giunchedi P (2016) Indocyanine Green Delivery Systems for Tumour Detection and Treatments. *Biotechnol Adv.* 34: 768-789
225. Wang F, Yang K, Wang Z, Ma Y, Gutkind JS, Hida N, Niu G, & Tian J (2016) Combined Image Guided Monitoring the Pharmacokinetics of Rapamycin Loaded Human Serum Albumin Nanoparticles With a Split Luciferase Reporter. *Nanoscale* 8: 3991-4000
226. Huynh AS, Estrella V, Stark VE, Cohen AS, Chen T, Casagni TJ, Josan JS, Lloyd MC, Johnson J, Kim J, Hruba VJ, Vagner J, & Morse DL (2016) Tumor Targeting and Pharmacokinetics of a Near-Infrared Fluorescent-Labeled Delta-Opioid Receptor Antagonist Agent, Dmt-Tic-Cy5. *Mol Pharm* 13: 534-544
227. Pereira P, Correia A, & Gama FM (2016) In Vivo Imaging of Glycol Chitosan-Based Nanogel Biodistribution. *Macromol. Biosci.* 16: 432-440
228. Li H, Zhang K, Pi F, Guo S, Shlyakhtenko L, Chiu W, Shu D, & Guo P (2016) Controllable Self-Assembly of RNA Tetrahedrons With Precise Shape and Size for Cancer Targeting. *Adv. Mater.* 28: 7501-7507
229. Lumiprobe (2017) Cyanine dyes. (<https://www.lumiprobe.com/tech/cyanine-dyes>).
230. Berlier JE, Rothe A, Buller G, Bradford J, Gray DR, Filanoski BJ, Telford WG, Yue S, Liu J, Cheung CY, Chang W, Hirsch JD, Beechem JM, Haugland RP, & Haugland RP (2003) Quantitative Comparison of Long-Wavelength Alexa Fluor Dyes to Cy Dyes: Fluorescence of the Dyes and Their Bioconjugates. *J Histochem. Cytochem.* 51: 1699-1712
231. Silverman BD (2003) Hydrophobicity of Transmembrane Proteins: Spatially Profiling the Distribution. *Protein Sci* 12: 586-599
232. Rees DC, DeAntonio L, & Eisenberg D (1989) Hydrophobic Organization of Membrane Proteins. *Science* 245: 510-513

233. Cornette JL, Cease KB, Margalit H, Spouge JL, Berzofsky JA, & DeLisi C (1987) Hydrophobicity Scales and Computational Techniques for Detecting Amphipathic Structures in Proteins. *J Mol Biol* 195: 659-685
234. Eisenberg D, Schwarz E, Komaromy M, & Wall R (1984) Analysis of Membrane and Surface Protein Sequences With the Hydrophobic Moment Plot. *J Mol Biol* 179: 125-142
235. Usman N, Ogilvie KK, Jiang MY, & Cedergren RJ (1987) The Automated Chemical Synthesis of Long Oligoribonucleotides Using 2'-O-Silylated Ribonucleoside 3'-O-Phosphoramidites on a Controlled-Pore Glass Support: Synthesis of a 43-Nucleotide Sequence Similar to the 3'-Half Molecule of an Escherichia Coli Formylmethionine TRNA. *J. Am. Chem. Soc.* 109: 7845-7854
236. Kyte J & Doolittle RF (1982) A Simple Method for Displaying the Hydrophobic Character of a Protein. *J Mol Biol* 157: 105-132
237. Engelman DM, Steitz TA, & Goldman A (1986) Identifying Nonpolar Transbilayer Helices in Amino Acid Sequences of Membrane Proteins. *Annu. Rev. Biophys Biophys Chem* 15: 321-353
238. Yardeni T, Eckhaus M, Morris HD, Huizing M, & Hoogstraten-Miller S (2011) Retro-Orbital Injections in Mice. *Lab Animal* 40: 155-160
239. Shargel, L., Susanna, W., and Yu, A. (2012) Chapter 10: Physiological Drug Distribution and Protein Binding. *Applied Biopharmaceutics & Pharmacokinetics*, McGraw-Hill Medical, New York
240. Hansch, C. and Leo, A. (1979) Chapter 5: Calculation of Octanol-Water Partition Coefficients from Fragments, etc. *Substituent Constants for Correlation Analysis in Chemistry and Biology*, **John Wiley & Sons Ltd.**, New York
241. Chen C, Zhang C, & Guo P (1999) Sequence Requirement for Hand-in-Hand Interaction in Formation of PRNA Dimers and Hexamers to Gear Phi29 DNA Translocation Motor. *RNA* 5: 805-818
242. Nagarajan Pattabiraman, Hugo M.Martinez, & Bruce A.Shapiro (2002) Molecular Modeling and Dynamics Studies of HIV-1 Kissing Loop Structures. *Journal of Biomolecular Structure & Dynamics* 20: 397-411

243. Li H, Lee T, Dziubla T, Pi F, Guo S, Xu J, Li C, Haque F, Liang X, & Guo P (2015) RNA As a Stable Polymer to Build Controllable and Defined Nanostructures for Material and Biomedical Applications. *Nano Today* 10: 631-655
244. Hao C, Li X, Tian C, Jiang W, Wang G, & Mao C (2014) Construction of RNA Nanocages by Re-Engineering the Packaging RNA of Phi29 Bacteriophage. *Nat. Commun.* 5: 3890
245. Erben CM, Goodman RP, & Turberfield AJ (2006) Single-Molecule Protein Encapsulation in a Rigid DNA Cage. *Angewandte Chemie-International Edition* 45: 7414-7417
246. Juul S, Iacovelli F, Falconi M, Kragh SL, Christensen B, Frohlich R, Franch O, Kristoffersen EL, Stougaard M, Leong KW, Ho YP, Sorensen ES, Birkedal V, Desideri A, & Knudsen BR (2013) Temperature-Controlled Encapsulation and Release of an Active Enzyme in the Cavity of a Self-Assembled DNA Nanocage. *ACS Nano* 7: 9724-9734
247. Lo PK, Karam P, Aldaye FA, McLaughlin CK, Hamblin GD, Cosa G, & Sleiman HF (2010) Loading and Selective Release of Cargo in DNA Nanotubes With Longitudinal Variation. *Nature Chemistry* 2: 319-328
248. Zhang C, Li X, Tian C, Yu GM, Li YL, Jiang W, & Mao CD (2014) DNA Nanocages Swallow Gold Nanoparticles (AuNPs) to Form AuNP@DNA Cage Core-Shell Structures. *ACS Nano* 8: 1130-1135
249. Edwardson TGW, Carneiro KMM, McLaughlin CK, Serpell CJ, & Sleiman HF (2013) Site-Specific Positioning of Dendritic Alkyl Chains on DNA Cages Enables Their Geometry-Dependent Self-Assembly. *Nature Chemistry* 5: 868-875
250. Nguyen DH, Defina SC, Fink WH, & Dieckmann T (2002) Binding to an RNA Aptamer Changes the Charge Distribution and Conformation of Malachite Green. *J. Am. Chem. Soc.* 124: 15081-15084
251. Xu W & Lu Y (2010) Label-Free Fluorescent Aptamer Sensor Based on Regulation of Malachite Green Fluorescence. *Anal. Chem.* 82: 574-578
252. Haque F, Wang S, Stites C, Chen L, Wang C, & Guo P (2015) Single Pore Translocation of Folded, Double-Stranded, and Tetra-Stranded DNA Through

Channel of Bacteriophage Phi29 DNA Packaging Motor. *Biomaterials* 53: 744-752

253. Shu Y, Cinier M, Fox SR, Ben-Johnathan N, & Guo P (2011) Assembly of Therapeutic PRNA-SiRNA Nanoparticles Using Bipartite Approach. *Molecular Therapy* 19: 1304-1311
254. Guex N & Peitsch MC (1997) SWISS-MODEL and the Swiss-PdbViewer: An Environment for Comparative Protein Modeling. *Electrophoresis* 18: 2714-2723
255. van Dongen HM, Masoumi N, Witwer KW, & Pegtel DM (2016) Extracellular Vesicles Exploit Viral Entry Routes for Cargo Delivery. *Microbiol. Mol. Biol. Rev.* 80: 369-386
256. Kolpashchikov DM (2005) Binary Malachite Green Aptamer for Fluorescent Detection of Nucleic Acids. *J. Am. Chem. Soc.* 127: 12442-12443
257. Ikehara M, Ohtsuka E, Tokunaga T, Nishikawa S, Uesugi S, Tanaka T, Aoyama Y, Kikyodani S, Fujimoto K, Yanase K, Fuchimura K, & Morioka H (1986) Inquiries Into the Structure-Function Relationship of Ribonuclease-T1 Using Chemically Synthesized Coding Sequences. *Proceedings of the National Academy of Sciences of the United States of America* 83: 4695-4699
258. Pfeiffer S, KarimiNejad Y, & Ruterjans H (1997) Limits of NMR Structure Determination Using Variable Target Function Calculations: Ribonuclease T-1, a Case Study. *J Mol Biol* 266: 400-423
259. Green NM & Toms EJ (1973) Properties of Subunits of Avidin Coupled to Sepharose. *Biochem. J.* 133: 687-698
260. Leamon CP & Low PS (2001) Folate-Mediated Targeting: From Diagnostics to Drug and Gene Delivery. *Drug Discovery Today* 6: 44-51
261. Afonin KA, Viard M, Tedbury P, Bindewald E, Parlea L, Howington M, Valdman M, Johns-Boehme A, Brainerd C, Freed EO, & Shapiro BA (2016) The Use of Minimal RNA Toeholds to Trigger the Activation of Multiple Functionalities. *Nano Lett* 16: 1746-1753

262. Afonin KA, Viard M, Koyfman AY, Martins AN, Kasprzak WK, Panigaj M, Desai R, Santhanam A, Grabow WW, Jaeger L, Heldman E, Reiser J, Chiu W, Freed EO, & Shapiro BA (2014) Multifunctional RNA Nanoparticles. *Nano Lett.* 14: 5662-5671
263. Grabow WW & Jaeger L (2014) RNA Self-Assembly and RNA Nanotechnology. *Accounts of Chemical Research* 47: 1871-1880
264. Liu Y, Kuan CT, Mi J, Zhang X, Clary BM, Bigner DD, & Sullenger BA (2009) Aptamers Selected Against the Unglycosylated EGFRvIII Ectodomain and Delivered Intracellularly Reduce Membrane-Bound EGFRvIII and Induce Apoptosis. *Biol. Chem.* 390: 137-144
265. Esposito CL, Passaro D, Longobardo I, Condorelli G, Marotta P, Affuso A, de F, V, & Cerchia L (2011) A Neutralizing RNA Aptamer Against EGFR Causes Selective Apoptotic Cell Death. *PLoS. One.* 6: e24071
266. Rockey WM, Hernandez FJ, Huang SY, Cao S, Howell CA, Thomas GS, Liu XY, Lapteva N, Spencer DM, McNamara JO, Zou X, Chen SJ, & Giangrande PH (2011) Rational Truncation of an RNA Aptamer to Prostate-Specific Membrane Antigen Using Computational Structural Modeling. *Nucleic Acid Ther.* 21: 299-314
267. Maslak M & Martin CT (1993) Kinetic Analysis of T7 RNA Polymerase Transcription Initiation From Promoters Containing Single-Stranded Regions. *Biochemistry* 32: 4281-4285
268. Chamberlin M & Ring J (1973) Characterization of T7-Specific Ribonucleic Acid Polymerase. 1. General Properties of the Enzymatic Reaction and the Template Specificity of the Enzyme. *J Biol Chem* 248: 2235-2244
269. Chamberlin M & Ring J (1973) Characterization of T7-Specific Ribonucleic Acid Polymerase. II. Inhibitors of the Enzyme and Their Application to the Study of the Enzymatic Reaction. *J Biol Chem* 248: 2245-2250
270. Roh YH, Deng JZ, Dreaden EC, Park JH, Yun DS, Shopsowitz KE, & Hammond PT (2015) A Multi-RNAi Microsponge Platform for Simultaneous Controlled Delivery of Multiple Small Interfering RNAs. *Angew. Chem. Int. Ed Engl.* 55: 3347-3351

271. Mohsen MG & Kool ET (2016) The Discovery of Rolling Circle Amplification and Rolling Circle Transcription. *Acc. Chem Res* 49: 2540-2550
272. Mezger A, Ohrmalm C, Herthnek D, Blomberg J, & Nilsson M (2014) Detection of Rotavirus Using Padlock Probes and Rolling Circle Amplification. *PLoS ONE* 9: e111874
273. Li X, Zheng F, & Ren R (2015) Detecting MiRNA by Producing RNA: a Sensitive Assay That Combines Rolling-Circle DNA Polymerization and Rolling Circle Transcription. *Chem Commun. (Camb.)* 51: 11976-11979
274. Daubendiek SL & Kool ET (1997) Generation of Catalytic RNAs by Rolling Transcription of Synthetic DNA Nanocircles. *Nat Biotechnol* 15: 273-277
275. Diegelman AM & Kool ET (1998) Generation of Circular RNAs and Trans-Cleaving Catalytic RNAs by Rolling Transcription of Circular DNA Oligonucleotides Encoding Hairpin Ribozymes. *Nucleic Acids Res* 26: 3235-3241
276. Shopsowitz KE, Roh YH, Deng ZJ, Morton SW, & Hammond PT (2014) RNAi-Microsponges Form Through Self-Assembly of the Organic and Inorganic Products of Transcription. *Small* 10: 1623-1633
277. Zheng HN, Ma YZ, & Xiao SJ (2014) Periodical Assembly of Repetitive RNA Sequences Synthesized by Rolling Circle Transcription With Short DNA Staple Strands to RNA-DNA Hybrid Nanowires. *Chem Commun. (Camb.)* 50: 2100-2103
278. Han D, Park Y, Kim H, & Lee JB (2014) Self-Assembly of Free-Standing RNA Membranes. *Nature Communications* 5: 4367
279. Kim H, Park Y, & Lee JB (2015) Self-Assembled Messenger RNA Nanoparticles (mRNA-NPs) for Efficient Gene Expression. *Sci Rep.* 5: 12737
280. Furukawa K, Abe H, Abe N, Harada M, Tsuneda S, & Ito Y (2008) Fluorescence Generation From Tandem Repeats of a Malachite Green RNA Aptamer Using Rolling Circle Transcription. *Bioorg. Med. Chem Lett* 18: 4562-4565
281. McCall MJ, Hendry P, & Jennings PA (1992) Minimal Sequence Requirements for Ribozyme Activity. *Proc Natl Acad Sci U. S A* 89: 5710-5714

282. Ruffner DE, Dahm SC, & Uhlenbeck OC (1989) Studies on the Hammerhead RNA Self-Cleaving Domain. *Gene* 82: 31-41
283. Ruffner DE, Stormo GD, & Uhlenbeck OC (1990) Sequence Requirements of the Hammerhead RNA Self-Cleavage Reaction. *Biochemistry* 29: 10695-10702
284. Wang X, Li C, Gao X, Wang J, & Liang X (2015) Preparation of Small RNAs Using Rolling Circle Transcription and Site-Specific RNA Disconnection. *Mol Ther. Nucleic Acids* 4: e215
285. Afonin KA, Desai R, Viard M, Kireeva ML, Bindewald E, Case CL, Maciag AE, Kasprzak WK, Kim T, Sappe A, Stepler M, Kewalramani VN, Kashlev M, Blumenthal R, & Shapiro BA (2014) Co-Transcriptional Production of RNA-DNA Hybrids for Simultaneous Release of Multiple Split Functionalities. *Nucleic Acids Res.* 42: 2085-2097
286. Ducani C, Bernardinelli G, & Hogberg B (2014) Rolling Circle Replication Requires Single-Stranded DNA Binding Protein to Avoid Termination and Production of Double-Stranded DNA. *Nucleic Acids Res* 42: 10596-10604
287. Kuman R, El-Sagheer A, Tumpane J, Lincoln P, Wilhelmsson LM, & Brown T (2007) Template-Directed Oligonucleotide Strand Ligation, Covalent Intramolecular DNA Circularization and Catenation Using Click Chemistry. *J. Am. Chem. Soc.* 129: 6859-6864
288. Murray JB, Terwey DP, Maloney L, Karpeisky A, Usman N, Beigelman L, & Scott WG (1998) The Structural Basis of Hammerhead Ribozyme Self-Cleavage. *Cell* 92: 665-673
289. Blount KF & Uhlenbeck OC (2002) The Hammerhead Ribozyme. *Biochem. Soc. Trans.* 30: 1119-1122
290. Lindstrom UM, Chandrasekaran RA, Orbai L, Helquist SA, Miller GP, Oroudjev E, Hansma HG, & Kool ET (2002) Artificial Human Telomeres From DNA Nanocircle Templates. *Proc Natl Acad Sci U. S A* 99: 15953-15958
291. Hartig JS, Fernandez-Lopez S, & Kool ET (2005) Guanine-Rich DNA Nanocircles for the Synthesis and Characterization of Long Cytosine-Rich Telomeric DNAs. *Chembiochem* 6: 1458-1462

292. Jang M, Kim JH, Nam HY, Kwon IC, & Ahn HJ (2015) Design of a Platform Technology for Systemic Delivery of SiRNA to Tumours Using Rolling Circle Transcription. *Nat Commun.* 6: 7930
293. Mitra S, Shcherbakova IV, Altman RB, Brenowitz M, & Laederach A (2008) High-Throughput Single-Nucleotide Structural Mapping by Capillary Automated Footprinting Analysis. *Nucleic Acids Res.* 36: e63
294. Shukla GC, Haque F, Tor Y, Wilhelmsson LM, Toulme JJ, Isambert H, Guo P, Rossi JJ, Tenenbaum SA, & Shapiro BA (2011) A Boost for the Emerging Field of RNA Nanotechnology. *ACS Nano* 5: 3405-3418
295. Shu Y, Pi F, Sharma A, Rajabi M, Haque F, Shu D, Leggas M, Evers BM, & Guo P (2014) Stable RNA Nanoparticles As Potential New Generation Drugs for Cancer Therapy. *Adv. Drug Deliv. Rev.* 66C: 74-89
296. Leontis N, Sweeney B, Haque F, & Guo P (2013) Conference Scene: Advances in RNA Nanotechnology Promise to Transform Medicine. *Nanomedicine* 8: 1051-1054
297. Trautmann L, Janbazian L, Chomont N, Said EA, Gimmig S, Bessette B, Boulassel MR, Delwart E, Sepulveda H, Balderas RS, Routy JP, Haddad EK, & Sekaly RP (2006) Upregulation of PD-1 Expression on HIV-Specific CD8+ T Cells Leads to Reversible Immune Dysfunction. *Nat. Med.* 12: 1198-1202
298. Zassenhaus HP, Butow RA, & Hannon YP (1982) Rapid Electroelution of Nucleic-Acids From Agarose and Acrylamide Gels. *Analyt Biochem* 125: 125-130
299. Anderson AC, Scaringe SA, Earp BE, & Frederick CA (1996) HPLC Purification of RNA for Crystallography and NMR. *RNA* 2: 110-117
300. Glisin V, Crkvenjar R, & Byus C (1974) Ribonucleic-Acid Isolated by Cesium-Chloride Centrifugation. *Biochemistry* 13: 2633-2637
301. Ali A & Roossinck MJ (2007) Rapid and Efficient Purification of Cowpea Chlorotic Mottle Virus by Sucrose Cushion Ultracentrifugation. *J Virol Meth* 141: 84-86

302. Higashi K, Narayana KS, Adams HR, & Busch H (1966) Utilization of Citric Acid Procedure and Zonal Ultracentrifugation for Mass Isolation of Nuclear Rna From Walker 256 Carcinosarcoma. *Cancer Research* 26: 1582-1590
303. Lin CX, Perrault SD, Kwak M, Graf F, & Shih WM (2013) Purification of DNA-Origami Nanostructures by Rate-Zonal Centrifugation. *Nucleic Acids Res.* 41: e40
304. Eikenber EF, Bickle TA, Traut RR, & Price CA (1970) Separation of Large Quantities of Ribosomal Subunits by Zonal Ultracentrifugation. *European Journal of Biochemistry* 12: 113-116
305. Patsch JR, Sailer S, Kostner G, Sandhofe F, Holasek A, & Braunste H (1974) Separation of Main Lipoprotein Density Classes From Human Plasma by Rate-Zonal Ultracentrifugation. *Journal of Lipid Research* 15: 356-366
306. Guo P, Erickson S, & Anderson D (1987) A Small Viral RNA Is Required for *in Vitro* Packaging of Bacteriophage Phi29 DNA. *Science* 236: 690-694
307. Hong G, Antaris A, & Dai H (2017) Near-Infrared Fluorophores for Biomedical Imaging. *Nature Biomedical Engineering* 1: 0010
308. Wang D, Zhang Z, O'Loughlin E, Lee T, Houel S, O'Carroll D, Tarakhovsky A, Ahn NG, & Yi R (2012) Quantitative Functions of Argonaute Proteins in Mammalian Development. *Genes Dev.* 26: 693-704
309. Moore CB, Guthrie EH, Huang MT, & Taxman DJ (2010) Short Hairpin RNA (ShRNA): Design, Delivery, and Assessment of Gene Knockdown. *Methods Mol. Biol.* 629: 141-158
310. Guo S, Tschammer N, Mohammed S, & Guo P (2005) Specific Delivery of Therapeutic RNAs to Cancer Cells Via the Dimerization Mechanism of Phi29 Motor PRNA. *Hum. Gene. Ther.* 16: 1097-1109
311. Kwon YJ (2011) Before and After Endosomal Escape: Roles of Stimuli-Converting SiRNA/Polymer Interactions in Determining Gene Silencing Efficiency. *Acc. Chem. Res.* 45: 1077-1088

312. Jasinski D, Schwartz C, Haque F, & Guo P (2015) Large Scale Purification of RNA Nanoparticles by Preparative Ultracentrifugation. *Methods in Molecular Biology* 1297: 67-82

Vita

Daniel L. Jasinski

Educational Institutions

Texas A&M University	2008 - 2012	Bachelor of Science	Chemistry
University of Kentucky	2012 - 2017	Doctor of Philosophy	Pharmaceutical Sciences

Professional Publications

- 1) **Jasinski, DL**; Li, H; and Guo, P. The Effect of Size and Shape of RNA Nanoparticles on Biodistribution. *Molecular Therapy. Under Revision. (First author)*
- 2) **Jasinski, DL**; Binzel, DW; Guo, P. Co-Transcriptional Assembly of RNA Nanoparticles *via* Rolling Circle Transcription of a Fully Double Stranded Circular DNA Template. *Under submission. (First author)*
- 3) **Jasinski, DL**; Yin, H; Li, Z; Guo, P. The Hydrophobic Effect from Conjugated Chemicals or Drugs on *in Vivo* Biodistribution of RNA Nanoparticles. *Human Gene Therapy. Under Revision. (First Author)*
- 4) Haque, F; Binzel, DW; **Jasinski, DL**; Guo, P. RNA as an Elastic Thermostable Material for Fabricating RNA Nanoarchitectures. *WIREs RNA. Under Revision.*
- 5) Xu, Z; Sun, Y; Weber, JK; Cao, Y; Wang, W; **Jasinski, DL**; Guo, P; Zhou, R; Li, J. Directional mechanical stability of Bacteriophage ϕ 29 motor's 3WJ-pRNA: extraordinary robustness along portal axis. *Science Advances.* 2017.
- 6) **Jasinski, DL**; Haque, F; Binzel, DW; Guo, P. The Advancement of the Emerging Field of RNA Nanotechnology. *ACS Nano.* 2017. **(First Author)**
- 7) Benkato, K; O'Brien, B; Bui, MN; **Jasinski, DL**; Guo, P; Khisamutdinov, EF. Evaluation of Thermal Stability of RNA Nanoparticles by Temperature Gradient Gel Electrophoresis (TGGE) in Native Condition. *Methods in Molecular Biology.* 2017.
- 8) Haque, F; Xu, C; **Jasinski, DL**; Li, H; Guo, P. Using Planar Phi29 pRNA Three-Way Junction to Control Size and Shape of RNA Nanoparticles for Biodistribution Profiling in Mice. *Methods in Molecular Biology.* 2017.
- 9) Khisamutdinov, EF*; **Jasinski, DL***; Li, H; Zhang, K; Chiu, W; Guo, P. Fabrication of RNA 3D Nanoprism for Loading and Protection of Small RNAs and Model Drugs. *Advanced Materials.* 2016. **(Co-First author)**

- 10) Lee, T; Abels, S; Khisamutdinov, EF; Qui, M; **Jasinski, DL**; Zhao, Z; Qu, T; Choi, JW; Guo, P. Conceptual, potential and advance in computer design and *in vivo* computation applying RNA nanotechnology. *Molecular Nanostructure and Nanotechnology*. 2016.
- 11) **Jasinski, DL**; Haque, F; Guo, P, Purification of RNA Nanoparticles by Ultracentrifugation. *Methods in Molecular Biology*. 2015. (**First Author**)
- 12) Khisamutdinov EF, Bui MN, **Jasinski DL**, Zhao Z, Cui Z, Guo P. Simple Method for Constructing RNA Triangle, Square, Pentagon by Tuning Interior RNA 3WJ Angle from 60° to 90° or 108°. *Methods in Molecular Biology*. 2015.
- 13) Schwartz, CT*; **Jasinski, DL***; Guo, P. Characterizing RNA Nanoparticle by Analytical Ultracentrifugation. *Beckman Coulter Life Sciences: Application Notes*. 2015. (**Co-First Author**)
- 14) Khisamutdinov, EF; **Jasinski, DL**; Guo, P. RNA as a Boiling-Resistant Anionic Polymer Material to Build Robust Structures with Defined Shape and Stoichiometry. *ACS Nano*. 2014. (**Editor's Choice Article**)
- 15) **Jasinski, DL**; Khisamutdinov, EF; Lyubchenko, YL; Guo, P. Physicochemically Tunable Poly-Functionalized RNA Square Architecture with Fluorogenic and Ribozymatic Properties. *ACS Nano*. 2014. (**First Author**)
- 16) Khisamutdinov, EF*; Li, H*; **Jasinski, DL***; Chen, J; Fu, J; Guo, P, Enhancing Immunomodulation on Innate Immunity by Shape Transition among RNA Triangle, Square and Pentagon Nanovehicles. *Nucleic Acids Research*. 2014. (**Co-First Author**)